UNDERSTANDING IONIC CONDUCTION IN SOLID ELECTROLYTES FOR LITHIUM AND SODIUM ION BATTERIES

A Dissertation
Presented to
The Academic Faculty

by

Shan Xiong

In Partial Fulfillment
of the Requirements for the Degree
Doctor of Philosophy in the
Georgia W. Woodruff School of Mechanical Engineering

Georgia Institute of Technology
December 2020

UNDERSTANDING IONIC CONDUCTION IN SOLID ELECTROLYTES FOR LITHIUM AND SODIUM ION BATTERIES

Approved by:

Dr. Hailong Chen, Advisor
School of Mechanical Engineering
Georgia Institute of Technology

Dr. Angus Wilkinson
School of Chemical and Biochemistry
Georgia Institute of Technology

Dr. Meilin Liu
School of Materials Science and Engineering
Georgia Institute of Technology

Dr. Ting Zhu
School of Mechanical Engineering
Georgia Institute of Technology

Dr. Matthew McDowell
School of Materials Science and Engineering
Georgia Institute of Technology

Date Approved: November 18, 2020

“For I know the plans I have for you,” declares the Lord, “plans to prosper you and not to harm you, plans to give you hope and a future.”

Jeremiah 29:11

ACKNOWLEDGEMENTS

Many people have inspired, supported, and accompanied me throughout my Ph.D. journey, without whom this dissertation would not have been possible. I would like to express my sincere gratitude to my mentors, my coworkers, my funding agencies, and my families and friends.

First, I would like to thank my advisor, Dr. Hailong Chen, for his continuous support, guidance, and trust. As one of his earliest graduate students at Georgia Tech, we worked closely together to build up the lab, set up equipment, and explore new ideas. There were many challenges and difficulties, but the experience was uniquely valuable to me with his help and encouragement, teaching me to be resourceful and creative. Dr. Chen is not only knowledgeable in science, passionate and diligent in his research, but also kind and supportive in my studies and career development. In addition to research, he also mentored me to be a critical thinker, a creative problem solver, and an effective communicator. I am very grateful for my time in Dr. Chen's group, which prepared me well for my future endeavors.

I would also like to thank my committee members, Dr. Meilin Liu, Dr. Matthew McDowell, Dr. Angus Wilkinson, and Dr. Ting Zhu for their insightful advice for this dissertation. Their passion and mastery in their respective disciplines has inspired me to strive for excellence in all that I do. Their constructive comments have made this thesis a better-refined product.

I am very fortunate to have worked with many excellent coworkers in Georgia Tech. In our lab, I enjoyed working with a group of self-driven, hard-working, and fun fellow students. Dr. Xuetian Ma, the only graduate student before I joined the group, helped me tremendously both in my schoolwork and my life as a new international student. We supported each other through numerous challenges in our journeys, from engineering classes, qualifying exams, to the painstaking night-long experiments in national labs. I will always be grateful for her company and mentorship that made my transition to graduate school easier and more enjoyable. Dr. Lufeng Yang and Dr. Hai Wang, who were visiting scholars in our group, set great examples of tackling challenging research problems and dedicated much time for lively discussions with me. Zhantao Liu, Malte McDaniel, and Dr. Haibo Rong are great research partners who have inspired and contributed greatly to my exploration in solid-state ionic conductors. I am especially thankful to Zhantao, who frequently shared great ideas and insights with me and never ceased to inspire me with his dedication to this field. In addition, there are many other graduate and undergraduate students in our group who have helped and motivated me in different ways. To name a few, I want to thank Yifan Ma, Shuan Ma, Aijie Han, Madison Ives, William Disser, Yangyang Li, Jacqueline Baidoo, Bo Nan, Changhao Chen, Shikai Jin, Zoe Holderness, Jake Thiemann, and many others for their collaboration and companionship.

Outside our group, I am grateful to many world-class colleagues and mentors in the broader Georgia Tech community. I would like to thank Pan Liu, Biao Wan, Dr. Qian Wang, and Dr. Hao Luo for their help and support in my research projects. I sincerely appreciate Dr. Yuanzhi Tang for generously sharing her perspectives in career development and for always encouraging me in my research and studies.

I would like to sincerely thank my research collaborators outside the Georgia Tech community – Dr. Yifei Mo, Dr. Xingfeng He, and Adelaide Nolan from University of Maryland, Dr. Shuo Chen, Dr. Zhensong Ren, and Brian McElhenny from University of Houston. Many thanks to their excellent work and contributions to our research projects. Special thanks go to Dr. Jianming Bai and Dr. Eric Dooryhee from Brookhaven National Laboratory, Dr. Wenqian Xu and Dr. Andrey Yakovenko from Argonne National Laboratory, as well as Dr. Jue Liu, Dr. Bohang Song, and Dr. Ashfia Huq from Oak Ridge National Laboratory. Their expertise was absolutely essential during our beamline trips, and their dedicated assistance and discussions were crucial to the completion of this dissertation. Dr. Ning Chen from Canadian Light Source also gave me insightful advice on my beamline results and I am very grateful for his help.

I also acknowledge the financial support from Georgia Tech's faculty startup fund, Georgia Tech's Institute for Materials (IMat) 2019 seed fund, and the National Science Foundation during my Ph.D. studies.

In addition to my research community, I have been blessed with great friends at the Westminster Christian Fellowship and North Avenue Presbyterian Church, who brightened my days in tough times. I am especially thankful to Jason Chen and Jasmine Shi for listening to my struggles and constantly praying for me. My sincere thanks go to so many other friends who have supported and cheered me up throughout graduate school and for being my family away from home.

I would like to express my heartfelt gratitude to my family for always loving me and supporting me unconditionally and selflessly. My parents have always had faith in me

and did their best to comfort, sympathize with, and lift me up. They traveled halfway around the globe to visit me when I could not fly back home. Thanks to my brother Sihui and my cousin Yilu for visiting me and cheering me up through bouts of loneliness and homesickness. I owe them much thanks.

I am genuinely grateful to Edwin for holding my hands, for loving me and praying for me, and for spending so much quality and memorable time with me during my Ph.D. and in the years to come. His love, patience, and optimism have made my Ph.D. journey so much more joyful than it would otherwise have been.

TABLE OF CONTENTS

LIST OF TABLES

LIST OF FIGURES

LIST OF SYMBOLS AND ABBREVIATIONS

AIMD	*ab initio* molecular dynamics
ANL	Argonne National Laboratory
APS	Advanced Photon Source
ASBs	all-solid-state batteries
ASLBs	all-solid-state Li-ion batteries
ASNBs	all-solid-state Na-ion batteries
bcc	body-centered-cubic
BM	ball mill
BNL	Brookhaven National Laboratory
CV	cyclic voltammogram
DFT	density functional theory
DOS	density of states
ED	electron diffraction
EDS/EDX	energy dispersive X-ray spectroscopy
EIS	electrochemical impedance spectroscopy
EXAFS	extended X-ray absorption fine structure
GB	grain boundary
GGA	generalized-gradient approximation
GOF	goodness-of-fit
HSE	Heyd-Scuseria-Erznerhof
ICP-ES	inductively coupled plasma emission spectrometry
LATP	$Li_{1.3}Al_{0.3}Ti_{1.7}(PO_4)_3$
LGPS	$Li_{10}GeP_2S_{12}$

LIBs	lithium-ion batteries
LLZO	$Li_7La_3Zr_2O_{12}$
MP	*Material Project*
ND	neutron diffraction
NIBs	sodium-ion batteries
NMR	nuclear magnetic resonance
NSLS-II	National Synchrotron Light Source II
PBE	Perdew-Burke-Ernzerhof
PDF	pair distribution function
r.t.	room temperature
SEI	solid electrolyte interphase
SEM	scanning electron microscope
SEs	solid electrolytes
SSRL	Stanford Synchrotron Radiation Light source
VASP	Vienna *Ab initio* Simulation package
VT	variable temperature
XAS	X-ray absorption spectroscopy
XRD	X-ray diffraction

SUMMARY

All-solid-state batteries (ASBs) have attracted extensive attention in recent years because of their enhanced safety, improved power and energy density, and stability compared to conventional Li-ion battery technologies based on organic liquid electrolytes. On the other hand, low-cost electrochemical energy storage technologies beyond lithium chemistry are also highly desired for large-scale energy storage applications. All-solid-state Na ion batteries (ASNBs) are one of the promising candidates for grid-level energy storage owing to their low cost and outstanding safety properties. The key enabler of these new battery technologies is solid electrolyte (SE) materials with sufficient Li/Na ionic conductivity at room temperature and good electrochemical stability. To design and develop promising material candidates for ASBs rationally and efficiently, in-depth understanding of ionic conduction mechanism in solids and elucidation of the key governing structural parameters are critically desired. In this dissertation, I start with an introduction to the fundamentals of ion transport in crystalline solids and current technical challenges in SE material development, followed by studies on four lithium and sodium ion conductor systems to reveal the structure-property relationships in these material groups and demonstrate rational SE design and improvement towards commercial applications.

In the first study, through a joint computational and experimental investigation, a new group of lithium ion conductors, Zr-doped $LiTaSiO_5$, is identified and synthesized with greatly improved conductivities. As guided by our design strategies and first principles computation, we predict that the doping of Zr at the Ta site in $LiTaSiO_5$ sphene structure and Li insertion can activate the concerted migration of multiple Li ions, and

thereby significantly enhance the lithium ionic conductivity. These computationally predicted materials were successfully synthesized in the lab aided with cutting edge *in situ* XRD for synthesis. The samples with a doping level of 12.5% Zr showed an ionic conductivity of approximately 10^{-5} $S \cdot cm^{-1}$ at 30°C, which is three orders of magnitude higher than the undoped $LiTaSiO_5$. This study reveals that the sphene structure is a novel crystal structure motif for fast Li ion conduction, which offers abundant opportunities for further materials design and optimization with tuning chemical compositions and crystallographic features. More importantly, this study demonstrates a paradigm of rational materials design and electrochemical energy storage technology development with combined computational and experimental methods.

In the next three studies, various chalcogenide-based Na ion conductor systems are investigated to elucidate how the key structural parameters impact their conduction behavior from different perspectives. First, the study on $Na_3SbSe_{4-x}S_x$ solid solution series explores the effectiveness of isovalent substitution, which facilitates the ion transport via tuning the unit cell sizes and expanding the diffusion channels. It also reveals a non-monotonic relationship between the unit cell size and its Na^+ conductivity, suggesting that other structural descriptors, such as local disordering and chemical bonding, are also important contributors and should be carefully examined in materials design. Second, the investigation on structural evolution of milled Na_3SbS_4-NaCl mixtures using *in situ* XRD and PDF analysis proves that intense milling processes will destruct the long-range periodic structure of Na_3SbS_4 conductor and impact the ionic conductivity negatively. Nevertheless, this impact is reversible since the remaining structural units of $[SbS_4]^{3-}$ will be rearranged to form conductive Na_3SbS_4 phase upon annealing. Lastly, the study on a

series of cation- and anion- doped Na_4SnS_4 compounds demonstrates the effectiveness and flexibility of alio-valent substitution on tuning the crystal structures and boosting ion conductivities. It also shows that the increased defect concentration and enlarged diffusion channels are the key drivers for the improved conductivities in this material group. This strategy can be applied in many similar material groups when the lack of defects is the limiting factor for their ionic conductivities.

Based on these studies, a few future directions are proposed in the end to address the remaining technical challenges in achieving practical ASB technologies. The studies in this dissertation have demonstrated multiple effective material design strategies that have successfully delivered enhanced conduction performance in various material systems, which provides valuable insights for future SE material development and implementation in new battery configurations.

CHAPTER 1. INTRODUCTION

1.1 Background and Motivation: A Solid Future of Batteries

Rechargeable batteries are crucial for multiple applications, from consumer electronics, electric vehicles, to grid-level energy storage units built for stabilizing intermittent energy sources, such as wind and solar energy. Particularly, rechargeable lithium-ion batteries (LIBs) have been widely used in mobile devices and electric vehicles, while emerging sodium-ion batteries (NIBs) are considered a low-cost alternative for large-scale stationary energy storage. However, despite the encouraging advancement in LIBs and NIBs in energy density over the past decades, they are still facing challenges from market demands. Specifically, safety issues and limited energy densities have become the major concerns of current LIBs with organic liquid electrolyte, for which all-solid-state batteries (ASBs) are considered one of the most promising solutions and have attracted extensive research and development efforts in both industry and academia communities.

1.1.1 Promises of All-solid-state Batteries (ASBs)

All-solid-state batteries (ASBs), featuring nonflammable inorganic solid electrolytes (SEs) as the ionic transport media between the two electrodes, can eliminate the risks of fire and explosion caused by the flammable organic liquid electrolytes used in conventional LIBs. This is especially advantageous for applications where batteries are subject to strict safety requirements, such as electric vehicles. On the other hand, ASBs can offer higher energy densities on condition that Li metal anode can be safely used, which has much higher theoretical capacity than commercial graphite anode but was not used in

conventional LIBs due to the safety problem caused by the dendritic growth of Li-metal [1-3]. ASBs with suitable SEs will also allow the use of high-voltage cathodes that are not viable in commercial LIBs due to the limited electrochemical window of liquid electrolyte. Therefore, ASB technologies will promise improved energy densities compared to current commercial LIBs.

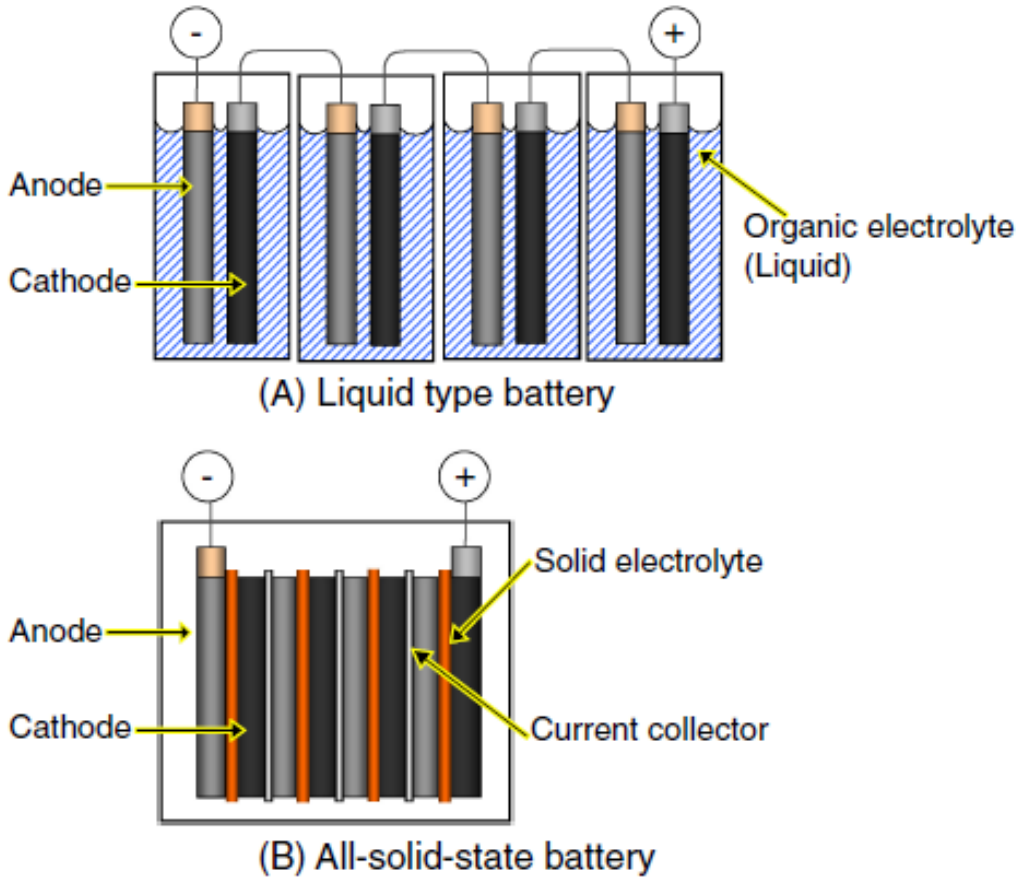

Figure 1.1 Schematic of (top) conventional lithium-ion batteries and (bottom) solid-state battery schematic. Reproduced with permission from [4].

In addition to advancement in battery chemistry, ASBs also provide a potentially more efficient battery pack configuration. With no presence of liquid components, ASB

systems can be designed as simplified, closely packed arrays of bipolar electrodes without internal short circuit, as shown in Figure 1.1 [4]. This consolidated configuration can further decrease the dead space between individual cells as in current battery modules and therefore deliver higher volumetric energy densities. This configuration is also promising and advantageous for vehicle power supplies where high voltage is often needed.

Because of technical advantages discussed above, battery researchers and engineers around the globe have been actively seeking and testing various materials to realize this new battery technology in the past decade. Recent reports on promising ASB systems in lab-scale tests have shown great progresses that are bringing this concept into practical prototypes. For example, Kanno *et al* have demonstrated that ASBs with an inorganic SE can outperform conventional LIBs in terms of power and energy density in a wide operational temperature range [5], as shown in Figure 1.2. Impressively, the power densities of all-solid-state Li-ion batteries (ASLBs) tested at 100°C were superior to supercapacitors, which was beyond the temperature region that convention LIBs can function.

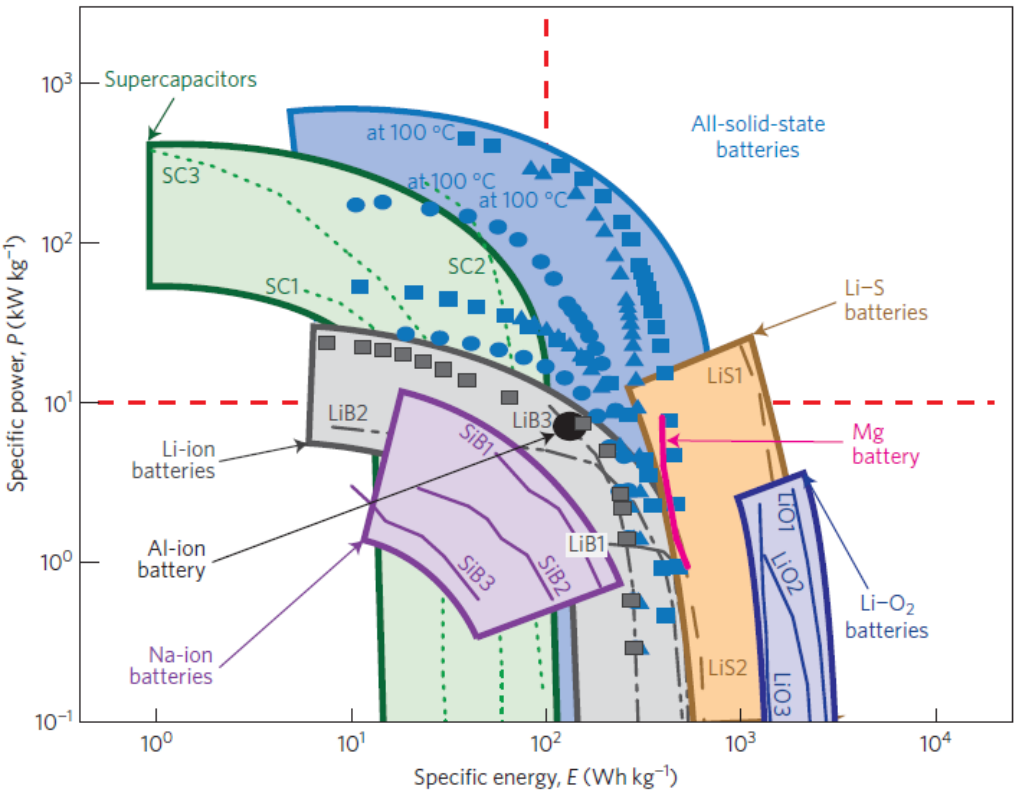

Figure 1.2 The Ragone plots of ASLBs and conventional batteries and capacitors. Reprinted by permission, Nature Publishing Group [5] © 2016.

In parallel with the rapid development of more powerful and safer LIBs, sodium-ion batteries (NIBs) stand out as a competitive and promising energy storage technology especially for large-scale applications where low materials and manufacturing costs are critically desired. Compared to limited and geographically scattered Li resources, sodium is among the most abundant elements in the Earth's crust [6] as shown in Figure 1.3. It can be considered as infinite resource in the ocean. With the global advocacy of renewable and clean energy sources such as solar and wind power, NIBs show great promises serving as a reliable and cost effective large-scale energy storage solution with readily available

material supply to level the fluctuations in the electrical grid powered by these intermittent energy sources [7-9].

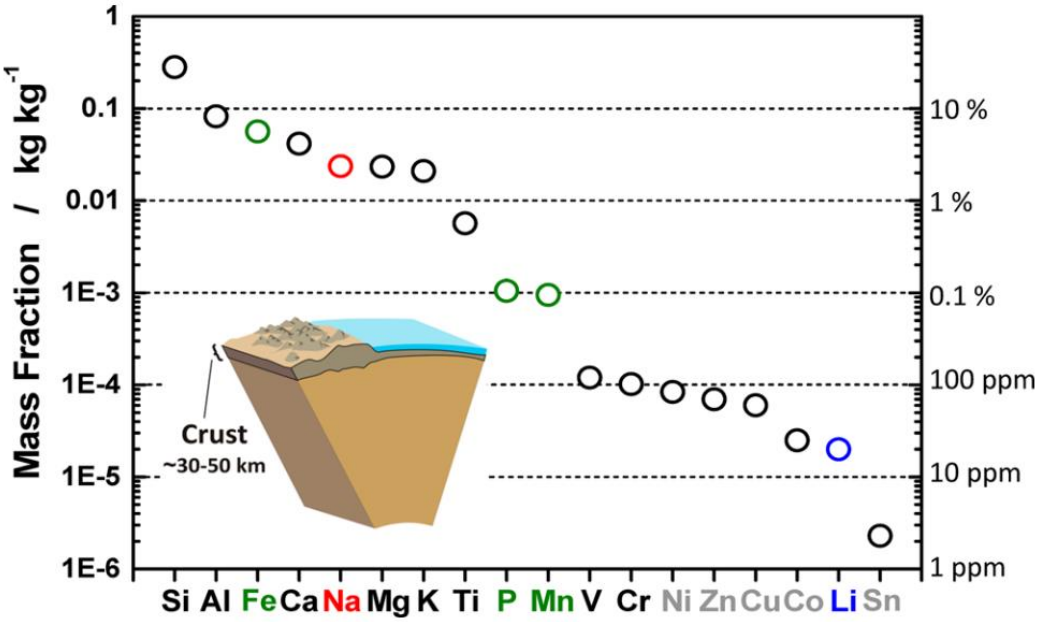

Figure 1.3 Elemental abundance in the Earth's crust. Reprinted with permission from [6]. © 2014 American Chemical Society.

Similar to the lithium counterpart, all-solid-state sodium-ion batteries (ASNBs) with non-flammable inorganic SEs are also attractive in terms of enhanced safety and potentially higher energy densities. Researchers have found that high temperatures may pose pronounced threats to battery systems with organic liquid electrolyte [10]. In such cases, solid-state electrolytes with better thermal stability can be an ideal alternative. Thus, ASNBs are considered one of the most promising energy storage solutions for practical large-scale grid-level applications in all climate conditions.

1.1.2 Grand Challenges in Solid-state Batteries

With widely recognized technological benefits, extensive research and development efforts across academic and industry communities have been invested on all-solid-state batteries (ASBs) and noticeable advancements have been demonstrated [2, 11-16]. However, there are still a number of major challenges towards the large-scale commercialization of ASBs.

At the material level, high-performance inorganic solid electrolytes (SEs), as the key enabler of ASBs, are greatly desired but not yet fully successfully identified. To replace liquid electrolyte and serve as the ionic transport media, the SE materials need to present sufficiently fast ionic conduction in the operating temperature range, typically around room temperature (r.t.). This could be challenging considering the sluggish ionic transport kinetics in most solids compared to liquids [17-19]. Beside the intrinsic bulk conductivity, it was found that synthesis methods and processing conditions are also critical in achieving superior ionic conductivities, especially for certain material categories that present high grain boundary resistance [20-23]. Therefore, special attentions are needed in terms of optimizing synthesis process to fully realize the material's optimal ionic conduction capabilities. Furthermore, high ionic conductivity alone is not sufficient to make a high-performance SE material in ASBs. Additional characteristics such as wide electrochemical window, good chemical, mechanical, and thermal stabilities, facile processability, and low cost are also critical metrics in evaluating promising material systems, which makes the task of designing and developing good SE material candidates complicated and challenging.

At the device or battery cell level, careful thoughts need to be given in the selection of electrode and electrolyte materials, considering their chemical, electrochemical and mechanical compatibilities. Simply replacing the liquid electrolyte in a conventional LIB/NIB system by a SE would not work as expected. Specifically, in an all-solid-state battery system, the interfaces between the SE and electrodes may exhibit large interfacial resistance and thus deteriorate the overall battery performance. A schematic of a typical ASB with Li metal anode is shown in Figure 1.4. For both anode and cathode sides, the main interfacial issues include physical contact, chemical stability, electrochemical stability, and dynamic volume and morphology variations during battery cycling, all of which are shown to have critical impacts to the battery performance by recent research [24-28].

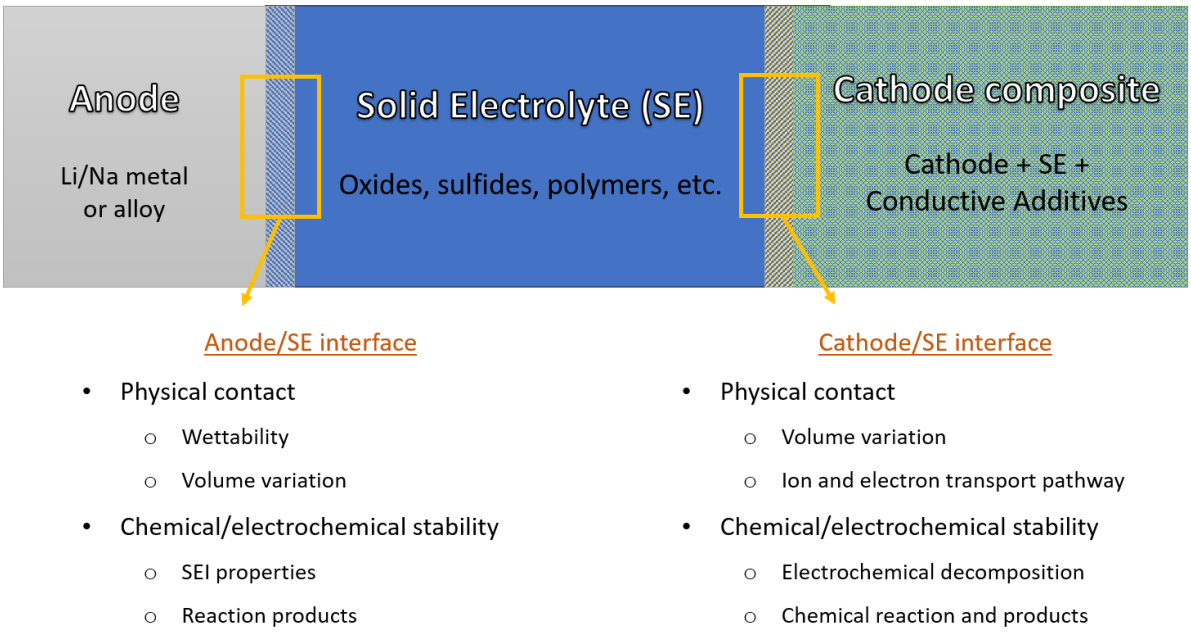

Figure 1.4 Schematic of compatibility issues associated with interfaces in ASBs. Derived from reference [29] - Published by The Royal Society of Chemistry.

In the composite cathode, intimate physical contact and good chemical/ electrochemical compatibility at the SE-cathode interfaces are the two key aspects to facilitate efficient ion and electron transport and ensure long cycle life. Due to the all-solid nature of SE-cathode or SE-cathode-additive combinations, point-to-point contacts are commonly observed, leading to small contacting area and large interfacial resistance and inhomogeneous electrical current density, which are detrimental to battery performance. The cyclic volume change of cathode component during charging and discharging makes it even more difficult to maintain intimate physical contacts among the particles. On the other hand, the chemical and electrochemical compatibility between active cathode and SE is another critical issue. A number of studies have reported severe performance degradation due to chemical or electrochemical reactions between SE and cathode materials during battery cycling [30-35].

On the anode side, taking an ASLB system with Li metal anode as an example, physical contact (i.e., Li wettability on SE surface) and electrochemical compatibility are also the critical issues. It was found that the decomposition/passivation products formed on the anode-SE interface play a critical role in the subsequent charge and discharge cycles. Fan *et al.* have summarized three types of interfaces formed between SEs and Li metal [36]: (1) thermodynamically stable interface with Li metal without side reactions, (2) ionically conducting and electronically insulating interfaces or solid electrolyte interphase (SEI), and (3) ionically and electronically conducting interfaces. While the first type is rarely formed in most SE-Li metal pairs, the formation of favorable SEI layers is a more commonly applicable way to ensure stable Li stripping and plating and suppress battery degradation. Specifically, type (2) SEI layer is preferred since an electronic insulator can

effectively block further reactions between SE and Li metal anode while maintaining ionic transport channels. For type (3) interfaces that are ionically and electronically conducting (or "mixed conductors"), continuous reactions will eventually consume the active materials and lead to cell failure. To avoid such failure, various interface engineering methods have been proposed and improved anode stability have been demonstrated in ASBs with a few particular SE materials [37-43].

Lastly, the scalable manufacturing of ASBs is still difficult and needs significant technological development. Currently most fabrication methods are limited to lab scale and certain material systems. Chen *et al.* have summarized four types of ASB configurations as shown in Figure 1.5 [11]. Among these methods, thin-film type of ASBs are less practical for large-scale energy storage applications due to high manufacturing costs despite its superior cycle life and compatibility with Li metal and high-voltage cathodes [44]. In comparison, fabrication methods of bulk type ASBs, such as heating, pressing, and roll-to-roll process, have a better chance to realize cost-effective ASB production, although there are still significant engineering obstacles to overcome for achieving economic mass production. Specifically, heat treatment is usually applied to ASBs with oxide electrolytes since high-temperature treatment can effectively decrease GB resistance and improve physical contact between SE particles. However, this method is energy-intensive and may present unfavorable mechanical properties. Cold-pressing for ASBs fabrication using sulfide electrolytes is more energy-efficient and usually shows better mechanical flexibility. But the downside is its poor air stability, which implies high storage, handling and transportation cost. The roll-to-roll stacking process, which is similar to current LIB production line, has the greatest potential of mass production based on existing

manufacturing technology. However, practical issues associated with polymer-based ASBs, such as low rate performance and interfacial instability [45-47], still requires advancements in material design and manufacturing technologies. Implementing other types of SEs into customized roll-to-roll process is potentially the ultimate solution for successful commercialization of ASBs if suitable materials and process conditions can be identified.

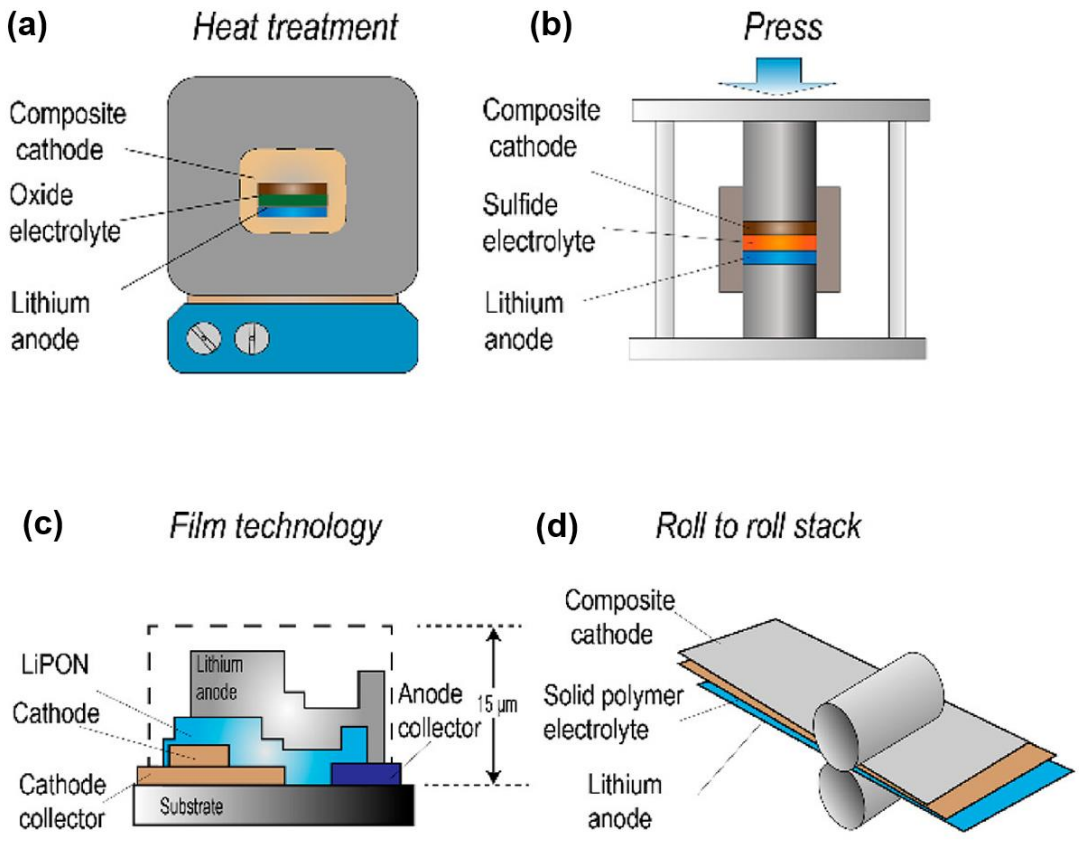

Figure 1.5 Four types of ASB fabrication methods. Reprinted with permission from [11] © (2020) American Chemical Society.

1.2 Superionic Conductors as Solid Electrolytes

As discussed above, one of the key tasks to facilitate practical ASBs is to find highly conductive solid materials to replace organic liquid electrolytes and serve as solid electrolytes (SEs) in all-solid-state Li- or Na-ion batteries. In a broader context, inorganic solid electrolytes also enable many other technologies such as solid oxide fuel cells and gas sensors. The development of fast ion conductors is therefore of broad impact. The studies on ionic conduction in solid materials has a long history. Observation of superionic conduction behavior in solids can be dated back to 1830s, when Ag_2S and β-PbF_2 were found to exhibit exceptionally high ionic conductivities under certain conditions [48]. While large groups of silver- and sodium-ion conductors have been identified with ionic conductivities comparable to that of liquid electrolytes after the 1960s [49-52], considerable research efforts have also led to remarkable breakthroughs in Li ion conductors for potential applications in energy storage systems.

1.2.1 Categories of Crystalline Superionic Conductors

In the past decades, a number of crystal structures with decent Li^+ conductivities have been identified, such as LISICON [53-56], argyrodites [57-59], garnets [60-62], NASICON [63-65], perovskites [66-68], and so on. As summarized by Yang *et al.* in Figure 1.6, we can see that a number of material categories are able to achieve high Li ionic conductivities close to liquid electrolyte benchmark at room temperature, such as LISICON-like, argyrodite, and garnet types [69]. Meanwhile, it is worth noticing that the conductivities within each material category may vary significantly (up to 8 orders of magnitude), suggesting a great potential of structure tuning in delivering enhanced ionic

conductivities. Furthermore, through structural and compositional adjustment within certain type of structure, high-performance SE materials with other promising properties, such as wide electrochemical stability, favorable mechanical flexibility, and wide operation temperature range, may be designed and obtained.

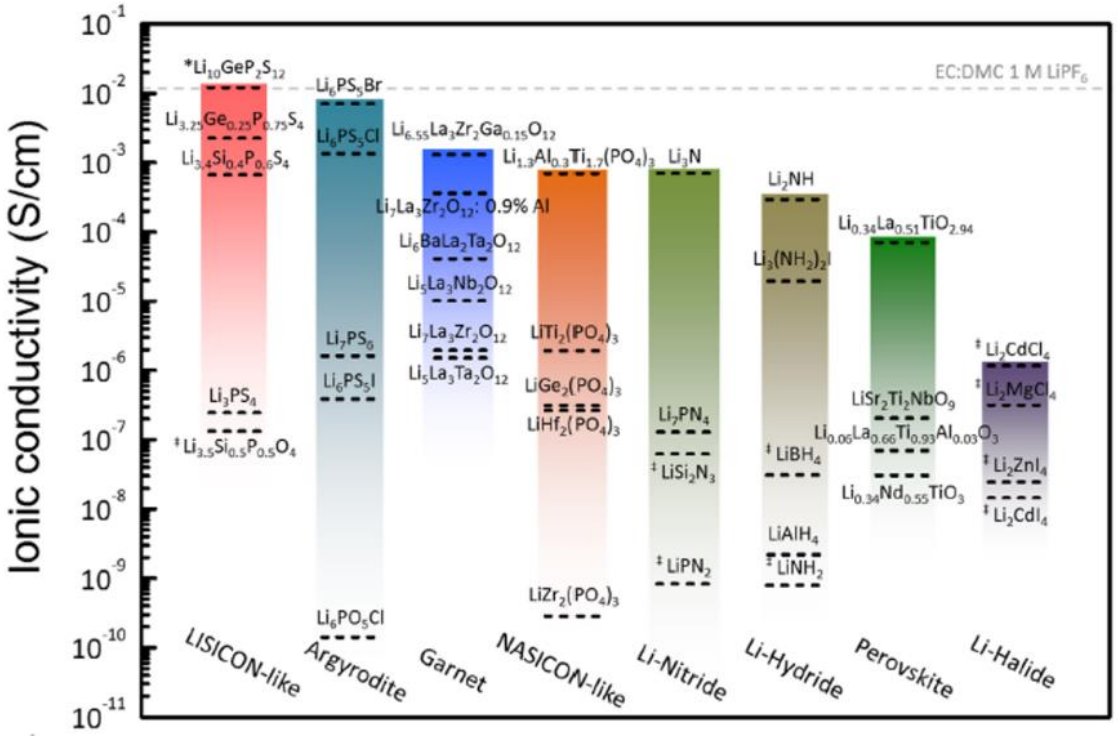

Figure 1.6 Reported total ionic conductivity of solid-state lithium-ion conductors at room temperature. Reprinted with permission from [69]. © (2016) American Chemical Society.

On the other hand, if we focus on the compositions of these Li ion conductors, they can be simply classified into sulfide, oxide, hydride, and halide, etc. Such classification neglects the crystal structural or lattice framework details and mainly focuses on their ionic conductivities, synthetic or processing costs, and chemical/electrochemical stability, etc. The comparison of the advantages and drawbacks of these material categories is shown in

the radar plots in Figure 1.7, which was derived from the review by Wang *et al* [70]. Since high ionic conductivity is not the sole criterion in selecting promising SE materials for ASBs, other dimensions included in this radar plot should also be examined to have a comprehensive evaluation of material candidates for practical battery applications.

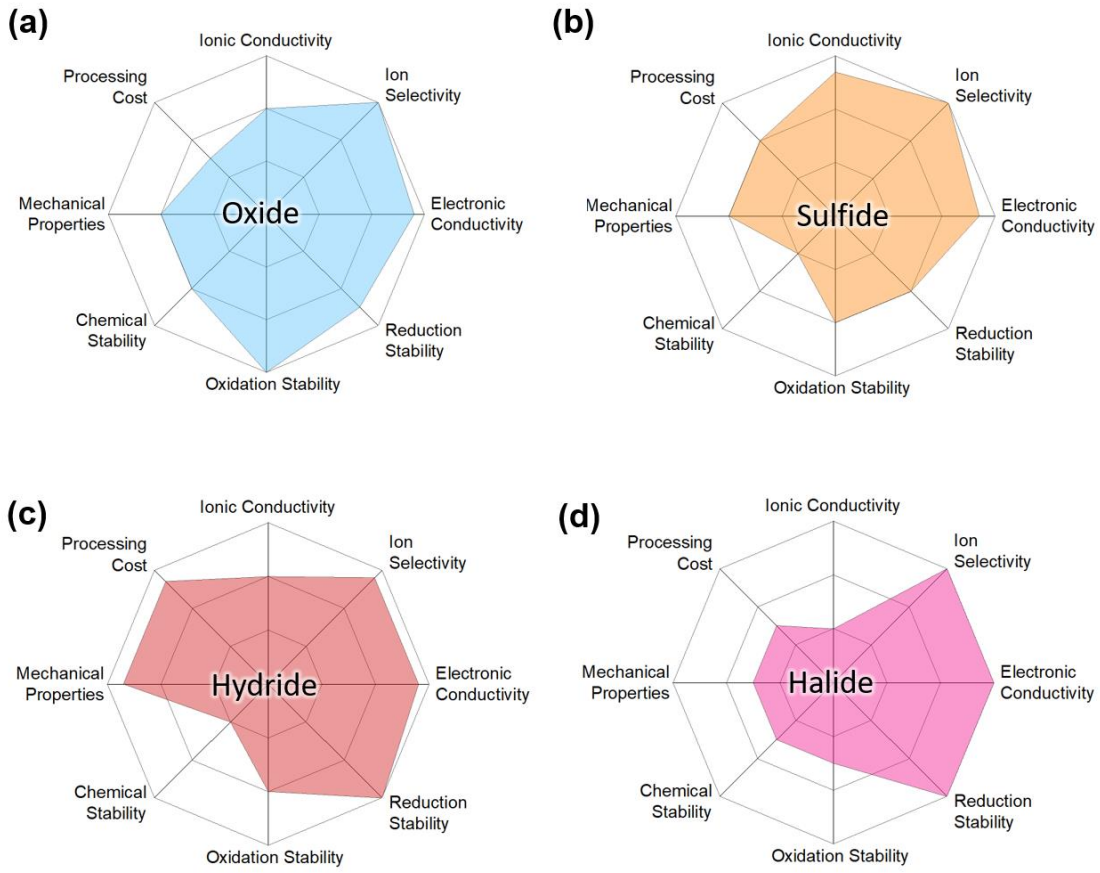

Figure 1.7 Radar plots for the performance properties of (a) oxide-based, (b) sulfide based, (c) hydride, and (d) halide solid electrolytes. Reprinted by permission, Nature Publishing Group [70] © 2017.

From Figure 1.7, we can see that oxide-based SEs exhibit excellent chemical and electrochemical stability compared to other categories but suffer from limited ionic conductivity, non-flexible mechanical properties, and high processing cost. Poor grain

boundary (GB) conductivities usually hindered a satisfactory overall ionic conduction throughout the bulk polycrystalline materials [71-73]. Oxide materials often require high-temperature treatment to decrease GB resistance, which adds to processing costs. In comparison, sulfide-based SEs exhibit high ionic conductivities and good mechanical flexibility. Since sulfides are more ductile and possess low GB resistance, they are generally easier to process at relatively low temperatures. However, due to high air and moisture sensitivity and problematic compatibility with oxide cathode materials, sulfide-based SEs often require additional processing steps for battery applications, such as surface coatings on cathodes [74, 75]. Similarly, other categories of SEs also exhibit their own promises and limitations. So far, none of the known material families or particular fast ionic conductors can yet satisfy all the desired performance attributes exhibited in Figure 1.7, suggesting an imperative and challenging task to continue exploring and developing novel SE materials.

Generally speaking, there are two directions to look for promising SE candidates with fast ionic conduction. One is to search for unknown or new material structures that have not been considered as ion conductors, and another is to modify and tune existing material structures for enhanced conductivities. Although structural tuning via various doping strategies have been proved to be effective for improving ionic conductivities [76-78], currently the tuning strategies are still material specific and not quite universally efficient for more materials, which reflects that our understanding on the ionic conduction mechanism and the structure-property relationship in solid ionic conductors is still quite limited.

1.2.2 Ionic Transport Mechanisms in Superionic Conductors

In order to rationally design and develop high-performance solid ionic conductors, an in-depth understanding of ion transport behavior is fundamental and essential. The ionic transport mechanisms in solid electrolytes are very different from those in liquid electrolytes. Ion transport in liquid electrolytes involves transporting solvated ions in the solvent medium. Due to the fast exchange between the ions and the solvent molecules, the energy barrier of mobile ions in liquid is almost flat. In comparison, the diffusion of mobile ions in a solid electrolyte needs to overcome periodic barriers formed by the immobile sublattice points. The classical model describes ion transport in solids as a random hopping process of individual ions between two sites with certain length [79]. The concentration of available hopping sites and the energy landscape along the pathways connecting the starting and destination sites are critical factors in determining the macroscopic ion conduction behavior. The conduction behavior of mobile ions in solids can be described with the following equation:

$$\sigma = \frac{A}{T} \exp\left(-\frac{E_a}{k_B T}\right) \quad (1)$$

where E_a is the activation energy, k_B is the Boltzmann constant, and T is the temperature in Kelvin. This equation shows the dependence of ionic conductivity on the structural energy barrier or the activation energy E_a.

To better reveal the underlying governing factors of ion transport in solids, the ionic conductivity can be described as $\sigma = nZ\mu$, where n is the concentration of mobile ions

with charge Z and mobility μ. The mobility μ is related to the diffusion coefficient D by the Nernst-Einstein equation:

$$\mu = \frac{D}{k_B T} \tag{2}$$

Here the diffusion coefficient satisfies $D = D_0 \exp\left(-\frac{E_a}{k_B T}\right)$ and therefore is dependent on activation energy and temperature. Based on these equations, the related underlying structural factors that govern ion conduction can be extracted and general strategies to improve ionic transport in solid electrolytes can also be derived accordingly, which include but are not limited to:

- Increasing the concentration of mobile ions (increase n)
- Introducing defects (vacant or interstitial sites) within the immobile sublattice (increase n and construct low energy pathways connecting these sites)
- Using elements with higher ionic polarizability for the immobile sublattice (which will easily deform to allow ions diffusion with low E_a)
- Using elements with larger ionic radius for the immobile sublattice (enlarged framework or diffusion bottleneck facilitates fast ion mobility with lower E_a)
- Selecting mobile ions with smaller ionic radius if applicable (a small mobile ion is easier to diffuse through the polyhedral faces of the immobile sublattice)

These general guidelines have been proved to be effective in modifying material structures and improving ionic conduction in multiple material families [80-83]. However, it needs to be noticed that these factors are usually interrelated. Certain structural tuning

method may bring conflicting impact on ionic conductivity and therefore needs to be carefully examined to deliver optimal ionic conduction. For example, it has been demonstrated that the polarizability of the immobile sublattice will affect the activation barrier and pre-factor A at the same time. As a result, substitution of more polarizable elements to construct "soft framework" may not always show positive impact on ionic conductivity [84, 85]. From a structure-property relationship point of view, it is difficult and usually inaccurate to use single structural factor in isolation to explain ionic conductivities, as observed extensively in the research of Li and Na ion conductors. Nevertheless, such intuitive notions provide useful rules of thumb to explain many experimental observations and to quickly promote certain strategies in real cases.

1.3 Strategies for Superionic Conductor Development

Based on current understanding of ion conduction in solids and the underlying structural factors proposed by classic ion-hopping model, there are various possible methods to enhance ionic conductivities for materials of interest. However, practically synthesizing the designed materials and delivering substantially improved conductivity is usually challenging. In addition to testing the performance of synthesized material candidates, an efficient material design and development strategy should emphasize the establishment of an in-depth understanding of the relationship between material structural parameters and its ionic conductivity. Such knowledge and insights will greatly contribute to rational material design and accelerate the development of SE materials for practical ASB applications.

In this section, general material development methodologies will be discussed with related examples from literature. To design suitable SE materials, we usually start from a certain type of parent or host structure, which can be a known structure that has been investigated as ionic conductors, or novel structures that have not been examined or even synthesized for SE-related applications. Starting from this host structure, multiple structural or compositional tuning methods can be tested depending on the ion diffusion mechanism in the original framework, such as iso-valent and alio-valent substitution. With a set of modified materials and the original material, the underlying relationship between the related structural variables and the ionic conduction performance of the material can be established and refined accordingly. This newly acquired knowledge will in turn serve as a more relevant material design guideline for this particular material family and can also be potentially applied to other similar systems on condition that the physical context and limitations are clearly understood. Considering the complex process of ion transport in solids, effective characterization techniques at various length scales to elucidate the micro- to mese-scale material structural features are critical, for which emerging advanced characterization techniques can be great complementary tools.

Such material design and development methodology is summarized and illustrated in Figure 1.8. More detailed methods for these steps and related material examples will be discussed in the following sessions.

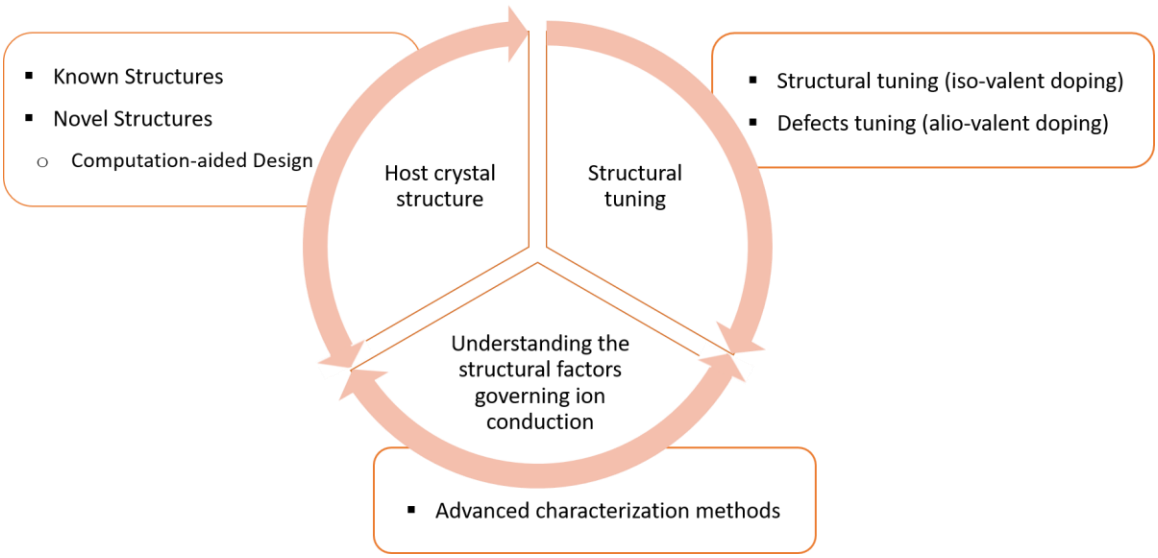

Figure 1.8 Material design and development methodology for solid electrolytes.

1.3.1 Structural Tuning Criterions and Experimental Approaches

In order to achieve fast ion conduction by modifying a certain material structure, chemical substitution is an extensively adopted approach. By substitution of particular elements, multiple structural parameters can be effectively tuned, such as lattice parameters, concentration of defects, framework softness, etc. Chemical substitution can be generally classified into two categories, iso- and alio-valent substitution, depending on whether the introduced elements have the same valence as the substituted ones in the original structure. While alio-valent doping can effectively introduce structural or compositional defects to affect ion transport phenomenon, iso-valent doping mainly focuses on the tuning of immobile sublattice to facilitate easier ion mobility in the framework. Specifically, by increasing the lattice parameters and decreasing the ion transport energy barrier through substituting larger atoms into the framework, enhanced

ionic conductions have been observed in multiple material structures, including both oxides [67, 83, 86, 87] and sulfides [80, 88-91]. However, it should be noted that although in most cases, such substitution will not directly change the concentration of defects and mobile ions, it does introduce other structural variations in addition to lattice sizes, such as local chemical environment, chemical bonding, site disordering, etc. As a result, exceptions do exist where substituting more larger atoms does not necessarily bring continuously improved ionic conductivity. For example, Yu *et al.* have found that the substitution of P by As in Na_3PS_4 not only expands the Na^+ diffusion bottleneck but also results in a weaker As-S bonding and a shorter Na-S bond length, leading to dual effects on Na-ion conductivity [80]. Consequently, total substitution of P by As exhibits lower conductivity than the optimal composition $Na_3P_{0.62}As_{0.38}S_4$, as confirmed by inductively coupled plasma emission spectrometry (ICP-ES) and conductivity measurements.

Compared with iso-valent substitution which mainly tailors the lattice sizes and corresponding bond lengths, alio-valent substitution that creates interstitial atoms or vacancies will have a direct impact on the concentration of mobile ions and the available sites for ion hopping by introducing point defects. Depending on the specific defect types and their interactions with ion transport, the effects of alio-valent substitution on material's thermodynamic stability and ion transport kinetics can be very complicated. For example, the Li^+ conductivity in perovskite $La_{0.67-x}Li_{3x}TiO_3$ solid solution exhibits a dome-shaped dependence on Li substitution level [92], as seen in Figure 1.9. Although the underlying conduction mechanism was found to be related to the Li mobility via the A-site vacancies, the conductivity was not solely controlled by the concentration of vacancies induced. The highest conductivity was obtained at x~0.1, and higher Li^+ content leads to decreased

conductivity due to the tetragonal distortions caused by smaller Li^+ than La^{3+}. Similar phenomenon was also observed in other material systems, such as NASICON-like structure [65] and sulfide-based argyrodites [93], which highlighted the promises and challenges associated with alio-valent substitution in promoting fast ion conduction.

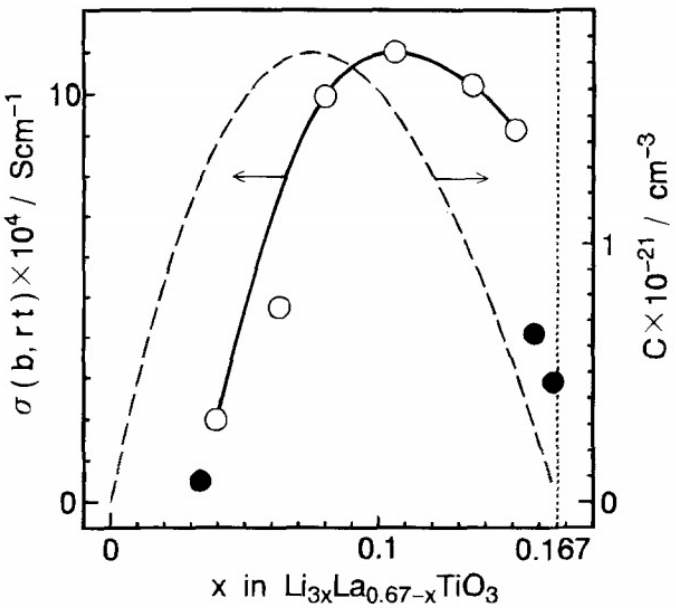

Figure 1.9 Conductivity variation for the compositions $La_{0.67-x}Li_{3x}TiO_3$, empty circles indicating a single phase and filled circles for mixed phases. Reprinted by permission from [92] IOP Publishing, Ltd © 1994.

In addition to compositional tuning for materials of interest, it should be noted that the experimental synthetic approaches in material preparation also play an essential role in practical material delivery and needs to be carefully examined, especially for material groups that are thermodynamically metastable or sensitive to synthetic conditions. For example, many sulfide-based conductors can be synthesized with ball-milling and subsequent annealing process, and the conditions in each step will have direct impacts on the crystallinity and ion conduction properties of the product materials. Specifically, ball-

milling speed and duration are two critical factors in controlling the crystallinity and reactivity of the products, as seen in mechanically milled Li_6PS_5Cl materials. Yi *et al.* have found that low milling speed was not sufficient to form well-mixed amorphous precursors and the subsequently formed crystalline Li_6PS_5Cl only showed improved ionic conductivity after extended milling duration of 8 hours, as seen in Figure 1.10 [94]. Therefore, systematic investigation on material synthesis approaches is important and should be taken into consideration for SE material development to fully achieve the materials' optimal conductivity.

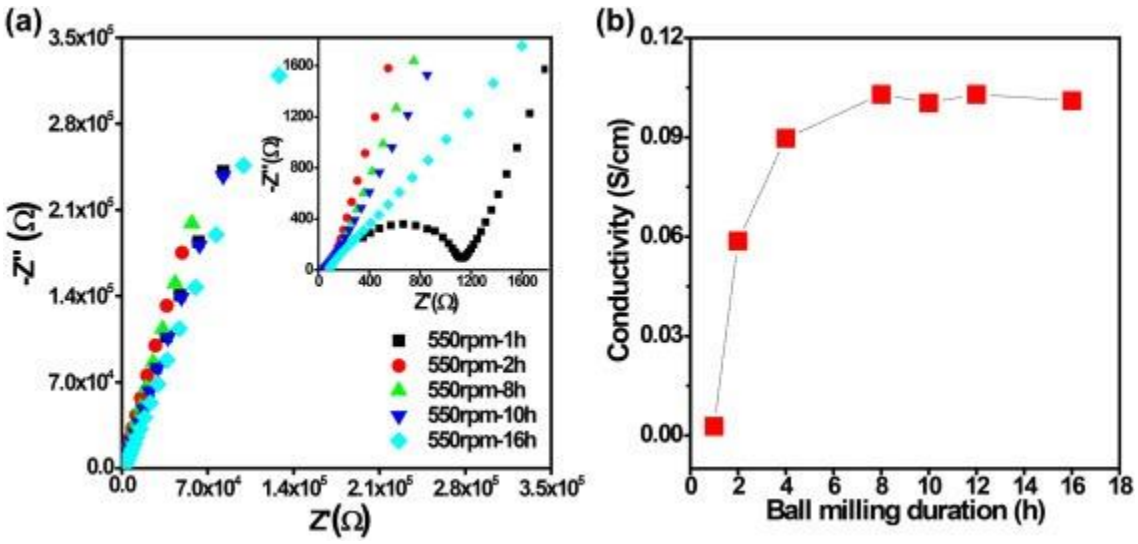

Figure 1.10 (a) Nyquist plot and (b) ionic conductivity of the ball-milled Li_6PS_5Cl samples for different durations. Reprinted from [94]. © (2016) with permission from Elsevier.

1.3.2 Advanced Characterization Methods

Various material characterization techniques are essential tools to elucidate the microscopic material structures for the development of desired material functions.

Depending on the length scale of the structural features to be probed, different characterization methods need to be adopted to obtain a comprehensive understanding of material structures. For long-range crystal structure characterization, diffraction techniques, such as X-ray diffraction (XRD), neutron diffraction (ND), and electron diffraction (ED), are effective tools to determine the averaged structure and the positions of mobile ions in the lattice, and have been extensively used in the research of ionic conductors. Particularly, when the diffraction technique is coupled with heat treatment apparatus, more details in the material formation process can be revealed. Such *in situ* or *operando* experimental techniques are powerful tools in probing material structural variation during precipitation or crystallization process and capturing the intermediate phases that cannot be easily identified with *ex situ* characterizations. The thermodynamic properties of particular material groups can also be investigated and used as important guidelines for the synthesis of target structures, as seen in various electrolyte and electrode materials for battery applications [95-99].

For the analysis of short-range or local structures, another set of characterization methods need to be employed, such as Pair distribution function (PDF) analysis, X-ray absorption spectroscopy (XAS), and solid state nuclear magnetic resonance (NMR), etc. PDF analysis is a powerful tool to investigate atomic pair distances, polyhedral structures, local distortions, etc., and can provides critical insights that may deviate from the view on long-range structure. For example, Krauskopf *et al.* have investigated the local structures of cubic and tetragonal Na_3PS_4 and found the better ionic conductor with a previously perceived cubic structure actually possesses the same local structure as the tetragonal phase, as shown in Figure 1.11 [100]. The conductivity variation was mainly attributed to

the different defect concentration caused by the ball-milling conditions and is independent of the crystal structure. This suggests that complex local structures may commonly exist in superionic conductors and impact ion conductions in implicit ways. Systematic studies with proper characterization techniques to probe local structures, such as PDF, XAS, and NMR, need to be conducted to obtain a more accurate and comprehensive view on material structural features.

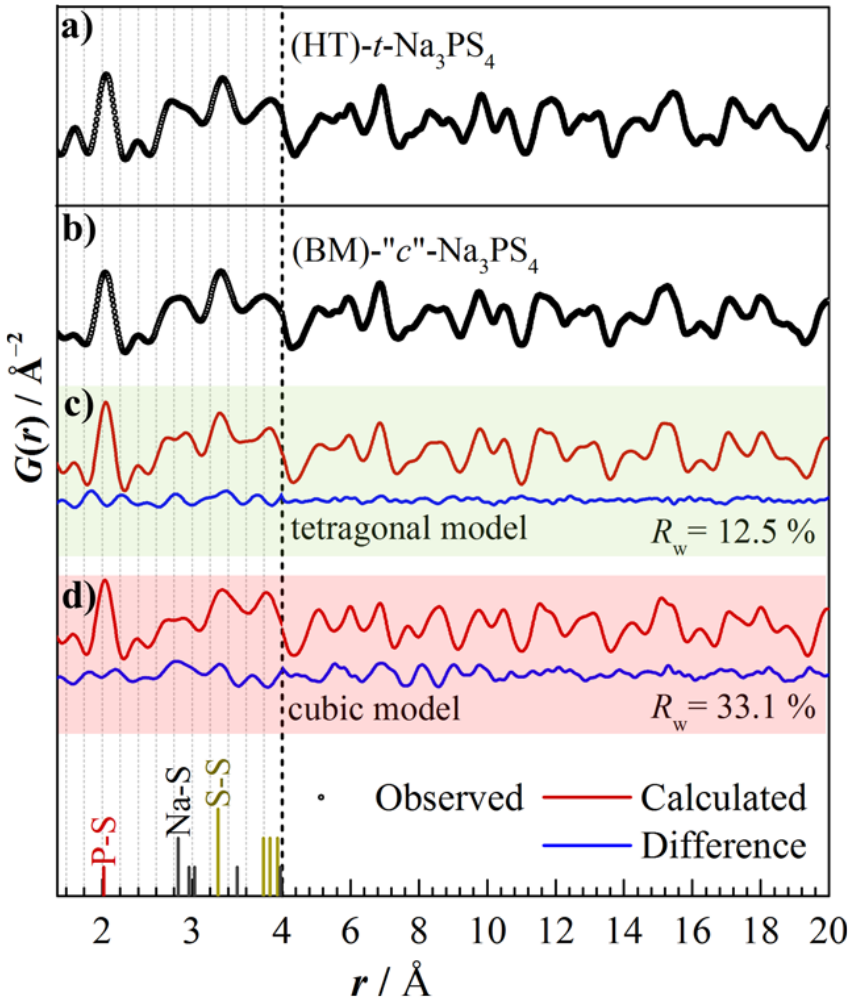

Figure 1.11 Experimental PDF G(r) data for (a) t-Na_3PS_4 and (b) "c"-Na_3PS_4. Reprinted with permission from [100]. © (2018) American Chemical Society.

1.3.3 Computation-aided Material Design Approaches

In addition to the empirical material design criterions and experimental approaches, modern computational methods are proved to be a powerful complement in the design of highly conducting materials, which can greatly accelerate the development of state-of-the-art Li/Na ionic conductors for ASB applications. Over the past decade, first-principles computation techniques have been developed and frequently deployed for SE material development and ASB interface analysis [88, 101-104]. Particularly, first-principles computation can be implemented to establish material databases, such as the Material Project (MP) [105], which provides easily accessible thermodynamic data, (electro)chemical stability, material properties, and phase diagrams to aid new material discovery and development.

Computational methods are also advantageous in revealing implicit structural features across various material groups to provide critical insights of ion diffusion mechanisms that may formulate universal guidelines for ionic conductor development. For example, Wang *et al.* have found that the anion sublattice will greatly affect cation diffusion behaviour. Specifically, based on *ab initio* molecular dynamics (AIMD) simulations on several Li-conducting materials and other ionic conductors, materials with a less densely packed body-centered-cubic (bcc) anion sublattice will facilitate Li^+ hopping between adjacent tetrahedral sites and therefore exhibit higher ionic conductivities [106]. In another example, He *et al.* have identified the concerted migration mechanism in many solid ionic conductors by visualizing ion dynamics using AIMD simulations [102]. Such diffusion mechanism can effectively decrease overall migration barrier and agrees well with various superionic conductors, such as $Li_{10}GeP_2S_{12}$ (LGPS), $Li_7La_3Zr_2O_{12}$ (LLZO),

and $Li_{1.3}Al_{0.3}Ti_{1.7}(PO_4)_3$ (LATP). This finding provides a general strategy to design promising conducting materials by inserting mobile ions into certain sites and triggering concerted ion migration so that a diffusion pathway with lower energy barrier can be constructed. Inspired by this computational work, a systematic study on a series of oxide-based Li ionic conductors will be discuss in detail in the next chapter.

1.4 Objective and Scope of This Work

The objective of this dissertation is to advance our understanding of the relationship between material structure and its ionic conduction behavior across various oxide- and sulfide-based solid electrolyte (SE) materials and to push the all-solid-state Li/Na-ion batteries ahead towards commercial applications. The ionic conduction mechanism in many material families and the critical structural factors are not well understood. To provide constructive and insightful guidelines for future SE material discovery and design, particular emphasis will be given to identifying the impact of governing structural factors on ionic conductivities throughout this work. Specifically, different material families will be investigated with a variety of structural tuning methods, mainly including iso- and alio-valent cation and anion substitution. Computation-aided material design methods and advanced characterization techniques to probe local structures are also employed and further developed to facilitate new material design and development.

In Chapter 2, a joint computational and experimental study on a new family of oxide-based fast lithium ion conductors is presented. A series of doped $LiTaSiO_5$ samples with sphene structure are successfully identified, synthesized, and demonstrated using a novel computational design strategy. First-principles computation predicts that through Zr-

doping, the ionic conductivity of $LiTaSiO_5$ sphene materials will be greatly improved by introducing interstitial Li sites and potentially activating concerted ion migration. It also predicts good phase stability and low electronic conductivity for this material family, which are ideal for solid electrolyte applications. Experiments then confirm that Zr-doped $LiTaSiO_5$ sphene structure exhibits decent ionic conductivity and can be successfully implemented in an all-solid-state battery cell. This study demonstrates a novel design strategy of activating fast Li ionic diffusion in lithium sphenes, which is a new material family of superionic conductors.

In Chapter 3, a group of novel fast Na-ion conductors, $Na_3SbSe_{4-x}S_x$, are synthesized, characterized, and tested to demonstrate the impact of iso-valent substitution on Na^+ ionic conductivity. The cubic Na_3SbSe_4 has been found to exhibit excellent ionic conductivity of 0.85 $mS \cdot cm^{-1}$ at room temperature and good stability in a wide voltage range. The application of this material as solid electrolyte is demonstrated in all-solid-state Na-ion cells cycled at room temperature. Meanwhile, a series of intermediate variants of $Na_3SbSe_{4-x}S_x$ system were also explored. Further analysis of crystal structure and conduction behavior of the $Na_3SbSe_{4-x}S_x$ system indicated a non-monotonic relationship between the size of unit cell and ionic conductivity, providing new insights on the ionic conduction mechanism for sulfide-based Na electrolytes.

In Chapter 4, I conduct a systematic investigation with *in situ* X-ray diffraction and pair distribution function (PDF) analysis to elucidate structural evolution details of milled Na_3SbS_4-NaCl mixture samples during heating processes. The milling process has been observed to change the long-range crystal structure of Na_3SbS_4 and decrease the Na^+ conductivity. The presence and amount of NaCl in the mixtures are critical parameters

influencing the structure and conductivity of milled products. Due to the limitation of conventional crystallographic techniques on probing local material structures, the real short-range structure of the milled Na_3SbS_4-NaCl samples is not well understood. With the help of synchrotron X-ray total scattering and PDF analysis, the structural units of $[SbS_4]^{3-}$ tetrahedra in the milled samples are identified and the structural evolution upon annealing is revealed, which provides critical intermediate local structure information that is not readily available by Bragg diffraction data.

In Chapter 5, I investigate the aliovalent cation and anion doping of Na_4SnS_4 for the development of sodium superionic conductors. Specifically, I describe the design, synthesis, characterization, and testing of a series of novel fast Na-ion conductors with the formula of $Na_{4-x-y}Sn_{1-x}A_xS_{4-y}X_y$ by aliovalent cation (P^{5+}/Sb^{5+}) and anion (Cl^-/Br^-) substitutions of the parent compound Na_4SnS_4. The doped samples crystalize in a new phase with space group $I4_1/acd$ and show ionic conductivities that are one to four orders of magnitude higher than that of undoped Na_4SnS_4. Room temperature conductivity of 0.64 $mS \cdot cm^{-1}$ is achieved in $Na_{3.7}Sn_{0.8}Sb_{0.2}S_{3.9}Cl_{0.1}$ with a low activation energy of 0.26 eV. Rietveld refinement against high resolution synchrotron X-ray powder diffraction data reveals that the distribution of the doping ions and the resulted Na vacancies are underlying causes for the enhanced conductivity.

This dissertation concludes by summarizing the key findings in the studies for each material group and highlighting the opportunities and perspectives for future research on superior solid electrolyte material development and its application in all-solid-state battery systems.

1.5 References

[1] Cheng, X.-B., R. Zhang, C.-Z. Zhao, and Q. Zhang, *Toward Safe Lithium Metal Anode in Rechargeable Batteries: A Review.* Chemical Reviews, 2017. **117**(15): p. 10403-10473.

[2] Cheng, X.-B., C.-Z. Zhao, Y.-X. Yao, H. Liu, and Q. Zhang, *Recent Advances in Energy Chemistry between Solid-State Electrolyte and Safe Lithium-Metal Anodes.* Chem, 2019. **5**(1): p. 74-96.

[3] Chen, Y., Y. Luo, H. Zhang, C. Qu, H. Zhang, and X. Li, *The Challenge of Lithium Metal Anodes for Practical Applications.* Small Methods, 2019. **3**(7): p. 1800551.

[4] Kato, Y., K. Kawamoto, R. Kanno, and M. Hirayama, *Discharge Performance of All-Solid-State Battery Using a Lithium Superionic Conductor $Li_{10}GeP_2S_{12}$.* Electrochemistry, 2012. **80**(10): p. 749-751.

[5] Kato, Y., S. Hori, T. Saito, K. Suzuki, M. Hirayama, A. Mitsui, M. Yonemura, H. Iba, and R. Kanno, *High-power all-solid-state batteries using sulfide superionic conductors.* Nature Energy, 2016. **1**(4): p. 16030.

[6] Yabuuchi, N., K. Kubota, M. Dahbi, and S. Komaba, *Research Development on Sodium-Ion Batteries.* Chemical Reviews, 2014. **114**(23): p. 11636-11682.

[7] Nithya, C. and S. Gopukumar, *Sodium ion batteries: a newer electrochemical storage.* WIREs Energy and Environment, 2015. **4**(3): p. 253-278.

[8] Pan, H., Y.-S. Hu, and L. Chen, *Room-temperature stationary sodium-ion batteries for large-scale electric energy storage.* Energy & Environmental Science, 2013. **6**(8): p. 2338-2360.

[9] Liu, T., et al., *Exploring competitive features of stationary sodium ion batteries for electrochemical energy storage.* Energy & Environmental Science, 2019. **12**(5): p. 1512-1533.

[10] Ponrouch, A., E. Marchante, M. Courty, J.-M. Tarascon, and M.R. Palacín, *In search of an optimized electrolyte for Na-ion batteries.* Energy & Environmental Science, 2012. **5**(9): p. 8572-8583.

[11] Chen, R., Q. Li, X. Yu, L. Chen, and H. Li, *Approaching Practically Accessible Solid-State Batteries: Stability Issues Related to Solid Electrolytes and Interfaces.* Chemical Reviews, 2020. **120**(14): p. 6820-6877.

[12] Lopez, J., D.G. Mackanic, Y. Cui, and Z. Bao, *Designing polymers for advanced battery chemistries.* Nature Reviews Materials, 2019. **4**(5): p. 312-330.

[13] Shoji, M., E.J. Cheng, T. Kimura, and K. Kanamura, *Recent progress for all solid state battery using sulfide and oxide solid electrolytes.* Journal of Physics D: Applied Physics, 2019. **52**(10): p. 103001.

[14] Wang, Y., S. Song, C. Xu, N. Hu, J. Molenda, and L. Lu, *Development of solid-state electrolytes for sodium-ion battery–A short review.* Nano Materials Science, 2019. **1**(2): p. 91-100.

[15] Kim, J.-J., K. Yoon, I. Park, and K. Kang, *Progress in the Development of Sodium-Ion Solid Electrolytes.* Small Methods, 2017. **1**(10): p. 1700219.

[16] Lee, Y.-G., et al., *High-energy long-cycling all-solid-state lithium metal batteries enabled by silver–carbon composite anodes.* Nature Energy, 2020. **5**(4): p. 299-308.

[17] Owens, B.B., *Solid state electrolytes: overview of materials and applications during the last third of the Twentieth Century.* Journal of Power Sources, 2000. **90**(1): p. 2-8.

[18] Knauth, P. and H.L. Tuller, *Solid-State Ionics: Roots, Status, and Future Prospects.* Journal of the American Ceramic Society, 2002. **85**(7): p. 1654-1680.

[19] Goodenough, J.B., *Fast Ionic Conduction in Solids*, in *Concise Encyclopedia of Advanced Ceramic Materials*, R.J. Brook, Editor. 1991, Pergamon: Oxford. p. 143-147.

[20] Okumura, T., S. Taminato, T. Takeuchi, and H. Kobayashi, *Minimizing the Grain Boundary Resistance of Li-Ion-Conducting Oxide Electrolyte by Controlling Liquid-Phase Formation During Sintering.* ACS Applied Energy Materials, 2018. **1**(11): p. 6303-6311.

[21] Dawson, J.A., P. Canepa, T. Famprikis, C. Masquelier, and M.S. Islam, *Atomic-Scale Influence of Grain Boundaries on Li-Ion Conduction in Solid Electrolytes for All-Solid-State Batteries.* Journal of the American Chemical Society, 2018. **140**(1): p. 362-368.

[22] Chen, B., C. Xu, and J. Zhou, *Insights into Grain Boundary in Lithium-Rich Anti-Perovskite as Solid Electrolytes.* Journal of The Electrochemical Society, 2018. **165**(16): p. A3946-A3951.

[23] Kim, J., J. Kim, M. Avdeev, H. Yun, and S.-J. Kim, *$LiTa_2PO_8$: a fast lithium-ion conductor with new framework structure.* Journal of Materials Chemistry A, 2018. **6**(45): p. 22478-22482.

[24] Banerjee, A., X. Wang, C. Fang, E.A. Wu, and Y.S. Meng, *Interfaces and Interphases in All-Solid-State Batteries with Inorganic Solid Electrolytes.* Chemical Reviews, 2020. **120**(14): p. 6878-6933.

[25] Xiao, Y., Y. Wang, S.-H. Bo, J.C. Kim, L.J. Miara, and G. Ceder, *Understanding interface stability in solid-state batteries.* Nature Reviews Materials, 2020. **5**(2): p. 105-126.

[26] Pervez, S.A., M.A. Cambaz, V. Thangadurai, and M. Fichtner, *Interface in Solid-State Lithium Battery: Challenges, Progress, and Outlook.* ACS Applied Materials & Interfaces, 2019. **11**(25): p. 22029-22050.

[27] Froboese, L., J.F.v.d. Sichel, T. Loellhoeffel, L. Helmers, and A. Kwade, *Effect of Microstructure on the Ionic Conductivity of an All Solid-State Battery Electrode.* Journal of The Electrochemical Society, 2019. **166**(2): p. A318-A328.

[28] Nakamura, T., K. Amezawa, J. Kulisch, W.G. Zeier, and J. Janek, *Guidelines for All-Solid-State Battery Design and Electrode Buffer Layers Based on Chemical Potential Profile Calculation.* ACS Applied Materials & Interfaces, 2019. **11**(22): p. 19968-19976.

[29] Tian, Y., T. Shi, W.D. Richards, J. Li, J.C. Kim, S.-H. Bo, and G. Ceder, *Compatibility issues between electrodes and electrolytes in solid-state batteries.* Energy Environ. Sci., 2017. **10**(5): p. 1150-1166.

[30] Miara, L.J., W.D. Richards, Y.E. Wang, and G. Ceder, *First-Principles Studies on Cation Dopants and Electrolyte|Cathode Interphases for Lithium Garnets.* Chemistry of Materials, 2015. **27**(11): p. 4040-4047.

[31] Auvergniot, J., A. Cassel, J.-B. Ledeuil, V. Viallet, V. Seznec, and R. Dedryvère, *Interface Stability of Argyrodite Li_6PS_5Cl toward $LiCoO_2$, $LiNi_{1/3}Co_{1/3}Mn_{1/3}O_2$, and $LiMn_2O_4$ in Bulk All-Solid-State Batteries.* Chemistry of Materials, 2017. **29**(9): p. 3883-3890.

[32] Richards, W.D., L.J. Miara, Y. Wang, J.C. Kim, and G. Ceder, *Interface Stability in Solid-State Batteries.* Chemistry of Materials, 2016. **28**(1): p. 266-273.

[33] Wenzel, S., S. Randau, T. Leichtweiß, D.A. Weber, J. Sann, W.G. Zeier, and J. Janek, *Direct Observation of the Interfacial Instability of the Fast Ionic Conductor $Li_{10}GeP_2S_{12}$ at the Lithium Metal Anode.* Chemistry of Materials, 2016. **28**(7): p. 2400-2407.

[34] Sakuda, A., H. Kitaura, A. Hayashi, K. Tadanaga, and M. Tatsumisago, *Modification of Interface Between $LiCoO_2$ Electrode and $Li_2S–P_2S_5$ Solid Electrolyte Using $Li_2O–SiO_2$ Glassy Layers.* Journal of The Electrochemical Society, 2009. **156**(1): p. A27.

[35] Wenzel, S., T. Leichtweiss, D. Krüger, J. Sann, and J. Janek, *Interphase formation on lithium solid electrolytes—An in situ approach to study interfacial reactions by photoelectron spectroscopy.* Solid State Ionics, 2015. **278**: p. 98-105.

[36] Fan, X., X. Ji, F. Han, J. Yue, J. Chen, L. Chen, T. Deng, J. Jiang, and C. Wang, *Fluorinated solid electrolyte interphase enables highly reversible solid-state Li metal battery.* Science Advances, 2018. **4**(12): p. eaau9245.

[37] Sun, B., Y. Jin, J. Lang, K. Liu, M. Fang, and H. Wu, *A painted layer for high-rate and high-capacity solid-state lithium–metal batteries.* Chemical Communications, 2019. **55**(47): p. 6704-6707.

[38] Han, X., et al., *Negating interfacial impedance in garnet-based solid-state Li metal batteries.* Nature Materials, 2017. **16**(5): p. 572-579.

[39] Luo, W., et al., *Reducing Interfacial Resistance between Garnet-Structured Solid-State Electrolyte and Li-Metal Anode by a Germanium Layer.* Advanced Materials, 2017. **29**(22): p. 1606042.

[40] Fu, K., et al., *Toward garnet electrolyte–based Li metal batteries: An ultrathin, highly effective, artificial solid-state electrolyte/metallic Li interface.* Science Advances, 2017. **3**(4): p. e1601659.

[41] Tian, Y., Y. Sun, D.C. Hannah, Y. Xiao, H. Liu, K.W. Chapman, S.-H. Bo, and G. Ceder, *Reactivity-Guided Interface Design in Na Metal Solid-State Batteries.* Joule, 2019. **3**(4): p. 1037-1050.

[42] Kato, T., T. Hamanaka, K. Yamamoto, T. Hirayama, F. Sagane, M. Motoyama, and Y. Iriyama, *In-situ $Li_7La_3Zr_2O_{12}/LiCoO_2$ interface modification for advanced all-solid-state battery.* Journal of Power Sources, 2014. **260**: p. 292-298.

[43] Liu, Y., C. Li, B. Li, H. Song, Z. Cheng, M. Chen, P. He, and H. Zhou, *Germanium Thin Film Protected Lithium Aluminum Germanium Phosphate for Solid-State Li Batteries.* Advanced Energy Materials, 2018. **8**(16): p. 1702374.

[44] Bates, J.B., N.J. Dudney, B. Neudecker, A. Ueda, and C.D. Evans, *Thin-film lithium and lithium-ion batteries.* Solid State Ionics, 2000. **135**(1): p. 33-45.

[45] Xia, Y., T. Fujieda, K. Tatsumi, P.P. Prosini, and T. Sakai, *Thermal and electrochemical stability of cathode materials in solid polymer electrolyte.* Journal of Power Sources, 2001. **92**(1): p. 234-243.

[46] Sun, B., C. Xu, J. Mindemark, T. Gustafsson, K. Edström, and D. Brandell, *At the polymer electrolyte interfaces: the role of the polymer host in interphase layer formation in Li-batteries.* Journal of Materials Chemistry A, 2015. **3**(26): p. 13994-14000.

[47] Xu, C., B. Sun, T. Gustafsson, K. Edström, D. Brandell, and M. Hahlin, *Interface layer formation in solid polymer electrolyte lithium batteries: an XPS study.* Journal of Materials Chemistry A, 2014. **2**(20): p. 7256-7264.

[48] Thomas, J., *Solid state electrochemistry. Edited by Peter G. Bruce, Cambridge University Press.* Advanced Materials, 1996. **8**(4): p. 360-360.

[49] Owens, B.B. and G.R. Argue, *High-Conductivity Solid Electrolytes: MAg_4I_5.* Science, 1967. **157**(3786): p. 308-310.

[50] Wiedersich, H. and W.V. Johnston, *On the thermodynamic properties of the solid electrolyte $RbAg_4I_5$.* Journal of Physics and Chemistry of Solids, 1969. **30**(3): p. 475-482.

[51] Briant, J.L. and G.C. Farrington, *Ionic conductivity in Li^+-Na^+ beta and beta ″ alumina.* Solid State Ionics, 1981. **5**: p. 207-210.

[52] Yung-Fang Yu, Y. and J.T. Kummer, *Ion exchange properties of and rates of ionic diffusion in beta-alumina.* Journal of Inorganic and Nuclear Chemistry, 1967. **29**(9): p. 2453-2475.

[53] Kanno, R. and M. Murayama, *Lithium Ionic Conductor Thio-LISICON: The Li_2S-GeS_2-P_2S_5 System.* Journal of The Electrochemical Society, 2001. **148**(7): p. A742.

[54] Kamaya, N., et al., *A lithium superionic conductor.* Nat Mater, 2011. **10**(9): p. 682-6.

[55] Minami, K., F. Mizuno, A. Hayashi, and M. Tatsumisago, *Lithium ion conductivity of the Li_2S–P_2S_5 glass-based electrolytes prepared by the melt quenching method.* Solid State Ionics, 2007. **178**(11-12): p. 837-841.

[56] Hayashi, A., *Characterization of Li_2S-P_2S_5 glass-ceramics as a solid electrolyte for lithium secondary batteries.* Solid State Ionics, 2004. **175**(1-4): p. 683-686.

[57] Deiseroth, H.J., S.T. Kong, H. Eckert, J. Vannahme, C. Reiner, T. Zaiss, and M. Schlosser, *Li_6PS_5X: a class of crystalline Li-rich solids with an unusually high Li^+ mobility.* Angew Chem Int Ed Engl, 2008. **47**(4): p. 755-8.

[58] Boulineau, S., M. Courty, J.-M. Tarascon, and V. Viallet, *Mechanochemical synthesis of Li-argyrodite Li_6PS_5X (X=Cl, Br, I) as sulfur-based solid electrolytes for all solid state batteries application.* Solid State Ionics, 2012. **221**: p. 1-5.

[59] Rao, R.P. and S. Adams, *Studies of lithium argyrodite solid electrolytes for all-solid-state batteries.* physica status solidi (a), 2011. **208**(8): p. 1804-1807.

[60] Cussen, E.J., *The structure of lithium garnets: cation disorder and clustering in a new family of fast Li^+ conductors.* Chemical Communications, 2006(4): p. 412-413.

[61] Kasper, H.M., *Series of rare earth garnets $Ln_3M_2Li_3O_{12}$ (M=Te, W).* Inorganic Chemistry, 1969. **8**(4): p. 1000-1002.

[62] Buschmann, H., et al., *Structure and dynamics of the fast lithium ion conductor "$Li_7La_3Zr_2O_{12}$".* Physical Chemistry Chemical Physics, 2011. **13**(43): p. 19378-19392.

[63] Goodenough, J.B., H.Y.P. Hong, and J.A. Kafalas, *Fast Na^+-ion transport in skeleton structures.* Materials Research Bulletin, 1976. **11**(2): p. 203-220.

[64] Anantharamulu, N., K. Koteswara Rao, G. Rambabu, B. Vijaya Kumar, V. Radha, and M. Vithal, *A wide-ranging review on Nasicon type materials.* Journal of Materials Science, 2011. **46**(9): p. 2821-2837.

[65] Aono, H., E. Sugimoto, Y. Sadaoka, N. Imanaka, and G.y. Adachi, *Ionic Conductivity of Solid Electrolytes Based on Lithium Titanium Phosphate.* Journal of The Electrochemical Society, 1990. **137**(4): p. 1023-1027.

[66] Inaguma, Y., C. Liquan, M. Itoh, T. Nakamura, T. Uchida, H. Ikuta, and M. Wakihara, *High ionic conductivity in lithium lanthanum titanate.* Solid State Communications, 1993. **86**(10): p. 689-693.

[67] Itoh, M., Y. Inaguma, W.-H. Jung, L. Chen, and T. Nakamura, *High lithium ion conductivity in the perovskite-type compounds $Ln_{12}Li_{12}TiO_3$(Ln=La,Pr,Nd,Sm).* Solid State Ionics, 1994. **70-71**: p. 203-207.

[68] Santibáñez-Mendieta, A.B., et al., *$La_3Li_3W_2O_{12}$: Ionic Diffusion in a Perovskite with Lithium on both A- and B-Sites.* Chemistry of Materials, 2016. **28**(21): p. 7833-7851.

[69] Bachman, J.C., et al., *Inorganic Solid-State Electrolytes for Lithium Batteries: Mechanisms and Properties Governing Ion Conduction.* Chem Rev, 2016. **116**(1): p. 140-62.

[70] Manthiram, A., X. Yu, and S. Wang, *Lithium battery chemistries enabled by solid-state electrolytes.* Nature Reviews Materials, 2017. **2**(4): p. 16103.

[71] Guo, X. and J. Maier, *Grain Boundary Blocking Effect in Zirconia: A Schottky Barrier Analysis.* Journal of The Electrochemical Society, 2001. **148**(3): p. E121.

[72] Moriwake, H., X. Gao, A. Kuwabara, C.A.J. Fisher, T. Kimura, Y.H. Ikuhara, K. Kohama, T. Tojigamori, and Y. Ikuhara, *Domain boundaries and their influence on Li migration in solid-state electrolyte (La,Li)TiO_3.* Journal of Power Sources, 2015. **276**: p. 203-207.

[73] Chung, H. and B. Kang, *Increase in grain boundary ionic conductivity of $Li_{1.5}Al_{0.5}Ge_{1.5}(PO_4)_3$ by adding excess lithium.* Solid State Ionics, 2014. **263**: p. 125-130.

[74] Lian, P.-J., B.-S. Zhao, L.-Q. Zhang, N. Xu, M.-T. Wu, and X.-P. Gao, *Inorganic sulfide solid electrolytes for all-solid-state lithium secondary batteries.* Journal of Materials Chemistry A, 2019. **7**(36): p. 20540-20557.

[75] Hayashi, A., A. Sakuda, and M. Tatsumisago, *Development of Sulfide Solid Electrolytes and Interface Formation Processes for Bulk-Type All-Solid-State Li and Na Batteries.* Frontiers in Energy Research, 2016. **4**(25).

[76] Richards, W.D., Y. Wang, L.J. Miara, J.C. Kim, and G. Ceder, *Design of $Li_{1+2x}Zn_{1-x}PS_4$, a new lithium ion conductor.* Energy & Environmental Science, 2016. **9**(10): p. 3272-3278.

[77] Krauskopf, T., S.P. Culver, and W.G. Zeier, *Bottleneck of Diffusion and Inductive Effects in $Li_{10}Ge_{1-x}Sn_xP_2S_{12}$.* Chemistry of Materials, 2018. **30**(5): p. 1791-1798.

[78] Luo, Y., X. Li, Y. Zhang, L. Ge, H. Chen, and L. Guo, *Electrochemical properties and structural stability of Ga- and Y- co-doping in $Li_7La_3Zr_2O_{12}$ ceramic electrolytes for lithium-ion batteries.* Electrochimica Acta, 2019. **294**: p. 217-225.

[79] Mehrer, H., *Diffusion in solids: fundamentals, methods, materials, diffusion-controlled processes*. Vol. 155. 2007: Springer Science & Business Media.

[80] Yu, Z., et al., *Exceptionally High Ionic Conductivity in $Na_3P_{0.62}As_{0.38}S_4$ with Improved Moisture Stability for Solid-State Sodium-Ion Batteries.* Adv Mater, 2017. **29**(16).

[81] Zhang, L., K. Yang, J. Mi, L. Lu, L. Zhao, L. Wang, Y. Li, and H. Zeng, *Na_3PSe_4: A Novel Chalcogenide Solid Electrolyte with High Ionic Conductivity.* Advanced Energy Materials, 2015. **5**(24): p. 1501294.

[82] Deng, Z., et al., *Ca-doped $Na_2Zn_2TeO_6$ layered sodium conductor for all-solid-state sodium-ion batteries.* Electrochimica Acta, 2019. **298**: p. 121-126.

[83] Arbi, K., J.M. Rojo, and J. Sanz, *Lithium mobility in titanium based Nasicon $Li_{1+x}Ti_{2-x}Al_x(PO_4)_3$ and $LiTi_{2-x}Zr_x(PO_4)_3$ materials followed by NMR and impedance spectroscopy.* Journal of the European Ceramic Society, 2007. **27**(13): p. 4215-4218.

[84] Bernges, T., S.P. Culver, N. Minafra, R. Koerver, and W.G. Zeier, *Competing Structural Influences in the Li Superionic Conducting Argyrodites $Li_6PS_{5-x}Se_xBr$ ($0 \leqslant x \leqslant 1$) upon Se Substitution.* Inorganic Chemistry, 2018. **57**(21): p. 13920-13928.

[85] Kraft, M.A., et al., *Influence of Lattice Polarizability on the Ionic Conductivity in the Lithium Superionic Argyrodites Li_6PS_5X (X = Cl, Br, I).* Journal of the American Chemical Society, 2017. **139**(31): p. 10909-10918.

[86] Rodger, A.R., J. Kuwano, and A.R. West, *Li^+ ion conducting γ solid solutions in the systems Li_4XO_4-Li_3YO_4: X=Si, Ge, Ti; Y=P, As, V; Li_4XO_4-$LiZO_2$: Z=Al, Ga, Cr and Li_4GeO_4-Li_2CaGeO_4.* Solid State Ionics, 1985. **15**(3): p. 185-198.

[87] Martínez-Juárez, A., C. Pecharromán, J.E. Iglesias, and J.M. Rojo, *Relationship between Activation Energy and Bottleneck Size for Li^+ Ion Conduction in NASICON Materials of Composition $LiMM'(PO_4)_3$; M, M' = Ge, Ti, Sn, Hf.* The Journal of Physical Chemistry B, 1998. **102**(2): p. 372-375.

[88] Ong, S.P., Y. Mo, W.D. Richards, L. Miara, H.S. Lee, and G. Ceder, *Phase stability, electrochemical stability and ionic conductivity of the $Li_{10\pm1}MP_2X_{12}$ (M = Ge, Si, Sn, Al or P, and X = O, S or Se) family of superionic conductors.* Energy & Environmental Science, 2013. **6**(1): p. 148-156.

[89] Bo, S.-H., Y. Wang, and G. Ceder, *Structural and Na-ion conduction characteristics of $Na_3PS_xSe_{4-x}$.* J. Mater. Chem. A, 2016. **4**(23): p. 9044-9053.

[90] Xiong, S., Z. Liu, H. Rong, H. Wang, M. McDaniel, and H. Chen, *$Na_3SbSe_{4-x}S_x$ as Sodium Superionic Conductors.* Scientific Reports, 2018. **8**(1): p. 9146.

[91] Minafra, N., S.P. Culver, C. Li, A. Senyshyn, and W.G. Zeier, *Influence of the Lithium Substructure on the Diffusion Pathways and Transport Properties of the Thio-LISICON $Li_4Ge_{1-x}Sn_xS_4$.* Chemistry of Materials, 2019. **31**(10): p. 3794-3802.

[92] Kawai, H. and J. Kuwano, *Lithium Ion Conductivity of A - Site Deficient Perovskite Solid Solution $La_{0.67-x}Li_{3x}TiO_3$.* Journal of The Electrochemical Society, 1994. **141**(7): p. L78-L79.

[93] Kraft, M.A., et al., *Inducing High Ionic Conductivity in the Lithium Superionic Argyrodites $Li_{6+x}P_{1-x}Ge_xS_5I$ for All-Solid-State Batteries.* Journal of the American Chemical Society, 2018. **140**(47): p. 16330-16339.

[94] Yu, C., L. van Eijck, S. Ganapathy, and M. Wagemaker, *Synthesis, structure and electrochemical performance of the argyrodite Li_6PS_5Cl solid electrolyte for Li-ion solid state batteries.* Electrochimica Acta, 2016. **215**: p. 93-99.

[95] Yoon, W.-S., et al., *In situ soft XAS study on nickel-based layered cathode material at elevated temperatures: A novel approach to study thermal stability.* Scientific Reports, 2014. **4**(1): p. 6827.

[96] Yang, L., et al., *Lithium-Doping Stabilized High-Performance P2–$Na_{0.66}Li_{0.18}Fe_{0.12}Mn_{0.7}O_2$ Cathode for Sodium Ion Batteries.* Journal of the American Chemical Society, 2019. **141**(16): p. 6680-6689.

[97] Liu, Z., et al., *$Li_{15}P_4S_{16}Cl_3$, a Lithium Chlorothiophosphate as a Solid-State Ionic Conductor.* Inorganic Chemistry, 2020. **59**(1): p. 226-234.

[98] Xiong, S., et al., *Computation-Guided Design of $LiTaSiO_5$, a New Lithium Ionic Conductor with Sphene Structure.* Advanced Energy Materials, 2019. **9**(22): p. 1803821.

[99] Xiong, S., Z. Liu, L. Yang, Y. Ma, W. Xu, J. Bai, and H. Chen, *Anion and cation co-doping of Na_4SnS_4 as sodium superionic conductors.* Materials Today Physics, 2020. **15**: p. 100281.

[100] Krauskopf, T., S.P. Culver, and W.G. Zeier, *Local Tetragonal Structure of the Cubic Superionic Conductor Na_3PS_4.* Inorganic Chemistry, 2018. **57**(8): p. 4739-4744.

[101] He, X., Q. Bai, Y. Liu, A.M. Nolan, C. Ling, and Y. Mo, *Crystal Structural Framework of Lithium Super-Ionic Conductors.* Advanced Energy Materials, 2019. **9**(43): p. 1902078.

[102] He, X., Y. Zhu, and Y. Mo, *Origin of fast ion diffusion in super-ionic conductors.* Nature Communications, 2017. **8**(1): p. 15893.

[103] Mo, Y., S.P. Ong, and G. Ceder, *First Principles Study of the $Li_{10}GeP_2S_{12}$ Lithium Super Ionic Conductor Material.* Chemistry of Materials, 2012. **24**(1): p. 15-17.

[104] Wang, Y., W.D. Richards, S.P. Ong, L.J. Miara, J.C. Kim, Y. Mo, and G. Ceder, *Design principles for solid-state lithium superionic conductors.* Nat Mater, 2015. **14**(10): p. 1026-31.

[105] Jain, A., et al., *Commentary: The Materials Project: A materials genome approach to accelerating materials innovation.* APL Materials, 2013. **1**(1): p. 011002.

[106] Wang, Y., W.D. Richards, S.P. Ong, L.J. Miara, J.C. Kim, Y. Mo, and G. Ceder, *Design principles for solid-state lithium superionic conductors.* Nature Materials, 2015. **14**(10): p. 1026-1031.

CHAPTER 2. AN INTEGRATED COMPUTATIONAL AND EXPERIMENTAL STUDY ON $Li_{1+x}Ta_{1-x}Zr_xSiO_5$, A NEW LITHIUM IONIC CONDUCTOR WITH SPHENE STRUCTURE

2.1 Introduction

All-solid-state Li-ion batteries (ASLBs) with inorganic solid electrolytes (SEs) are considered one of the most promising alternatives to current Li-ion batteries (LIBs), which use organic liquid electrolytes, as ASLBs offer enhanced safety, wide operating temperature range, and potentially high energy density if combined with Li-metal anodes [107-110]. As the key enabler of ASLBs, solid state Li-ion conductors with high Li ionic conductivity, a wide electrochemical window, and good chemical stability are greatly desirable. Despite significant research efforts in the past decades, out of thousands of known lithium-containing inorganic compounds, only a limited number of materials have been identified as superionic conductors with Li^+ conductivities comparable to conventional liquid electrolyte (~1-10 $mS \cdot cm^{-1}$ at room temperature), including $Li_{10}GeP_2S_{12}$ (LGPS) [54], $Li_7P_3S_{11}$ [111], garnet $Li_7La_3Zr_2O_{12}$ (LLZO) [112, 113], and LISICON $Li_{1.3}Al_{0.3}Ti_{1.7}(PO_4)_3$ (LATP) [114], However, many of these superionic conductors suffer from limited stability either in the air or against Li metal [110, 115-117]. Therefore, it is still necessary to explore, discover, and design new compounds with both high ionic conductivity and outstanding stability as solid electrolytes for ASLBs.

In the past, the design and discovery of Li ionic conductors have been largely based on trial-and-error, due to the limited understanding of ionic conductivity in existing ionic

conductors. A general design strategy for fast ion conduction can be tremendously helpful yet is currently absent. Recently, computational studies by Mo *et al* [118] revealed that the fast ion diffusion in Li super-ionic conductors can occur through concerted migration of multiple Li ions, where the migration of high-energy-site Li ions effectively reduces the energy barrier. Based on this understanding, Mo *et al* proposed a general design strategy to drastically lower the energy barriers by intentionally inducing Li ions into high energy sites to activate the concerted migration of multiple ions [118]. The rationale of this design strategy may explain the increase of Li ionic conductivity in a number of existing Li ion conductors [118]. The ion conductivity of garnet $Li_7La_3Zr_2O_{12}$ (LLZO) can achieve 0.1 - 1 $mS{\cdot}cm^{-1}$ after inserting additional Li into the original garnet $Li_5La_3M_2O_{12}$ (M=Ta, Nb) or $Li_3Ln_3Te_2O_{12}$ (Ln=Y, Pr, Nd, Sm–Lu), which exhibit much lower ionic conductivity ($< 10^{-3}$ $mS{\cdot}cm^{-1}$) [112]. The increase of the conductivity of LISICON $Li_{1+x}Al_xTi_{2-x}(PO_4)_3$ when increasing the Li amount from 1 to 1.2-1.3 can also be explained by this mechanism [83, 114]. This design strategy has yet to be demonstrated in predicting a new material system with high ionic conductivity.

Here, through a combined computational and experimental study, the proposed design strategy was demonstrated to activate concerted migration in a new family of materials, lithium sphene. The sphene compounds, with the general formula $ABXTO_4$ (A = Li, Na or Ca, etc., B = Ti, Ta or other metals, X=O or F, T=Si, Ge, P, or S, etc.), is a well-known large materials family [119, 120], but has rarely been explored for ionic conduction properties. $LiTaSiO_5$ is a known sphene compound [121] with a crystal structural framework comprising of corner-sharing TaO_6 and SiO_4 polyhedrons (Figure 2.1a). Li ions located at 4e tetrahedral sites are bonded with 4 oxygen ions, and the LiO_4

tetrahedrons share edges to neighboring TaO_6 and SiO_4 polyhedrons. The crystal structural framework of $LiTaSiO_5$ has lithium diffusion channels of decent size and a well-connected Li^+ percolation network, but has not yet been studied for Li^+ transport.

In this study, we first evaluated the structures and properties of $LiTaSiO_5$ using first principles computation. Following the aforementioned design strategy proposed by Mo *et al.* [118], we computationally designed $Li_{1+x}Ta_{1-x}Zr_xSiO_5$ through aliovalent doping of Zr at the Ta sites in $LiTaSiO_5$ to insert Li into the high-energy sites (as charge compensation) and thus to activate low-barrier concerted migration in the lattice. Then we experimentally synthesized a series of $Li_{1+x}Ta_{1-x}Zr_xSiO_5$ compounds and measured their ionic conductivities. The experiments indeed demonstrated $Li_{1+x}Ta_{1-x}Zr_xSiO_5$ can achieve a significantly lower activation energy of 0.38 eV and a high conductivity of >0.01 $mS \cdot cm^{-1}$ at room temperature. This suggests our computationally guided rational design has led to the discovery of a new family of promising Li ionic conductors.

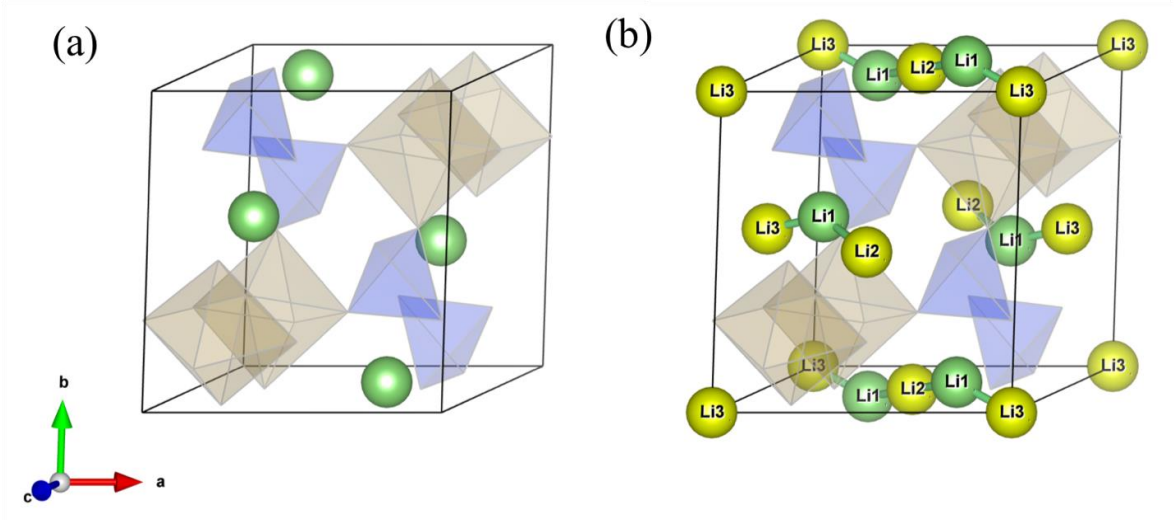

Figure 2.1 (a) Experimental crystal structures of $LiTaSiO_5$, and (b) crystal structure of $LiTaSiO_5$ with the experimental Li site (Li1) and computationally predicted additional interstitial sites Li2 and Li3 for extra Li (shown as yellow spheres). TaO_6 and SiO_4 are shown as brown and blue polyhedrons, respectively. Green bars represent the connection between these Li sites.

2.2 Results and Discussion

2.2.1 Computational Results

2.2.1.1 Crystal Structure

We performed topological analysis of the crystal structural framework of $LiTaSiO_5$ to determine the Li diffusion channels and potential space to accommodate more Li ions. The topological analysis identified three Li sites that are large enough to accommodate Li ions. Consistent with previously experimentally identified Li sites in $LiTaSiO_5$ [121], the Li1 site was identified as the largest space for Li ions (Figure 2.1). Two octahedral sites, Li2 and Li3, neighboring the Li1 site (Figure 2.1b), were identified as potential new Li interstitial sites with smaller size. More Li ions could be inserted into these Li2 and Li3

sites if aliovalent doping is applied, as a mechanism of charge compensation (i.e., the use of a 4+ cation to substitute the Ta^{5+}). It is important to note that the Li2 and Li3 sites are located in the middle of two neighboring Li1 sites. The connection through these alternating Li1, Li2, and Li3 sites forms a well-connected 1D Li diffusion channel along the [101] direction (Figure 2.1b). This 1D diffusion channel with alternating sites is similar to the 1D Li diffusion channel in $Li_{10}GeP_2S_{12}$ (LGPS). These Li sites and diffusion channels with low barriers were confirmed by DFT calculations and AIMD simulations.

2.2.1.2 Phase Stability

Following the design strategy of inducing concerted migration by Mo *et al* [118], in the computational model we inserted extra Li into these Li2 and Li3 interstitial sites through doping of Zr^{4+} at Ta^{5+} sites, and created the composition $Li_{1+x}Ta_{1-x}Zr_xSiO_5$. The DFT calculations confirmed the crystal structural stability and the predicted interstitial sites in the compositions of $Li_{1+x}Ta_{1-x}Zr_xSiO_5$ at x = 0.125, 0.25, and 0.5. After DFT relaxation the sphene structure remains with little distortion. The relaxed positions of newly inserted Li ions agreed with the newly predicted Li2 and Li3 sites (Figure 2.1), with local relaxation of less than 0.3 Å from the original predicted positions. The Li ions at Li1 sites also exhibited small local relaxation to compensate the strong Li-Li interactions due to Li insertion. The volume of the unit cell of $Li_{1+x}Ta_{1-x}Zr_xSiO_5$ at x = 0.125, 0.25, and 0.5 was increased by 0.9%, 1.9%, and 3.6% compared to pristine $LiTaSiO_5$ (Table 2.1). All these compositions have good phase stability as evaluated using the phase diagrams based on DFT energies from the *Materials Project* [122]. $LiTaSiO_5$ is a thermodynamically stable phase. All doped compositions of $Li_{1+x}Ta_{1-x}Zr_xSiO_5$ at x = 0.125, 0.25, and 0.5 have

relatively small energies above the hull of 11, 15, and 28 meV per atom, respectively, as determined via the decomposition reaction:

$$Li_{1+x}Ta_{1-x}Zr_xSiO_5 \rightarrow (1-x)\ LiTaSiO_5 + x\ ZrO_2 + x\ Li_2SiO_3$$

These small values of energy above hull suggest good phase stability of the sphene structure upon Zr doping and Li insertion.

2.2.1.3 Electronic Structure

The band gap calculated using the HSE functional was 5.3 eV, 4.8 eV and 5.4 eV for $Li_{1+x}Ta_{1-x}Zr_xSiO_5$ at x = 0, 0.25, and 0.5, respectively (Figure 2.2). The large band gap indicates the poor electronic conductivity of $Li_{1+x}Ta_{1-x}Zr_xSiO_5$, which agrees well with experimental observations. The introduction of Zr dopants and Li interstitials did not have a significant effect on the value of the band gap, nor introduce any new defect states within the band gap (Figure 2.2).

Table 2.1 Calculated lattice parameters of $Li_{1+x}Ta_{1-x}Zr_xSiO_5$ from DFT.

x	cell	# of f.u.	*a* (Å)	*b* (Å)	*c* (Å)	*α* (°)	*β* (°)	*γ* (°)	Unit cell Volume (Å^3)	Volume change
0	unit cell	4	7.49	8.01	7.53	90.00	119.19	90.00	394.19	0.00%
0.125	supercell	8	13.14	7.99	7.57	89.97	89.15	90.10	397.66	0.88%
0.25	supercell	8	13.22	8.00	7.59	90.00	88.97	90.00	401.62	1.87%
0.5	supercell	8	13.38	8.00	7.63	90.00	89.11	90.00	408.43	3.55%

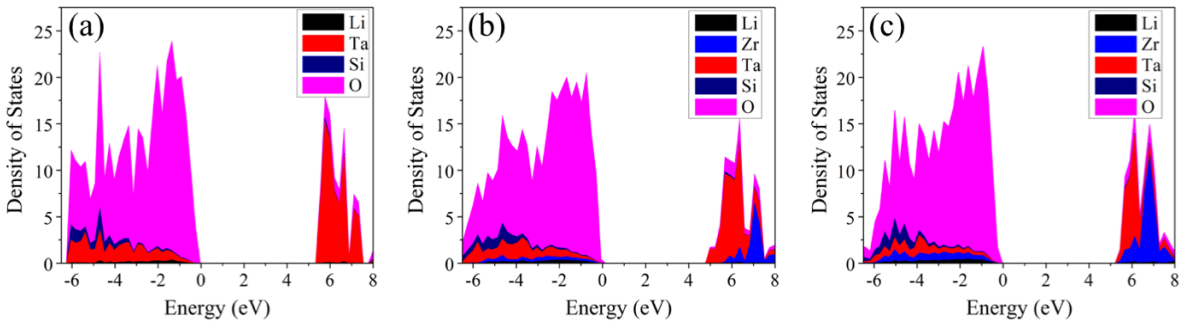

Figure 2.2 Calculated density of states for (a) $LiTaSiO_5$, (b) $Li_{1.25}Ta_{0.75}Zr_{0.25}SiO_5$, and (c) $Li_{1.5}Ta_{0.5}Zr_{0.5}SiO_5$ using HSE functional.

2.2.1.4 Thermodynamic Intrinsic Electrochemical Window

Thermodynamic analyses were performed to evaluate the thermodynamic intrinsic window of $LiTaSiO_5$, which is an important property of solid electrolytes in all-solid-state Li-ion batteries. $LiTaSiO_5$ shows a decent electrochemical window with a thermodynamic intrinsic anodic limit of 3.96 V (referenced to Li/Li^+), indicating its good stability at high voltage. However, $LiTaSiO_5$ is not thermodynamically stable against Li metal and has a thermodynamic intrinsic cathodic limit of 1.40 V (referenced to Li/Li^+). The reduction of Ta and Si limits the Li metal stability of $LiTaSiO_5$ [117].

2.2.1.5 Li^+ Diffusion Mechanism

AIMD simulations were performed for $Li_{1+x}Ta_{1-x}Zr_xSiO_5$ compositions to evaluate their Li^+ diffusivity. For all $Li_{1+x}Ta_{1-x}Zr_xSiO_5$ compositions, the Li diffusivities evaluated at different temperatures follow an Arrhenius relationship (Figure 2.3). The stoichiometric composition $LiTaSiO_5$ shows very low Li^+ diffusion with a high activation energy of 0.70 eV and an extrapolated conductivity of 7.6×10^{-7} $mS\cdot cm^{-1}$ at 300K (Table 2.2). The

predicted slow Li diffusion at room temperature is consistent with our experimental observations.

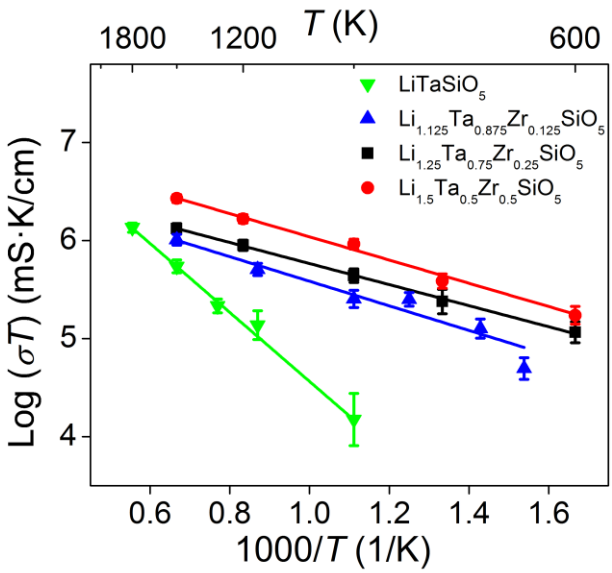

Figure 2.3 Arrhenius plots of Li^+ diffusion in $Li_{1+x}Ta_{1-x}Zr_xSiO_5$ (x = 0, 0.125, 0.25, and 0.5) from AIMD simulations. The error bar is estimated using the scheme in ref [123].

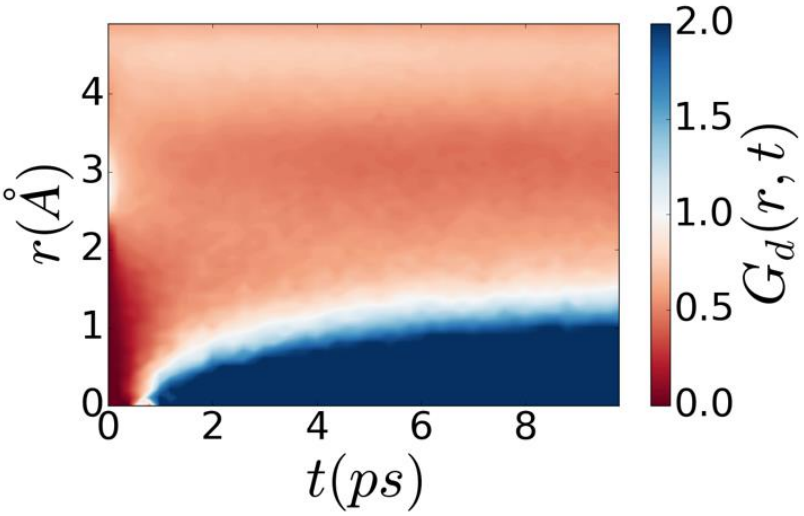

Figure 2.4 Van Hove correlation functions of Li^+ dynamics on distinctive Li ions from the AIMD simulations of $Li_{1.25}Ta_{0.75}Zr_{0.25}SiO_5$, confirming the concerted migration of Li ions.

Table 2.2 Diffusional properties and phase stability of $Li_{1+x}Ta_{1-x}Zr_xSiO_5$. Error bar of the ionic conductivity is estimated based on the error bars of E_a and D obtained during the linear fitting using the scheme in ref [123].

Composition	Energy above hull (meV/atom)	E_a (eV)	σ at 300 K ($mS \cdot cm^{-1}$)	Error bound [σ_{min}, σ_{max}] ($mS \cdot cm^{-1}$)
$LiTaSiO_5$	0	0.70 ± 0.06	7.6×10^{-7}	[8.0×10^{-8}, 7.3×10^{-6}]
$Li_{1.125}Ta_{0.875}Zr_{0.125}SiO_5$	11	0.25 ± 0.02	1.5	[0.7, 3.5]
$Li_{1.25}Ta_{0.75}Zr_{0.25}SiO_5$	15	0.21 ± 0.02	6.1	[2.6, 14.0]
$Li_{1.5}Ta_{0.5}Zr_{0.5}SiO_5$	28	0.23 ± 0.02	6.3	[3.3, 12.0]

Compared with $LiTaSiO_5$, $Li_{1+x}Ta_{1-x}Zr_xSiO_5$ compositions have greatly increased Li conductivities of 1.5, 6.1, and 6.3 $mS \cdot cm^{-1}$ at 300 K for x = 0.125, 0.25, and 0.5, respectively. The activation energies also decrease to 0.25, 0.21, and 0.23 eV for x = 0.125, 0.25, and 0.5, respectively (Table 2.2). These predicted conductivities for $Li_{1+x}Ta_{1-x}Zr_xSiO_5$ at 300K are comparable to the best existing oxide Li ionic conductors, such as doped garnet LLZO (0.1 to 1 $mS \cdot cm^{-1}$). In addition, we observed that the concerted migration of multiple Li ions with lower migration barriers was activated at x = 0.125 - 0.5 during our AIMD simulations (Figure 2.4), consistent with the proposed design strategy. The Li2 and Li3 sites, where new Li ions were inserted, have higher energy in the energy landscape than Li1 sites. As a result, in $Li_{1+x}Ta_{1-x}Zr_xSiO_5$, the activated concerted migrations exhibit a significantly lower energy barrier of 0.21 to 0.25 eV, compared to 0.7 eV in pristine $LiTaSiO_5$. This decrease in activation energy greatly increases the Li conductivity by several orders of magnitude as observed in AIMD simulations.

AIMD simulations also revealed the Li ion diffusion mechanism in $Li_{1+x}Ta_{1-x}Zr_xSiO_5$ at different Li concentrations of $1+x$. The spatial occupancy density of Li ions in $Li_{1+x}Ta_{1-x}Zr_xSiO_5$ at $x = 0$ and 0.25 is shown in Figure 2.5. We found that the stoichiometric $LiTaSiO_5$ shows a 1D percolating diffusion channel along the [101] direction, in agreement with our topological structural analysis. There is a large region of Li density at Li1 sites, corresponding to a large space for accommodating Li, and a flat energy landscape for Li migration. In $Li_{1+x}Ta_{1-x}Zr_xSiO_5$ with $x \geq 0.125$, the [101] diffusion channel connecting Li1-Li3 sites is still the fastest Li diffusion channel. In addition, the diffusion across these [101] channels is activated, as shown by the Li spatial occupancy density (Figure 2.5b). Therefore, $Li_{1+x}Ta_{1-x}Zr_xSiO_5$ is a 3D Li-ion conductor with fast 1D diffusion channels, similar to LGPS [103, 124].

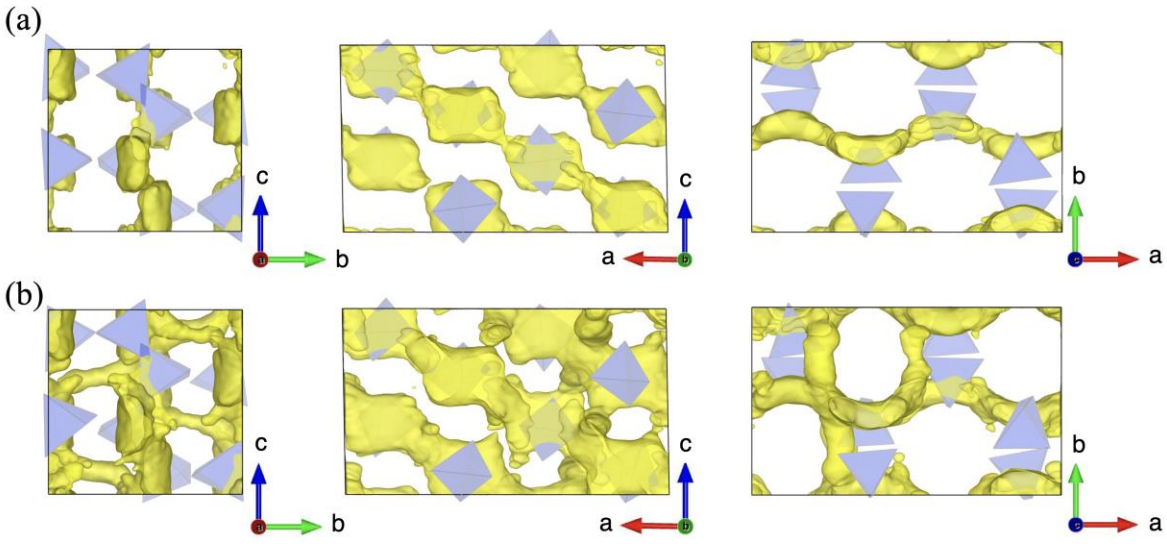

Figure 2.5 The probability density of Li ions spatial occupancy during AIMD simulations in (a) $LiTaSiO_5$ and (b) $Li_{1.25}Ta_{0.75}Zr_{0.25}SiO_5$, in different perspectives. The isosurface is plotted at the mean value of the probability density in each structure over the entire AIMD simulation. Only SiO_4 polyhedrons (blue) are shown for clarity.

2.2.2 Experimental Results

2.2.2.1 Crystal Structure and Microstructure Characterizations

Based on the computational results, a minimum amount of 12.5% Zr-doping is required to achieve a conductivity over 0.1 $mS \cdot cm^{-1}$. On the other hand, the computational results also indicate that when the Zr-doping exceeds 25%, the energy above hull will greatly increase to above 15 meV/atom, suggesting that a doping level of >25% may be difficult to achieve experimentally. The syntheses of the solid solution series with various Zr-doping levels within the predicted solubility range (12.5%, 20%, 25%, 30%, and 50%) were attempted and the composition and crystal structures were examined by powder X-ray diffraction (XRD).

$Li_{1+x}Ta_{1-x}Zr_xSiO_5$ samples were prepared with x = 0, 0.125, 0.20, 0.25, 0.30, and 0.50, respectively, with solid state synthesis method. The starting materials were mixed using high energy ball-milling and the pellets of the samples were sintered at 1100 °C between 24 and 48 hours. The XRD patterns of the samples are shown in Figure 2.6. The as-synthesized undoped $LiTaSiO_5$ was in good agreement with PDF#77-0896. The doped sample $Li_{1.125}Ta_{0.875}Zr_{0.125}SiO_5$ (x=0.125) shows a very similar XRD pattern with a small amount of $LiTaO_3$ impurity formed in the heating process. Compared with the pattern of undoped $LiTaSiO_5$, major peaks of the 12.5% Zr-doped sample, such as ones at $2\theta = 8.2°, 10.3°, 12.2°, \text{and } 12.7°$, etc., slightly shift toward lower two-theta angles, indicating an expansion of the unit cell. This indicates that most Zr from the starting materials dopes into the $LiTaSiO_5$ lattice at the Ta sites, despite the formation of the very minor amounts

of the secondary phase. The increased unit cell volume is expected due to the replacement of the smaller sized Ta^{5+} by large Zr^{4+} in the lattices.

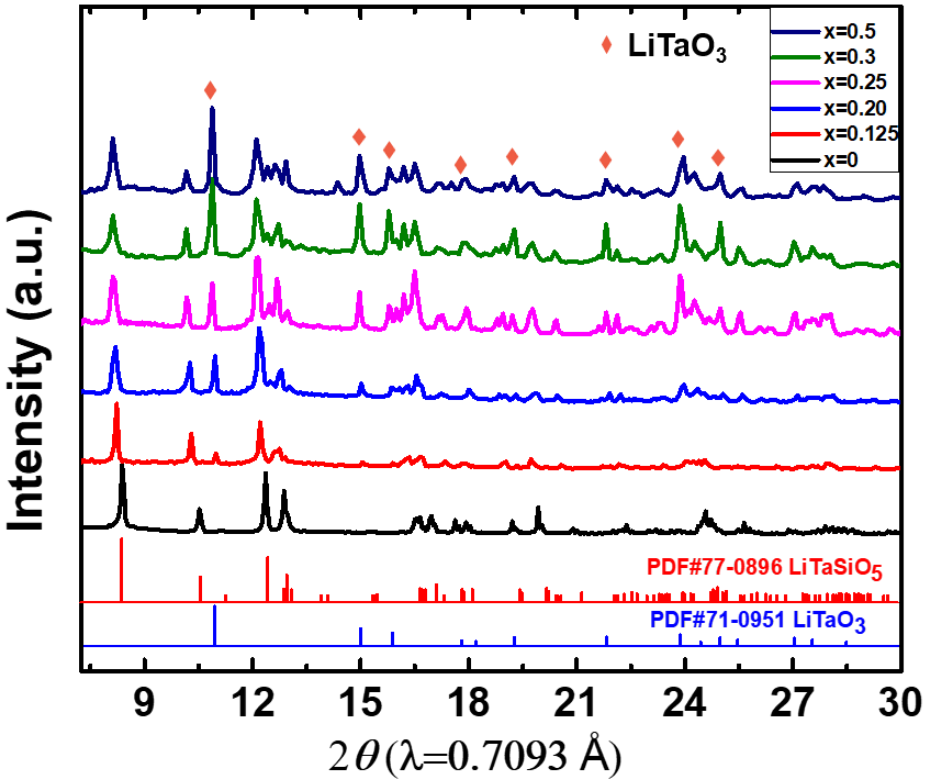

Figure 2.6 The XRD patterns of as-synthesized $Li_{1+x}Ta_{1-x}Zr_xSiO_5$ samples for x=0, 0.125, 0.2, 0.25, 0.3 and 0.5.

For the samples with higher doping levels (x > 0.2), the primary phase with the $LiTaSiO_5$ structure was still obtained in all the samples, with the reflections shifting towards lower two-theta angles as the amount of Zr in the starting materials increased. However, evident impurity of $LiTaO_3$ (or $Li_{1+x}Ta_{1-x}Zr_xO_3$) was also observed, and the fraction of the impurity increased greatly as the amount of Zr in the starting materials

increased. For samples with 30% and 50% Zr-doping (x = 0.3 and 0.5), a longer synthesis time, up to 48 hours, was attempted to convert the impurity to the target phase, but the purity did not obviously improve. This implies that the formation of the impurities is not due to the slow reaction kinetics but more likely due to the thermodynamic instability of the desired composition. It is also worth noting that obvious softening and partial melting of the pellets were observed with increasing amounts of ZrO_2 added to the starting materials.

Synchrotron XRD patterns and the corresponding Rietveld refinement results of both undoped and 12.5% Zr-doped $LiTaSiO_5$ are shown in Figure 2.7(a) and (b), respectively. For the undoped sample, the refinement results confirmed the formation of the primary $LiTaSiO_5$ phase with a space group of $P12_1/c1$ (No. 14) and the lattice parameters were refined to a = 7.3973(2) Å, b=7.9308(7) Å, and c=7.4444(5) Å, β=119.15°. The impurity $LiTaO_3$ phase was also identified with a space group of $R3c$ (No. 161) and the phase weight fraction was estimated to be less than 4% based on the refinement results. The primary phase of 12.5% Zr-doped sample ($Li_{1.125}Ta_{0.875}Zr_{0.125}SiO_5$) was refined using the same space group of $P12_1/c1$ (No. 14) with 12.5% Ta sites occupied by Zr and accordingly with additional Li at Li sites predicted by the computation. The lattice parameters of the primary phase were refined to a = 7.3485(3) Å, b=7.9937(1) Å, and c=7.4298(9) Å, β=118.41°. The unit cell volume of the 12.5% Zr-doped sample increased by 0.64% compared with the undoped sample, which is consistent with the computational results and the fact that the ionic radius of Zr^{4+} (0.72 Å) is slightly larger than that of Ta^{5+} (0.64 Å). The secondary impurity, the $LiTaO_3$ phase, refined with a space group of $R3c$ (No. 161), was estimated to be less than 5% in the 12.5% Zr-doped $LiTaSiO_5$ sample. The

crystallographic details extracted from the Rietveld refinement results are summarized in Table 2.3. These results are also confirmed by Rietveld refinement of the same samples based on neutron diffraction data, which were shown in Figure 2.8. HR-TEM image and electron diffraction were taken for the 12.5% Zr doped sample, as shown in Figure 2.9. The electron diffraction patterns are consistent with the crystal structure determined by X-ray and neutron diffractions.

Table 2.3 Full pattern fitting refinement results for synchrotron XRD patterns of $LiTaSiO_5$ (x=0) and $Li_{1.125}Ta_{0.875}Zr_{0.125}SiO_5$ (x=0.125) samples.

Sample	Phases	Space group	Lattice parameters (Å)			Lattice Parameters (°)			Phase Fraction
			a	*b*	*c*	*α*	*β*	*γ*	
$LiTaSiO_5$ (*x*=0)	$LiTaSiO_5$	P 1 2_1/c 1 (No. 14)	7.3973(2)	7.9308(7)	7.4444(5)	90	119.15	90	96.15%
	$LiTaO_3$	R 3 c (No. 161)	5.1568(6)	5.1568(6)	13.7700(2)	90	90	120	3.85%
$Li_{1.125}Ta_{0.875}Zr_{0.125}SiO_5$ (*x*=0.125)	$Li_{1+x}Ta_{1-x}Zr_{1-x}SiO_5$	P 1 2_1/c 1 (No. 14)	7.3485(3)	7.9937(1)	7.4298(9)	90	118.41	90	95.01%
	$LiTaO_3$	R 3 c (No. 161)	5.1733(3)	5.1733(3)	13.7473(1)	90	90	120	4.99%

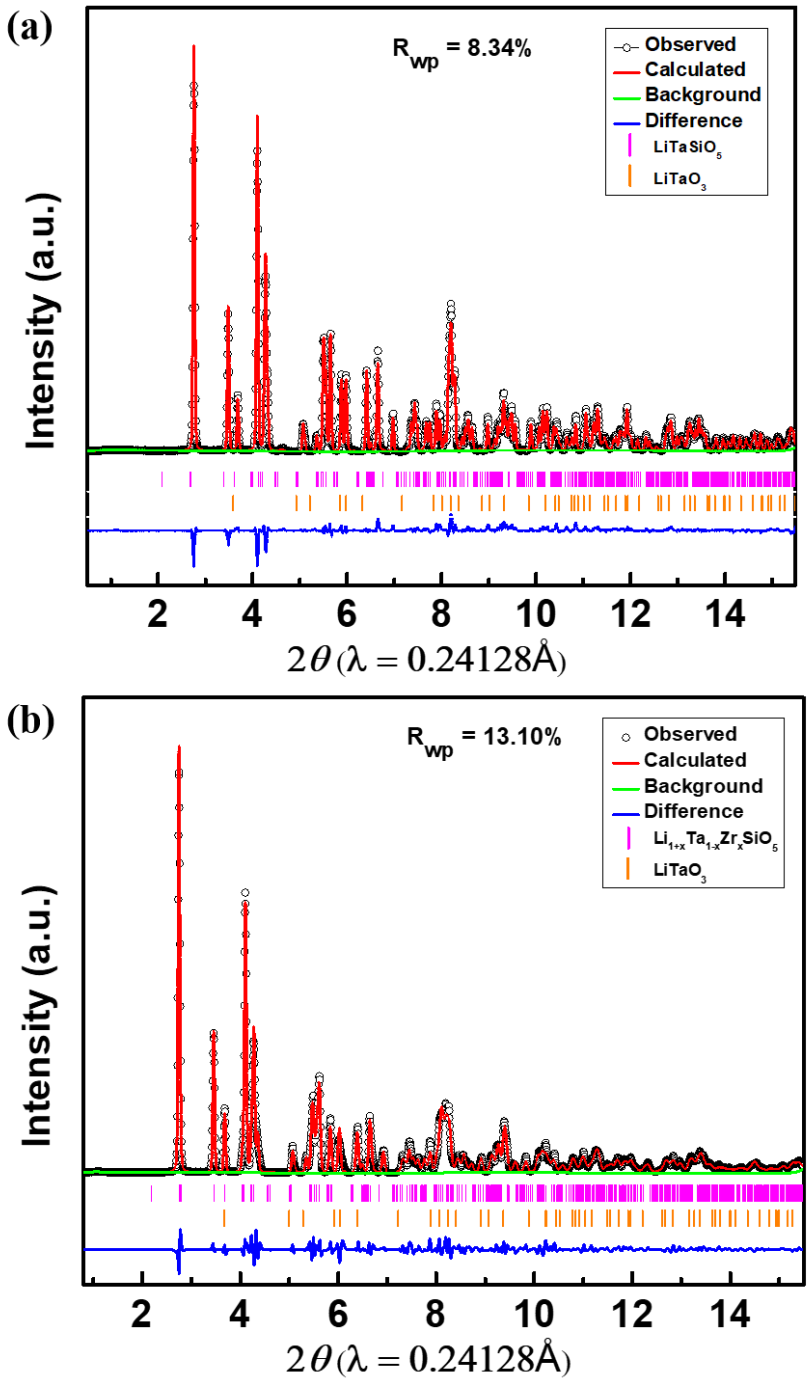

Figure 2.7 (a) XRD pattern and Rietveld refinement of $LiTaSiO_5$ (x=0) sample. (b) XRD pattern and Rietveld refinement of $Li_{1.125}Ta_{0.875}Zr_{0.125}SiO_5$ (x=0.125) sample.

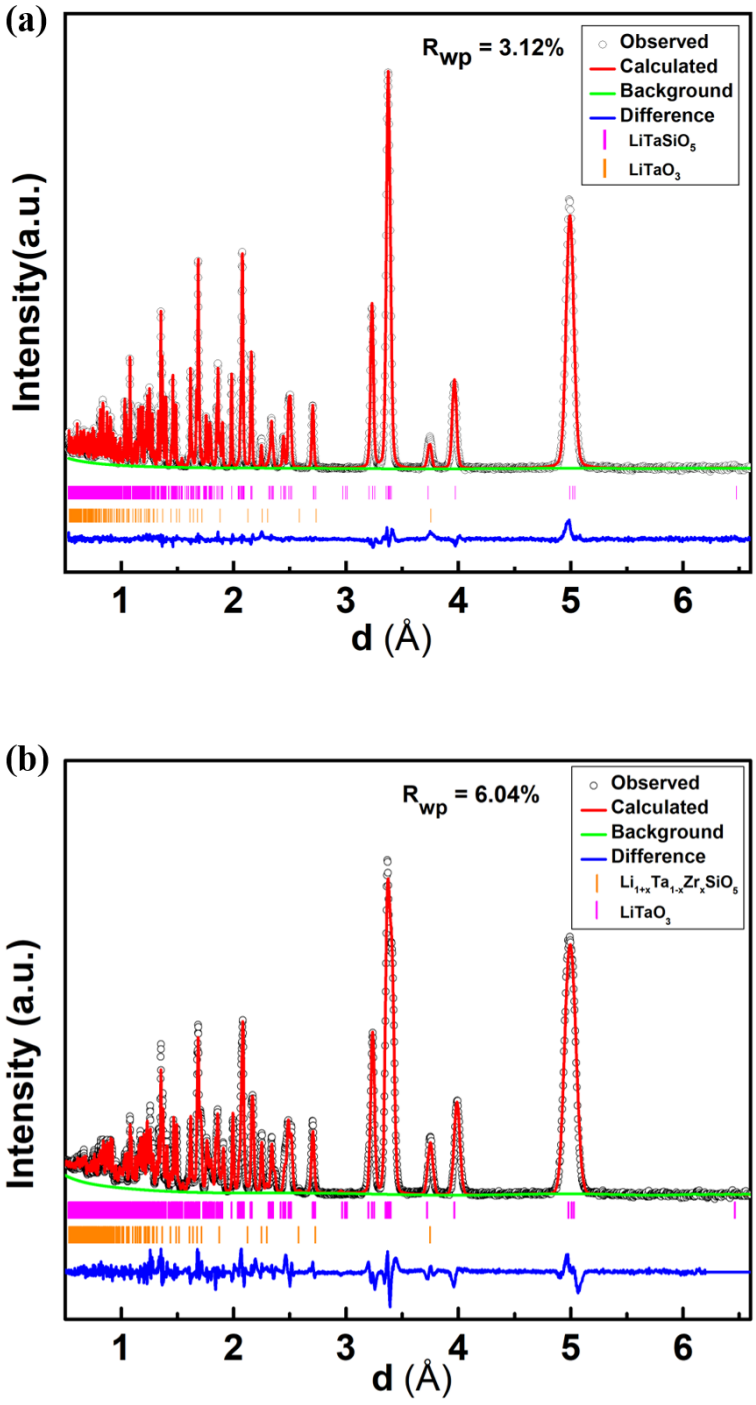

Figure 2.8 Rietveld Refinement of $LiTaSiO_5$ (x=0) and $Li_{1.125}Ta_{0.875}Zr_{0.125}SiO_5$ (x=0.125) samples based on neutron diffraction.

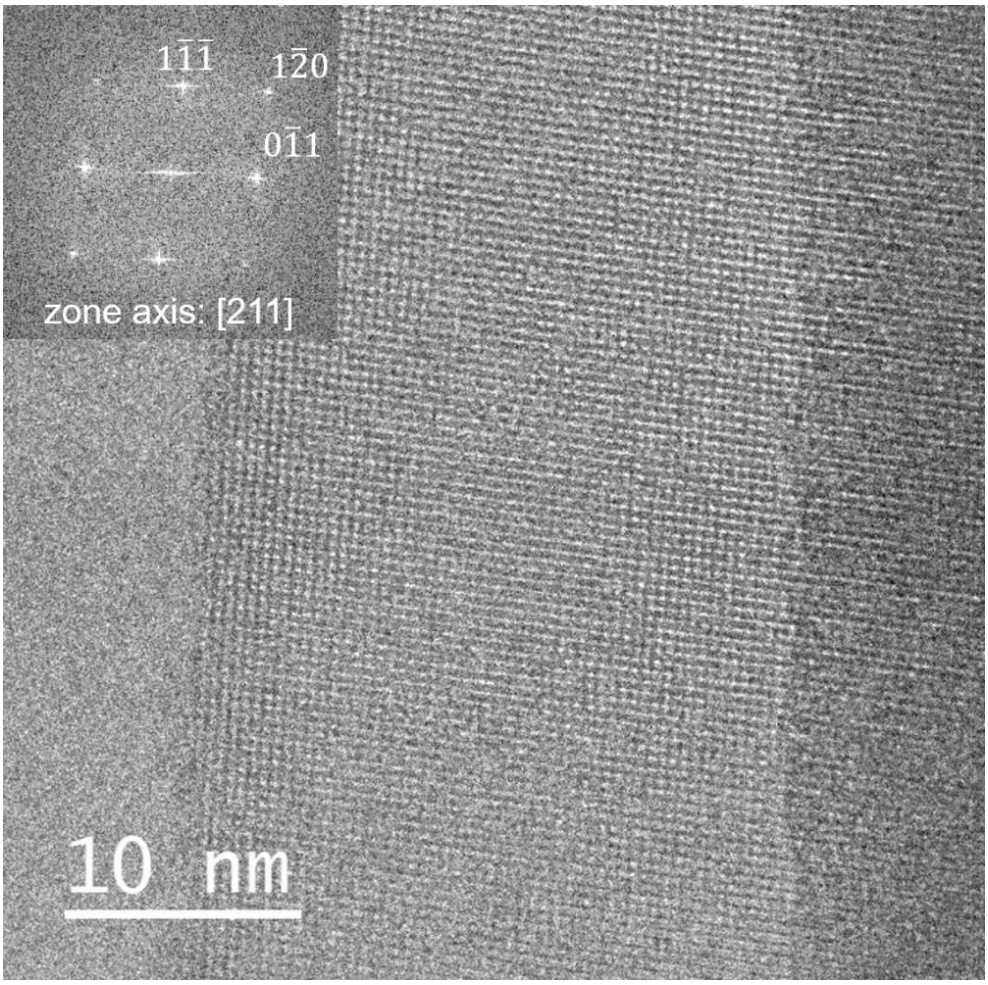

Figure 2.9 HR-TEM image and SAED pattern of 12.5% Zr-doped $LiTaSiO_5$ sample.

Scanning electron microscope (SEM) was used to investigate the morphology of $Li_{1+x}Ta_{1-x}Zr_xSiO_5$ samples. Figure 2.10 shows the SEM images for the synthesized $Li_{1.125}Ta_{0.875}Zr_{0.125}SiO_5$ (x=0.125) powder and hot-pressed pellets. For the as-synthesized powder, the particles show irregular shapes and a relatively wide distribution of particle sizes (1~10 μm), which is plausibly due to the melting-quenching process in the synthesis. After hot-pressing, the sample shows smoother surfaces and much higher density with less voids and grain boundaries, as shown in Figure 2.10(b). The morphology and density

change under hot-press led to tight contact among the particles and reduced grain boundary resistance, which is favorable for conductivity measurements. The SEM image and the corresponding elemental mapping with energy dispersive X-ray (EDX) spectroscopy of $Li_{1.125}Ta_{0.875}Zr_{0.125}SiO_5$ was shown in Figure 2.11. The distribution of Si, Ta, Zr and O elements in the EDX mapping confirms the uniform formation of $Li_{1.125}Ta_{0.875}Zr_{0.125}SiO_5$ with no evident element or phase segregations. The SEM images of both surface and cross section for undoped, 12.5% Zr, and 20% Zr-doped $LiTaZrSiO_5$ pellets are also shown in Figure 2.12. It can be seen that denser pellets are formed after hot pressing, especially for the doped samples. The cross-section images show well-fused particles and reduced grain boundaries, which confirms the effectiveness of the hot-pressing method. The relative densities of the hot-pressed pellets are measured to be 74%, 86%, and 88% for undoped, 12.5% Zr, and 20% Zr doped $LiTaSiO_5$ pellets, respectively. Compared with cold-pressed pellets, densities of which are measured to be below 60%, hot-pressed pellets present better contact among particles, less gain boundaries, and much higher relative densities. Therefore, hot-pressing was used for all three samples for the EIS measurements.

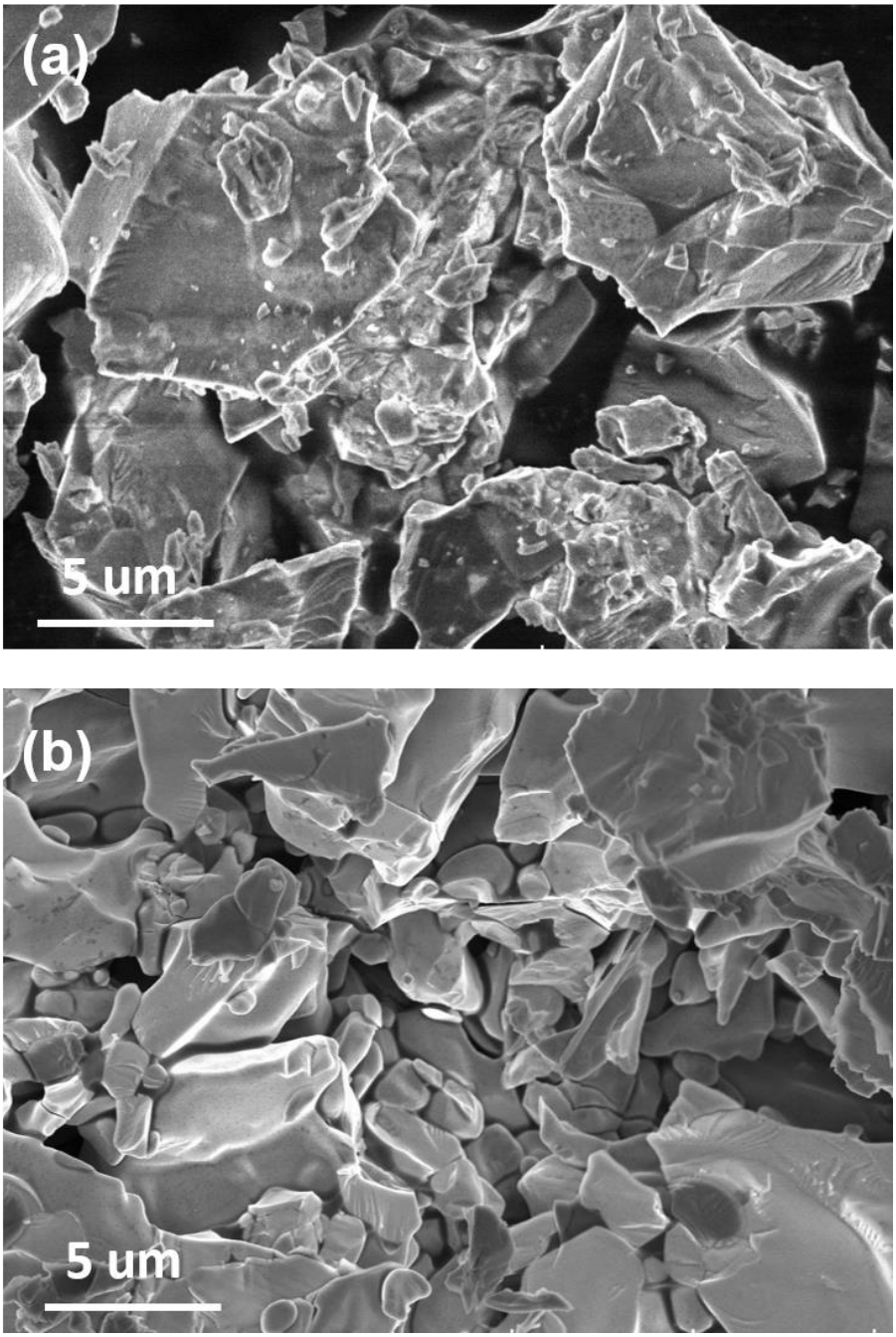

Figure 2.10 SEM images of $Li_{1.125}Ta_{0.875}Zr_{0.125}SiO_5$ (x=0.125) sample in the forms of (a) powder and (b) hot-pressed pellet.

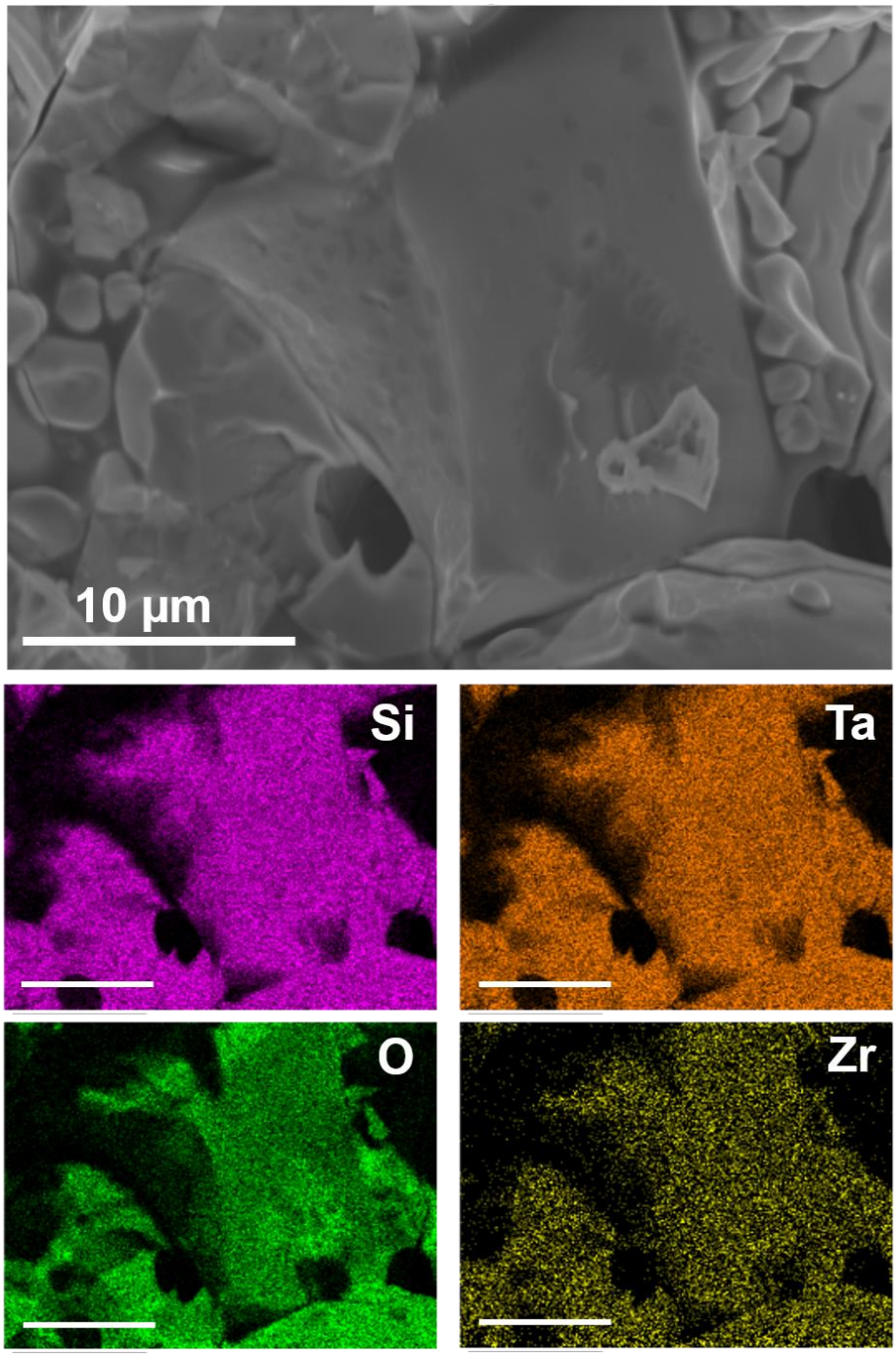

Figure 2.11 SEM image and EDX spectroscopy elemental mappings of $Li_{1.125}Ta_{0.875}Zr_{0.125}SiO_5$ (x=0.125) sample.

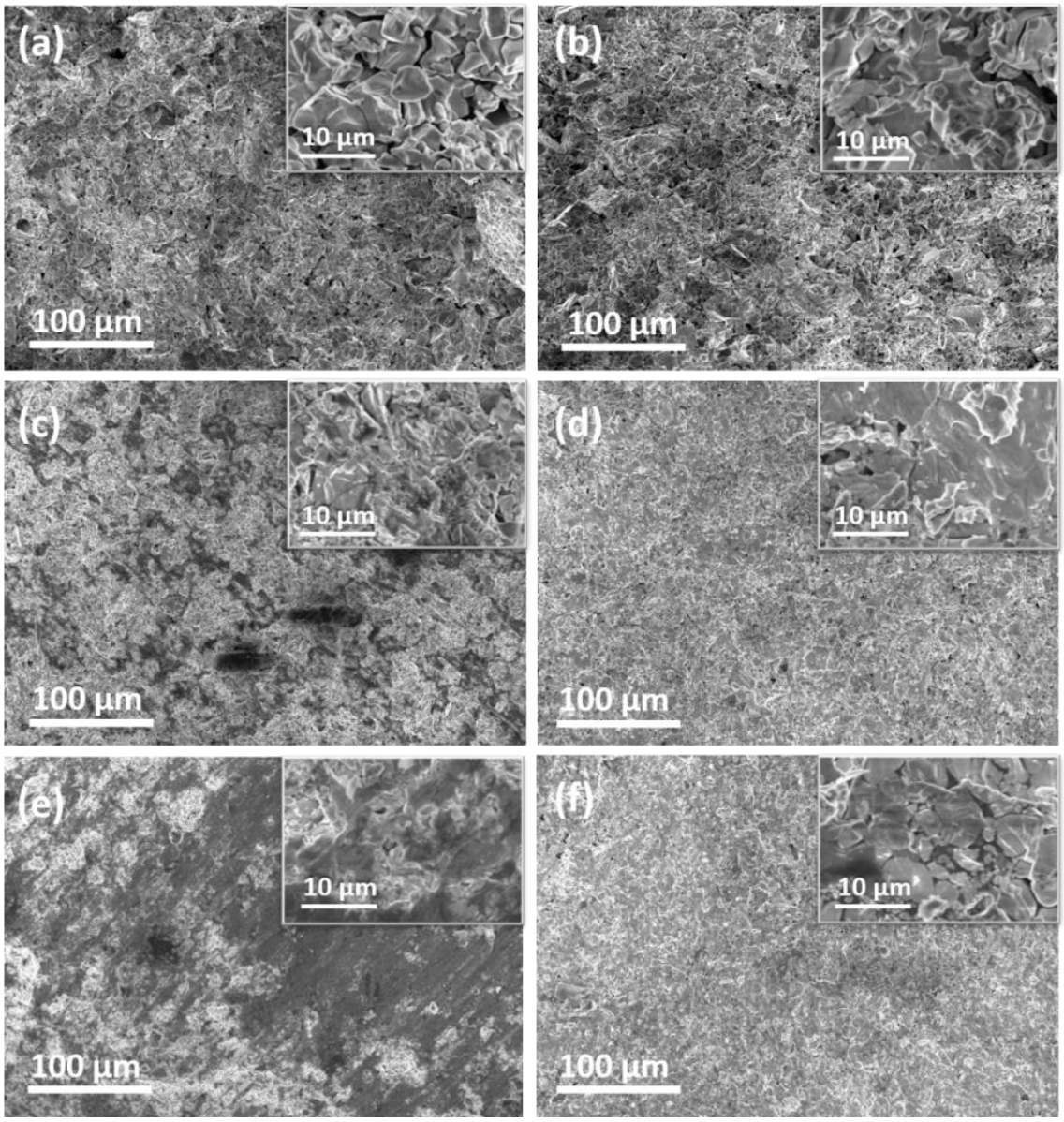

Figure 2.12 SEM images of (a, b) $LiTaSiO_5$ (x=0), (c, d) $Li_{1.125}Ta_{0.875}Zr_{0.125}SiO_5$ (x=0.125), and (e, f) $Li_{1.2}Ta_{0.8}Zr_{0.2}SiO_5$ (x=0.2) samples. The left column (a, c, e) shows the morphology on the surface of the pellets, and the right column (b, d, f) shows the cross-section images of the pellets.

In order to evaluate the chemical stability, an air-stability experiment was conducted by exposing the as-synthesized $Li_{1.125}Ta_{0.875}Zr_{0.125}SiO_5$ (x = 0.125) sample in an ambient atmosphere for a reasonably long time. As shown in Figure 2.13, the as-synthesized $Li_{1.125}Ta_{0.875}Zr_{0.125}SiO_5$ presents the $LiTaSiO_5$-like main phase and minor

impurity of $LiTaO_3$-like phase. After being exposed in the air for 5 and 12 days, no extra diffraction peaks or distinct peak changes are observed, indicating good chemical stability of this group of oxide materials against air and moisture. This good stability is also confirmed in first principles computation.

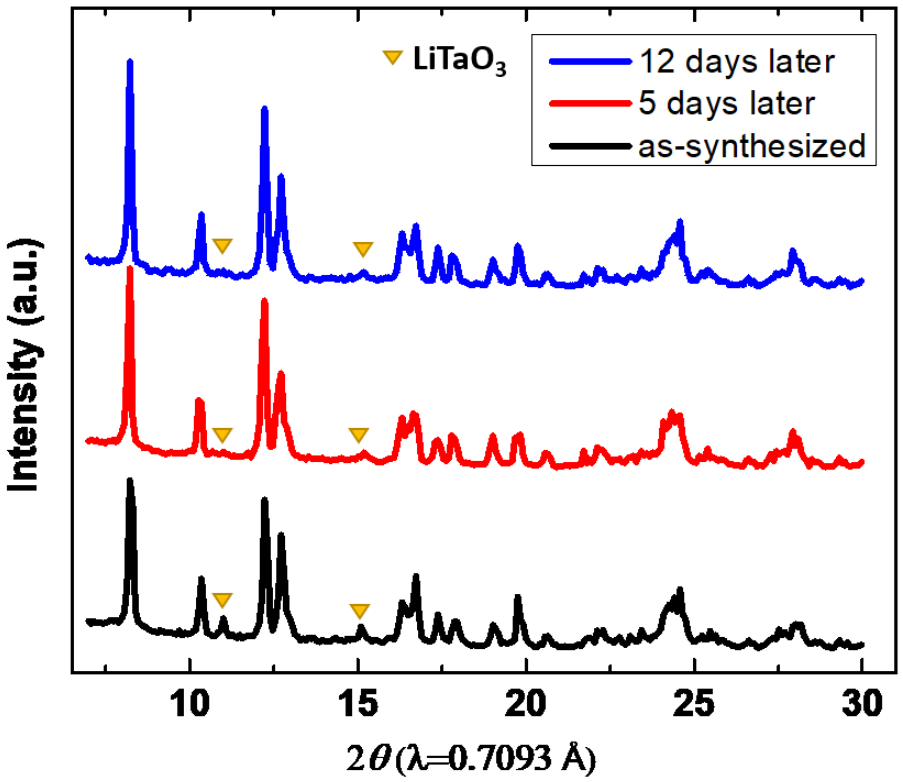

Figure 2.13 XRD patterns of as-synthesized and air-exposed 12.5% Zr-doped $Li_{1+x}Ta_{1-x}Zr_xSiO_5$ after 5 and 12 days.

2.2.2.2 Reaction Mechanism of the Solid-State Synthesis

In order to further explore the kinetics and thermodynamics associated with the formation process of $Li_{1+x}Ta_{1-x}Zr_xSiO_5$ with various Zr-doping levels, *in situ* XRD for

synthesis was performed by heating up the pellet of ball-milled precursor in an Anton Paar HTK1200N furnace mounted in the X-ray diffractometer. The temperature was raised from room temperature to 1050 °C with multiple steps and XRD data was collected while the temperature was held constant in each step. Evolution of the XRD patterns from samples with x = 0 and 0.2 are shown in Figure 2.14**(**a) and (b), respectively. *In situ* XRD of 50% Zr-doped sample was also conducted and the patterns are shown Figure 2.15.

As shown in Figure 2.14**(**a), for the undoped $LiTaSiO_5$ sample, reflections of starting materials (Ta_2O_5 and Li_2CO_3) can be observed at room temperature and remain intact below 600 °C. Peaks of SiO_2 are not seen because amorphous SiO_2 was used as the starting material. When heated to 600 °C, $LiTaO_3$ phase starts to form as a product of the reaction between Ta_2O_5 and Li_2CO_3. The peaks of Ta_2O_5 and Li_2CO_3 gradually decreases when temperature increases and eventually disappear at 850 °C. As the temperature goes up, $LiTaSiO_5$ starts to form at 950 °C as a product of the reaction between $LiTaO_3$ and amorphous SiO_2. The fraction of $LiTaO_3$ decreases as the fraction of $LiTaSiO_5$ increases accordingly, as the temperature further increases to 1050 °C. However, a small amount of $LiTaO_3$ phase still exists, even after cooling down to room temperature. Phase-pure $LiTaSiO_5$ product was obtained in lab synthesis, but not in the *in-situ* XRD experiment, because only a 4-hour dwelling time at 1050°C was used in the *in-situ* XRD experiment, which was not long enough to convert all the $LiTaO_3$ phase into the target $LiTaSiO_5$ phase given the rather slow kinetics of this reaction.

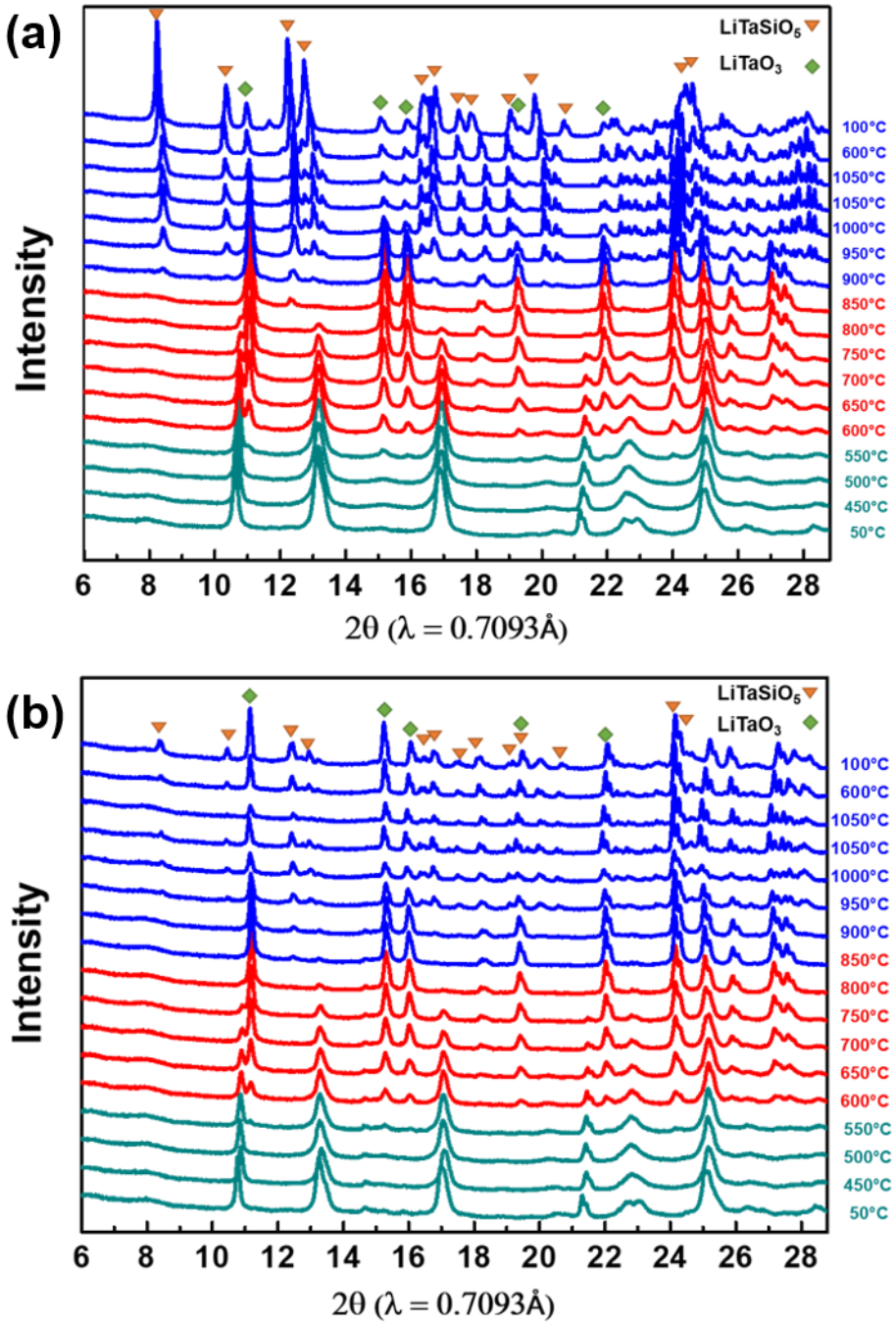

Figure 2.14 *In situ* XRD pattern of $Li_{1+x}Ta_{1-x}Zr_xSiO_5$ samples with various Zr-doping levels. (a) $LiTaSiO_5$ (x=0), (b) $Li_{1.2}Ta_{0.8}Zr_{0.2}SiO_5$ (x=0.2).

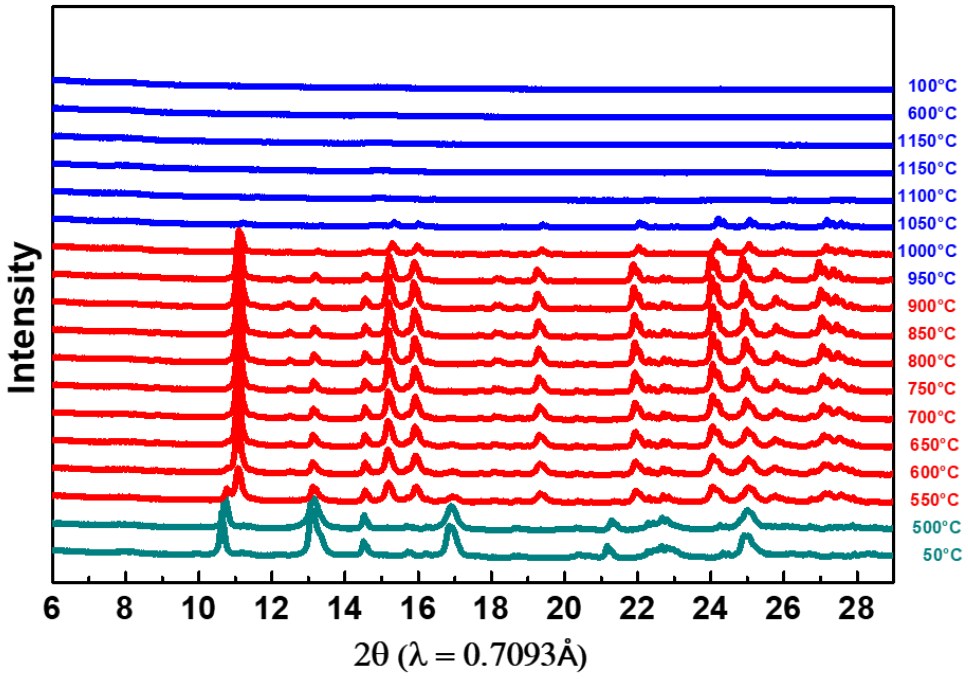

Figure 2.15 *In situ* XRD patterns of $Li_{1+x}Ta_{1-x}Zr_xSiO_5$ samples with 50% Zr-doping (x=0.5).

A similar reaction pathway was observed for the 20% Zr-doped sample ($Li_{1.2}Ta_{0.8}Zr_{0.2}SiO_5$, x = 0.2) as shown in Figure 2.14(b). The intermediate $LiTaO_3$ phase starts to form at 600°C and the starting materials are all consumed upon reaching 850°C with only $LiTaO_3$ phase being observed. Meanwhile a $LiTaSiO_5$-like phase starts to form at 850°C. The increased background at low angle range implies that the sample may be partially melted. Due to the limited reaction time, only a small amount of a $LiTaSiO_5$-like phase was form during the *in-situ* XRD experiment with a large amount of the $LiTaO_3$ phase remaining in the final product. Evidence of this is seen in the significantly lower peak intensities of the $LiTaSiO_5$-like phase than that of the $LiTaO_3$ phase. While this reaction can be facilitated by longer reaction time in a box furnace, this *in situ* XRD result

clearly indicates that with increased amount of Zr in the starting materials, the thermodynamic driving force toward the formation of the $Li_{1+x}Ta_{1-x}Zr_xSiO_5$ solid solution phase becomes much smaller, and accordingly the kinetics of the reaction become significantly more sluggish. This can be further confirmed by the *in situ* XRD results of the 50% Zr doped sample, shown in Figure 2.15, which was performed using a higher ending temperature of 1150 °C. Similarly, the intermediate $LiTaO_3$ phase formed below 600°C. However, the pellet completely melted at 1050 °C, which led to the disappearance of all detectable peaks, even after cooling down to room temperature. Similar phenomenon was also observed during the synthesis process in box furnaces, where the pellets of 30% and 50% Zr-doped samples melted and deformed severely. Only limited amount of $Li_{1+x}Ta_{1-x}Zr_xSiO_5$ phase was obtained even after high temperature calcination at 1200°C for 48 hours. Significant amount of $LiTaO_3$ remained in the final product, as shown in the XRD patterns in Figure 2.6. This indicates that practically, at least within the experimental conditions we have explored so far, the solubility limit of Zr in $Li_{1+x}Ta_{1-x}Zr_xSiO_5$ phases is below 12.5%. Higher doping amount leads to formation of $LiTaO_3$ and other amorphous impurities.

2.2.2.3 Ionic Conductivity Measurement and Proof-of-Concept Electrochemical Testing

Powder of the undoped, 12.5%, and 20% Zr-doped samples were pressed into pellets at 1100 °C with DC heating for 2 minutes to densify the pellet and reduce the grain boundary resistance. These pellets were then analyzed with electrochemical impedance spectroscopy (EIS). The results for samples with higher Zr-doping levels ($\geq$ 25%), which are not shown, all contained relatively high amount of low-conduction $LiTaO_3$ impurity and yielded very low ionic conductivities. The Nyquist plots of the impedances for

$Li_{1.125}Ta_{0.875}Zr_{0.125}SiO_5$ (x=0.125) sample at variable temperatures are shown in Figure 2.16. The impedance spectra show a semicircle in the high-frequency region followed by a spike at low-frequency region. The low-frequency spike represents the impedance response due to the blocking of mobile Li ions at the electrode interface, which is typical behavior for an ionic conductor. The ionic conductivities were calculated based on the total resistance (including bulk and grain boundary resistance) obtained from the intercept of the semicircle and the spike on the *x*-axis and the dimensions of the pellets. Arrhenius plot of the samples are shown in Figure 2.17. The $\log(\sigma)$ versus $1/T$ curves of the samples show good linearity, indicating no phase transition or ordering change within the measured temperature range. For the undoped $LiTaSiO_5$ sample, Nyquist plots can be obtained only above 100°C due to the large resistance and frequency limits. The ionic conductivity of $LiTaSiO_5$ is measured to be 1.47×10^{-6} S·cm^{-1} at 100°C. Based on the linear fitting of Arrhenius plots, the conductivity of $LiTaSiO_5$ at room temperature was estimated to be 3.11×10^{-8} S·cm^{-1} through extrapolation.

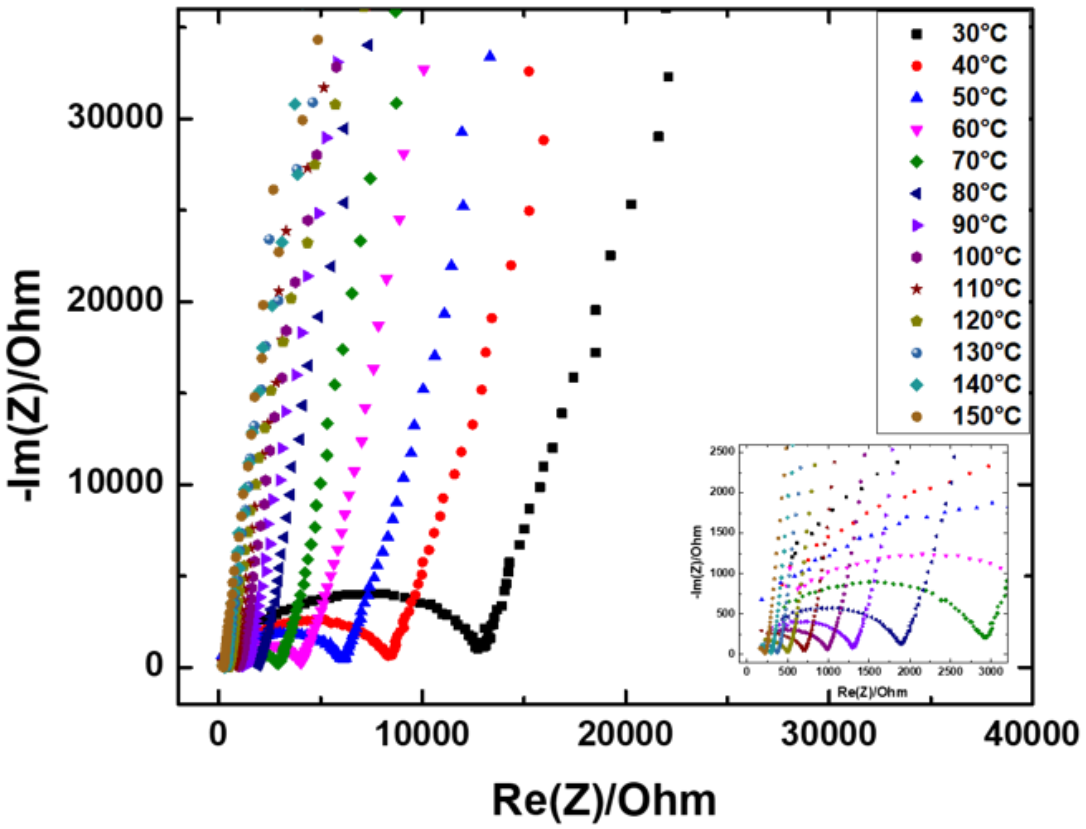

Figure 2.16 Nyquist impedance plots of $Li_{1.125}Ta_{0.875}Zr_{0.125}SiO_5$ (x=0.125) from 30°C to 150°C (the inset shows the zoomed-in region for details at higher temperatures).

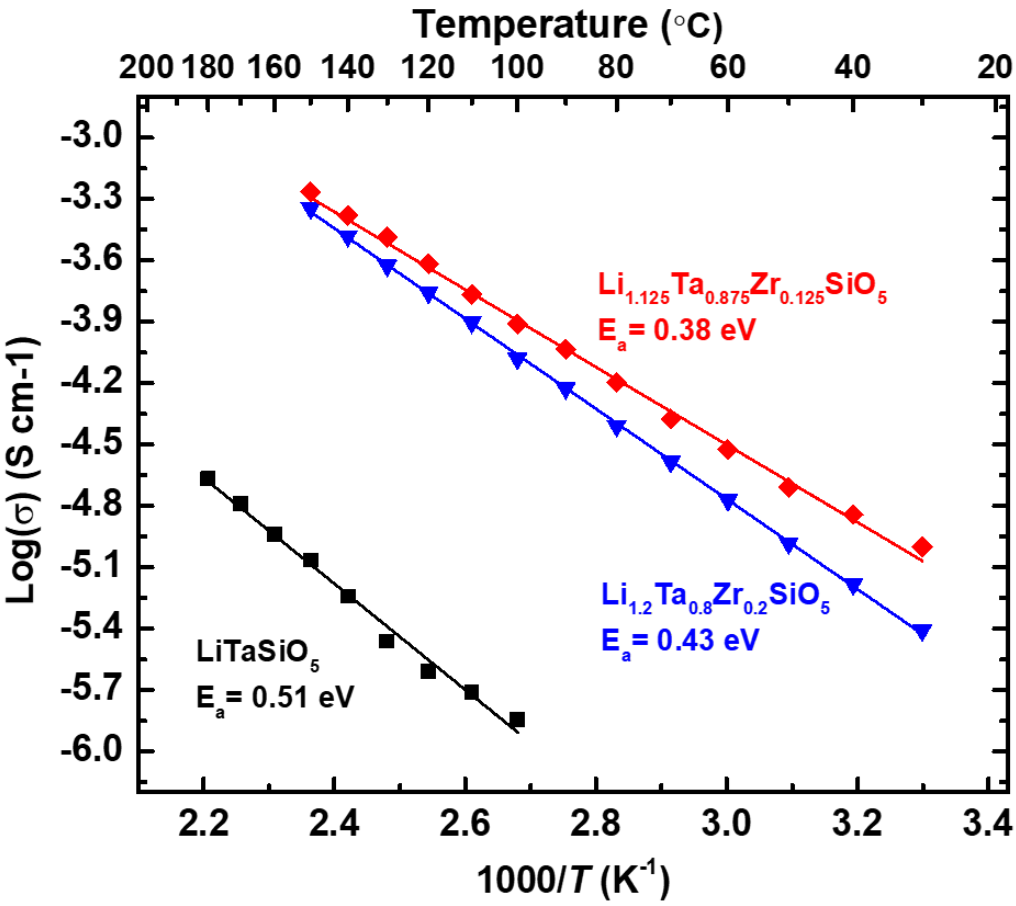

Figure 2.17 Arrhenius plots of $Li_{1+x}Ta_{1-x}Zr_xSiO_5$ for x = 0, 0.125, and 0.2, corresponding to 0%, 12.5%, and 20% Zr-doped $LiTaSiO_5$ samples.

Table 2.4 Activation energy and ionic conductivity (30°C) of $Li_{1+x}Ta_{1-x}Zr_xSiO_5$ for x=0, 0.125, and 0.2 based on experimental results.

Composition	E_a (eV)	Ionic conductivity at 30°C (mS·cm^{-1})
$LiTaSiO_5$	0.51 eV	3.11×10^{-5} (extrapolated)
$Li_{1.125}Ta_{0.875}Zr_{0.125}SiO_5$	0.38 eV	0.010
$Li_{1.2}Ta_{0.8}Zr_{0.2}SiO_5$	0.43 eV	0.0039

For 12.5% and 20% Zr-doped samples, Li^+ conductivity (σ) at 30°C was calculated to be 1.00×10^{-5} S·cm^{-1} and 3.9×10^{-6} S·cm^{-1}, respectively. Additional results of 5% and 10% Zr-doped samples are also obtained, including their XRD patterns (Figure 2.18), ionic conductivities, and activation energy (Figure 2.19 and Table 2.5). Compared with undoped $LiTaSiO_5$ sample, the Zr-doped samples showed two to three orders of magnitude higher conductivity at room temperature. This can be explained by the additional Li^+ interstitial sites introduced by cation doping with lower valence and the resultant lower energy barrier potentially activated by these interstitial sites. The difference in ionic radii between Ta^{5+} (0.64 Å) and Zr^{4+} (0.72 Å) also gives rise to structure distortions and can possibly create more space to accommodate extra Li ions and facilitate faster Li^+ diffusion. It is also noteworthy that the room temperature conductivity of 12.5% Zr-doped sample (1.00×10^{-5} S·cm^{-1}) is lower than computational results (2.8×10^{-3} S·cm^{-1}), and more Zr-doping (20%) did not improve the conductivity but resulted in a lower value instead, which is opposite to the trend predicted computationally. Both observations are closely

related to the formation of poorly conductive $Li_{1+x}Ta_{1-x}Zr_xO_3$ impurities. Higher Zr-doping level results in higher fraction of the $Li_{1+x}Ta_{1-x}Zr_xO_3$ phase, as shown in Figure 2.6, which is detrimental to the percolation of the conducting $Li_{1+x}Ta_{1-x}Zr_xSiO_5$ phase through the pellet and therefore significantly lowers the measured overall conductivity. These two competing effects suggest that the optimal amount of Zr-doping to achieve the highest Li^+ conductivities should range between 10% and 20%, while the actual value will also depend on the synthesis and pressing conditions and can vary within a certain range.

Based on the linear fits of the Arrhenius plots in Figure 2.19, the diffusion activation energy can be calculated using the equation $\sigma = A\exp(-E_a/k_bT)$, where A is the pre-exponential parameter, E_a is the activation energy, and k_b is the Boltzmann constant. The results are listed in Table 2.5. From undoped samples to 12.5% Zr-doped $LiTaSiO_5$ samples, the activation energy decreases from 0.51 eV to 0.38 eV, while the 20% Zr-doped sample shows an activation energy of 0.43 eV, higher than the 12.5% Zr-doped sample. As predicted, Zr-doping can effectively decrease the diffusion barriers and result in a lower activation energy than the undoped $LiTaSiO_5$ sample, although the activation energy is still higher than computational results (0.21 - 0.25 eV). This phenomenon, again, can be ascribed to the existence of the poorly conductive $Li_{1+x}Ta_{1-x}Zr_xO_3$ impurity. Among all the samples synthesized and tested experimentally, 12.5% Zr-doped sample ($Li_{1.125}Ta_{0.875}Zr_{0.125}SiO_5$) showed the lowest activation energy and the highest ionic conductivity, suggesting a significant improvement over the $LiTaSiO_5$ phase potentially due to the concerted migration with a lower energy barrier activated by the Zr^{4+} doping.

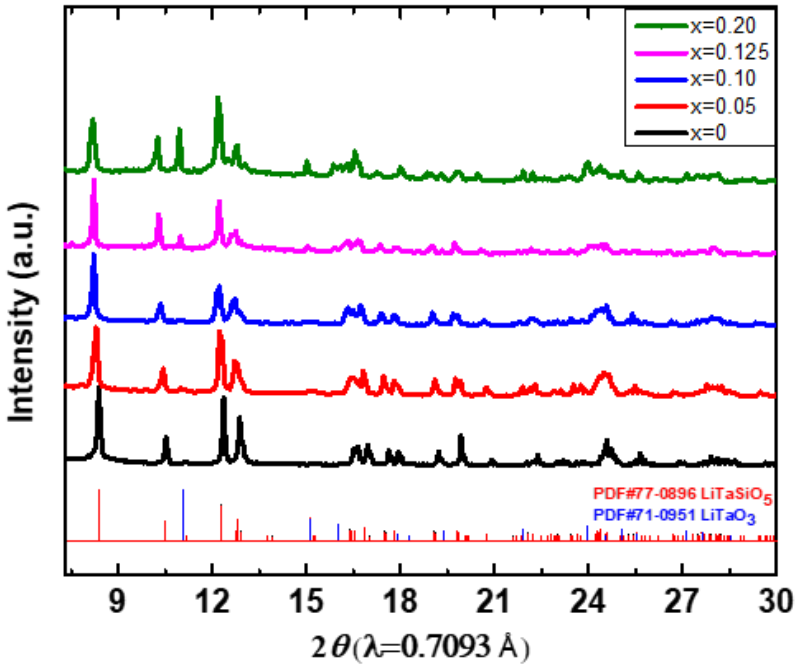

Figure 2.18 The XRD patterns of as-synthesized $Li_{1+x}Ta_{1-x}Zr_xSiO_5$ samples for x=0, 0.05, 0.10, 0.125, and 0.20.

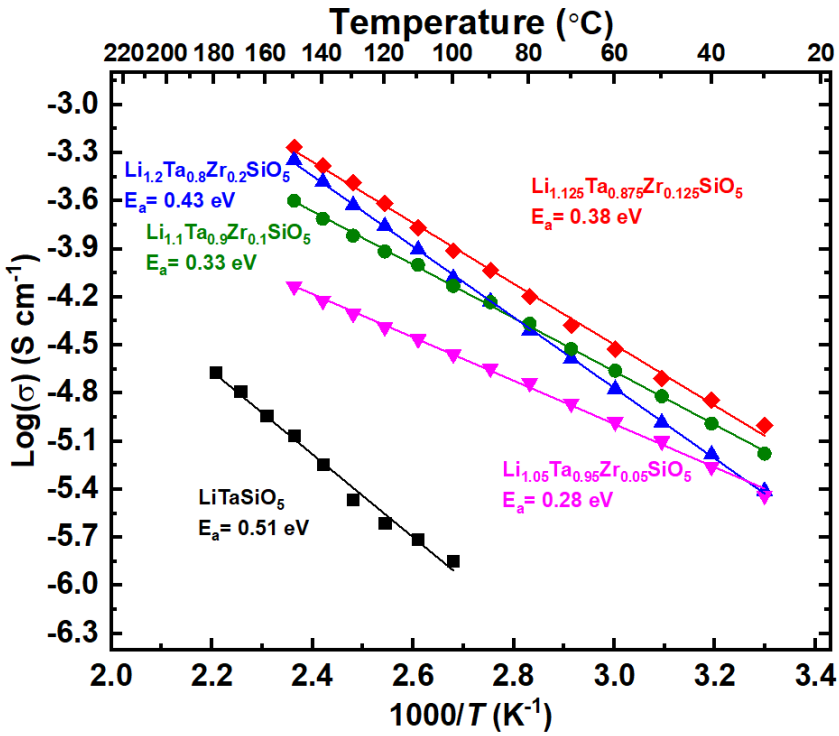

Figure 2.19 Arrhenius plots of $Li_{1+x}Ta_{1-x}Zr_xSiO_5$ for x = 0, 0.05, 0.10, 0.125, and 0.2, corresponding to 0%, 5%, 10%, 12.5%, and 20% Zr doped $LiTaSiO_5$ samples.

Table 2.5 Experimentally obtained activation energy and ionic conductivity (at 30°C) of $Li_{1+x}Ta_{1-x}Zr_xSiO_5$ for x = 0, 0.05, 0.10, 0.125, and 0.2.

Composition	E_a (eV)	Ionic conductivity at 30°C ($mS \cdot cm^{-1}$)	Relative Density
$LiTaSiO_5$ (x=0)	0.51	3.11×10^{-5} (extrapolated)	74.40%
$Li_{1.05}Ta_{0.95}Zr_{0.05}SiO_5$ (x=0.05)	0.28	0.0036	77.83%
$Li_{1.1}Ta_{0.9}Zr_{0.1}SiO_5$ (x=0.10)	0.33	0.0067	81.50%
$Li_{1.125}Ta_{0.875}Zr_{0.125}SiO_5$ (x=0.125)	0.38	0.010	86.40%
$Li_{1.2}Ta_{0.8}Zr_{0.2}SiO_5$ (x=0.20)	0.43	0.0039	88.07%

The electronic conductivities of the doped samples were evaluated using DC polarization measurements. The DC electronic conductivities for 12.5% Zr and 20% Zr doped $LiTaSiO_5$ samples are estimated to be 3.23×10^{-9} $S \cdot cm^{-1}$ and 1.89×10^{-10} $S \cdot cm^{-1}$, respectively, and the Li ion transport numbers are both calculated to be close to 1.0 (>0.9997 and >0.9999, respectively). These results suggest that the doped materials are pure lithium ion conductors.

Cyclic voltammogram (CV) tests of these materials were also conducted (Figure 2.20). The results indicate that this compound is stable against most cathodes. Redox of Ta and Si may be activated at low voltage range, indicating protection mechanism need to be used when Li metal is used as the anode. An all-solid-state cell was also assembled to

demonstrate the feasibility of this material as solid electrolyte. The cell with $LiFePO_4$ cathode, Li-In alloy anode, and 12.5% Zr-doped sample as the electrolyte was successfully cycled at 80 °C and a reasonably good capacity was achieved (Figure 2.21). Optimizations are necessary to improve the rate capability, cycling stability, and reversible capacity of the cells. But for a new compound that was synthesized for the first time and not fully optimized, the successful cycling of the solid-state cell is encouraging and warrants more work on this class of materials in the future.

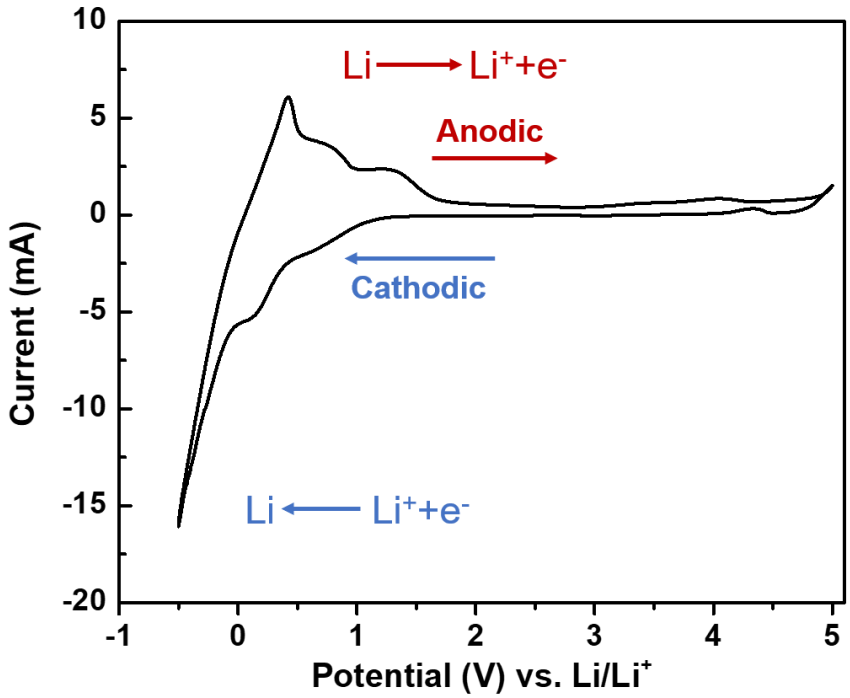

Figure 2.20 Cyclic voltammogram (CV) curve of the Li-LTZSO coin cell at 5 mV s^{-1}.

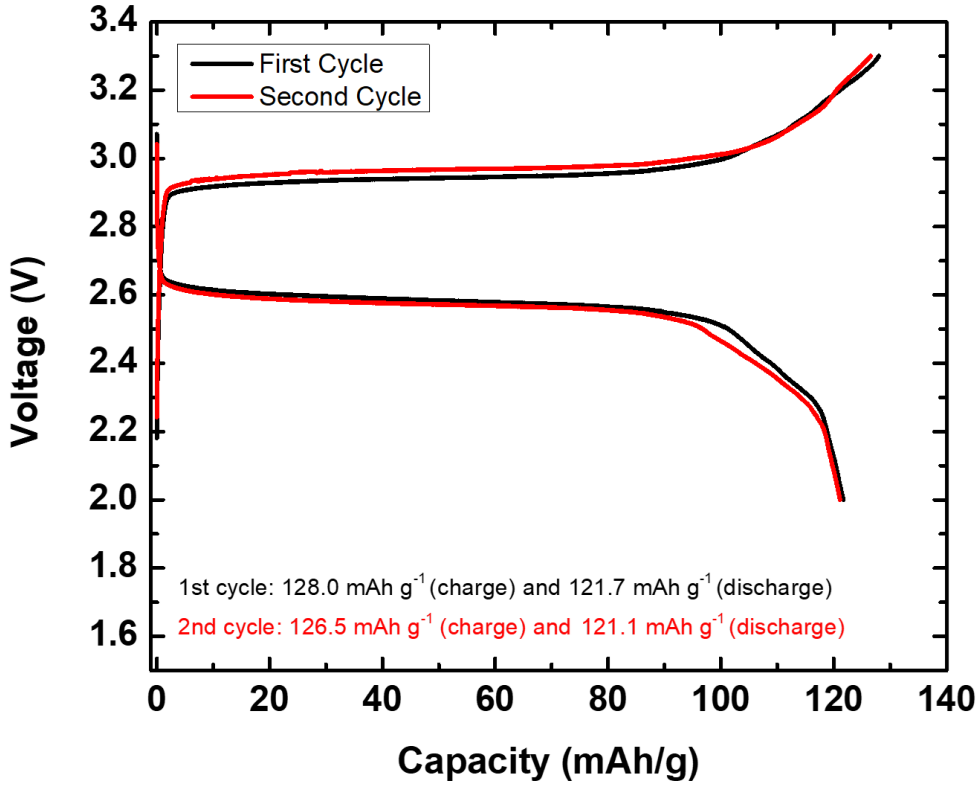

Figure 2.21 Charge and discharge voltage profiles of an $LiFePO_4$ | $Li_{1.125}Ta_{0.875}Zr_{0.125}SiO_5$ | Li-In all-solid-state battery at 80 °C.

2.2.3 Discussion

In this integrated computational and experimental study, we designed a group of $Li_{1+x}Ta_{1-x}Zr_xSiO_5$ compounds based on a rational strategy of activating concerted migration to achieve higher ionic conductivity in a given crystal structure. This strategy is demonstrated by the successful synthesis of $Li_{1+x}Ta_{1-x}Zr_xSiO_5$ sphene compounds and the significant improvement of ionic conductivity by three orders of magnitude over the original sphene $LiTaSiO_5$. Although currently it is difficult to experimentally verify the

concerted migration mechanism with known characterization techniques, this design strategy is demonstrated to be effective in realizing high conductivity in a number of known super ionic conductors, such as garnet LLZO, LGPS, and LATP [118], and now in a newly discovered family of fast ionic conductors. The sphene structure has long been known but not investigated for ion transport. The computationally predicted Zr-doping converts a non-conductive structure ($< 10^{-8}$ $S \cdot cm^{-1}$) to a highly conductive structure with ionic conductivities of 10^{-5} - 10^{-4} $S \cdot cm^{-1}$, making this new family of compounds potential competitors to the known oxide super-ionic conductors such as LLZO.

In our experiments, the 12.5% Zr-doped sample showed a promising room-temperature conductivity of $>10^{-5}$ $S \cdot cm^{-1}$. Since this is the first study on this new compound, the synthesis conditions are not yet optimized for this materials system. The discrepancy between computation and experiments are attributed to two major reasons: (1) the existence of the insulating impurity phases in the sample, such as lithium tantalum oxides (fraction of impurity evaluated by Rietveld refinement was provided in Table 2.3). Such insulating impurity certainly lowers the measured conductivity. (2) The low density and large grain boundary resistance of the pellets. From Table 2.5, it can be seen that the highest density that we currently achieve is < 90%, which can be a factor significantly lowering the measured conductivity.

To evaluate the impact of grain boundary (GB) resistance to the measured conductivity, I have repeated EIS measurements for the 12.5% Zr-doped sample in a wider frequency range of 1 Hz to 30 MHz with using a Solartron Impedance Analyzer. With a much higher frequency limit, the ionic conductivity governed by the intrinsic bulk

component and the grain boundary component can be better differentiated. As shown in Figure 2.22, the Nyquist plot of the 12.5% Zr-doped pellet at 30°C is composed of two semi-circles in the high frequency range and a spike in the low frequency range. The solid line represents a fit using the equivalent circuit shown in the figure. Each group of the resistance (R) and constant phase element (CPE) connected in parallel represents one semi-circle, and the two semi-circles are corresponding to bulk resistance and grain boundary resistance, respectively. This assignment follows a similar manner in previous research on oxide-based ionic conductors [125] and may need verification using samples with controlled grain sizes to ensure accuracy. Based on this preliminary analysis, the fitting results show a large difference between R1 and R2, indicating the Li ion conduction across the grain boundary is significantly reduced compared with intragranular conduction. The bulk and grain boundary conductivity of the 12.5% Zr-doped sample under various temperatures and the corresponding Arrhenius plots are shown in Figure 2.23, together with the conductivity results of undoped sample plotted for reference. The bulk conductivity of the 12.5% Zr doped sample is about one order of magnitude higher than the GB conductivity. Accordingly, the measured total conductivity is dominated by GB conductivity. Therefore, if we compare the bulk conductivity measured for the 12.5% Zr doped sample in Figure 2.22 (estimated to be ~ 0.1 mS cm^{-1} at 30 °C) and the computed conductivity at 300 K, the difference is about one order of magnitude. This discrepancy is not significantly large, considering this sample was just synthesized for the first time and was not fully optimized.

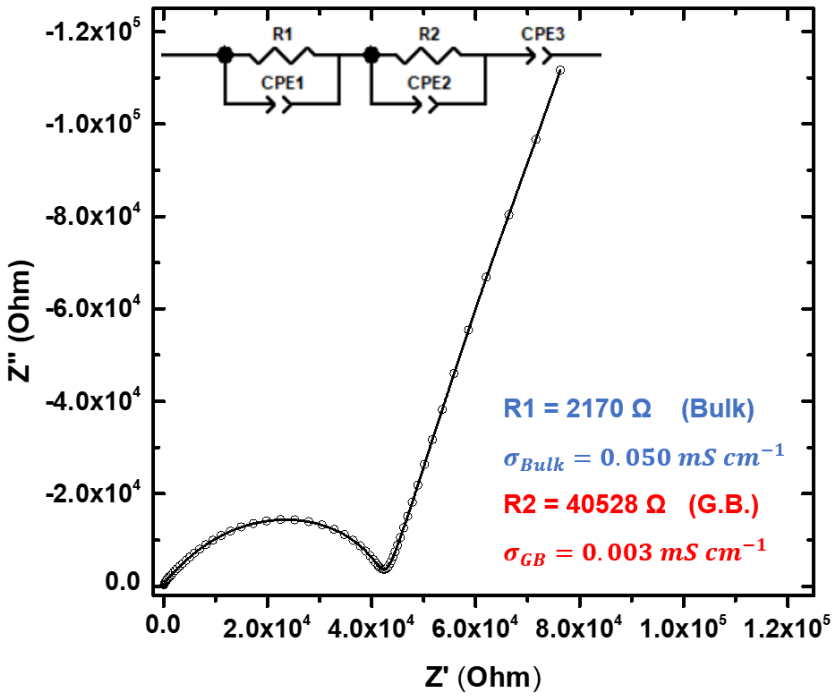

Figure 2.22 AC-impedance diagram of the $Li_{1.125}Ta_{0.875}Zr_{0.125}SiO_5$ (x = 0.125) sample at 30 °C. The solid line represents a fit using the equivalent circuit as shown.

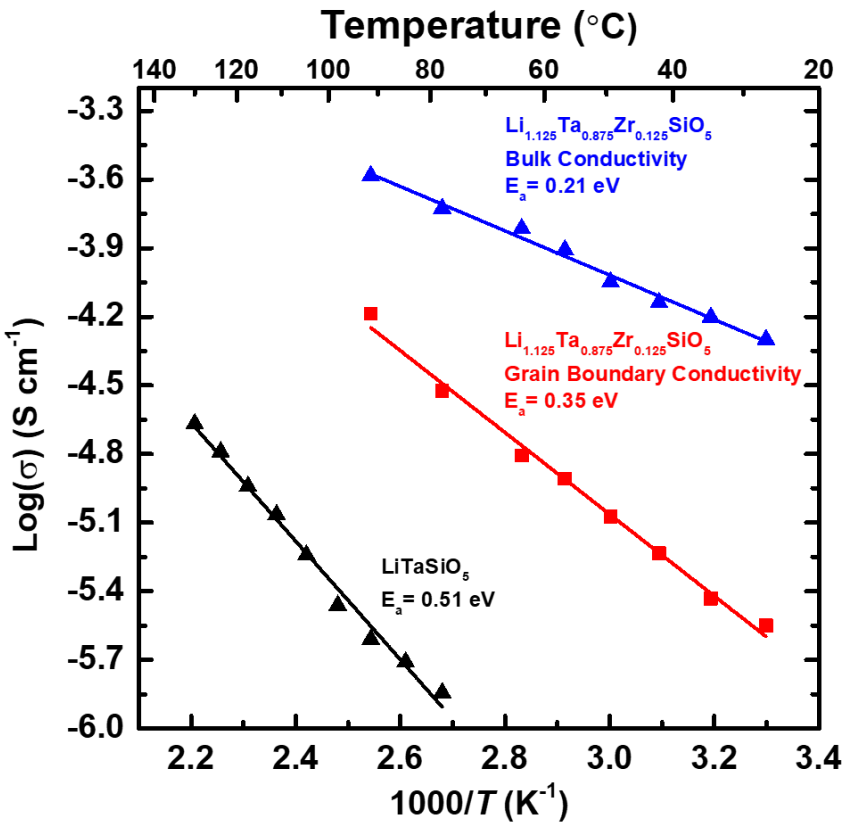

Figure 2.23 Arrhenius plot of the grain boundary (GB) and bulk ionic conductivities of the $Li_{1.125}Ta_{0.875}Zr_{0.125}SiO_5$ (x = 0.125) sample. The data were deducted from the AC-impedance diagrams (shown in Figure 2.22) at various temperatures. The conductivity results of undoped $LiTaSiO_5$ sample are also shown in black for reference.

The measured conductivity was improved after hot-pressing compared to the results from the simply sintered pellets. Even after hot pressing, the density of the pellets was still relatively low, around 86-89%, because the size of the primary particle was large, and the morphology was irregular, which is a result of long-time high temperature synthesis. Investigations on other oxide conductors such as LLZO demonstrated that high conductivity can only be achieved when the pellet density is >99% [126]. The first study of lithium garnet reported an ionic conductivity of about 10^{-5} S·cm^{-1} [127], which is similar

to the conductivity obtained in this study of the lithium sphene structure. We believe the ionic conductivity of this lithium sphene family has great potential for future improvement and can be increased to the level of computation prediction.

With more optimization in the synthesis processes, the purity of the synthesized materials can be improved, and this new family of sphene structure can be made in many different compounds. In addition to Zr-doping, a number of dopants were experimentally attempted. We selected Zr in this study because of its good integration as a dopant in this structure and the decent electrochemical stability at both high and low voltages. We found that the Ti^{4+} doped sphene phase can also form with a low solubility limit, but Ti may have poor reduction stability. Ga^{3+} and Sn^{4+} dopants were also tried and successfully yield the sphene phase as the major phase and various amounts of $LiTaO_3$-like phase as the secondary phase. The XRD pattern of Sn-doped $LiTaSiO_5$ is shown in Figure 2.24 as an example. However, the measured ionic conductivities are not as high as the 20% Zr-doped samples, as shown in Figure 2.25. Our novel computation-based design strategy distinguishes itself from conventional doping design or combinatorial design, because not every dopant can convert a structure into good ionic conductor, and combinatorial trials of aliovalent doping in experiments are time-consuming. The promising structures that may produce high conductivity can be effectively screened and identified by the computation integrated with topological analysis, DFT calculations, and AIMD simulations, as demonstrated in this study. This rational design strategy guided by first principles computation can potentially lead to the discovery of more promising fast ion conductors.

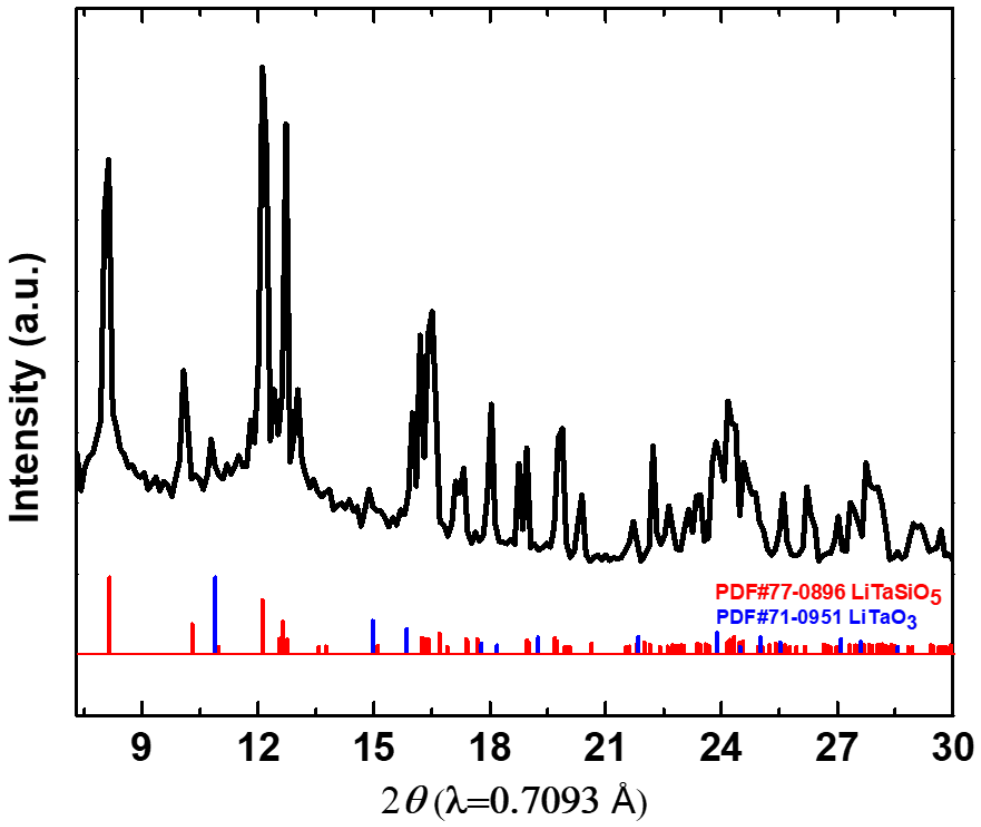

Figure 2.24 XRD pattern of 20% Sn-doped $LiTaSiO_5$ sample.

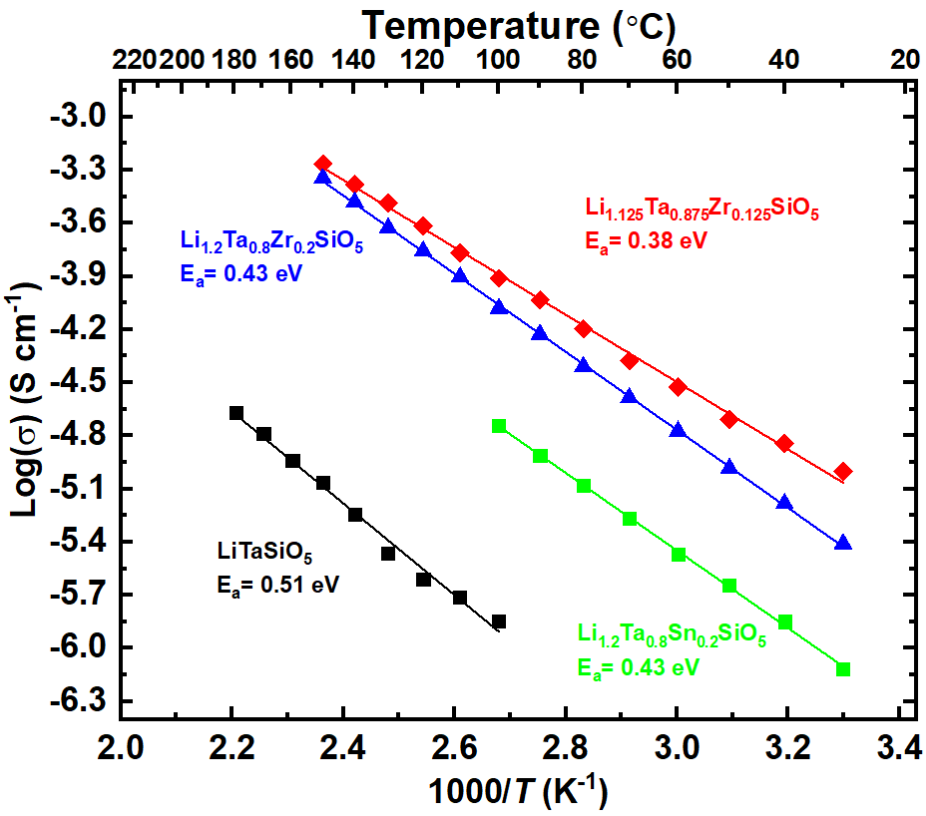

Figure 2.25 Arrhenius plots of $Li_{1+x}Ta_{1-x}Sn_xSiO_5$ (x=0.2) and $Li_{1+x}Ta_{1-x}Zr_xSiO_5$ (x = 0, 0.125, and 0.2) samples.

2.3 Summary

In this combined computational and experimental materials study, we identify and design the doped $LiTaSiO_5$ sphene compounds, $Li_{1+x}Ta_{1-x}Zr_xSiO_5$ ($0 \leq x \leq 0.5$), as new Li-ion conductors. As guided by our design strategies and first principles computation, we predicted that a modification of the $LiTaSiO_5$ sphene structure, by Zr-to-Ta doping and Li insertion, would activate the concerted migration of multiple Li ions, thereby significantly enhancing the ionic conductivity. These computation-predicted materials were successfully synthesized and confirmed in experiments. With a doping level of 12.5% Zr, $Li_{1.125}Ta_{0.875}Zr_{0.125}SiO_5$ showed a total ionic conductivity of approximately 10^{-5} S·cm^{-1} at

30°C, which is three orders of magnitude higher than the undoped $LiTaSiO_5$. Our study uncovers the sphene as a new structure of the fast Li^+ conductor family. More importantly, the sphene family includes many chemical compositions and expands the space for future materials design of new Li-ion conductors. Further exploration of this new sphene structure is promising for achieving even higher conductivities. Finally, our combined computational and experimental study demonstrates the rational design strategy of activating concerted migration for fast ion conductors and serves as an example for future materials design of fast ion conductor materials.

2.4 Methods

2.4.1 Computational Methods

In this study, all density functional theory (DFT) calculations were performed using the Vienna *Ab initio* Simulation package (VASP) [128] within the projector augmented-wave approach with Perdew-Burke-Ernzerhof (PBE) [129] generalized-gradient approximation (GGA). The materials entries for the phase diagram were obtained from the *Materials Project* (MP) [105, 130, 131] database. The density of states (DOS) were calculated using the Heyd-Scuseria-Erznerhof (HSE) functional with Monkhorst-Park $2 \times 2 \times 2$ *k*-point grid. We evaluated the phase stability and chemical stability of $Li_{1+x}Ta_{1-x}Zr_xSiO_5$ using the same scheme in previous work [103, 132].

2.4.1.1 Li Site and Structure

We performed topological analysis of the $LiTaSiO_5$ crystal structural framework to identify the potential Li sites. The topological analysis was performed using the Voronoi-

Dirichlet partition algorithm implemented in *Zeo++* [133, 134] on the $LiTaSiO_5$ crystal structural framework with all Li removed and with the crystal ionic radius of ion species in the analysis [135]. The Voronoi nodes obtained from the Voronoi-Dirichlet partition of the non-Li structural framework correspond to the center of local void space that may occupy a Li ion. For $Li_{1+x}Ta_{1-x}Zr_xSiO_5$, we used the extra Li sites determined by topological analysis and substituted Ta with Zr. A $\left(\sqrt{3}/2 \times 1 \times 1\right)\mathrm{R}30°$ supercell model with eight formula unit was used for doped compositions (Table 2.1). Using *pymatgen*, we generated 50 symmetrically distinctive structures. All these structures were statically relaxed in the DFT calculations, and the structure with the lowest DFT energy was identified as the ground state structure for other calculations.

2.4.1.2 Phase Stability

We evaluated the phase stability of the doped compositions using the same scheme in references [88, 132]. The phase stability is measured by the 'energy above hull' as the decomposition energy to the thermodynamic phase equilibria [116]. The energy above hull ΔE of $Li_{1+x}Ta_{1-x}Zr_xSiO_5$ was evaluated using pymatgen based on the DFT energies from the *Materials Project* [122]. The electrochemical window is evaluated using the grand potential phase diagrams as in the previous study [115].

2.4.1.3 Li-ion Diffusion

We performed *ab initio* molecular dynamic (AIMD) simulations to investigate the Li diffusional properties. We used the setting of a Γ-centered *k*-point in the non-spin-polarized DFT calculations. The time step was set to 2 fs. During the estimation of Li ion diffusion, NVT ensemble using Nosé-Hoover thermostat [136] was adopted. The total time

of AIMD simulations were in the range of 100 ps to 600 ps until the diffusivity was converged. The ionic conductivity and their error bars were calculated following established methods in previous studies [137].

2.4.2 Experimental Methods

2.4.2.1 Synthesis of $Li_{1+x}Ta_{1-x}Zr_xSiO_5$

The $Li_{1+x}Ta_{1-x}Zr_xSiO_5$ (x=0, 0.125, 0.2, 0.25, 0.3, 0.5) samples were synthesized by solid state reactions. Starting materials including Li_2CO_3(Alfa Aesar, 99.0%), Ta_2O_5(Sigma Aldrich, 99.5%), ZrO_2(Alfa Aesar, 99.5%) and SiO_2(Alfa Aesar, 99.5%) were weighed and mixed with the stoichiometric ratios of the designed formulas. Li_2CO_3 was used in 10% excess to compensate the loss of lithium during heating. The mixture was ball-milled at 500 rpm for 1 hour and then pressed into pellets with a diameter of 0.5 inch. Each pellet is about 0.5 g. The pellets were calcinated in alumina boats at 1100°C for 45 hours, followed by quenching on a copper plate in air to room temperature. The synthesized pellets and powder were stored in an Ar filled glove box to avoid exposure to moisture.

2.4.2.2 Characterization

Crystal structures of the obtained samples were analyzed by X-Ray Diffraction (XRD) using a D8 Advance X-ray Diffractometer (Bruker) equipped with a LynxEye detector and a Molybdenum tube ($\lambda\ K\alpha_1 = 0.7093$ Å). The samples were scanned in an air-tight sample container covered with a Kapton tape to avoid exposure to air and moisture. High resolution synchrotron XRD data was also collected at beam line 17-BM at the Advanced Photon Source (APS) at the Argonne National Laboratory (ANL). Rietveld

refinement was performed on the synchrotron XRD data with the EXPGUI suite of GSAS code [138].

To investigate the reaction pathway in the synthesis process, *in situ* XRD was conducted on various $Li_{1+x}Ta_{1-x}Zr_xSiO_5$ (x=0, 0.2 and 0.5) pellets using an Anton Paar HTK1200N furnace installed on the D8 Advance diffractometer. For x = 0 and 0.2 samples, the temperature profile includes a ramping process (30°C/min) from room temperature to 1050°C with multiple intermediate temperature holding steps. XRD patterns were collected first at 50°C, then at each constant temperature from 450°C to 1050°C with a step size of 50°C. After being held at 1050°C for 4 hours, the chamber was cooled down to room temperature and another two XRD patterns were collected at 600°C and 100°C. For the sample with x = 0.5, a similar ramping program was adopted with holding at a highest temperature of 1150°C for 4 hours to facilitate the doping of more Zr.

2.4.2.3 Electrochemical Tests

Electrochemical Impedance Spectroscopy (EIS) was used to determine the Li ion conductivity of the samples. The AC impedance measurements were performed using a Bio-Logic VMP3 impedance analyzer in the frequency range from 1 MHz to 0.5 Hz with a voltage amplitude of 300mV. Temperature-dependent conductivity measurements were performed from room temperature to 150°C (200°C for $LiTaSiO_5$) using two stainless-steel rods as ion-blocking electrodes [90]. To perform the measurements, pellets of 0.5-inch diameter and ~1.5 mm thickness were obtained by sintering nano/micro powder using a direct current-induced hot press with uniaxial pressure of 1 ton. The samples were heated up at a rate of 100 °C/min to 1100~1150 °C, maintained for 2 minutes and cooled naturally

to room temperature in air. The relative density of the sintered pellets is calculated by carefully measuring the dimensions of the well-shaped pellets and their masses.

The electronic conductivity of the doped samples was evaluated through DC polarization measurements. Symmetric cells with two stainless steel (SS) rods as blocking electrodes and the doped samples $Li_{1+x}Ta_{1-x}Zr_xSiO_5$ (or LTZSO, x=0.125 and 0.20) as electrolyte were assembled, represented as SS|LTZSO|SS. A voltage of 0.75 V is applied to the cells. The currents are recorded and the stable currents are used to calculate DC electron conductivities.

2.5 Notes to Chapter 2

This chapter is based on the paper entitled "Computation-Guided Design of $LiTaSiO_5$, a New Lithium Ionic Conductor with Sphene Structure" published in Advanced Energy Materials [98].

2.6 References

[54] Kamaya, N., et al., *A lithium superionic conductor.* Nat Mater, 2011. **10**(9): p. 682-6.

[83] Arbi, K., J.M. Rojo, and J. Sanz, *Lithium mobility in titanium based Nasicon $Li_{1+x}Ti_{2-x}Al_x(PO_4)_3$ and $LiTi_{2-x}Zr_x(PO_4)_3$ materials followed by NMR and impedance spectroscopy.* Journal of the European Ceramic Society, 2007. **27**(13): p. 4215-4218.

[88] Ong, S.P., Y. Mo, W.D. Richards, L. Miara, H.S. Lee, and G. Ceder, *Phase stability, electrochemical stability and ionic conductivity of the $Li_{10\pm1}MP_2X_{12}$ (M = Ge, Si, Sn, Al or P, and X = O, S or Se) family of superionic conductors.* Energy & Environmental Science, 2013. **6**(1): p. 148-156.

[90] Xiong, S., Z. Liu, H. Rong, H. Wang, M. McDaniel, and H. Chen, *$Na_3SbSe_{4-x}S_x$ as Sodium Superionic Conductors.* Scientific Reports, 2018. **8**(1): p. 9146.

[98] Xiong, S., et al., *Computation-Guided Design of $LiTaSiO_5$, a New Lithium Ionic Conductor with Sphene Structure.* Advanced Energy Materials, 2019. **9**(22): p. 1803821.

[103] Mo, Y., S.P. Ong, and G. Ceder, *First Principles Study of the $Li_{10}GeP_2S_{12}$ Lithium Super Ionic Conductor Material.* Chemistry of Materials, 2012. **24**(1): p. 15-17.

[105] Jain, A., et al., *Commentary: The Materials Project: A materials genome approach to accelerating materials innovation.* APL Materials, 2013. **1**(1): p. 011002.

[107] Bachman, J.C., et al., *Inorganic Solid-State Electrolytes for Lithium Batteries: Mechanisms and Properties Governing Ion Conduction.* Chemical Reviews, 2016. **116**(1): p. 140-162.

[108] Wang, Y., W.D. Richards, S.P. Ong, L.J. Miara, J.C. Kim, Y. Mo, and G. Ceder, *Design principles for solid-state lithium superionic conductors.* Nature Materials, 2015. **14**: p. 1026.

[109] Janek, J. and W.G. Zeier, *A solid future for battery development.* Nature Energy, 2016. **1**: p. 16141.

[110] Park, K.H., Q. Bai, D.H. Kim, D.Y. Oh, Y. Zhu, Y. Mo, and Y.S. Jung, *Design Strategies, Practical Considerations, and New Solution Processes of Sulfide Solid Electrolytes for All-Solid-State Batteries.* Advanced Energy Materials, 2018. **8**(18).

[111] Seino, Y., T. Ota, K. Takada, A. Hayashi, and M. Tatsumisago, *A sulphide lithium super ion conductor is superior to liquid ion conductors for use in rechargeable batteries.* Energy Environ. Sci., 2014. **7**(2): p. 627-631.

[112] Thangadurai, V., S. Narayanan, and D. Pinzaru, *Garnet-type solid-state fast Li ion conductors for Li batteries: critical review.* Chem Soc Rev, 2014. **43**(13): p. 4714-27.

[113] Murugan, R., V. Thangadurai, and W. Weppner, *Fast Lithium Ion Conduction in Garnet-Type $Li_7La_3Zr_2O_{12}$.* Angewandte Chemie International Edition, 2007. **46**(41): p. 7778-7781.

[114] Aono, H., E. Sugimoto, Y. Sadaoka, N. Imanaka, and G.-y. Adachi, *Ionic conductivity and sinterability of lithium titanium phosphate system.* Solid State Ionics, 1990. **40-41**: p. 38-42.

[115] Zhu, Y., X. He, and Y. Mo, *Origin of Outstanding Stability in the Lithium Solid Electrolyte Materials: Insights from Thermodynamic Analyses Based on First-Principles Calculations.* ACS Applied Materials & Interfaces, 2015. **7**(42): p. 23685-23693.

[116] Nolan, A.M., Y. Zhu, X. He, Q. Bai, and Y. Mo, *Computation-Accelerated Design of Materials and Interfaces for All-Solid-State Lithium-Ion Batteries.* Joule, 2018. **2**(10): p. 2016-2046.

[117] Zhu, Y., X. He, and Y. Mo, *Strategies Based on Nitride Materials Chemistry to Stabilize Li Metal Anode.* Adv Sci (Weinh), 2017. **4**(8): p. 1600517.

[118] He, X., Y. Zhu, and Y. Mo, *Origin of fast ion diffusion in super-ionic conductors.* Nature Communications, 2017. **8**: p. 15893.

[119] Zachariasen, W.H., *II. The Crystal Structure of Titanite.* Zeitschrift für Kristallographie - Crystalline Materials, 1930. **73**(1): p. 7-16.

[120] Sebastian, L., J. Gopalakrishnan, and Y. Piffard, *Synthesis, crystal structure and lithium ion conductivity of $LiMgFSO_4$.* Journal of Materials Chemistry, 2002. **12**(2): p. 374-377.

[121] Genkina, E.A., B. Mill, and S. Kirsch, *Crystal structures of the sphenes $NaSbGeO_5$, $NaTaGeO_5$, and $LiTaSiO_5$.* Soviet physics. Crystallography, 1992. **37**: p. 769-772.

[122] Jain, A., et al., *Commentary: The Materials Project: A materials genome approach to accelerating materials innovation.* APL Materials, 2013. **1**(1).

[123] He, X., Y. Zhu, A. Epstein, and Y. Mo, *Statistical variances of diffusional properties from ab initio molecular dynamics simulations.* npj Computational Materials, 2018. **4**(1).

[124] Weber, D.A., A. Senyshyn, K.S. Weldert, S. Wenzel, W. Zhang, R. Kaiser, S. Berendts, J. Janek, and W.G. Zeier, *Structural Insights and 3D Diffusion Pathways within the Lithium Superionic Conductor Li10GeP2S12.* Chemistry of Materials, 2016. **28**(16): p. 5905-5915.

[125] Breuer, S., D. Prutsch, Q. Ma, V. Epp, F. Preishuber-Pflügl, F. Tietz, and M. Wilkening, *Separating bulk from grain boundary Li ion conductivity in the sol–gel prepared solid electrolyte $Li_{1.5}Al_{0.5}Ti_{1.5}(PO_4)_3$.* Journal of Materials Chemistry A, 2015. **3**(42): p. 21343-21350.

[126] Han, F., et al., *Interphase Engineering Enabled All-Ceramic Lithium Battery.* Joule, 2018. **2**(3): p. 497-508.

[127] Thangadurai, V., H. Kaack, and W.J.F. Weppner, *Novel Fast Lithium Ion Conduction in Garnet-Type $Li_5La_3M_2O_{12}$ (M = Nb, Ta).* Journal of the American Ceramic Society, 2003. **86**(3): p. 437-440.

[128] Kresse, G. and J. Furthmuller, *Efficient iterative schemes for ab initio total-energy calculations using a plane-wave basis set.* Physical Review B, 1996. **54**(16): p. 11169–11186.

[129] Perdew, J.P., M. Ernzerhof, and K. Burke, *Rationale for mixing exact exchange with density functional approximations.* The Journal of Chemical Physics, 1996. **105**(22): p. 9982–9985.

[130] Jain, A., G. Hautier, C.J. Moore, S. Ping Ong, C.C. Fischer, T. Mueller, K.A. Persson, and G. Ceder, *A high-throughput infrastructure for density functional theory calculations.* Computational Materials Science, 2011. **50**(8): p. 2295–2310.

[131] Jain, A., G. Hautier, S.P. Ong, C.J. Moore, C.C. Fischer, K.A. Persson, and G. Ceder, *Formation enthalpies by mixing GGA and GGA+U calculations.* Physical Review B, 2011. **84**(4): p. 045115.

[132] He, X. and Y. Mo, *Accelerated materials design of $Na_{0.5}Bi_{0.5}TiO_3$ oxygen ionic conductors based on first principles calculations.* Physical Chemistry Chemical Physics, 2015. **17**(27): p. 18035-18044.

[133] Willems, T.F., C.H. Rycroft, M. Kazi, J.C. Meza, and M. Haranczyk, *Algorithms and tools for high-throughput geometry-based analysis of crystalline porous materials.* Microporous and Mesoporous Materials, 2012. **149**(1): p. 134-141.

[134] Martin, R.L., B. Smit, and M. Haranczyk, *Addressing challenges of identifying geometrically diverse sets of crystalline porous materials.* J Chem Inf Model, 2012. **52**(2): p. 308-18.

[135] Shannon, R.D., *Revised effective ionic radii and systematic studies of interatomic distances in halides and chalcogenides.* Acta crystallographica section A: crystal physics, diffraction, theoretical and general crystallography, 1976. **32**(5): p. 751-767.

[136] Nose, S., *Constant temperature molecular dynamics methods.* Progress of Theoretical Physics Supplement, 1991. **103**: p. 1–46.

[137] He, X., Y. Zhu, A. Epstein, and Y. Mo, *Statistical variances of diffusional properties from ab initio molecular dynamics simulations.* npj Computational Materials, 2018. **4**(1): p. 18.

[138] Toby, B.H., *EXPGUI, a graphical user interface for GSAS.* Journal of Applied Crystallography, 2001. **34**.

CHAPTER 3. INVESTIGATION OF $Na_3SbSe_{4-x}S_x$ AS SODIUM SUPERIONIC CONDUCTORS

3.1 Introduction

With the rapid global growth of electricity generation from renewable and clean energy sources such as solar and wind power, the demand for stable, safe, and low-cost energy storage solutions to flatten and level the fluctuations and intermittence in the electrical grid are becoming critical. Lithium-ion batteries (LIBs) are expensive for grid level storage due to the use of precious Li, Ni, and Co metals. Sodium based electrochemical storage, such as Na-ion batteries (NIBs), are considered as a promising technology for grid storage owing to the high natural abundance and availability of sodium [139-145]. Sodium ion batteries with inorganic solid electrolyte, i.e. all-solid-state NIBs, are particularly attractive in terms of safety, as no flammable organic liquid is used in the cell.

As the key component of all-solid-state NIBs, solid state Na-ion conductors with comparable room temperature (r.t.) conductivity as organic liquid electrolytes and good stability are very much desired. In the past, some super Na-ion conductors have been discovered, including β-alumina [146] and NASICON type oxides [64]. However, the high grain boundary resistance in these materials commonly requires sintering at very high temperature, and high conductivity at r.t. is not easy to achieve. Recently the fast progress on chalcogenide-based alkali-metal-ion conductors have attracted a great deal of attention [69, 75, 147]. The promise has been well demonstrated first in Li-ion conductors.

High ionic conductivities of 1~10 $mS \cdot cm^{-1}$ at r.t. have been achieved in sulfides such as $Li_{10}GeP_2S_{12}$ [54], $Li_7P_3S_{11}$ [111], and $Li_{9.54}Si_{1.74}P_{1.44}S_{11.7}Cl_{0.3}$ [5], which have enabled a number of well performing all-solid-state LIBs. Promise has also been achieved in chalcogenide sodium-ion conductors. High conductivity was computationally predicted and then experimentally achieved in $Na_{10}MP_2S_{12}$ (M = Si, Ge, and Sn) [148, 149]. A cubic Na_3PS_4 phase with Na^+ ion conductivity greater than 0.1 mS cm^{-1} at 25 °C was reported by Tatsumisago *et al*. [150]. The conductivity of Na_3PS_4 was further improved by introducing Si on P sites [151] and by Cl doping on S sites [152]. High conductivities of ~1 $mS \cdot cm^{-1}$ were also reported in other compounds with similar structures, such as Na_3PSe_4 [81, 153], Na_3SbS_4 [154, 155], and $Na_3P_{1-x}As_xS_4$ [80]. The high conductivity in these body-centered-cubic (*bcc*) based structures was proposed by Ceder *et al*. [106] due to the existence of low barrier diffusion pathways alternatively connecting the tetrahedral and octahedral sites. It is interesting and important to explore if the diffusion barrier can be further lowered in this *bcc* structure by tuning other critical factors, such as the size of the tetrahedral and octahedral sites, the electronegativity and polarizability of the anions.

For this reason, Na_3SbSe_4 was chosen for our investigation. The crystal structure of Na_3SbSe_4 has been identified previously [156] and it has the same space group ($I\bar{4}3m$) as cubic Na_3PS_4 [150]. Compared with Na_3PS_4, the replacement of Se at S sites and Sb at P sites may effectively enlarge the unit cell, so as to have larger size of the intermediate sites connecting the octahedral sites, which may be beneficial for the diffusion of Na ions. In addition, bigger ionic radius and higher polarizability of Se^{2-} and Sb^{5+} are also considered to be beneficial for the diffusion of alkaline ions, as demonstrated in Na_3PSe_4

[153] and Na_3SbS_4 [154]. Although selenides are more expensive than sulfides and oxides, it is worth to explore their ionic conduction properties in the context of understanding the conductivity in this group of Na-ion conductors with cubic structures. In this work, cubic Na_3SbSe_4 was synthesized, characterized, and electrochemically tested. A group of $Na_3SbSe_{4-x}S_x$ samples were also synthesized and tested. An all-solid-state sodium-ion battery using Na_3SbSe_4 as the electrolyte was demonstrated for the first time with reasonably well performance at room temperature. The details of the experimental results are elaborated and discussed as follows.

3.2 Results and Discussion

3.2.1 Synthesis and Structural Characterizations

Na_3SbSe_4 was successfully synthesized through calcination of the mixture of Na and Sb metals and Se powder in a sealed quartz tube at 650 °C for 18 hours. The crystal structure of Na_3SbSe_4 was characterized with X-ray diffraction (XRD). Figure 3.1 shows the synchrotron XRD pattern of as-synthesized Na_3SbSe_4 along with the Rietveld refinement results, which confirmed the formation of cubic Na_3SbSe_4 with trace amount of unknown secondary phase. A crystal structure model with space group $I\bar{4}3m$ was used for the refinement. The refined cell parameters are listed in Table 3.1. The unit cell has a lattice parameter of a = b = c = 7.501(2) Å, which is larger than that of the isostructural compounds such as Na_3PS_4 [157] (a = 6.9781 Å) and Na_3PSe_4 [81] (a = 7.3094 Å). These results are also consistent with the parameters reported by Eisenmann *et al* [156].

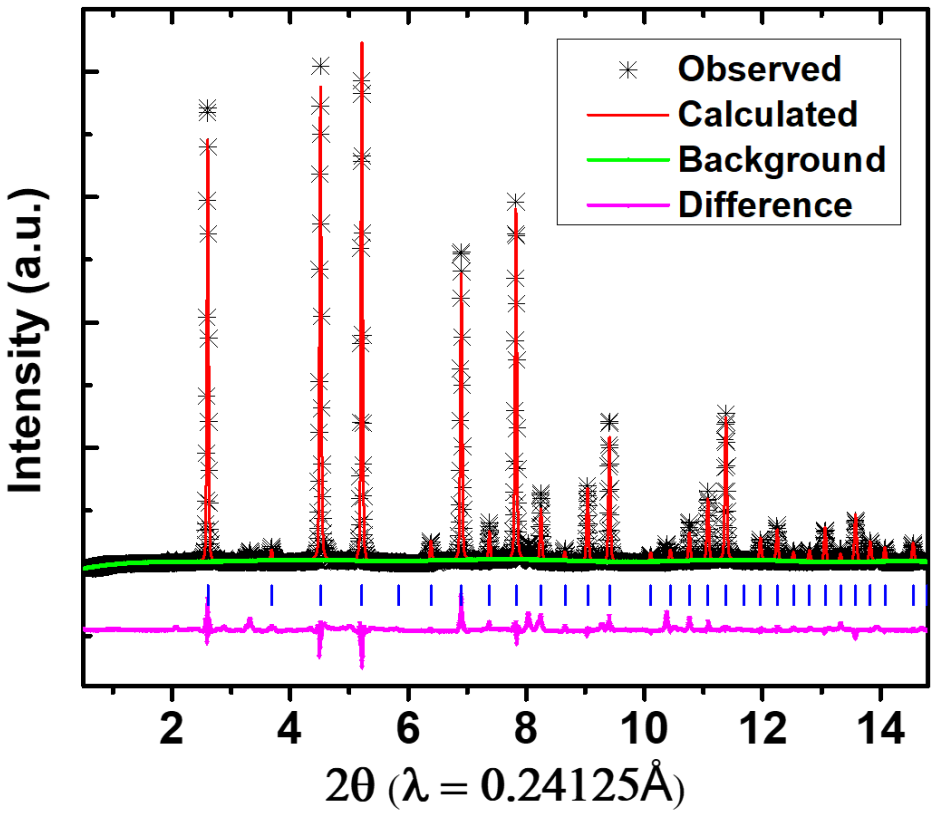

Figure 3.1 XRD pattern of Na_3SbSe_4 and the Rietveld refinement results.

To further investigate the impact of unit cell size and anion polarizability on Na ion diffusion in this cubic structure, $Na_3SbSe_{4-x}S_x$ samples with substitution of the smaller S^{2-} anion at the Se^{2-} sites were also attempted and successfully obtained using the same synthesis method. $Na_3SbSe_{4-x}S_x$ samples with x = 1, 2, 3 and 4 are hereafter noted as S1, S2, S3 and S4, together with S0 noting Na_3SbSe_4 with no S doping in the structure. Figure 3.2 shows the synchrotron XRD patterns of S0 to S4. Peaks of minor impurities are observed in S1 at $2\theta = 4.7°$ and 6.6°, which are from intermediate product $NaSbSe_2$ and possibly due to

the loss of S and Se during the heating process. With the increased S content from S0 to S4, all reflections shift toward higher two-theta angles, as more clearly demonstrated in the zoomed area. This peak shifting indicates a gradual shrinkage of the unit cell volume, which is consistent with the substitution of Se^{2-} by the smaller S^{2-}. Obvious peak splitting such as at 2θ = 3.82°, 4.66°, 5.44°, 6.08°, etc. is observed in S4, which indicates that Na_3SbS_4 has a tetragonal unit cell, while others in the series are all cubic. Details of the refinement results for S1, S2, S3 and S4 are also listed in Table 3.1. The refinement results confirmed that S1, S2, and S3 also have $I\bar{4}3m$ space group with a = 7.420(5) Å, 7.346(4) Å, and 7.271(7) Å, respectively, while S4 was refined with a tetragonal space group $P\bar{4}2_1c$ with a slightly elongated *c*-axis (a = 7.163(3) Å, c = 7.295(3) Å and c/a = 1.018). The cell volume of the $Na_3SbSe_{4-x}S_x$ phases is shown in Figure 3.3 and a linear decrease as the function of S concentration is observed.

Table 3.1 Full pattern fitting refinement results for synchrotron X-ray diffraction patterns of $Na_3SbSe_{4-x}S_x$ compounds.

Phase	S0 (Na_3SbSe_4)	S1	S2	S3	S4
Space group	$I\bar{4}3m$ (217)	$I\bar{4}3m$ (217)	$I\bar{4}3m$ (217)	$I\bar{4}3m$ (217)	$P\bar{4}2_1c$ (114)
Cell parameter	a = 7.501 (2) Å	a = 7.420 (5) Å	a = 7.346 (4) Å	a = 7.271 (7) Å	$a = b$ = 7.163 (3) Å, c = 7.295 (3) Å
Cell volume (calculated)	422.04 Å^3	408.52 Å^3	396.42 Å^3	384.40 Å^3	374.30 Å^3
R_{wp}	8.83%	9.44%	7.97%	9.50%	9.38%
R_p	6.02%	5.31%	5.75%	7.49%	6.93%
No. of variables	29	32	28	31	36

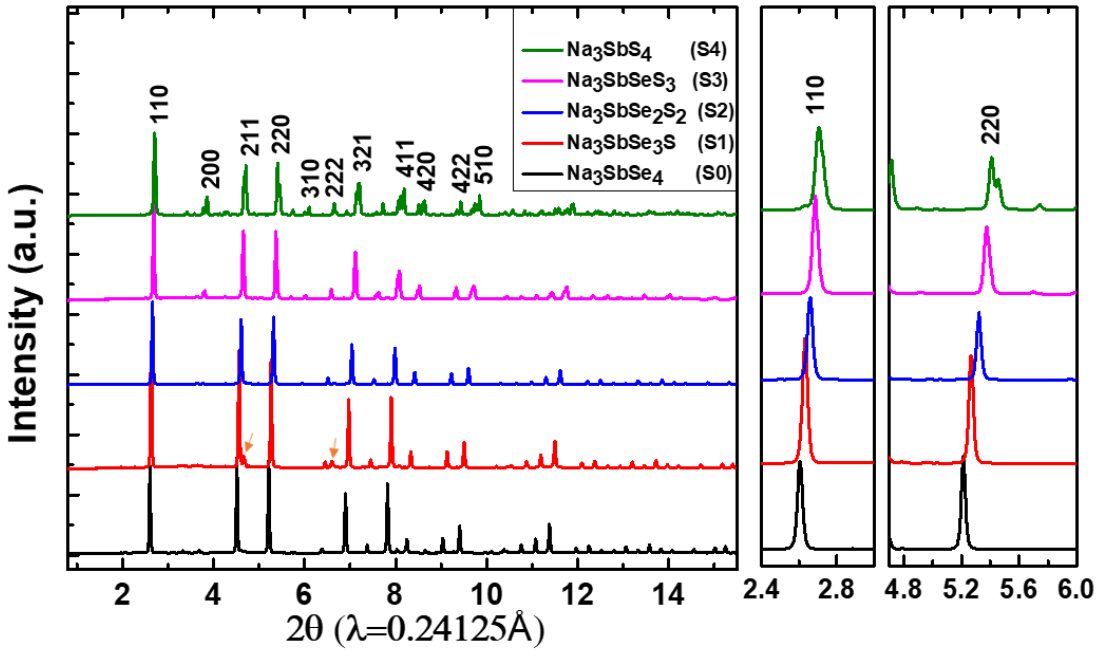

Figure 3.2 XRD patterns of $Na_3SbSe_{4-x}S_x$ (minor impurities of $NaSbSe_2$ in S1 are labeled with arrows).

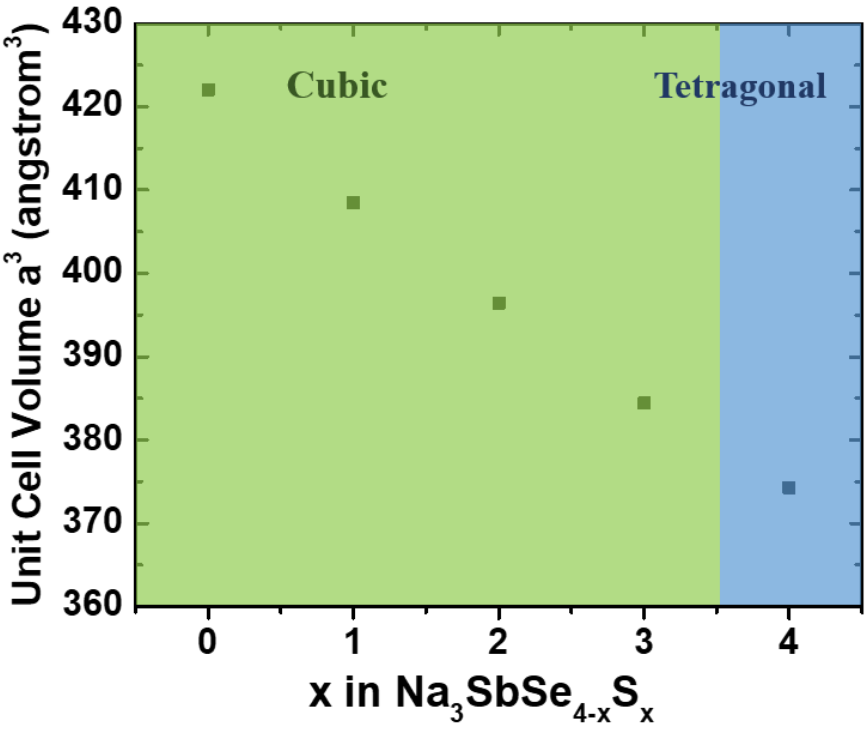

Figure 3.3 Cell volume variation with respect to S content in $Na_3SbSe_{4-x}S_x$.

Scanning electron microscope (SEM) was used to investigate the morphology of the as-synthesized samples. Figure 3.4 shows the SEM images for the synthesized Na_3SbSe_4 and the elemental mapping with energy dispersive X-ray (EDX) spectroscopy. SEM images and elemental mapping for S1–S4 were also shown in Figure 3.5. For all the compounds in this solid solution series, the particles show irregular shapes and a relatively wide distribution of particle sizes. This inhomogeneity in particle size and morphology is possibly due to the melting-quenching process in synthesis. The distribution of Na, Sb, and Se elements in the EDX mapping on the other hand confirms the uniform formation of Na_3SbSe_4 with no evident element or phase segregations. The elemental mappings for

S1~S4 samples also show uniform distribution throughout the selected areas, indicating a series of solid-solution compounds in the designed system have been successfully obtained.

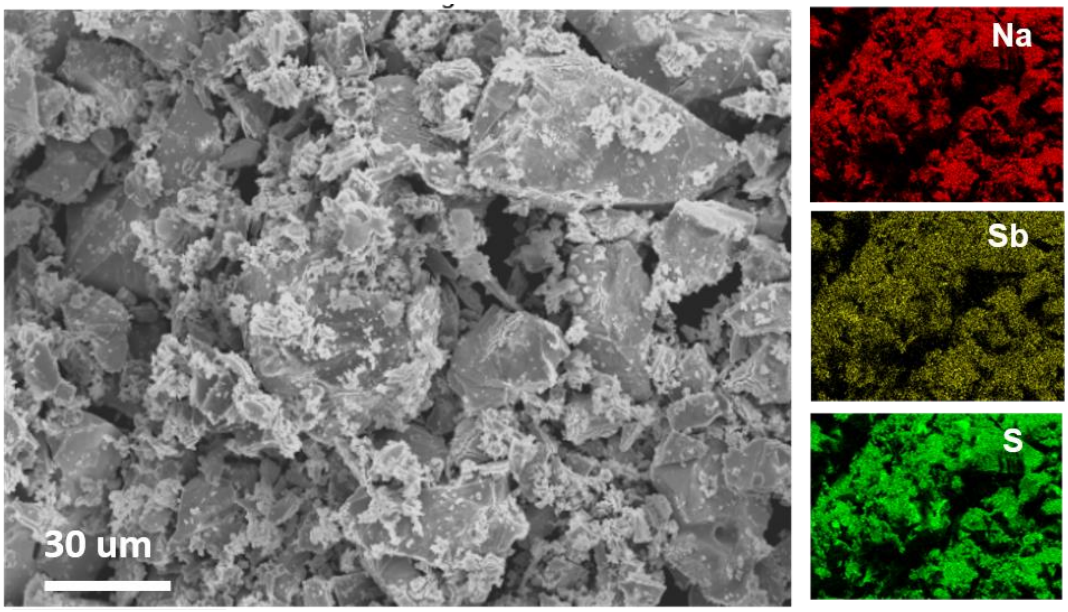

Figure 3.4 SEM images and corresponding EDX mapping of as-synthesized Na_3SbSe_4.

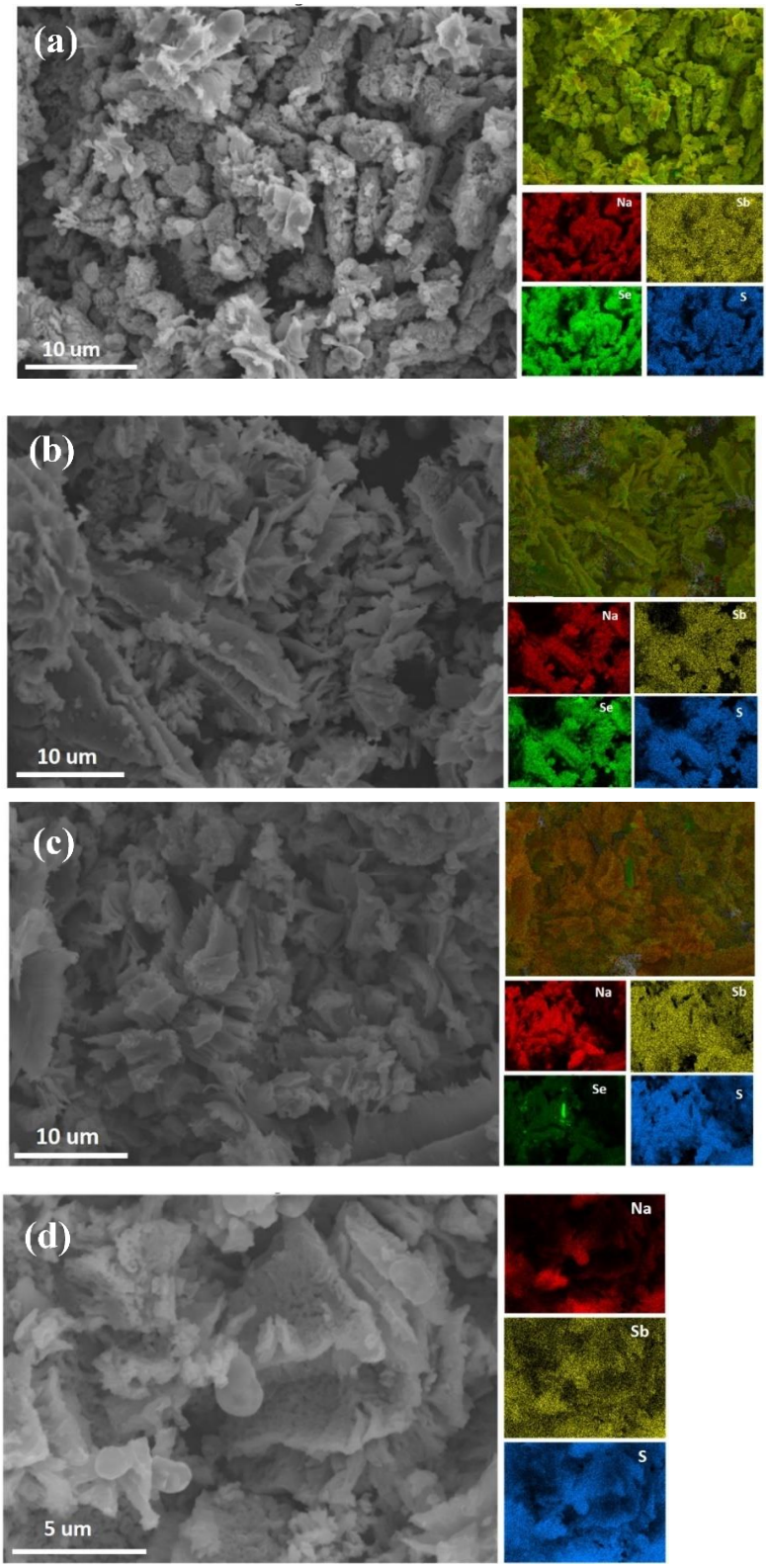

Figure 3.5 SEM images and EDX spectroscopy elemental mappings of (a) S1, (b) S2, (c) S3, and (d) S4 in the $Na_3SbSe_{4-x}S_x$ system (corresponding to x = 1, 2, 3 and 4).

3.2.2 Ionic Conductivity of Cubic Na_3SbSe_4 and $Na_3SbSe_{4-x}S_x$ System

Powder of the samples was pressed into pellets and analyzed with electrochemical impedance spectroscopy (EIS). The measurement was conducted with the standard method described in an earlier work [158] to minimize the error. The Nyquist plots of the impedance for Na_3SbSe_4 at different temperatures are shown in Figure 3.6. The impedance spectra in the high-frequency region show a small semicircle, suggesting that the grain boundary resistance is low, and the overall resistance is dominated by the bulk conductivity. This feature is similar to previously reported sulfide conductors, which typically have lower grain boundary resistance than oxides [81, 150]. Based on the total resistance of Na_3SbSe_4 including the bulk and grain boundary resistances and the dimensions of the pellet, Na^+ conductivity (σ) of the synthesized Na_3SbSe_4 was calculated to be 0.85 $mS \cdot cm^{-1}$ at room temperature, which is higher than those of cubic-Na_3PS_4 [150], Si-doped [151], Sn-doped [157], and Se-doped [153] cubic Na_3PS_4 phases. This conductivity is also comparable to those of recently reported sulfides such as Na_3SbS_4 [154] and $Na_3P_{0.62}As_{0.38}S_4$ [80]. This high ionic conductivity can be explained by the large unit cell of Na_3SbSe_4 and the high polarizability of Se^{2-}, which lowers the electrostatic binding energy and weakens the attraction between Na^+ and the tetrahedron of $[SbSe_4]^{3-}$ [159, 160].

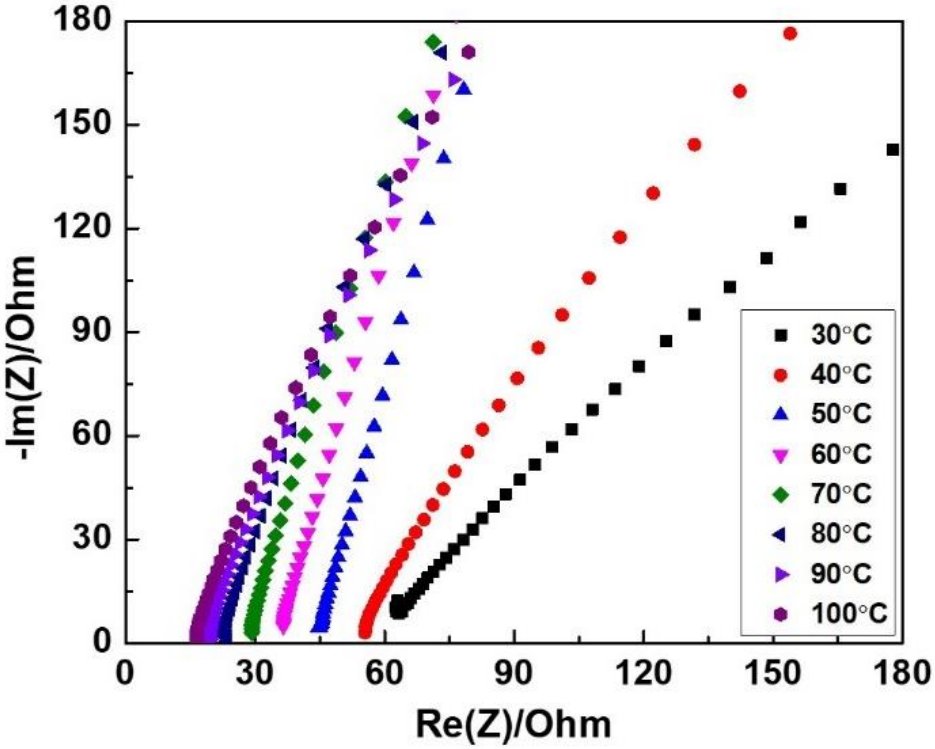

Figure 3.6 Nyquist impedance plots of Na_3SbSe_4 from 30°C to 100°C.

S0–S4 samples with different S content and therefore different unit cell sizes were all tested for ionic conductivity at variable temperatures from 30 °C to 100 °C. Arrhenius plots of the samples are shown in Figure 3.7**.** The log(σ) versus 1/T curves of all samples show good linearity, indicating no phase transition or ordering change in this temperature range. Based on the slope of the linear fitting curve, the diffusion activation energy of Na_3SbSe_4 is calculated to be 0.193 eV using the equation $\sigma = A \exp\left(-\frac{E_a}{k_B T}\right)$, where A is the pre-exponential parameter, E_a is the activation energy, and k_B is the Boltzmann constant. This activation energy is lower than most of those previously reported for sulfide-

based Na ionic conductors [80, 81, 152-155], which ranges from 0.20–0.26 eV. With a lower activation energy, this solid-state electrolyte can maintain a relatively high conductivity at low temperatures, which is significantly advantageous over organic liquid electrolytes and benefits applications in low temperature environments.

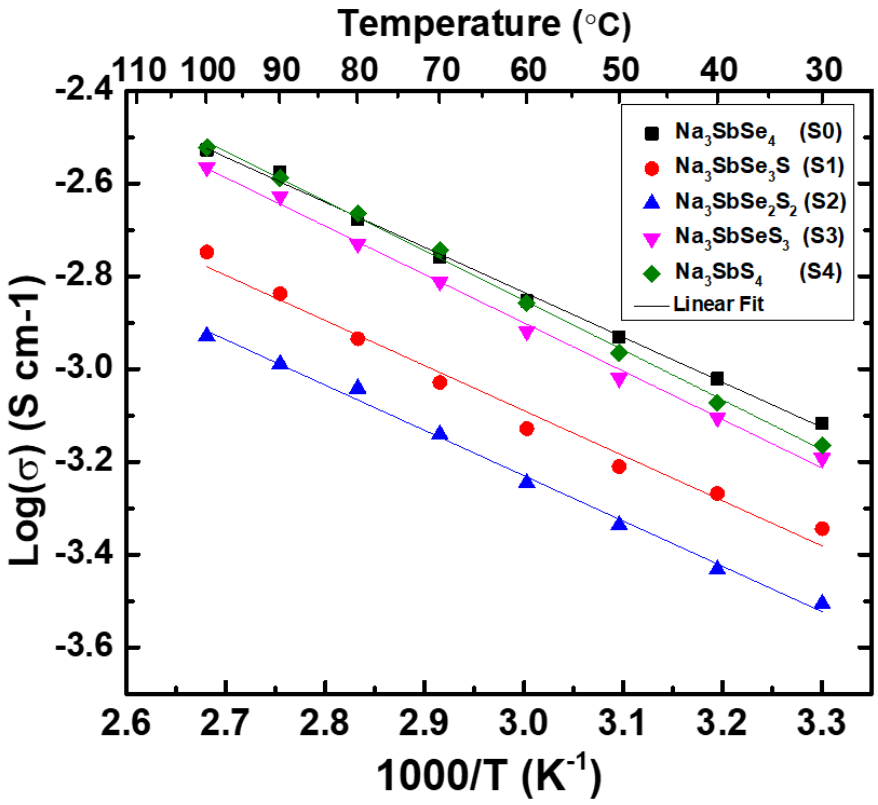

Figure 3.7 Arrhenius conductivity plots of the $Na_3SbSe_{4-x}S_x$ series.

The linear fitting of conductivities of S1–S4 are also shown in Figure 3.7 and the calculated activation energies are shown in Figure 3.8(a). With the increased S concentration in the solid solution phases, a gradual increase of activation energy can be observed for Na^+ migration. This trend is similar to what was observed in other Se-S solid

solution ionic conductors [160, 161], resulted from a softer lattice with more polarizable Se^{2-}. The values of activation energies are listed in the Table 3.2, together with the ionic conductivities of the compounds at room temperature.

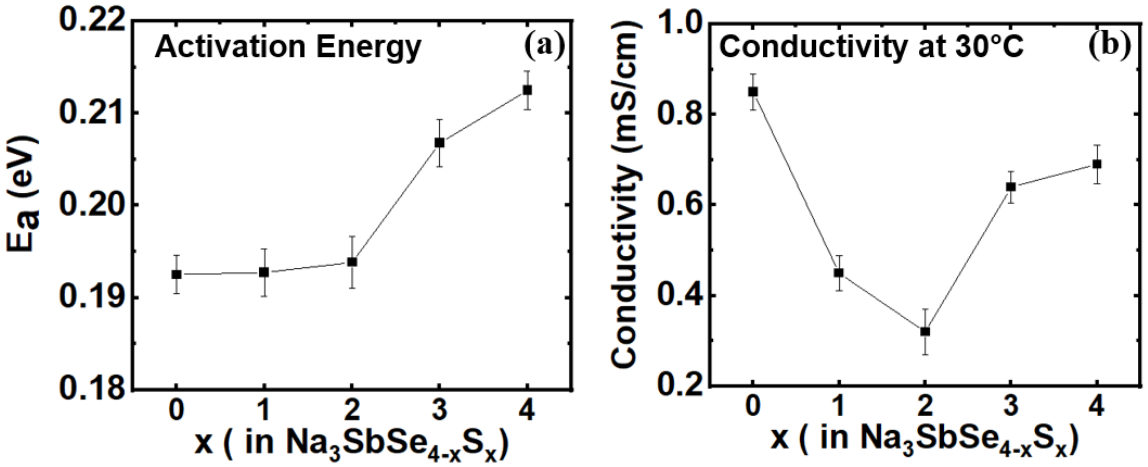

Figure 3.8 (a) Activation energy and (b) ionic conductivity (at 30°C) of $Na_3SbSe_{4-x}S_x$ series.

Table 3.2 Ionic conductivity at 30°C and activation energy of the synthesized compounds in the $Na_3SbSe_{4-x}S_x$ system.

Compound	Ionic conductivity at 30°C ($mS \cdot cm^{-1}$)	Activation Energy (eV)
S0 (x=0)	0.85	0.193
S1 (x=1)	0.45	0.193
S2 (x=2)	0.32	0.194
S3 (x=3)	0.64	0.207
S4 (x=4)	0.69	0.213

Comparing the conductivities of S0–S4 samples at 30°C as shown in Figure 3.8(b), it can be seen that with increased concentration of S in the solid solution, the conductivity first decreases from S0 to S2, and then increases from S2 to S4, with the two end members showing the highest conductivity. Since the sizes of the unit cell from S0 to S4 almost linearly decreases, as shown in Figure 3.3, it is clear that the diffusivity is not solely controlled by the averaged size of the diffusion channels. The non-monotonic trend of conductivity was also reported by Yu *et al.* in the solid solution series of $Na_3P_{1-x}As_xS_4$. The highest conductivity of this series of compounds was obtained in an intermediate composition of $Na_3P_{0.62}As_{0.38}S$ [80]. This effect was explained by Yu *et al.* that the dual effects of lattice expansion and a shorter Na-S bond length caused by the increased As content together resulted in the lowest diffusion barrier in this tetrahedral structure at the composition of As = 0.38. However, in the case of $Na_3SbSe_{4-x}S_x$ series, the two end members are not in exactly the same structure. Na_3SbSe_4 is in cubic with an $I\bar{4}3m$ space group while Na_3SbS_4 is tetragonal $P\bar{4}2_1c$. The larger unit cell in Na_3SbSe_4 has symmetric low barrier diffusion pathways along all three directions among Na ions sitting at 6b sites. On the other hand, although the unit cell size of Na_3SbS_4 is smaller, the tetragonal distortion plausibly provides similarly low barrier pathways along *ab* planes in the price of having higher barriers along *c*-axis [162]. In addition, the shorter Sb-S bonds in S4 compared to Sb-S/Se bonds in mixed anion compounds may result in weaker Na-(S/Se) interactions and therefore facilitate faster Na diffusion. Ionic conductivity is influenced by many factors, such as structure symmetry, lattice softness, sizes of diffusion channels, bond lengths, defects, etc. At this point, it is difficult to differentiate what is the predominate factor that increases the conductivity of S4. It may be ascribed to the change of the bond length and

diffusion channel sizes caused by the tetragonal distortion. As for S1–S3 samples with intermediate S concentrations and cubic structure, their smaller unit cell size than that of Na_3SbSe_4 and their lack of tetragonal distortion as in Na_3SbS_4, are likely to be the reasons for their lower conductivities than both end members.

It should also be noted that the r.t. conductivity of S4 (Na_3SbS_4) in this work is lower than the values reported in the recent works by Wang *et al.* [154] and Zhang *et al.* [163]. This may be due to the different starting materials and synthesis procedures, which may introduce slight variations in amorphous phase composition, particle size, local ordering, and grain boundary conditions that can have non-negligible impacts on the conductivity measurement. An additional ball-milling step prior to the impedance measurements was used in Zhang's work to increase the conductivity of the pressed pellets. However, in our tests the ball-milled samples showed lower conductivity than as-synthesized product. This again indicates that the conductivity measurement is sensitive to many factors other than bulk phase composition and that there may still be room to further optimize and explore this series of $Na_3SbSe_{4-x}S_x$ compounds for even higher conductivities. Another important issue that was not explored in current work is the local ordering of Se and S. In our model, a random mixing of Se and S at 8c site was assumed and it agrees very well with the refinement. However, due to the insensitivity of XRD for local structure, local ordering of Se and S cannot be excluded at this point. The local ordering may create higher (or lower) hopping barriers and therefore impact the overall conductivity. To address these issues, further investigation with other techniques, such as neutron diffraction, are needed to reveal more information of the local ordering.

3.2.3 Electrochemical Properties and Performance of All-solid-state Batteries

The electrochemical stability of Na_3SbSe_4 was evaluated with cyclic voltammetry (CV) of a Na | SE | Sn cell at room temperature, with as-synthesized Na_3SbSe_4 as the solid electrolyte (SE), metallic Na as the reference and counter electrode, and Sn as the working electrode. In the scan from −0.5 V to 5 V at a rate of 5 mV/s, as shown in Figure 3.9(a), no significant current due to electrolyte decomposition is detected at high voltage. Cathodic and anodic currents are only observed near 0 V, corresponding to sodium plating and stripping. XRD patterns of Na_3SbSe_4 before and after CV tests are shown in Figure 3.9(b). No extra peaks other than from residue Sn are observed after the CV cycles, suggesting good compatibility with metallic Na and good electrochemical stability in a wide voltage window for this material.

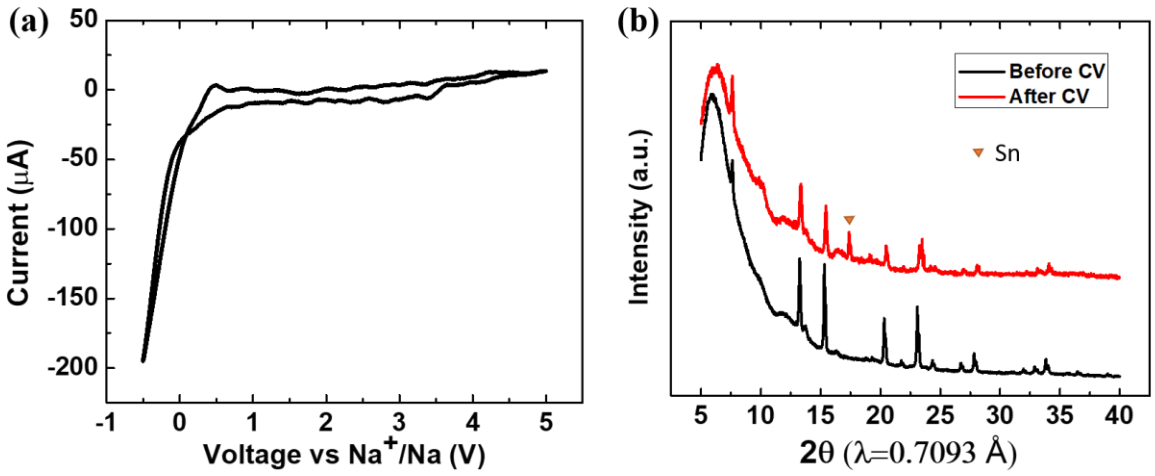

Figure 3.9 (a) Cyclic voltammetry (CV) curves of Na_3SbSe_4. (b) XRD patterns of Na_3SbSe_4 before and after CV measurements.

All-solid-state Na-ion battery Na-Sn | SE | TiS_2 was fabricated by using synthesized Na_3SbSe_4 as the solid electrolyte (SE), TiS_2-SE mixed powder as the cathode, and Sn-Na alloy as the anode. The cell was cycled at room temperature under a current density of 0.01 mA cm^{-2} (~0.015 C based on theoretical capacity of 239 mAh g^{-1} for TiS_2) within the voltage range from 0.9 V to 2.6 V. The charge–discharge curves were shown in Figure 3.10. The cell exhibits discharge and charge capacities of 90 mAh g^{-1} and 64 mAh g^{-1}, respectively, in the first cycle. It is worth noting that the voltage profiles in solid state batteries are commonly more sloping and featureless than those in liquid electrolyte cells, due to the lower conductivity of the solid electrolyte itself and the sluggish ionic transport at the solid-solid interfaces. Similar sloping voltage curves of TiS_2 was also reported by other attempts of all-solid-state Na-ion batteries, such as work by Ong *et al.* [152]. The cycling curves and reasonable capacities demonstrated the capability of Na_3SbSe_4 to enable all-solid-state Na-ion batteries at room temperature and the promise of the selenide-based solid electrolytes. The subsequent cycling of the cell showed relatively fast decay in capacity as the cell was not optimized in pressure, ratio of materials, and interface treatment. Although no visible degradation phases were detected by XRD, interface reactions did take place, indicated by the significantly increased impedance and a fast decay of the capacity. The interface degradation and the compatibility and stability between the electrolyte and the electrode will need further investigation. Further improvement calls for not only the optimization of the cell fabrication and test conditions, but also a better understanding on the mechanical and chemical degradation of solid-state batteries.

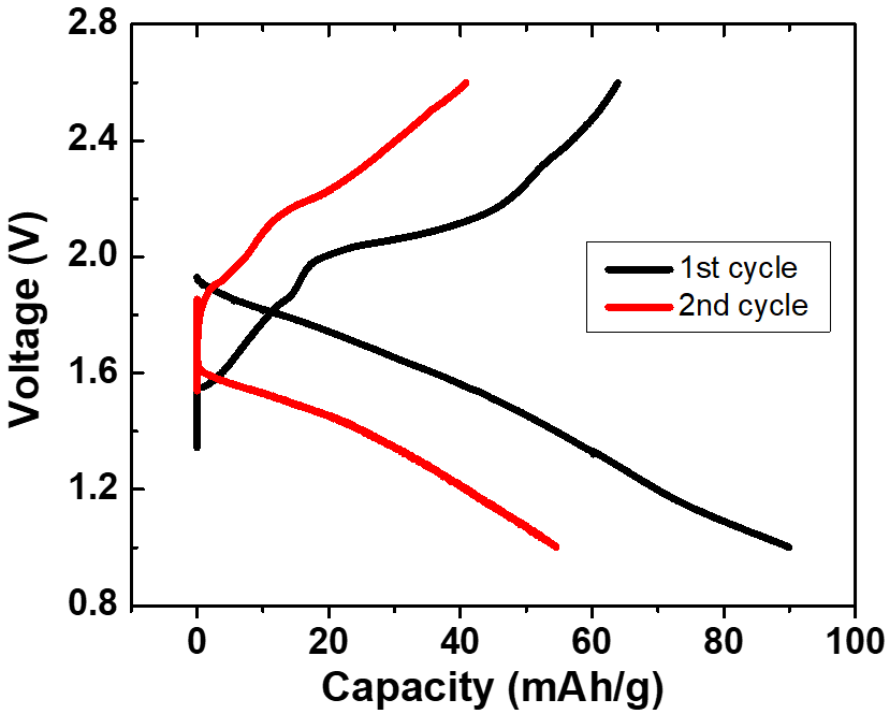

Figure 3.10 Charge–discharge curves of all-solid-state Na-Sn | Na_3SbSe_4 | TiS_2 cell cycled at room temperature.

3.3 Summary

In this work, a new Na ion conductor, cubic Na_3SbSe_4 and a group of S-doped solid solution phases have been synthesized and demonstrated with high conductivities up to 0.85 $mS \cdot cm^{-1}$ at room temperature, which is among the highest conductivities reported in chalcogenide-based Na-ion conductors. Structure characterizations reveal that the large unit cell size may be the key factor for higher conductivity than cubic Na_3PS_4. Na_3SbSe_4 also shows excellent electrochemical stability and enables the cycling of an all-solid-state

Na-ion battery at room temperature. This work will open opportunities in designing new chalcogenide ionic conductors and developing new Na-based all-solid-state batteries.

3.4 Methods

3.4.1 Synthesis of $Na_3SbSe_{4-x}S_x$

Na_3SbSe_4 compounds were synthesized by solid-state reaction. Starting materials including Na metal (99.8%, Sigma Aldrich), Sb (99.5%, Alfa Aesar), and Se (99.99%, Sigma Aldrich) were weighed and mixed with stoichiometric ratio. Se was used with 10% excess to compensate the loss during heating. The mixture was loaded into a quartz tube in an Ar-filled glove box, and then the tube was sealed under vacuum. The tube has an inner diameter of 14 mm and a length of 8 inches. Typically, each tube contained 1 g of mixed starting materials per batch. The tube was then heated to 650 °C with a 3 °C/min ramp in a box furnace, dwelling for 18 h, and quenched on a copper plate in the ambient atmosphere. Then the tube was moved into the glove box and the product powder was obtained through hand grinding with a mortar and a pestle after breaking the tube. $Na_3SbSe_{4-x}S_x$ (x = 1, 2, 3, 4) samples were synthesized with the same protocol by replacing stoichiometric amount of Se by S (99.5%, Alfa Aesar) in the starting materials, also with 10% excess.

3.4.2 Characterizations

Crystal structures of the obtained samples were analyzed first by X-ray diffraction (XRD) with a D8 Advance X-ray Diffractometer (Bruker) equipped with a strip detector and a Molybdenum tube [λ K α1 = 0.7093 Å]. The powder samples were scanned in an air-

tight sample container covered with a Kapton tape to avoid exposure to the air and moisture. The samples were also investigated in sealed capillaries with synchrotron X-ray diffraction at beam line 17-BM at the Advanced Photon Source (APS) at the Argonne National Laboratory (ANL) and at 28-ID-2 at the National Synchrotron Light Source II at Brookhaven National Laboratory. Rietveld refinement was performed using the synchrotron XRD data with the EXPGUI suite of GSAS code [164]. Hitachi SU8230 Scanning Electron Microscope (SEM) was used to characterize the morphology and elementary distribution of the as-synthesized samples. Energy-dispersive X-ray spectroscopy (EDX) was conducted to analyze the element distribution using Oxford EDS detector with 10 kV accelerating voltage, high probe current, and 30 μA emission current.

3.4.3 Electrochemical Tests

AC impedance measurements were conducted using a Bio-Logic VMP3 impedance analyzer in the frequency range from 1 MHz to 0.5 Hz with a voltage amplitude of 100 mV. The pellets for the measurements were cold-pressed from as-synthesized powders at 100 MPa pressure in an acrylic tube with an inner diameter of 0.5 inch. Two stainless-steel rods were used as blocking electrodes. Temperature-dependent conductivity measurements were performed from room temperature to 100 °C with two stainless-steel rods as electrodes and a heatable pressing die with a temperature controller. Cyclic voltammetry (CV) curves of Na | Na_3SbSe_4 | Sn cell was measured with Sn as the work electrode and Na metal as the counter and reference electrode.

All-solid-state Na-ion battery was fabricated using TiS_2 (99.9%, Sigma-Aldrich) as the cathode material, Na_3SbSe_4 as the solid electrolyte (SE), and a Na-Sn alloy as the anode.

The composite cathode consists of TiS_2 active material and the synthesized SE powder in a weight ratio of 2:3. They were well-mixed with hand milling in an agate mortar. About 10 mg of mixed cathode powder was pressed on one side of the SE pellet (200 mg) by applying a pressure of 50 MPa in an acrylic tube with an inner diameter of 0.50 inch between two stainless-steel rods. Then a Sn foil and a Na foil were successively pressed onto the other side of the bilayer assembly by applying a pressure less than 10 MPa to form a tri-layer cell, with two stainless steel rods as the current collectors. All the fabrication processes were conducted in an Ar-filled glove box. Then the whole cell was sealed with Parafilm and Teflon tape and cycled in ambient environment. The cell was cycled galvanostatically at a current density of 0.01 mA cm^{-2} within the voltage window from 0.9 V to 2.6 V using an Arbin BT2043 battery cycler at room temperature.

3.5 Notes to Chapter 3

This chapter is based on the paper entitled "$Na_3SbSe_{4-x}S_x$ as Sodium Superionic Conductors" published in Scientific Reports [90].

3.6 References

[5] Kato, Y., S. Hori, T. Saito, K. Suzuki, M. Hirayama, A. Mitsui, M. Yonemura, H. Iba, and R. Kanno, *High-power all-solid-state batteries using sulfide superionic conductors.* Nature Energy, 2016. **1**(4): p. 16030.

[54] Kamaya, N., et al., *A lithium superionic conductor.* Nat Mater, 2011. **10**(9): p. 682-6.

[64] Anantharamulu, N., K. Koteswara Rao, G. Rambabu, B. Vijaya Kumar, V. Radha, and M. Vithal, *A wide-ranging review on Nasicon type materials.* Journal of Materials Science, 2011. **46**(9): p. 2821-2837.

[69] Bachman, J.C., et al., *Inorganic Solid-State Electrolytes for Lithium Batteries: Mechanisms and Properties Governing Ion Conduction.* Chem Rev, 2016. **116**(1): p. 140-62.

[75] Hayashi, A., A. Sakuda, and M. Tatsumisago, *Development of Sulfide Solid Electrolytes and Interface Formation Processes for Bulk-Type All-Solid-State Li and Na Batteries.* Frontiers in Energy Research, 2016. **4**(25).

[80] Yu, Z., et al., *Exceptionally High Ionic Conductivity in $Na_3P_{0.62}As_{0.38}S_4$ with Improved Moisture Stability for Solid-State Sodium-Ion Batteries.* Adv Mater, 2017. **29**(16).

[81] Zhang, L., K. Yang, J. Mi, L. Lu, L. Zhao, L. Wang, Y. Li, and H. Zeng, *Na_3PSe_4: A Novel Chalcogenide Solid Electrolyte with High Ionic Conductivity.* Advanced Energy Materials, 2015. **5**(24): p. 1501294.

[90] Xiong, S., Z. Liu, H. Rong, H. Wang, M. McDaniel, and H. Chen, *$Na_3SbSe_{4-x}S_x$ as Sodium Superionic Conductors.* Scientific Reports, 2018. **8**(1): p. 9146.

[106] Wang, Y., W.D. Richards, S.P. Ong, L.J. Miara, J.C. Kim, Y. Mo, and G. Ceder, *Design principles for solid-state lithium superionic conductors.* Nature Materials, 2015. **14**(10): p. 1026-1031.

[111] Seino, Y., T. Ota, K. Takada, A. Hayashi, and M. Tatsumisago, *A sulphide lithium super ion conductor is superior to liquid ion conductors for use in rechargeable batteries.* Energy Environ. Sci., 2014. **7**(2): p. 627-631.

[139] Ellis, B.L. and L.F. Nazar, *Sodium and sodium-ion energy storage batteries.* Current Opinion in Solid State and Materials Science, 2012. **16**(4): p. 168-177.

[140] Larcher, D. and J.M. Tarascon, *Towards greener and more sustainable batteries for electrical energy storage.* Nature Chemistry, 2015. **7**(1): p. 19-29.

[141] Bai, Q., L. Yang, H. Chen, and Y. Mo, *Computational Studies of Electrode Materials in Sodium-Ion Batteries.* Advanced Energy Materials, 2018. **8**(17): p. 1702998.

[142] Yang, L., et al., *Design of high-performance cathode materials with single-phase pathway for sodium ion batteries: A study on P2-$Na_x(Li_yMn_{1-y})O_2$ compounds.* Journal of Power Sources, 2018. **381**: p. 171-180.

[143] Hong, S.Y., Y. Kim, Y. Park, A. Choi, N.-S. Choi, and K.T. Lee, *Charge carriers in rechargeable batteries: Na ions vs. Li ions.* Energy & Environmental Science, 2013. **6**(7): p. 2067-2081.

[144] Ma, X., K. An, J. Bai, and H. Chen, *$NaAlTi_3O_8$, A Novel Anode Material for Sodium Ion Battery.* Scientific Reports, 2017. **7**(1): p. 162.

[145] Dunn, B., H. Kamath, and J.-M. Tarascon, *Electrical Energy Storage for the Grid: A Battery of Choices.* Science, 2011. **334**(6058): p. 928-935.

[146] Lu, X., G. Xia, J.P. Lemmon, and Z. Yang, *Advanced materials for sodium-beta alumina batteries: Status, challenges and perspectives.* Journal of Power Sources, 2010. **195**(9): p. 2431-2442.

[147] Jung, Y.S., D.Y. Oh, Y.J. Nam, and K.H. Park, *Issues and Challenges for Bulk-Type All-Solid-State Rechargeable Lithium Batteries using Sulfide Solid Electrolytes.* Israel Journal of Chemistry, 2015. **55**(5): p. 472-485.

[148] Richards, W.D., T. Tsujimura, L.J. Miara, Y. Wang, J.C. Kim, S.P. Ong, I. Uechi, N. Suzuki, and G. Ceder, *Design and synthesis of the superionic conductor $Na_{10}SnP_2S_{12}$.* Nature Communications, 2016. **7**(1): p. 11009.

[149] Kandagal, V.S., M.D. Bharadwaj, and U.V. Waghmare, *Theoretical prediction of a highly conducting solid electrolyte for sodium batteries: $Na_{10}GeP_2S_{12}$.* Journal of Materials Chemistry A, 2015. **3**(24): p. 12992-12999.

[150] Hayashi, A., K. Noi, A. Sakuda, and M. Tatsumisago, *Superionic glass-ceramic electrolytes for room-temperature rechargeable sodium batteries.* Nat Commun, 2012. **3**: p. 856.

[151] Tanibata, N., K. Noi, A. Hayashi, and M. Tatsumisago, *Preparation and characterization of highly sodium ion conducting Na_3PS_4–Na_4SiS_4 solid electrolytes.* RSC Advances, 2014. **4**(33): p. 17120-17123.

[152] Chu, I.-H., C.S. Kompella, H. Nguyen, Z. Zhu, S. Hy, Z. Deng, Y.S. Meng, and S.P. Ong, *Room-Temperature All-solid-state Rechargeable Sodium-ion Batteries with a Cl-doped Na_3PS_4 Superionic Conductor.* Scientific Reports, 2016. **6**(1): p. 33733.

[153] Bo, S.-H., Y. Wang, J.C. Kim, W.D. Richards, and G. Ceder, *Computational and Experimental Investigations of Na-Ion Conduction in Cubic Na_3PSe_4.* Chemistry of Materials, 2016. **28**(1): p. 252-258.

[154] Wang, H., Y. Chen, Z.D. Hood, G. Sahu, A.S. Pandian, J.K. Keum, K. An, and C. Liang, *An Air-Stable Na_3SbS_4 Superionic Conductor Prepared by a Rapid and Economic Synthetic Procedure.* Angew Chem Int Ed Engl, 2016. **55**(30): p. 8551-5.

[155] Banerjee, A., K.H. Park, J.W. Heo, Y.J. Nam, C.K. Moon, S.M. Oh, S.T. Hong, and Y.S. Jung, *Na_3SbS_4 : A Solution Processable Sodium Superionic Conductor for All-Solid-State Sodium-Ion Batteries.* Angew Chem Int Ed Engl, 2016. **55**(33): p. 9634-8.

[156] Eisenmann, B.a.R.Z., *Selenoantimonate: Darstellung und Struktur von Na_3SbSe_4, K_3SbSe_4 und $[Ba(en)_4]_2[Ba(en)_3](SbSe_4)_2$/ Selenoantimonates(V): Preparation and Crystal Structure of Na_3SbSe_4, K_3SbSe_4 and $[Ba(en)_4]_2[Ba(en)_3](SbSe_4)_2$.* Zeitschrift für Naturforschung B, 1989. **44**(3): p. 8.

[157] Rao, R.P., H. Chen, L.L. Wong, and S. Adams, *$Na_{3+x}M_xP_{1-x}S_4$ (M = Ge^{4+}, Ti^{4+}, Sn^{4+}) enables high rate all-solid-state Na-ion batteries $Na_{2+2\delta}Fe_{2-\delta}(SO_4)_3|Na_{3+x}M_xP_{1-x}S_4|Na_2Ti_3O_7$.* Journal of Materials Chemistry A, 2017. **5**(7): p. 3377-3388.

[158] Ohno, S., et al., *How Certain Are the Reported Ionic Conductivities of Thiophosphate-Based Solid Electrolytes? An Interlaboratory Study*. ACS Energy Letters, 2020. **5**(3): p. 910-915.

[159] Kraft, M.A., et al., *Influence of Lattice Polarizability on the Ionic Conductivity in the Lithium Superionic Argyrodites Li_6PS_5X (X = Cl, Br, I).* J Am Chem Soc, 2017. **139**(31): p. 10909-10918.

[160] Krauskopf, T., C. Pompe, M.A. Kraft, and W.G. Zeier, *Influence of Lattice Dynamics on Na^+ Transport in the Solid Electrolyte $Na_3PS_{4-x}Se_x$.* Chemistry of Materials, 2017. **29**(20): p. 8859-8869.

[161] Bo, S.-H., Y. Wang, and G. Ceder, *Structural and Na-ion conduction characteristics of $Na_3PS_xSe_{4-x}$.* Journal of Materials Chemistry A, 2016. **4**(23): p. 9044-9053.

[162] Zhu, Z., I.-H. Chu, Z. Deng, and S.P. Ong, *Role of Na^+ Interstitials and Dopants in Enhancing the Na^+ Conductivity of the Cubic Na_3PS_4 Superionic Conductor*. Chemistry of Materials, 2015. **27**(24): p. 8318-8325.

[163] Zhang, L., D. Zhang, K. Yang, X. Yan, L. Wang, J. Mi, B. Xu, and Y. Li, *Vacancy-Contained Tetragonal Na_3SbS_4 Superionic Conductor*. Adv Sci (Weinh), 2016. **3**(10): p. 1600089.

[164] Toby, B.H., *EXPGUI, a graphical user interface for GSAS.* Journal of Applied Crystallography, 2001. **34**(2): p. 210-213.

CHAPTER 4. A STUDY ON LOCAL STRUCTURE EVOLUTION OF Na_3SbS_4-CONTAINING CONDUCTORS WITH *IN SITU* X-RAY CHARACTERIZATION

4.1 Introduction

Chalcogenide-based glass-ceramic compounds have received broad attentions due to their good processability and superior ionic conductivity [81, 90, 165-170]. With the growth of market demands on safe and high-performance battery technology for large-scale renewable energy storage, the development of solid-state Na-ion batteries and its key component, i.e., fast Na-ion conductors, has gain extensive research efforts over the past decade. During the investigation of $Na_3SbSe_{4-x}S_x$ (x=0~4) chalcogenide material family in Chapter 3, it was observed that the sample pellets with or without high energy ball milling show orders of magnitude differences in measured conductivity, which led to the hypothesis that the different particle sizes, the presence of grain boundary, and potential local structure variations caused by different post-processing methods may play a critical role in the performance of solid ionic conductors.

From material processing perspective, ball-milling is a widely adopted technique for material processing in the preparation of solid electrolytes. High-energy ball milling is proved to be able to improve the reactivity of starting material for doping strategies, to obtain fine-sized particles, and to achieve intimate contact between solid electrolytes and electrode materials [171-173]. However, ball-milling may also influence the long-range structure of the as-synthesized materials, form large amount of grain boundaries with lower

conduction, and/or introduce unexpected impurities or microstructures [5, 58, 90, 174-176]. The competing positive and negative effects of ball-milling remains somewhat mysterious and can be critical to the preparation of solid electrolytes and the fabrication of all-solid-state batteries. To have a better understanding of these effects, one end member of the $Na_3SbSe_{4-x}S_x$ solid solution series, Na_3SbS_4, is selected as the model compound to systematically investigate the microstructural variation and their impact on ionic conductivities with *in situ* synchrotron X-ray diffraction (XRD) and pair distribution function (PDF) analysis. This study will also help us gain more insights on material properties under various processing conditions and with the presence of other compounds in a mixture.

As the key structure analysis tool in this study, pair distribution function (or PDF) is essentially obtained from the reverse Fourier transform of total scattering function. This method has been adopted extensively to understand material structures of both crystalline and amorphous phases [177, 178], especially for material families possessing deviated or unrevealed local structure features from their averaged periodic structures [100, 179, 180]. PDF method based on synchrotron X-ray scattering data is therefore considered an effective complementary crystallographic technique to elucidate short-range structural information in addition to diffraction analysis, which will provide valuable structural details for the analysis of chalcogenide-based glass-ceramic compounds under various mechanical milling and heat treatment conditions.

In this study, high energy ball-milling is adopted to process Na_3SbS_4-containing samples, i.e., Na_3SbS_4-NaCl mixtures with different ratios, to obtain various crystal structures in terms of long-range or short-range features. Similar chalcogenide

compositions with VA-elements and halides have been greatly investigated for Li or Na-ion conductor development [152] and therefore Na_3SbS_4-NaCl mixtures are also an interesting precursor system for new structure exploration. The characteristic signals of the microstructure and local environment can be identified by obtaining the XRD and PDF results and comparing these results of the ball-milled and well-crystalized samples. More importantly, *in situ* powder XRD/PDF will be used to track the structural variation during the heating process of ball-milled samples, meaning the evolution of both long range and local structures of the samples during the crystallization process will be tracked and analyzed. Variable temperature (VT) electrochemical impedance spectroscopy (EIS) is also conducted to reveal the change of conductivity while ball-milled Na_3SbS_4 crystalizes under various temperatures. Detailed results of these chalcogenide-based compounds are shown in the following sections.

4.2 Results and Discussion

4.2.1 Average Crystal Structure of Milled Na_3SbS_4-containing Systems

Crystallized Na_3SbS_4 pure phase and mixtures of Na_3SbS_4-NaCl powder are first ball-milled (BM) with a speed of 370 rpm for 12 hours. After high-energy ball milling, the crystal structures of these samples show different diffraction patterns. As shown in Figure 4.1, pure Na_3SbS_4 can still be identified as the same structure before milling despite the decreased crystallinity, whereas the mixtures with NaCl generate different patterns. With 1:1 molar ratio of Na_3SbS_4 and NaCl, the mixture shows lower intensities of Na_3SbS_4 peaks after milling. For mixture of Na_3SbS_4 and NaCl with 1:2 molar ratio, the peaks from Na_3SbS_4 almost disappear. The remaining peaks are similar to the patterns of NaCl, with

slight shift of the peak at 2θ=14.1° and at 2θ=12.8° compared with (200) and (111) peaks of NaCl, respectively. Same shifting trends of these peaks are also observed in the 1:1 mixture. This suggests that the milled products with the presence of NaCl have lost its long-range ordering of the sulfide component, which leads to the formation of either an averaged disordered structure or a mixture with amorphized sulfide components.

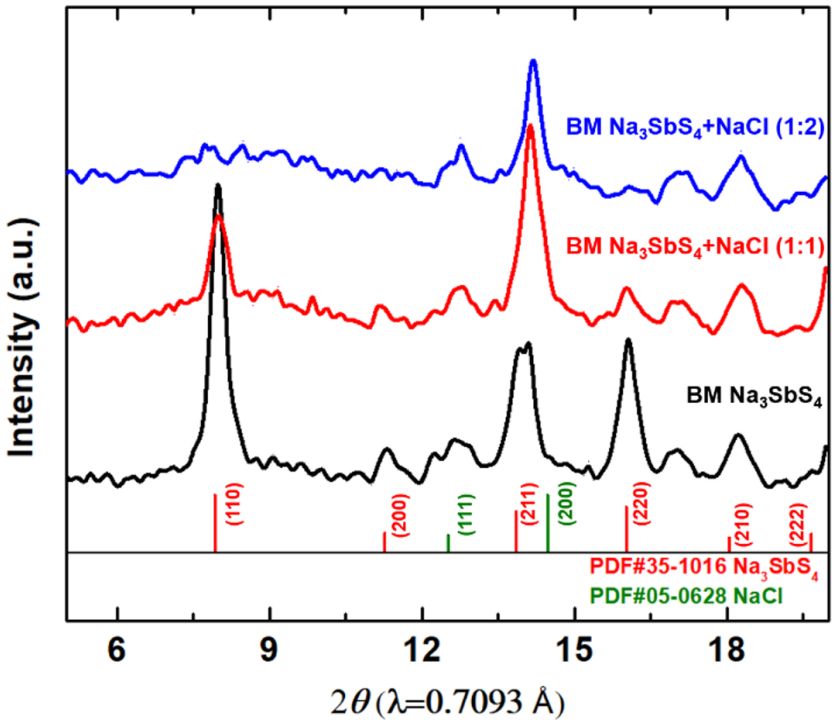

Figure 4.1 XRD patterns of ball-milled (BM) Na_3SbS_4 and BM Na_3SbS_4-NaCl mixture, with molar ratios of 1:1 and 1:2, respectively.

To understand the stability of the ball-milled products, *in situ* XRD of the two mixtures was conducted in our lab, as shown in Figure 4.2. With limited resolution, the peak at 2θ=14.1° can still be clearly observed to split into two peaks at 230℃. The left one can be identified to be (211) peak of Na_3SbS_4 and the right one to be (200) peak of NaCl.

The (110) and (220) peaks of Na_3SbS_4 are also showing up from 190℃. These results suggest that the ball-milled product remains relatively stable up to ~190℃ and will decompose to the starting materials of Na_3SbS_4 and NaCl at higher temperatures, meaning the formation of the new structure is reversible upon moderate heating. Similar evolution is also observed for the 1:1 mixture with a lower amount of NaCl. What is different is that the peak splitting at around 2θ=14° starts to appear at a lower temperature, namely 200℃. This indicates that under the same ball-milling conditions, the amount of NaCl is critical to determine the crystal structure and the stability of BM products. More NaCl tends to convert the mixture into the new disordered or amorphous structure with better stability up to a higher temperature.

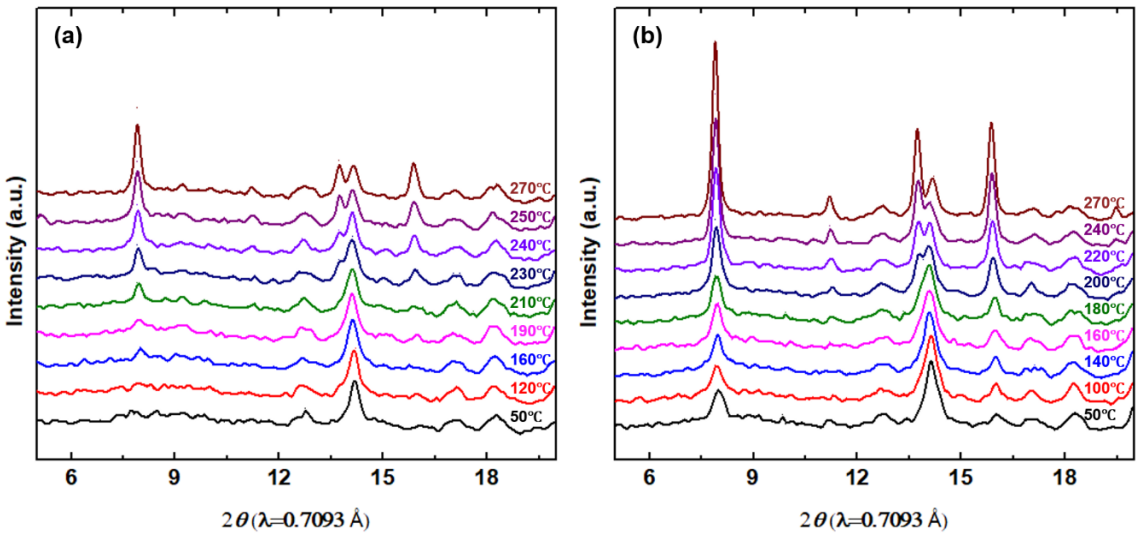

Figure 4.2 *In situ* XRD patterns of ball-milled Na_3SbS_4-NaCl mixture with molar ratios of (a) 1:2 and (b) 1:1 during the heating process, respectively.

To better illustrate the crystal structure of the obtained BM products, high quality data with synchrotron XRD is obtained for the BM Na_3SbS_4 and the BM 1:2 mixture of

(Na_3SbS4 + NaCl), as shown in Figure 4.3. Compared to milled Na_3SbS_4 sample, the ball-milled mixture presents a structure mainly containing a NaCl-like phase with low-intensity signals from remaining Na_3SbS_4-phase at $2\theta=1.8°$. This structure may not deliver prominent conductivities considering the lack of continuous long-range diffusion channels for mobile ions, but the formation mechanism and the underlying structural evolution, such as chemical bonds, local orderings, polyhedrons, etc., may reveal valuable information for both fundamental understanding of this material family and processing criterions for all-solid-state battery applications.

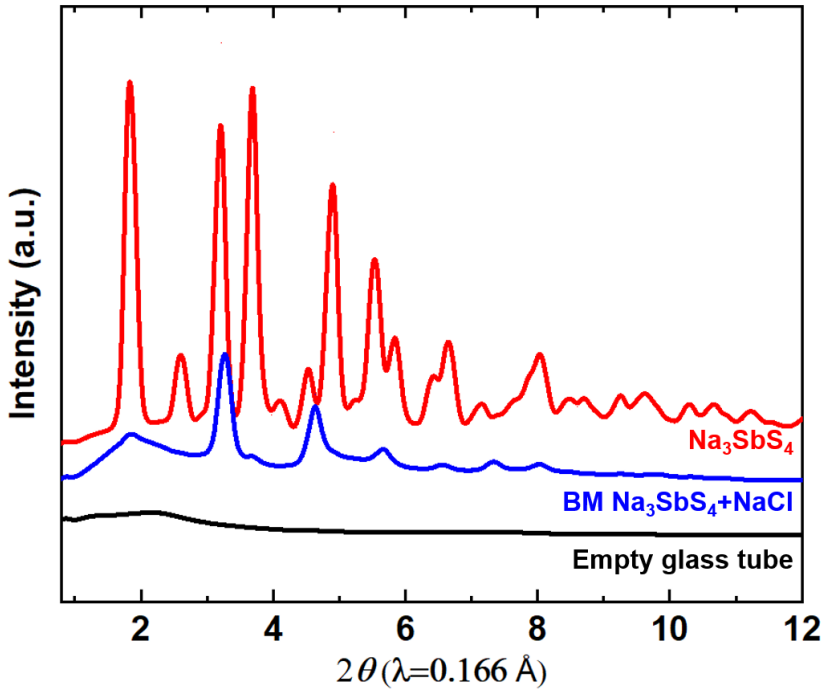

Figure 4.3 Synchrotron XRD patterns of Na_3SbS_4, ball-milled (370 rpm) mixture of Na_3SbS_4 + NaCl (1:2) and empty glass tube (as background signals).

To further tune the newly formed rock-salt-like structure and eliminate the remaining signals from Na_3SbS_4 phase in the products, mixtures of (Na_3SbS_4 + NaCl) with

two molar ratios of 1:1 and 1:2 are ball milled with a higher speed of 500 rpm for 16 hours. After more intense ball milling, the crystal structures of both samples show similar rock-salt-like patterns with slight difference in Na_3SbS_4-like signals. As shown in Figure 4.4, for the 1:1 Na_3SbS_4-NaCl mixture sample, the XRD pattern still shows minor intensities of Na_3SbS_4 peaks after milling, while for 1:2 mixtures with more NaCl, there are no detectable signals from Na_3SbS_4 even in high resolution synchrotron XRD results. The remaining peaks are purely a NaCl- or rock-salt-like phase. These results are consistence with the lab XRD results where higher NaCl content leads to less Na_3SbS_4 signal and a purer rock-salt-like structure. Compared with the 1:2 sample in Figure 4.3, it also indicates that higher mechanical milling power leads to a more thorough conversion to this new disordered or amorphous structure.

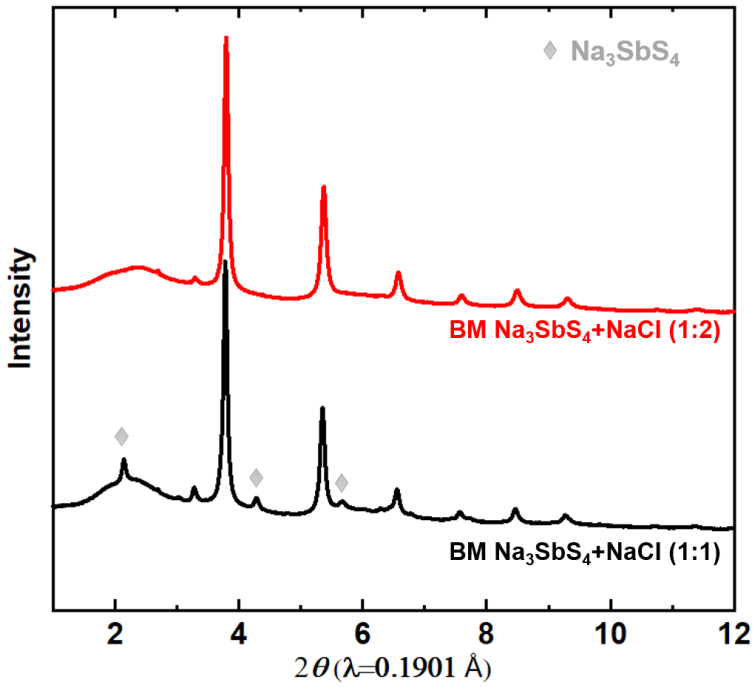

Figure 4.4 Synchrotron XRD patterns of ball-milled (500 rpm) mixture of Na_3SbS_4 + NaCl with molar ratio of 1:1 (black) and 1:2 (red), respectively.

In situ synchrotron XRD patterns at various temperatures during the heating process were then obtained for both 500 rpm milled mixture samples as well as pure Na_3SbS_4 processed by the same milling conditions in order to elucidate more thermodynamic properties and formation details of these Na_3SbS_4-containing samples. The results are summarized in Figure 4.5. In Figure 4.5(a), the pure Na_3SbS_4 sample at room temperature maintains the same tetragonal structure as previous reported [154, 155] despite the lower intensities caused by the high-speed ball-milling process. This suggests that without the presence of other solid additives, such as NaCl, the crystal structure of Na_3SbS_4 is relatively stable without obvious decomposition or phase transition under high-energy ball-milling. During the heating process, the crystallinity of the ball-milled sample gradually increases,

indicating a re-crystallization process of the precursor, which is similar to the formation of other glass-ceramic compounds as sulfide-based Na ion conductors [150, 181, 182]. Upon reaching 120°C, the sample is well crystallized with no more evident peak intensity changes observed at higher temperatures.

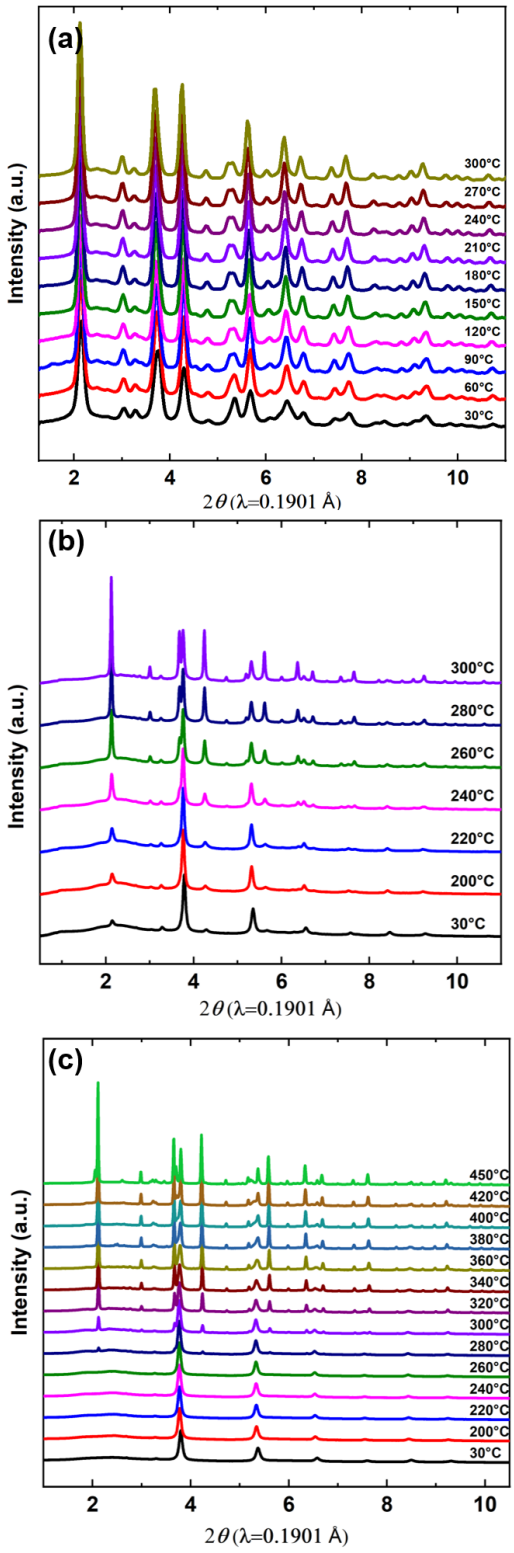

Figure 4.5 *In situ* synchrotron XRD patterns of 500 rpm ball-milled (a) Na_3SbS_4, and Na_3SbS_4-NaCl mixture with molar ratios of (b) 1:1 and (c) 1:2 during the heating process, respectively.

For the milled mixtures with the presence of NaCl, the *in situ* XRD patterns revealed more structural variations at elevated temperatures. In Figure 4.5(b), the mixture with 1:1 Na_3SbS_4-NaCl composition starts from a major NaCl-like phase and minor signals from Na_3SbS_4 phase at room temperature. During the heating process, the characteristic peaks of the Na_3SbS_4 phase, such as the (110) peak at 2θ=2.14°, keep increasing gradually. From 240 to 260 °C, the original (200) peak of NaCl at 2θ=3.77° (2θ at r.t.) starts to split into two peaks at 2θ=3.67° and 2θ=3.76° (2θ at 300 °C), and are identified as the (211) peak of Na_3SbS_4 and the (200) peak of NaCl phase, respectively. The intensity of these two peaks keeps increasing at high temperatures, suggesting the decomposition of the precursor and the crystallization of individual components before ball-milling. This is consistent with previous observation with lab XRD data, suggesting that despite the more intense ball-milling conditions, the newly milled structure is still reversible and will decompose to two starting materials upon heating to a higher temperature, i.e. ~260°C in the case of 1:1 Na_3SbS_4-NaCl mixture.

Similarly, equivalent evolution is observed for the 1:2 mixture with a higher NaCl content, as shown in Figure 4.5(c). At the beginning, only a pure rock-salt-like phase is detected, which can be identified to be a modified-NaCl structure. During the heating process, the characteristic (110) peak of the Na_3SbS_4 phase starts to appear at 2θ=2.13° from 280 °C and then keeps increasing at higher temperatures. The splitting of the NaCl (200) peak at 2θ=3.82° (2θ at r.t.) initiates at around 300 °C and the two resulting peaks are clearly observed at 2θ=3.66° and 2θ=3.80° at 300 °C, which can again be identified as the (211) peak of the Na_3SbS_4 phase and the (200) peak of the NaCl phase, respectively. This again confirms that the presence of NaCl additive plays a direct role in tuning the

structure of sulfide-based mixtures under the same ball-milling conditions. More NaCl leads to higher thermodynamic stability of the milled rock-salt-like structure compared to less NaCl or no NaCl systems. Nevertheless, despite a higher decomposition temperature, i.e., ~300°C in this case, the milled 1:2 Na_3SbS_4-NaCl precursor still decomposes and forms the two starting materials reversibly.

At this point, the long-range structures and thermodynamic stability of various Na_3SbS_4-NaCl mixtures with different ratios and ball-milling speeds have been characterized using *ex situ* and *in situ* XRD. However, the structural details of the mixture samples after ball-milling are still not clear. Our initial hypotheses of either a disordered rock-salt structure or a mixture of amorphous sulfides and distorted NaCl remain untested. Since the information revealed by Bragg peaks in XRD patterns is not sufficient to differentiate the structure of milled samples and prove (or disprove) either initial hypotheses, a systematic PDF analysis is conducted to further investigate the local structures, as discussed in the next session.

4.2.2 Local Crystal Structure of Milled Na_3SbS_4-containing Systems

In order to better understand the local structural variations of the ball-milled Na_3SbS_4-NaCl systems, synchrotron X-ray pair distribution function (PDF) analyses are performed. The experimentally obtained raw total scattering data and the corresponding PDF G(r) results for the 500 rpm milled Na_3SbS_4 sample are first analyzed as baseline, as shown in Figure 4.6(a) and (b), respectively. Based on visual inspection of the G(r) result in Figure 4.6(b), the local structure of ball-milled Na_3SbS_4 remains the same during the annealing process up to 300 °C. There are no evident pattern changes observed except for

gradual peak shifts to the right due to thermal expansion at elevated temperatures. This is consistent with the observation in diffraction data from Figure 4.5(a) that without the presence of NaCl additives, milled Na_3SbS_4 sample still maintains the tetragonal phase structure despite its lower crystallinity, which will not be reflected in short-range crystallographic results such as PDF data.

In an attempt to elucidate more local structural details, the reduced G(r) data at 30 °C were fitted using a tetragonal-phase model (same as the one used in Chapter 3 for S4) and a least-square refinement method. The plot of the refined G(r) is shown in Figure 4.7. Reasonably good fit with a low residual value of 12.6% was achieved using the tetragonal-phase model. The characteristic local atomic pair signals of Sb-S and Sb-Sb can be identified, as labelled by arrows in orange and blue in Figure 4.7, respectively. The shortest distance of Sb-S pair locates at 2.34 Å, which agrees well with the reported Sb-S bond length in $[SbS_4]^{3-}$ tetrahedra of the crystalline Na_3SbS_4 tetragonal phase with a $P\bar{4}2_1c$ space group [154, 155]. The second shortest Sb-S pair is 3.81 Å, slightly shorter than the length of 3.92 Å in well-crystalized Na_3SbS_4 phase. This deviation may be ascribed to the minor amorphous component caused by ball-milling or a milled phase with lower coherence lengths. Similar phenomenon in the low *r* region ($r \leq 5$ Å) has also been observed in other sulfide-based compounds [183, 184]. Another set of characteristic signals in the local range are Sb-Sb pairs locating at 6.22 Å and 7.20 Å, which are identical to the reported tetragonal crystalline Na_3SbS_4, indicating the short- to mid-range structure of the milled Na_3SbS_4 is almost intact despite 16-hour high-energy milling at 500 rpm.

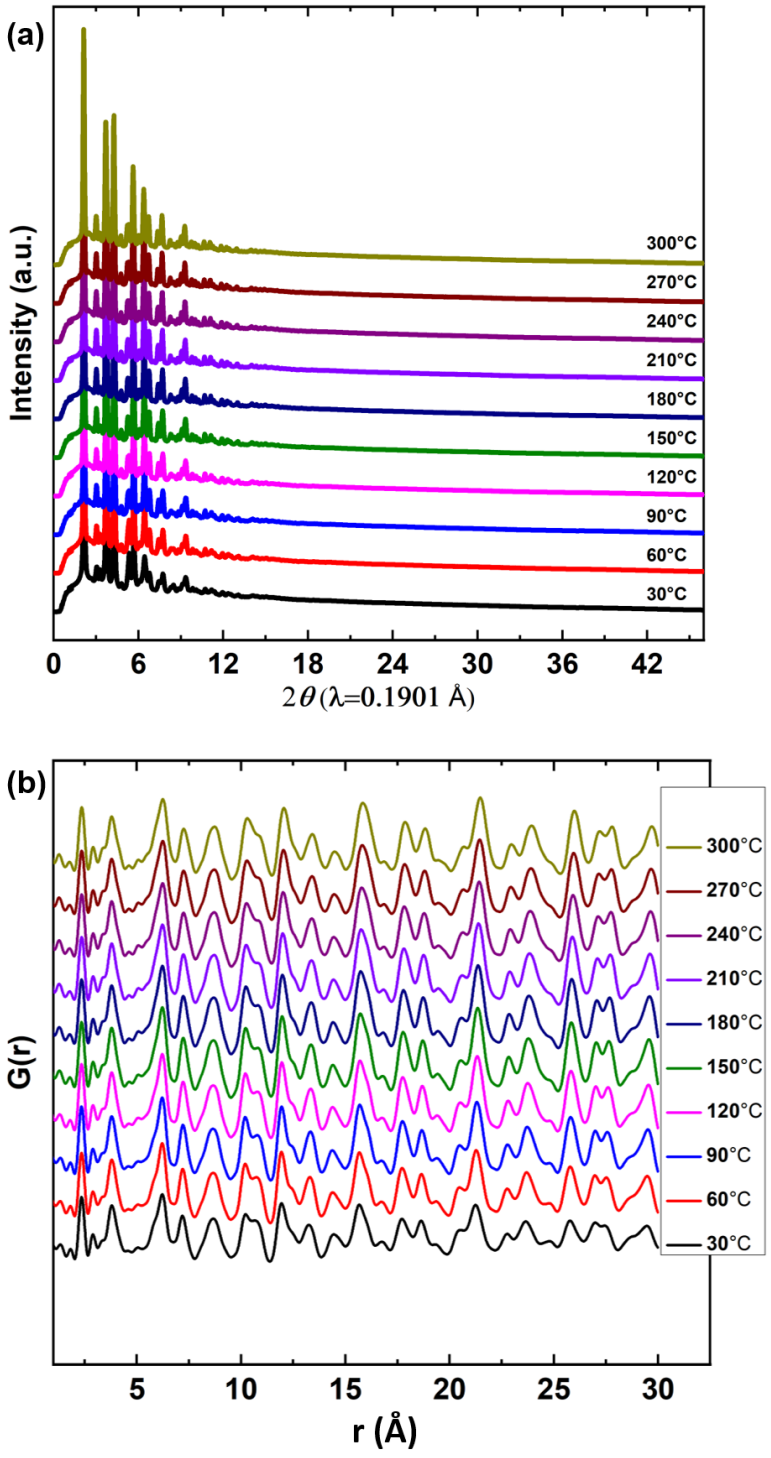

Figure 4.6 Experimentally obtained (a) *in situ* total scattering diffraction pattern of ball-milled Na_3SbS_4 and (b) the corresponding *in situ* PDF G(r) data at various temperatures.

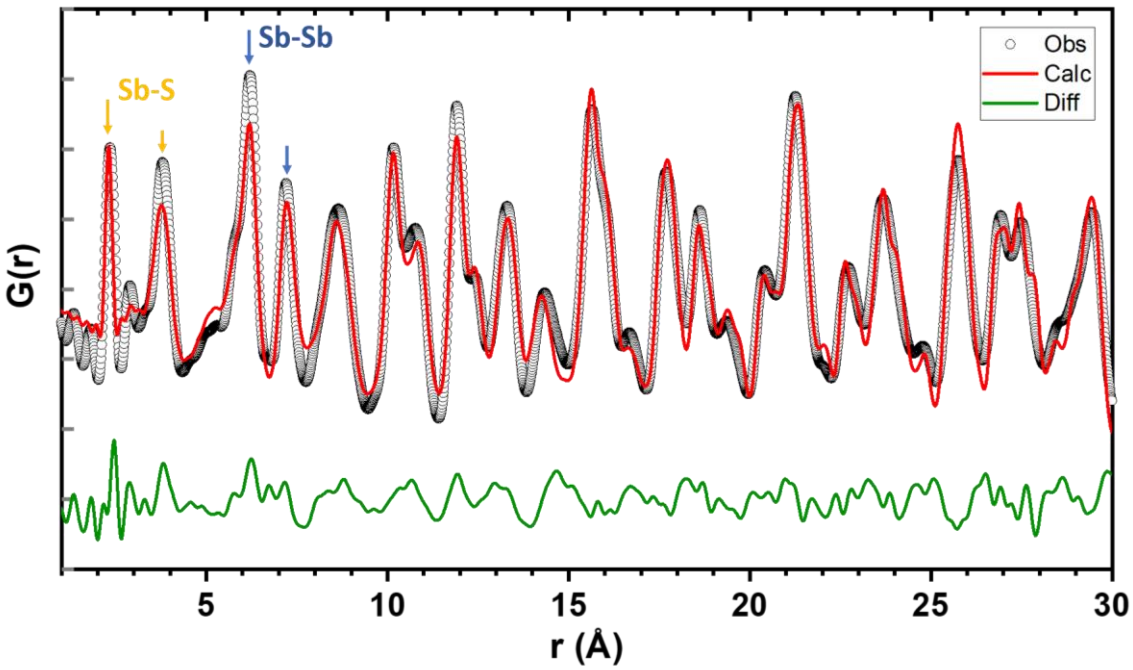

Figure 4.7 Fit of tetragonal model to G(r) data obtained from ball-milled Na_3SbS_4 sample at 30 °C. The black open circles represent the observed experimental G(r), the red curve represent the model, and the green curve shows the difference between the two.

For the milled mixture samples with NaCl, similar analyses are conducted. The reduced PDF G(r) results from the experimental *in situ* X-ray total scattering data of the 500 rpm milled 1:1 and 1:2 Na_3SbS_4-NaCl samples are shown in Figure 4.8(a) and (b), respectively. Based on visual inspection, the local structures in the low *r* region ($r \leq 3$ Å) for both samples are almost constant during the annealing process, while the longer *r* region (3 Å ≤ r ≤ 30 Å) witnesses an evident pattern change, such as the peaks in 6~8 Å, 12~14 Å, 17~19 Å, and 22~25 Å, etc. This may be related to the re-crystallization or precipitation of Na_3SbS_4 phase as observed in Figure 4.5(b) and (c), which is also supported by the similarity between the high temperature patterns in Figure 4.8 and the PDF patterns of Na_3SbS_4 in Figure 4.6(b).

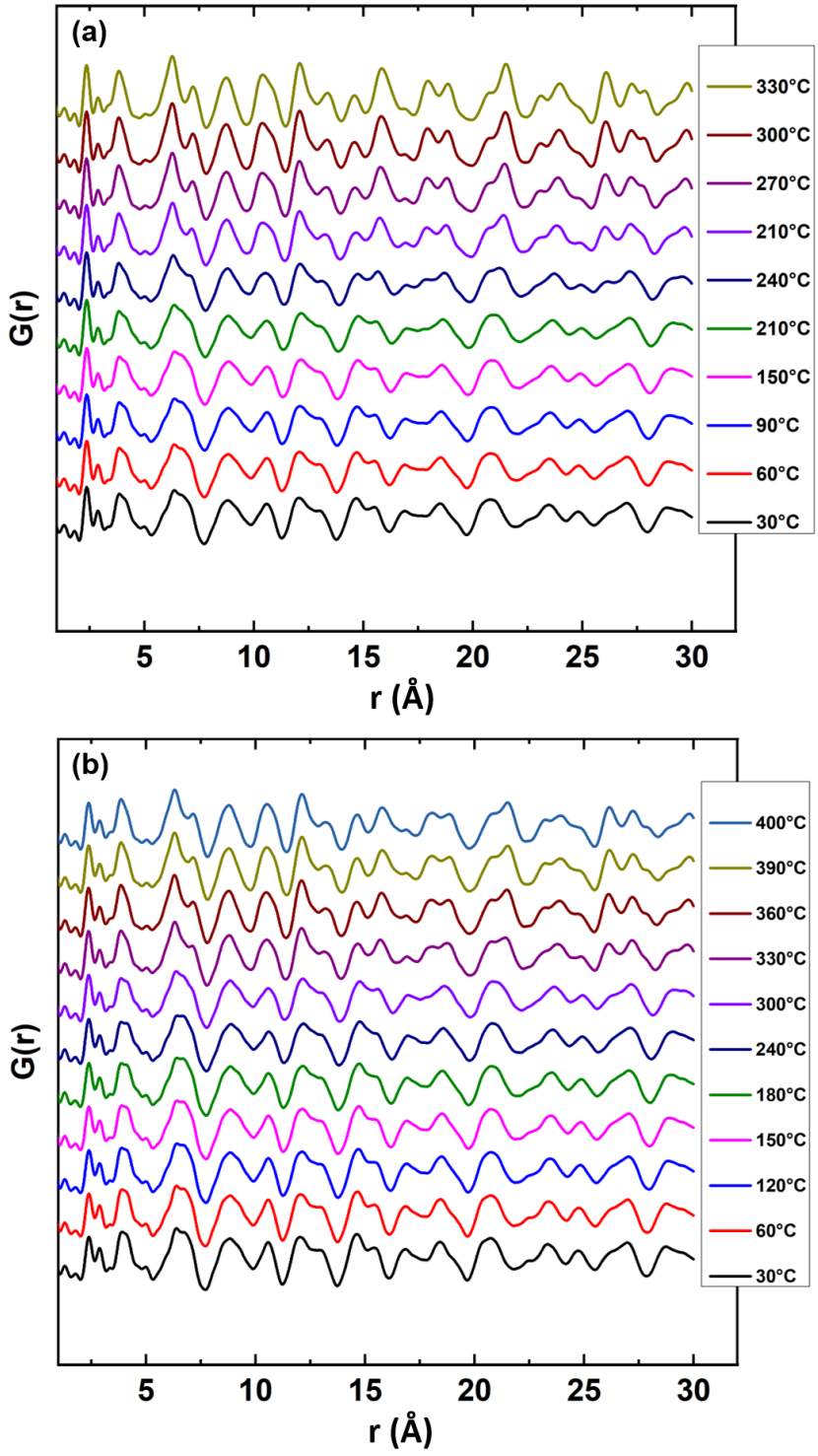

Figure 4.8 *In situ* PDF G(r) data of Na_3SbS_4-NaCl mixture with molar ratios of (a) 1:1 and (b) 1:2 at various temperatures.

To compare the PDF results of the three milled samples with various Na_3SbS_4 to NaCl ratios (i.e., 1:0, 1:1, and 1:2), a replot of the reduced G(r) data for these samples at room temperature and elevated temperatures is shown in Figure 4.9(a) and (b), respectively. Comparing the signals in the local short-range area at the same temperature, which excludes the thermal effect on material structures, some interesting and critical structural information can be extracted. First, the shortest Sb-S pair at ~2.34 Å was observed in all samples at both room temperature and high temperatures. This indicates that the $[SbS_4]^{3-}$ tetrahedra units are still intact despite the destruction of long-range periodic structure of Na_3SbS_4 after being milled with NaCl additives. It therefore suggests that one of the initial hypotheses that the ball-milled mixture forms a highly disordered rock-salt-like structure is untrue based on the existence of the $[SbS_4]^{3-}$ tetrahedra. Second, the signal at 3.8 ~ 3.9 Å shifts and reforms across different samples. Since both signals of secondary Sb-S (3.81 Å) in Na_3SbS_4 and Na-Na or Cl-Cl (~3.86 Å) in NaCl are in this range, more in-depth analysis or fitting is needed. Third, a significant signal variation is observed in the 5.5 ~ 7.5 Å region, as highlighted by dashed box in Figure 4.9. The characteristic signals of Sb-Sb pairs at 6.22 Å and 7.20 Å in Na_3SbS_4 sample are absent in the two mixture samples at room temperature. These signals show up again after annealing at 300°C for 1:1 sample and at 400°C for the 1:2 sample. This observation indicates that although the $[SbS_4]^{3-}$ tetrahedra units of Na_3SbS_4 still exist, the long-range periodic arrangement of these units is destructed by high-energy ball-milling with the presence of NaCl. Nevertheless, the original structure can be recovered upon annealing process.

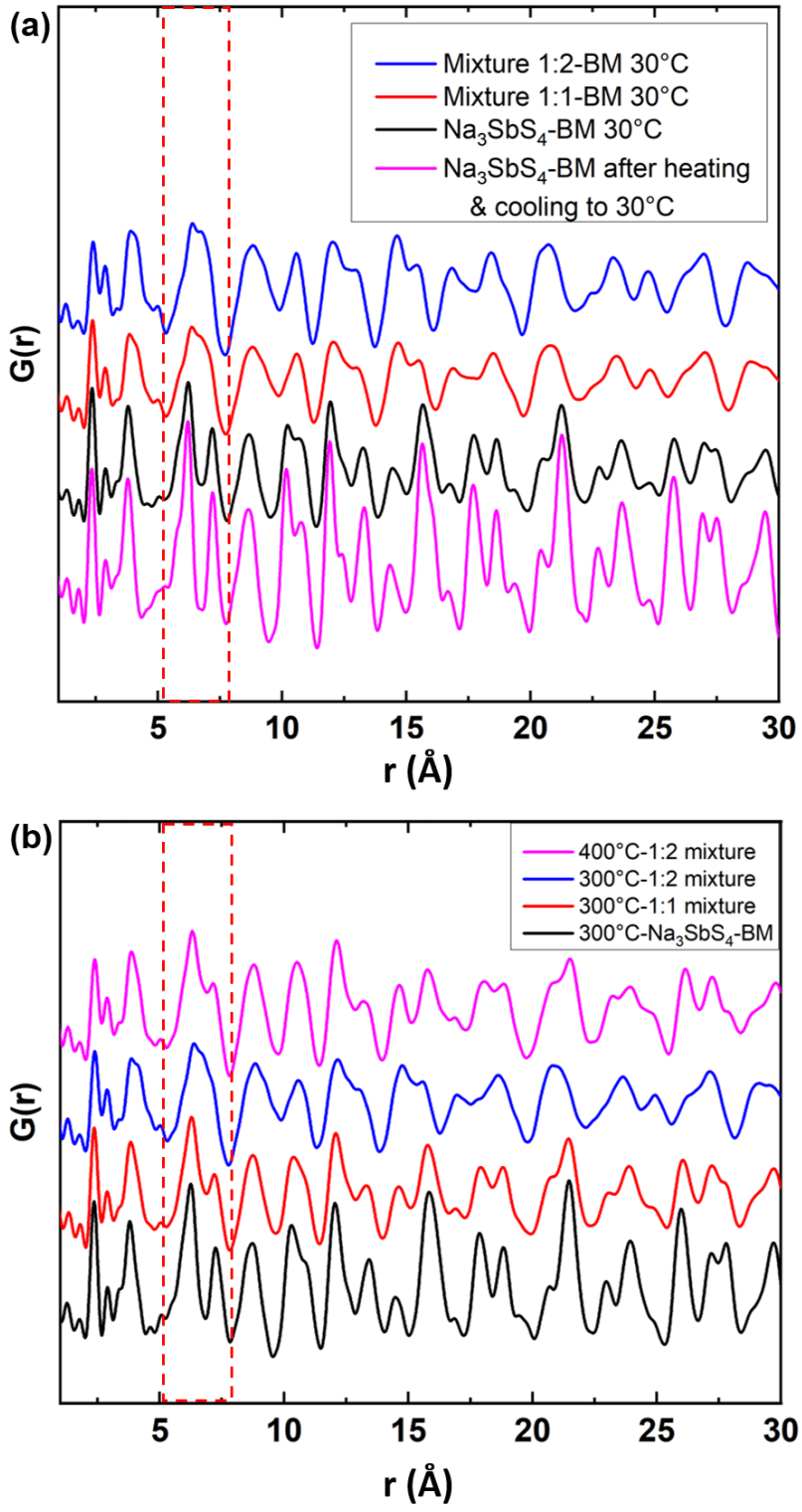

Figure 4.9 PDF G(r) data of Na_3SbS_4-NaCl mixture with various molar ratios of 1:1 and 1:2 at (a) low temperatures (30°C) and (b) high temperatures (300 and 400 °C).

To reveal more accurate structural details throughout the obtained *r* region, the reduced G(r) data of 1:2 Na_3SbS_4-NaCl mixture sample at 30 °C were fitted with a two-phase model using the diffpy.SrFit package developed by the Billinge group [185]. A cubic NaCl model and a tetragonal Na_3SbS_4 model (same as the model in Figure 4.7) are used as the starting models. The refined G(r) against experimental data is shown in Figure 4.10. It should be noted that due to the structural complexity of the two-phase mixture sample containing a glass-like component with unknown structure, it is difficult to obtain acceptable fitting result throughout the entire *r* range from 1 to 30 Å. The G(r) data is therefore fitted in the two ranges of $r \leq 6$ Å and $r \geq 6$ Å independently, as divided by the dashed grey line in Figure 4.10. Significant improvements of fitting are achieved and reasonably good residual values R_w are obtained for both ranges. More details of the two-phase fitting are illustrated in Figure 4.11 by plotting the individual contribution of the two models. The refined structural parameters are summarized in Table 4.1.

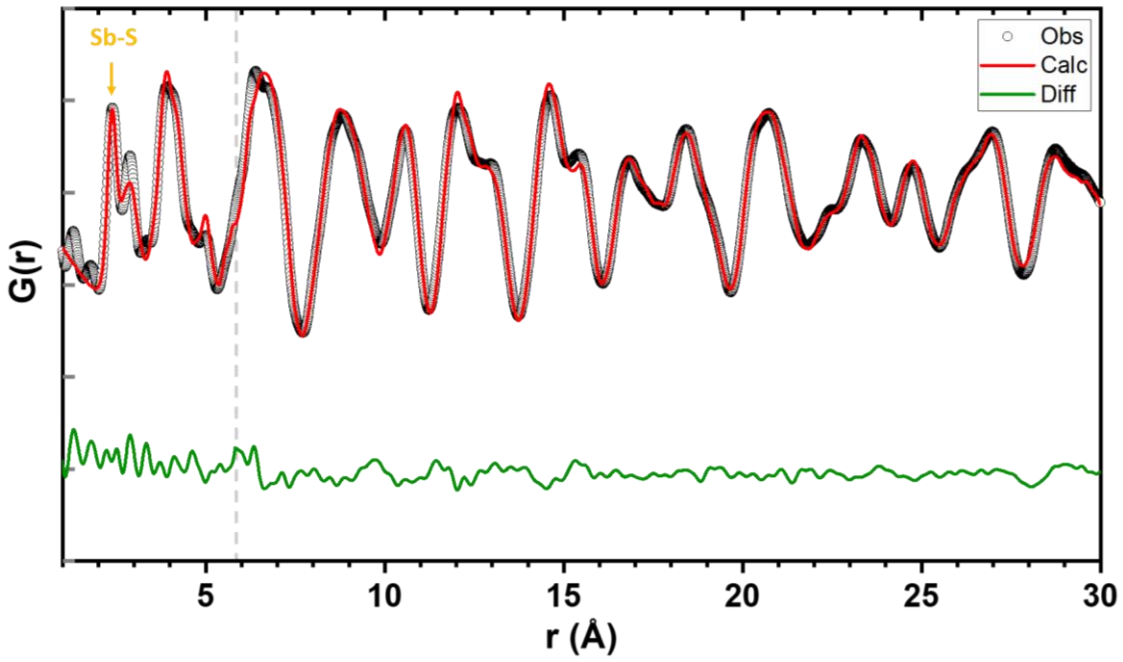

Figure 4.10 Two-phase fit of a [tetragonal Na_3SbS_4 + cubic NaCl] model to G(r) data obtained from ball-milled 1:2 Na_3SbS_4-NaCl sample at 30 °C. The black open circles represent the observed G(r), the red curve represent the model, and the green curve shows the difference between the two.

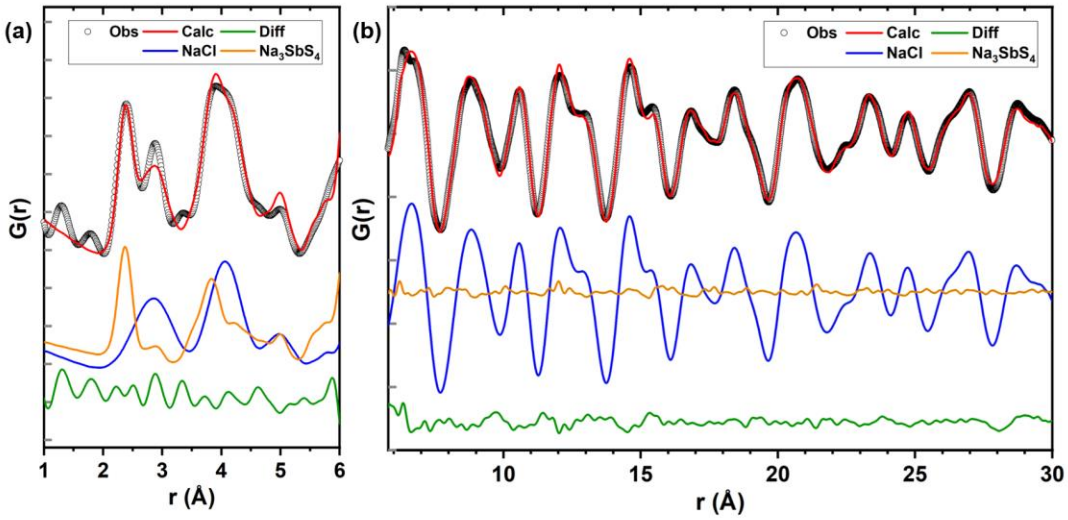

Figure 4.11 Two-phase fit of G(r) data for ball-milled 1:2 Na_3SbS_4-NaCl sample at 30 °C in (a) 1~6 Å and (b) 6~30 Å regions with individual phase plots of NaCl (blue curve) and Na_3SbS_4 (orange curve).

Table 4.1 Refined structural parameters of 1:2 Na_3SbS_4-NaCl mixture sample, obtained from PDF analysis of synchrotron X-ray diffraction data using a two-phase model.

R-space Regions	1~6 Å		6~30 Å	
Phase Models	**Na_3SbS_4**	**NaCl**	**Na_3SbS_4**	**NaCl**
Phase Fraction (mol%)	36.8	63.2	3.2	96.8
Lattice Parameter a (Å)	7.06	5.77	7.21	5.73
Lattice Parameter c (Å)	7.71	= a	7.27	= a
R_w (%)	19.0		14.4	

For the low *r* region of *r* = 1~6 Å, as seen in Figure 4.11(a), the signal at ~2.3 Å is confirmed to belong to the Na_3SbS_4 phase, or specifically from the Sb-S in $[SbS_4]^{3-}$ tetrahedra units. This again verifies the existence of the $[SbS_4]^{3-}$ units after high-energy ball-milling, indicating the strong bonding and high stability of these tetrahedral units. The signal at ~3.9 Å is a combination of both Sb-S in Na_3SbS_4 and Na-Na/Cl-Cl signal in NaCl, which explains its shift to the higher *r* values due to the increasing amount of NaCl in the Na_3SbS_4-NaCl samples with ratios from 1:0, 1:1, to 1:2 in Figure 4.9. The refined phase fraction shown in Table 4.1 is also consistent with the mixing ratio of Na_3SbS_4 and NaCl (1:2). The lattice parameter *a* of NaCl is a bit larger than pure NaCl (5.64 Å), plausibly due to the mixing and milling process with the presence of Na_3SbS_4 that may introduce minor impurities in the structure. The parameters of Na_3SbS_4 also deviate from pure phase (*a* = 7.16 Å, *c* = 7.29 Å [154]), which may be similarly caused by the mixing and milling process or due to the errors caused by limited data points in this refinement range.

For the region of r = 6~30 Å, as shown in Figure 4.11(b), the pattern is mostly identical to the curve based on pure NaCl (blue curve). The refined parameters in Table 4.1 also confirm that the identified signals are based on a high fraction of ~96.8% NaCl and the contribution from Na_3SbS_4 is marginal. This suggests that at the length scale of equivalent to or above the unit cell scale (~7 Å), the mid- to long-range structural periodicity of Na_3SbS_4 has been destructed with the only remaining $[SbS_4]^{3-}$ units intact. A glass-like Na_3SbS_4 phase is formed after ball-milling with NaCl. This conversion is reversible upon annealing and the required temperature is related to the amount of NaCl in the mixture and the ball-milling conditions. Based on the *in situ* XRD and PDF analyses in this study, higher ball-milling energy and more NaCl mixing lead to a higher temperature for the re-crystallization of the Na_3SbS_4 phase.

In addition, Sb L1-edge extended X-ray absorption fine structure (EXAFS) spectroscopy has been employed for the milled Na_3SbS_4 and 1:2 Na_3SbS_4-NaCl mixture samples to confirm the local environment of Sb in the milled samples. The EXAFS data reduction is performed by ATHENA software [186] and the nearest neighbour environment of Sb is reflected in the R space as shown in Figure 4.12. The Sb-S bond distance obtained by EXAFS is 2.32 Å in BM Na_3SbS_4 and 2.28 Å in BM 1:2 Na_3SbS_4-NaCl mixture as summarized in Table 4.2, confirming that the $[SbS_4]^{3-}$ units remain intact in the 1:2 mixture sample and represent the dominant Sb immediate local structure.

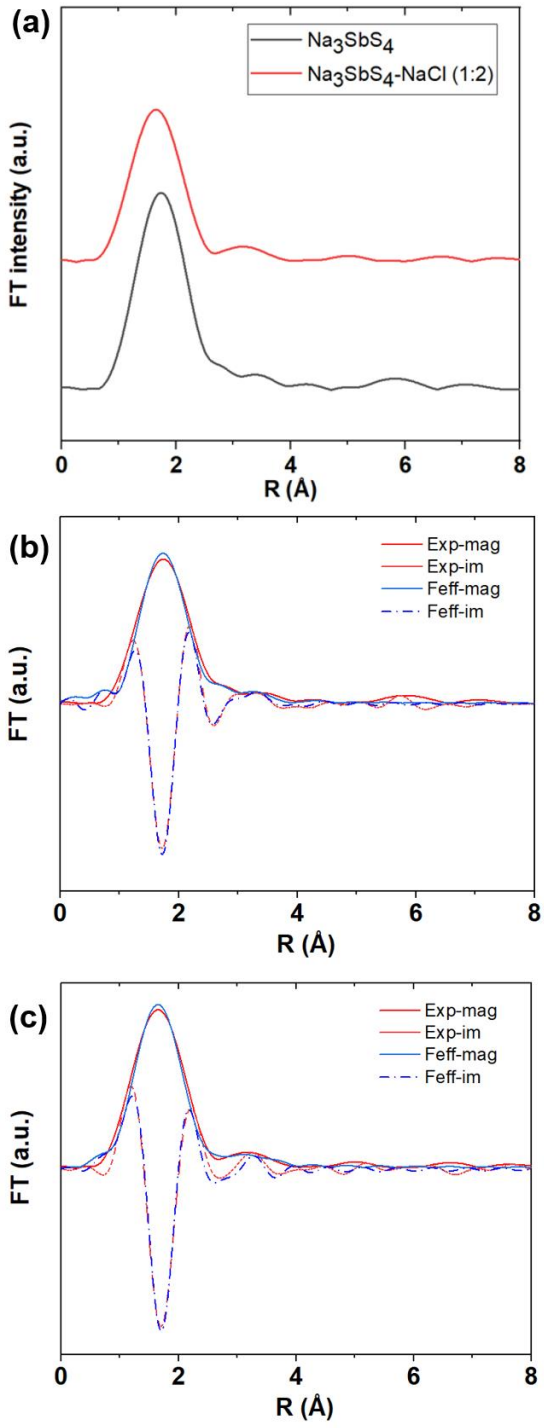

Figure 4.12 (a) Fourier transforms (FT) of Sb L1-edge EXAFS spectra of ball-milled samples. (b-c) Magnitude and imaginary part of FT between the experimental (red solid and red dash traces) and the Feff modeling (blue solid and blue dash traces) of Sb in (b) BM Na_3SbS_4 and (c) BM 1:2-Na_3SbS_4-NaCl, respectively.

Table 4.2 Fitting results from Fig. 4.12 (b-c) using tetragonal Na_3SbS_4 structure model.

	Model to fit		BM Na_3SbS_4		BM Na_3SbS_4-NaCl	
Path	CN	R (Å)	CN	R (Å)	CN	R (Å)
Sb-S	4	2.31	4.1	2.32	4.1	2.28
			k space data range:2.74-8.30 R fitting window: 0.65-4.00		k space data range:2.73-7.95 R fitting window: 0.64-4.0	

4.2.3 Ionic Conduction Analysis

The conduction behavior of the ball-milled samples was characterized with variable temperature (VT) electrochemical impedance spectroscopy (EIS). The results of both milled Na_3SbS_4 and 1:2 Na_3SbS_4-NaCl mixture samples are shown in Figure 4.13. In Figure 4.13(a), the conductivity of BM Na_3SbS_4 at 30 ℃ is ~8.4×10^{-5} S·cm^{-1}, lower than the well-crystallized phase ($0.5 \sim 1 \times 10^{-3}$ S·cm^{-1}) by about one order of magnitude. As the temperatures during measurement increases, the Arrhenius conductivity pattern can be roughly divided into two stages, i.e., below 100 ℃ and above 100 ℃. As indicated by the different slopes in these two regions, the tested samples experienced a transition from a high-activation-energy phase to a lower one. In the cooling process, the conductivity drop follows the same linear pattern as seen in the >100℃ heating range. After cooling to 30 ℃, the conductivity is 4.3×10^{-4} S cm^{-1}, higher than the starting point and is close to the as-synthesized crystalline Na_3SbS_4. The conduction behavior observed in this heating and cooling process shows that the lower crystallinity in Na_3SbS_4 caused by high-energy ball milling leads to a poorer ionic conductivity, possibly due to the lack of long-range

percolated diffusion networks for Na ions. As the long-range structure recovers upon annealing, the conductivity can also be restored.

Similarly, for the 1:2 mixture sample with NaCl, as shown in Figure 4.13(b), the initial ionic conductivity at 30 ℃ is very low, at the level of 10^{-7} $S \cdot cm^{-1}$ at room temperature. Upon heating, there are roughly two jumps of conductivity at around 150℃ and 180℃, which may be related to the transitions observed in the *in situ* XRD at 190℃ and 230℃ in Figure 4.2(a), respectively. The deviation of critical temperatures between *in situ* XRD experiments and EIS measurements is mainly due to the application of high pressure during the latter. After reaching 180℃, the conductivity is close to the value of crystalline Na_3SbS_4 at the same temperature, and the conductivities in the cooling process roughly follow a linear manner with much higher values than in the heating process, confirming the formation of crystalline Na_3SbS_4 with better conduction properties.

The conductivity results of both samples have confirmed the reversible yet negative impact of ball-milling on Na_3SbS_4-containing system with or without the presence of NaCl. The observation is indicative of the structural evolution revealed by *in situ* synchrotron XRD and PDF analyses, which highlights the formation of a glass-like Na_3SbS_4 phase through milling and a recrystallization process during heating. For this particular system, by milling the mixed components, it is difficult, if possible at all, to obtain Cl-doped sulfide compounds or to form distinct structures. Other synthetic approaches or computation-aided composition tuning are needed for new material design purposes. For similar sulfide-based conductors, it is therefore critical to examine the post-milling process conditions, which are usually designed to eliminate the grain boundary or interface resistance, in order to minimize the negative effect on the conduction properties.

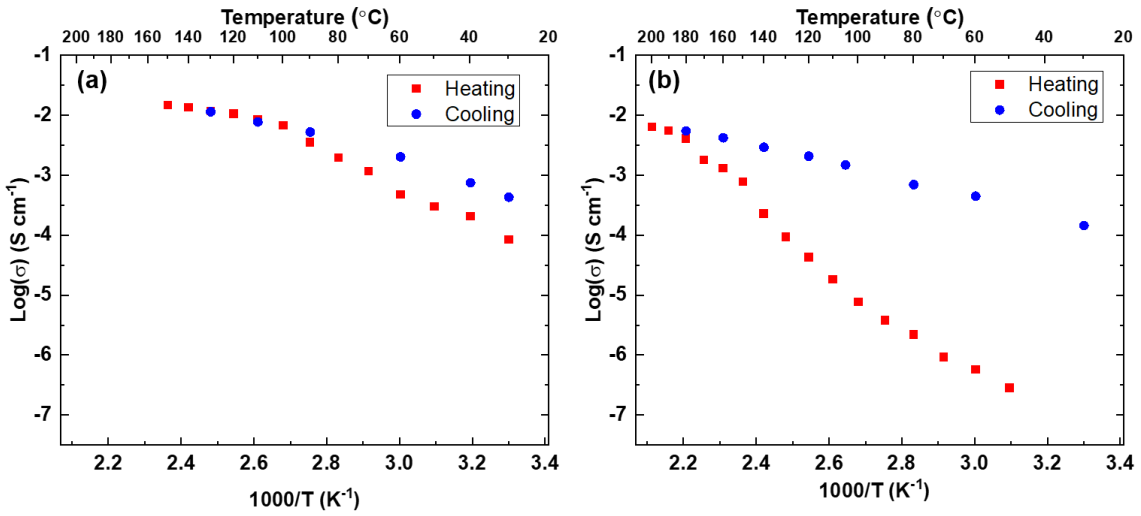

Figure 4.13 Arrhenius conductivity plots of milled (a) Na_3SbS_4 and (b) 1:2 Na_3SbS_4-NaCl mixture samples, respectively.

4.3 Summary

In this study, a systematic investigation using *in situ* X-ray diffraction (XRD) and pair distribution function (PDF) analysis is conducted to elucidate structural evolution of Na_3SbS_4-NaCl mixture samples after high-energy ball milling and during heating process. Milling process has been proved to destruct the long-range crystal structure of Na_3SbS_4 and decrease the Na ion conductivity. The presence of more NaCl in the mixture intensifies this negative impact on conductivities. However, it is confirmed by PDF analysis that the $[SbS_4]^{3-}$ tetrahedral units remain intact despite the disappear of long-range periodicity in XRD results. The milled glass-like phase will recrystallize upon annealing and the conductivity will also be restored. This study highlights the use of PDF analysis to probe and clarify local structural details of sulfide-based mixtures, which is not readily available with conventional crystallographic techniques.

4.4 Methods

4.4.1 Na_3SbS_4-NaCl Sample Preparation

Crystalline Na_3SbS_4 compounds were synthesized by solid-state reaction. Starting materials including Na metal (99.8%, Sigma Aldrich), Sb (99.5%, Alfa Aesar) and S (99.5%, Alfa Aesar) were weighed and mixed with stoichiometric ratio. S was used with 10% excess to compensate the loss during heating. The mixture was loaded into a quartz tube in an Ar-filled glove box, which was then sealed under vacuum. The tube was heated to 650 °C with a 3 °C/min ramp in a box furnace, dwelling for 18 h, and quenched on a copper plate. Then the tube was moved into the glove box and the product powder was obtained through hand grinding with a mortar and a pestle after breaking the tube.

The mixture samples were prepared by mixing and milling the as-synthesized Na_3SbS_4 powder and NaCl (99.5%, Sigma Aldrich) with various molar ratios of 1:0 (no NaCl), 1:1, and 1:2. The powders were loaded into the grinding jars and sealed with parafilm in an Ar-filled glove box to avoid exposure to the air and moisture. Then the mixtures were milled using a Retsch planetary ball mill machine at a speed of 370 rpm for 12 hours and a higher speed of 500 rpm for 16 hours. The milled powder was then collected in the glove box for next-step characterization and measurements.

4.4.2 In situ Synchrotron X-ray Structure Analysis

The samples were investigated in sealed quartz capillaries with synchrotron *in situ* X-ray diffraction at 28-ID-2 at the National Synchrotron Light Source II at Brookhaven National Laboratory. The sealed capillaries were mounted on the sample holder and heated

up to desired temperatures by a spiral heating wire. The real-time temperatures were calibrated with a thermal couple placed at the tip of the capillary. The quartz capillary was spun constantly using an electric motor during the heating process to average the orientations of the powder. During the heating process, high resolution X-ray total scattering data ($\lambda = 0.1901$ Å) for diffraction analysis and pair distribution function (PDF) analysis were collected at various temperatures.

PDF G(r) data were extracted from the raw diffraction data using the PDFgetX2 software [187]. Normalized structure functions S(Q) were obtained and reduced to G(r) through Fourier transform, with a maximum scattering vector (Qmax) of 20 $Å^{-1}$. Structural refinements were carried out using the PDFgui software and Diffpy.SrFit package [185, 188]. For the modeling of experimental PDF in the *r* range of interest, the following parameters were refined: (1) scale factor, (2) fraction or scale of individual phase model if applicable, (3) lattice parameters, (4) atomic coordinates, and (5) atomic isotropic displacement parameters. The R_w indicator was employed to evaluate the fitting quality.

4.4.3 Other Characterizations

Crystal structures of the 370 rpm milled samples were initially analyzed by X-ray diffraction (XRD) with a D8 Advance X-ray Diffractometer (Bruker) equipped with a strip detector and a Molybdenum tube [λ K $\alpha 1 = 0.7093$ Å] in our lab. The powder samples were scanned in sealed capillaries. *In situ* XRD was conducted on various mixture samples using an Anton Paar HTK1200N furnace installed on the D8 Advance diffractometer. The temperature profile includes a ramping process (30°C/min) from room temperature to

270 °C with multiple intermediate temperature holding steps for XRD patterns collection. After being held at 270°C for 3 hours, the chamber was cooled down to room temperature.

Sb L1-edge EXAFS spectra were collected from the solid mixture samples in fluorescence mode using a PIPS detector at beamline 14-3 at the Stanford Synchrotron Radiation Light source (SSRL), Menlo Park, CA. To avoid air exposure, the solids were scattered evenly on the adhesive side of Sb-free Kapton tapes and sealed using the Kapton tapes in an anaerobic chamber. During the whole data collection period, the sample chamber was kept under He atmosphere at room temperature. The chemical of calcium acetate was used for energy calibration. Athena was used for energy calibration, raw spectra average, post-edge normalization, and background removal.

4.4.4 Electrochemical Impedance Spectroscopy

AC impedance measurements were conducted using a Bio-Logic VMP3 impedance analyzer in the frequency range from 1 MHz to 0.5 Hz with a voltage amplitude of 100 mV. The pellets for the measurements were cold-pressed from as-synthesized powders at 100 MPa pressure in an acrylic tube with an inner diameter of 0.5 inch. Two stainless-steel rods were used as blocking electrodes. Temperature-dependent conductivity measurements were performed from room temperature to 160 ~ 200 °C using a heatable pressing die with a temperature controller.

4.5 References

[5] Kato, Y., S. Hori, T. Saito, K. Suzuki, M. Hirayama, A. Mitsui, M. Yonemura, H. Iba, and R. Kanno, *High-power all-solid-state batteries using sulfide superionic conductors.* Nature Energy, 2016. **1**(4): p. 16030.

[58] Boulineau, S., M. Courty, J.-M. Tarascon, and V. Viallet, *Mechanochemical synthesis of Li-argyrodite Li_6PS_5X (X=Cl, Br, I) as sulfur-based solid electrolytes for all solid state batteries application.* Solid State Ionics, 2012. **221**: p. 1-5.

[81] Zhang, L., K. Yang, J. Mi, L. Lu, L. Zhao, L. Wang, Y. Li, and H. Zeng, *Na_3PSe_4: A Novel Chalcogenide Solid Electrolyte with High Ionic Conductivity.* Advanced Energy Materials, 2015. **5**(24): p. 1501294.

[90] Xiong, S., Z. Liu, H. Rong, H. Wang, M. McDaniel, and H. Chen, *$Na_3SbSe_{4-x}S_x$ as Sodium Superionic Conductors.* Scientific Reports, 2018. **8**(1): p. 9146.

[100] Krauskopf, T., S.P. Culver, and W.G. Zeier, *Local Tetragonal Structure of the Cubic Superionic Conductor Na_3PS_4.* Inorganic Chemistry, 2018. **57**(8): p. 4739-4744.

[150] Hayashi, A., K. Noi, A. Sakuda, and M. Tatsumisago, *Superionic glass-ceramic electrolytes for room-temperature rechargeable sodium batteries.* Nat Commun, 2012. **3**: p. 856.

[152] Chu, I.-H., C.S. Kompella, H. Nguyen, Z. Zhu, S. Hy, Z. Deng, Y.S. Meng, and S.P. Ong, *Room-Temperature All-solid-state Rechargeable Sodium-ion Batteries with a Cl-doped Na_3PS_4 Superionic Conductor.* Scientific Reports, 2016. **6**(1): p. 33733.

[154] Wang, H., Y. Chen, Z.D. Hood, G. Sahu, A.S. Pandian, J.K. Keum, K. An, and C. Liang, *An Air-Stable Na_3SbS_4 Superionic Conductor Prepared by a Rapid and Economic Synthetic Procedure.* Angew Chem Int Ed Engl, 2016. **55**(30): p. 8551-5.

[155] Banerjee, A., K.H. Park, J.W. Heo, Y.J. Nam, C.K. Moon, S.M. Oh, S.T. Hong, and Y.S. Jung, *Na_3SbS_4 : A Solution Processable Sodium Superionic Conductor for All-Solid-State Sodium-Ion Batteries.* Angew Chem Int Ed Engl, 2016. **55**(33): p. 9634-8.

[165] Kim, S.K., A. Mao, S. Sen, and S. Kim, *Fast Na-Ion Conduction in a Chalcogenide Glass–Ceramic in the Ternary System $Na_2Se–Ga_2Se_3–GeSe_2$.* Chemistry of Materials, 2014. **26**(19): p. 5695-5699.

[166] Yamanaka, T., A. Hayashi, A. Yamauchi, and M. Tatsumisago, *Preparation of magnesium ion conducting $MgS–P_2S_5–MgI_2$ glasses by a mechanochemical technique.* Solid State Ionics, 2014. **262**: p. 601-603.

[167] Canepa, P., et al., *High magnesium mobility in ternary spinel chalcogenides.* Nature Communications, 2017. **8**(1): p. 1759.

[168] Minami, K., A. Hayashi, and M. Tatsumisago, *Crystallization Process for Superionic $Li_7P_3S_{11}$ Glass-Ceramic Electrolytes.* Journal of the American Ceramic Society, 2011. **94**(6): p. 1779-1783.

[169] Hayashi, A., K. Minami, F. Mizuno, and M. Tatsumisago, *Formation of Li^+ superionic crystals from the Li_2S–P_2S_5 melt-quenched glasses.* Journal of Materials Science, 2008. **43**(6): p. 1885-1889.

[170] Ramos, E.P., Z. Zhang, A. Assoud, K. Kaup, F. Lalère, and L.F. Nazar, *Correlating Ion Mobility and Single Crystal Structure in Sodium-Ion Chalcogenide-Based Solid State Fast Ion Conductors: $Na_{11}Sn_2PnS_{12}$ (Pn = Sb, P).* Chemistry of Materials, 2018. **30**(21): p. 7413-7417.

[171] Fukushima, A., A. Hayashi, H. Yamamura, and M. Tatsumisago, *Mechanochemical synthesis of high lithium ion conducting solid electrolytes in a Li_2S-P_2S_5-Li_3N system.* Solid State Ionics, 2017. **304**: p. 85-89.

[172] Tarascon, J.-M., M. Morcrette, J. Saint, L. Aymard, and R. Janot, *On the benefits of ball milling within the field of rechargeable Li-based batteries.* Comptes Rendus Chimie, 2005. **8**(1): p. 17-26.

[173] Rao, R.P., X. Zhang, K.C. Phuah, and S. Adams, *Mechanochemical synthesis of fast sodium ion conductor $Na_{11}Sn_2PSe_{12}$ enables first sodium–selenium all-solid-state battery.* Journal of Materials Chemistry A, 2019. **7**(36): p. 20790-20798.

[174] Rangasamy, E., Z. Liu, M. Gobet, K. Pilar, G. Sahu, W. Zhou, H. Wu, S. Greenbaum, and C. Liang, *An Iodide-Based $Li_7P_2S_8I$ Superionic Conductor*. Journal of the American Chemical Society, 2015. **137**(4): p. 1384-1387.

[175] Sedlmaier, S.J., S. Indris, C. Dietrich, M. Yavuz, C. Dräger, F. von Seggern, H. Sommer, and J. Janek, *Li_4PS_4I: A Li^+ Superionic Conductor Synthesized by a Solvent-Based Soft Chemistry Approach.* Chemistry of Materials, 2017. **29**(4): p. 1830-1835.

[176] Ujiie, S., A. Hayashi, and M. Tatsumisago, *Structure, ionic conductivity and electrochemical stability of Li_2S–P_2S_5–LiI glass and glass–ceramic electrolytes.* Solid State Ionics, 2012. **211**: p. 42-45.

[177] Wang, X., S. Tan, X.-Q. Yang, and E. Hu, *Pair distribution function analysis: Fundamentals and application to battery materials.* Chinese Physics B, 2020. **29**(2): p. 028802.

[178] Billinge, S.J.L., *The rise of the X-ray atomic pair distribution function method: a series of fortunate events.* Philosophical Transactions of the Royal Society A: Mathematical, Physical and Engineering Sciences, 2019. **377**(2147): p. 20180413.

[179] Shiotani, S., K. Ohara, H. Tsukasaki, S. Mori, and R. Kanno, *Pair distribution function analysis of sulfide glassy electrolytes for all-solid-state batteries: Understanding the improvement of ionic conductivity under annealing condition.* Scientific Reports, 2017. **7**(1): p. 6972.

[180] Dong, B., M.P. Stockham, P.A. Chater, and P.R. Slater, *X-ray pair distribution function analysis and electrical and electrochemical properties of cerium doped $Li_5La_3Nb_2O_{12}$ garnet solid-state electrolyte.* Dalton Transactions, 2020. **49**(33): p. 11727-11735.

[181] Tanibata, N., K. Noi, A. Hayashi, and M. Tatsumisago, *Preparation and characterization of highly sodium ion conducting Na_3PS_4–Na_4SiS_4 solid electrolytes.* RSC Adv., 2014. **4**(33): p. 17120-17123.

[182] Hibi, Y., N. Tanibata, A. Hayashi, and M. Tatsumisago, *Preparation of sodium ion conducting Na_3PS_4–NaI glasses by a mechanochemical technique.* Solid State Ionics, 2015. **270**: p. 6-9.

[183] Dietrich, C., et al., *Local Structural Investigations, Defect Formation, and Ionic Conductivity of the Lithium Ionic Conductor $Li_4P_2S_6$.* Chemistry of Materials, 2016. **28**(23): p. 8764-8773.

[184] Dietrich, C., D.A. Weber, S.J. Sedlmaier, S. Indris, S.P. Culver, D. Walter, J. Janek, and W.G. Zeier, *Lithium ion conductivity in Li_2S–P_2S_5 glasses – building units and local structure evolution during the crystallization of superionic conductors Li_3PS_4, $Li_7P_3S_{11}$ and $Li_4P_2S_7$.* Journal of Materials Chemistry A, 2017. **5**(34): p. 18111-18119.

[185] Juhás, P., C.L. Farrow, X. Yang, K.R. Knox, and S.J. Billinge, *Complex modeling: a strategy and software program for combining multiple information sources to solve ill posed structure and nanostructure inverse problems.* Acta Crystallographica Section A, 2015. **71**(6): p. 562-568.

[186] Ravel, B. and M. Newville, *ATHENA, ARTEMIS, HEPHAESTUS: data analysis for X-ray absorption spectroscopy using IFEFFIT.* Journal of Synchrotron Radiation, 2005. **12**(4): p. 537-541.

[187] Qiu, X., J.W. Thompson, and S.J. Billinge, *PDFgetX2: a GUI-driven program to obtain the pair distribution function from X-ray powder diffraction data.* Journal of Applied Crystallography, 2004. **37**(4): p. 678-678.

[188] Farrow, C.L., P. Juhas, J.W. Liu, D. Bryndin, E.S. Božin, J. Bloch, T. Proffen, and S.J.L. Billinge, *PDFfit2 and PDFgui: computer programs for studying nanostructure in crystals.* Journal of Physics: Condensed Matter, 2007. **19**(33): p. 335219.

CHAPTER 5. ALIO-VALENT ANION AND CATION SUBSTITUTION OF Na_4SnS_4 AS SODIUM SUPERIONIC CONDUCTORS

5.1 Introduction

As the global demand for clean and renewable energy sources such as solar and wind increases rapidly, reliable and low-cost electricity storage solutions are critically important to stabilize the power input from these intermittent sources. As a promising alternative to conventional Li-ion batteries (LIBs), Na-ion batteries (NIBs) are attracting great attentions for grid-level storage applications, benefiting from the high natural abundance and low cost of sodium compared to lithium [96, 139, 142, 145]. Recently, fast growing research efforts are focused on the development of all-solid-state NIBs (ASNBs), which further improve the safety by using nonflammable solid electrolyte to replace conventionally used flammable liquid electrolyte as a safer and cost-effective energy storage technology.

As the key enabler of ASNBs, suitable solid electrolyte (SE) materials with sufficiently high Na ionic conductivity at room temperature (r.t.) are highly desired yet challenging to develop. Among the known types of solid electrolytes, sulfides-based compounds show great promises in terms of high ionic conductivity, low grain boundary resistance, low synthesis and processing temperatures, and favorable mechanical properties. Sulfides are also feasible for facile fabrication of all-solid-state full cells, as demonstrated by the good performances of solid state LIBs with sulfide electrolytes, such

as $Li_{10}GeP_2S_{12}$ [54], $Li_7P_3S_{11}$ [111], Li_6PS_5X (X=Cl, Br, I) [57, 159], and $Li_{9.54}Si_{1.74}P_{1.44}S_{11.7}Cl_{0.3}$ [5]. Recently, progresses have been reported in developing sulfide-based Na ion conductors with high conductivities exceeding 0.1 $mS \cdot cm^{-1}$. The discovery of cubic-Na_3PS_4 [150] with a r.t. conductivity of 0.2 $mS \cdot cm^{-1}$ stimulated the development of several new compounds based on this structure through iso- and alio-valent doping. Specifically, iso-valent substitutions of P^{5+} and S^{2-} led to the discovery of Na_3SbS_4 [154, 155, 163], $Na_3P_{1-x}As_xS_4$ [80], $Na_3PS_xSe_{4-x}$ [89], and $Na_3SbS_xSe_{4-x}$ [90], many of which exhibit conductivities up to 0.1 ~ 1 $mS \cdot cm^{-1}$. While these iso-valent substitutions can effectively improve ionic conductivities by tuning the size and polarizability of the unit cell, aliovalent substitutions can further tune the crystal structure and enhance conductivity by introducing Na defects, such as interstitial sites and vacancies, as seen in the substitution of P^{5+} with Si^{4+} [181] and S^{2-} with Cl^- [152]. All the above-mentioned highly conductive candidates are obtained through structural tuning based on Na_3PS_4, while less investigations were conducted on design and development around other parent compounds such as Na_4SnS_4 with the similar anion framework but different cation occupancy.

Na_4SnS_4 possesses the same space group as Na_3SbS_4 with the similar structural units of $[SnS_4]^{4-}$ tetrahedra to $[SbS_4]^{3-}$ but exhibits a much lower Na ionic conductivity (~10^{-8} $mS \cdot cm^{-1}$). As shown in Figure 5.1, the structure of Na_4SnS_4 is similar to Na_3SbS_4 in the sense that they both consist of *bcc*-like (Sn/Sb)S4 polyanion framework. The details of their crystal structures are listed in Table 5.1, which suggest that the Na distribution in two compounds are different. There are two Na sites (2a, 4d) in Na_3SbS_4 that form the Na^+ transport tunnels by alternatively arranged NaS6 and NaS8 polyhedra with shared faces [154]. In comparison, there are only one fully occupied Na site (8e) in Na_4SnS_4 [189],

forming distorted NaS5 polyhedra with shared edges, which lacks well connected diffusion pathways for fast ion transport. The lack of vacancies in Na_4SnS_4 is also a key distinction from Na_3SbS_4 which has a direct impact on its ionic conduction. The concentration of Na vacancy is regarded as one of the critical factors to facilitate high conductivity in Na_3SbS_4 [163] and several other Na conductors [190-193].

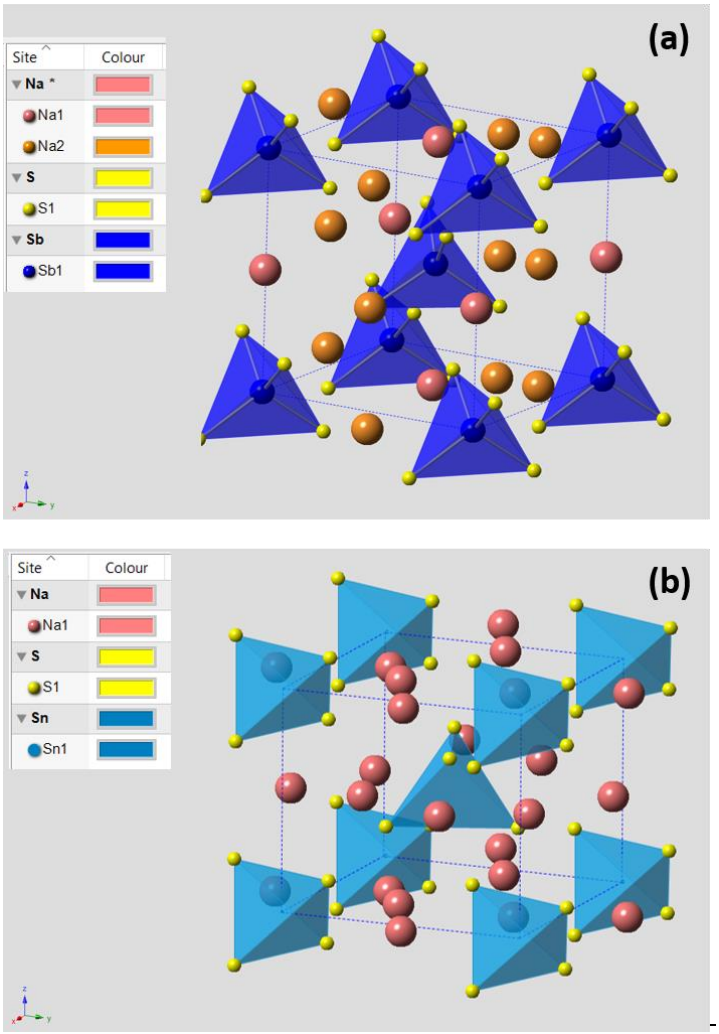

Figure 5.1 Crystal structure of (a) Na_3SbS_4 and (b) Na_4SnS_4. $[SbS_4]^{3-}$ and $[SnS_4]^{4-}$ units are shown in dark blue and light blue, respectively.

Table 5.1 Lattice parameters of Na_4SnS_4 and Na_3SbS_4.

Formula	a=b (Å)	c (Å)	α, β, γ	Cell volume ($Å^3$)	Site	Wyckoff Symbol	x	y	z	Occ.
Na_4SnS_4	7.837	6.940	90	426.9	Na1	8e	0.0910	0.3003	0.4687	1
					Sn1	2a	0	0	0	1
					S1	8e	0.2376	0.0922	0.1883	1
Na_3SbS_4	7.157	7.287	90	373.3	Na1	4d	0	0.5	0.4365	1
					Na2	2a	0	0	0	0.96
					Sb1	2b	0	0	0.5	1
					S1	8e	0.2876	0.3269	0.1817	1

It is then fundamentally interesting to explore when more vacancies are introduced into the crystal structure of Na_4SnS_4 through aliovalent substitution, whether or not higher conductivities can be achieved and rationally tuned. Very recently, by substituting Sn^{4+} with Sb^{5+} and P^{5+}, $Na_{11}Sn_2PS_{12}$ [191, 194] and $Na_{11}Sn_2SbS_{12}$ [170] have been discovered to exhibit a distinct crystal structure with Na vacancies and show fast Na ionic conduction, further demonstrated the high promise of this group of compounds.

In this study, we systematically designed and synthesized a series of Na superionic conductors through aliovalent-doping of Na_4SnS_4 in order to explore the phase diagram and elucidate the roles of Na vacancy and anion framework in the tuning of Na-ion conduction. Specifically, cation doping of Sn^{4+} by P^{5+}/Sb^{5+} and anion doping of S^{2-} by Cl^- /Br^- was attempted and a new crystal structure was identified with enhanced conductivities despite the presence of impurities. Co-doping with both cation-(P^{5+}, Sb^{5+}) and anion-(Cl^-,

Br^-) dopants was also conducted and the obtained compounds show even higher purity and greatly improved conductivity by 4 orders of magnitude higher than that of original Na_4SnS_4. In-depth crystal structure characterizations reveal the role of Na vacancies and confirmed the effectiveness of the design strategy, as elaborated as follows.

5.2 Results and Discussion

5.2.1 Synthesis of aliovalent doped Na_4SnS_4

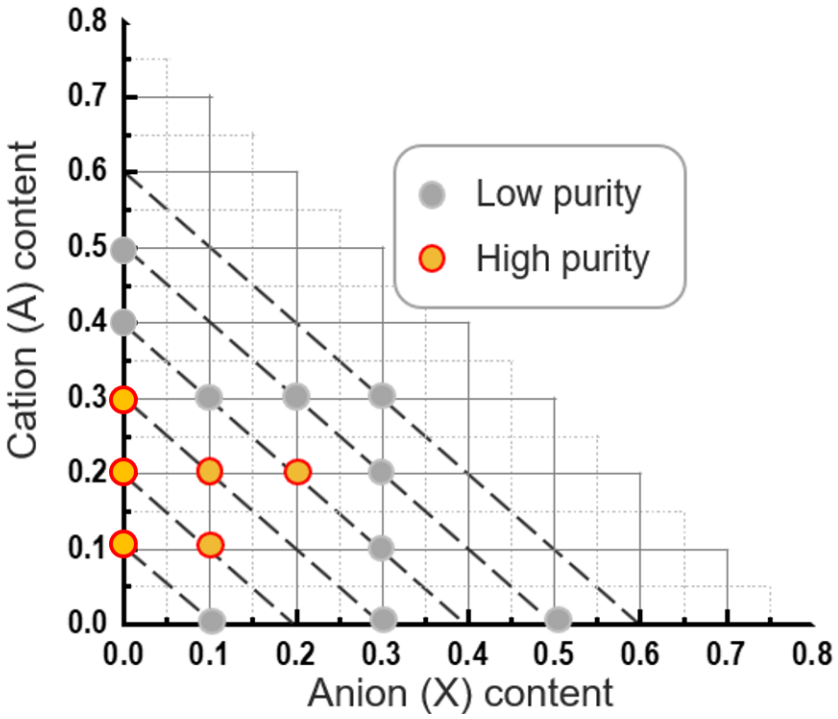

Figure 5.2 Composition diagram of synthesized aliovalent doped Na_4SnS_4 (or $Na_{4-x-y}Sn_{1-x}A_xS_{4-y}X_y$, A=$P^{5+}$/$Sb^{5+}$, X=$Cl^-$/$Br^-$).

A series of aliovalent doped Na_4SnS_4 samples, denoted as $Na_{4-x-y}Sn_{1-x}A_xS_{4-y}X_y$ (A=P^{5+} or Sb^{5+}, X=Cl^- or Br^-), were synthesized via solid state reaction. Their compositions

are described in a diagram with respect to the type and amount of dopants as shown in Figure 5.2, where the *x*-axis indicates the doping amount of anion (X = Cl^- or Br^-) and the *y*-axis shows the amount of cation (A = P^{5+}or Sb^{5+}).

5.2.1.1 Cation doping with Sb^{5+}

To introduce Sb^{5+} on the Sn^{4+} sites in Na_4SnS_4, precursors of both Na_4SnS_4 and Na_3SbS_4 are synthesized first. Then the following reaction is designed to dope *x* amount of Sb^{5+} ($0 < x < 1$) into Na_4SnS_4:

$$(1\text{-}x)\ Na_4SnS_4 + x\ Na_3SbS_4 \rightarrow Na_{4-x}Sn_{1-x}Sb_xS_4$$

In situ XRD is conducted to investigate the reaction process and the formation temperature of the doped products. An example of *in situ* XRD for the formation of $Na_{3.8}Sn_{0.8}Sb_{0.2}S_4$ (x=0.2) is shown in Figure 5.3. During the heating process from 50 ℃ to 400 ℃, peaks of Na_4SnS_4, the major phase in starting materials, can be observed and the intensities decrease as the temperature elevates, indicating Na_4SnS_4 is consumed in the reaction. Meanwhile, a new set of peaks show up during heating, which is different from either Na_4SnS_4 or Na_3SbS_4. Upon reaching 450℃, there is no peak detected from any starting materials. Instead, the crystallinity of the new set of peaks increases and the phase remains stable up to 500℃ and after cooling down to room temperature. A new structure different from the two starting materials formed during the reaction, indicating the doping of Sb^{5+} has effectively tuned or changed the crystal structure of Na_4SnS_4.

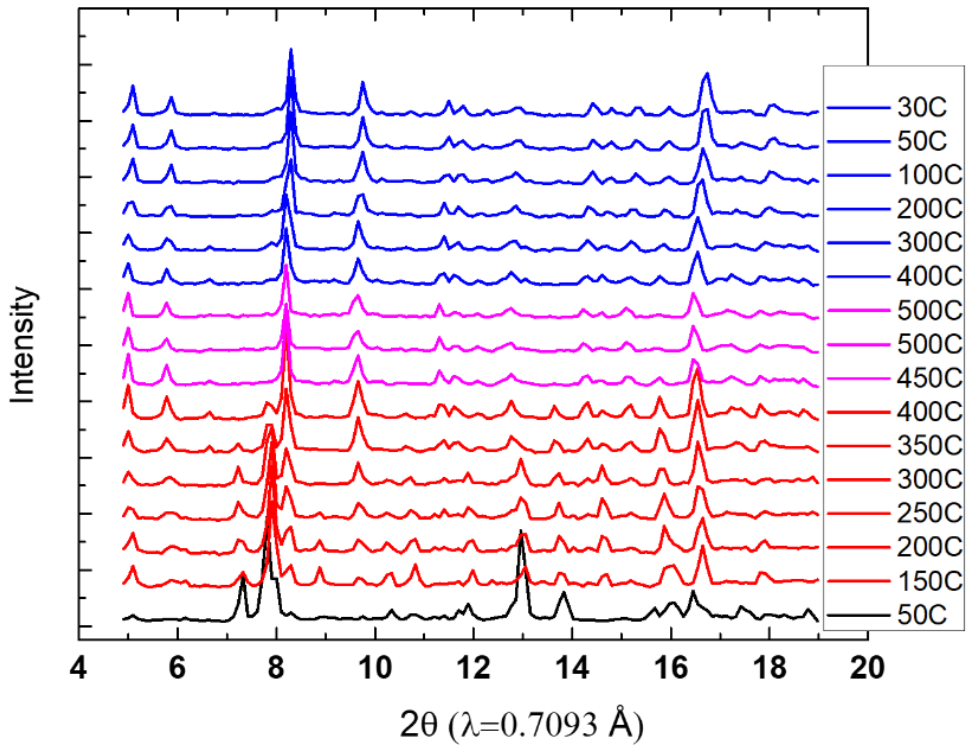

Figure 5.3 *In situ* XRD during the heating and cooling process of $Na_{3.8}Sn_{0.8}Sb_{0.2}S_4$ (a mixture of $0.8Na_4SnS_4 + 0.2Na_3SbS_4$).

Similar phenomenon of structural variation is observed in multiple combinations of starting material with different doping levels (x = 0.1, 0.2, 0.33, 0.4, 0.5, 0.67, 0.7, 0.8, and 0.9). XRD patterns of the final products in all these attempted doping levels are shown in Figure 5.4. From top to bottom, the doping level changes from x=0 (pure Na_4SnS_4) to x=1.0 (pure Na_3SbS_4), with two starting material included in the series. With lower amount of Sb^{5+} doping (x = 0.1, 0.2, 0.33), the same set of diffraction peaks of the new structure (reaction product) were observed without obvious impurities, whereas with higher amount of Sb^{5+} (x = 0.4, 0.5, …, 0.9), a mixture of the reaction product and Na_3SbS_4 was identified, indicating certain amounts of Sb^{5+} from starting material is left without doping into the structure. Therefore, under current synthesis method, the limit of Sb^{5+} doping in the

Na_4SnS_4 structure is roughly $0.1 \leq x \leq 0.33$ or $0 < x < 0.4$. A distinct crystal structure is formed with Sb^{5+} doping, as labeled by the triangles in Figure 5.4. This structure is very similar to the Na ion conductor $Na_{11}Sn_2PS_{12}$, which has a similar composition with P^{5+} being used instead of Sb^{5+}. The crystal structure is then identified to have the same space group of $Na_{11}Sn_2PS_{12}$, namely $I4_1/acd$. The crystal structure associated with the synthesized compounds is shown in Figure 5.5, which is consistent to the reported structure of $Na_{11}Sn_2SbS_{12}$ [170]. Both SbS_4^{3-} and SnS_4^{4-} tetrahedrons from the starting materials are also present in the doped products. The arrangement of these tetrahedrons plays critical roles in the Na ion conduction as analyzed in the comparison of Na_3SbS_4 and Na_4SnS_4.

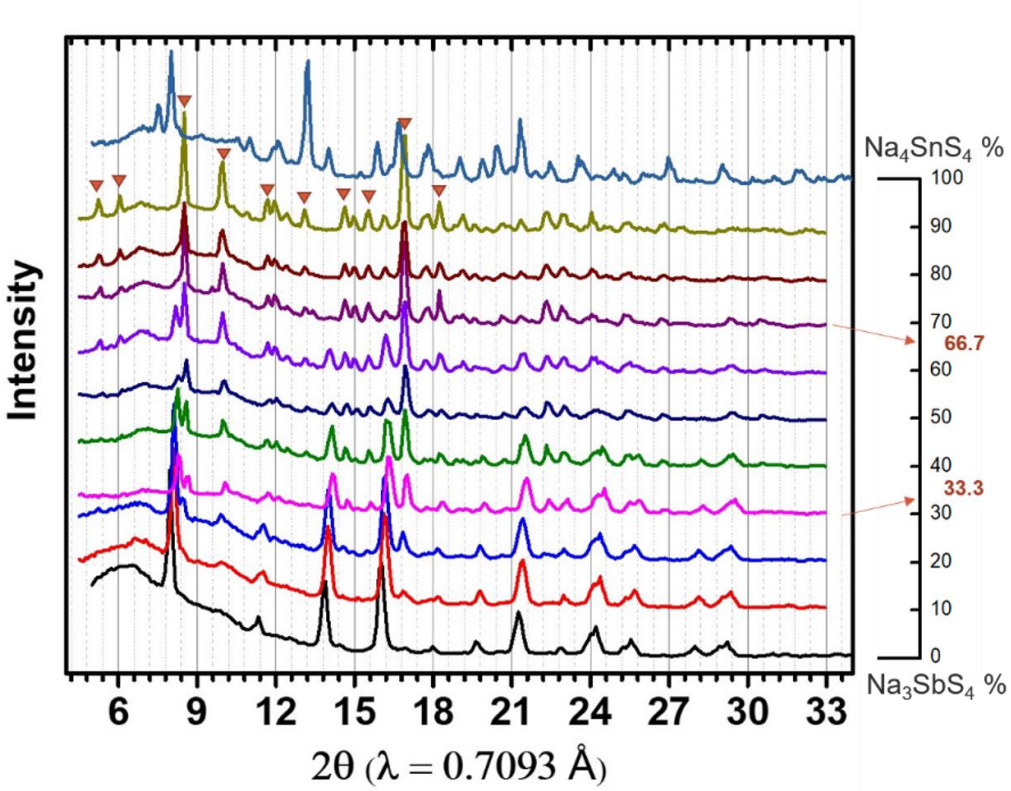

Figure 5.4 XRD patterns of $Na_{4-x}Sn_{1-x}Sb_xS_4$ series ($0 \leq x \leq 1$), the triangles labeling diffraction peaks of the products with a different crystal structure from the starting materials.

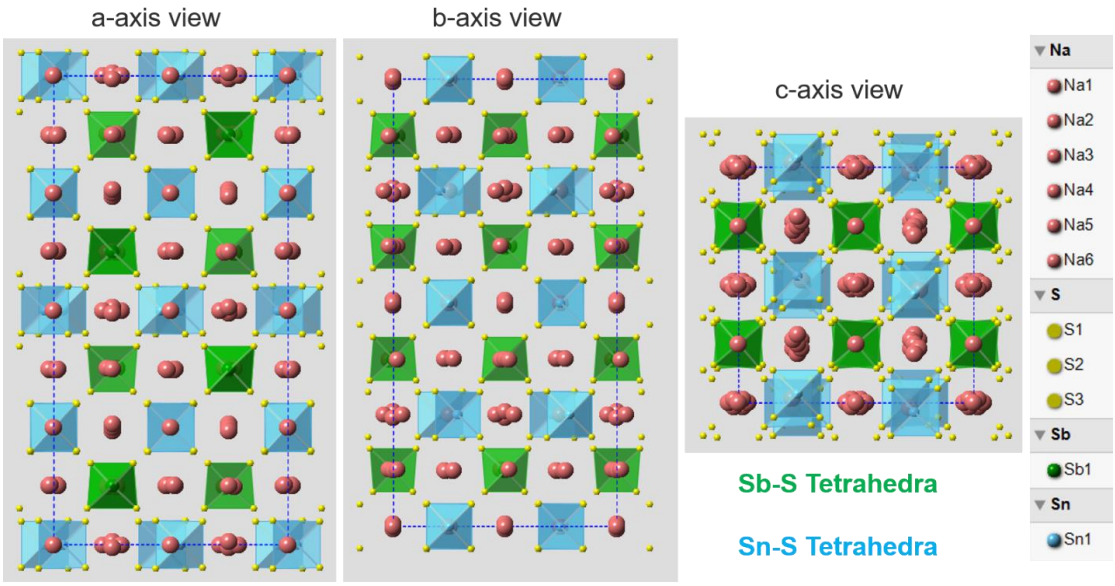

Figure 5.5 Crystal structure of $Na_{4-x}Sn_{1-x}Sb_xS_4$ ($0.1 \leq x \leq 0.33$) in various views.

5.2.1.2 Anion doping with halogen

Anion-doping to substitute S^{2-} by Cl^- or Br^- with *x* ranging from 0.1 to 0.5 were attempted, as shown in Figure 5.2, which by design should create *x* amount of Na vacancies in the lattice due to the lower valence of Cl^-/Br^- than S^{2-}. Specifically, the following reaction is designed to dope x amount of X^- (X=Cl, Br, I, $0 < x < 4$) into Na_4SnS_4:

$$(2\text{-}x)\ Na_2S + SnS_2 + x\ NaX \rightarrow Na_{4-x}SnS_{4-x}X_x$$

As shown in XRD patterns of three anion-doped (A = 0) compounds in Figure 5.6, with Cl^- = 0.5, Br^- = 0.5, or I^- = 0.5, a new phase distinct from the starting materials and Na_4SnS_4 was formed and identified to be in $I4_1/acd$ space group. However, the products showed significant amount of unknown impurities. Similarly, other anion-doped compounds, with various amount of Cl^- and Br^- dopants (x = 0.1, 0.3), all exhibited low

purity despite various synthesis temperatures attempted. Due to poorer crystallinity and purity, I-doped samples show less promising ionic conductivity and will not be elaborated in the following discussions.

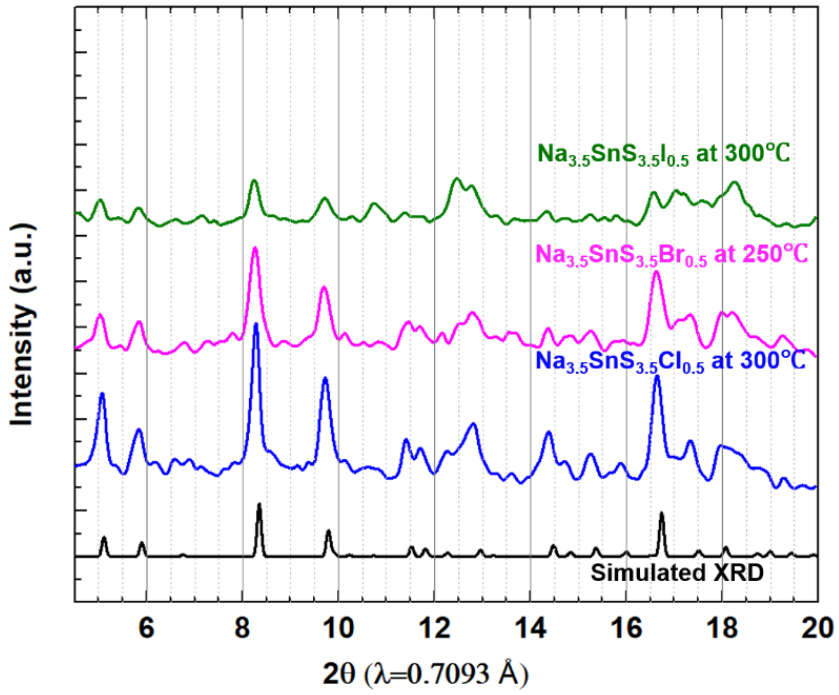

Figure 5.6 XRD patterns of $Na_{3.5}SnS_{3.5}X_{0.5}$ (X=Cl, Br, I) compared with simulated XRD pattern with a *I*4$_1$/*acd* space group.

In order to explore the thermodynamics and kinetics of the reaction, *in situ* XRD was performed by heating up and cooling down the ball-milled precursors in an Anton Paar HTK1200N furnace mounted in the X-ray diffractometer. The *in situ* XRD patterns of $Na_{3.5}SnS_{3.5}Br_{0.5}$ ball-milled precursor are shown as an example in Figure 5.7. A new set of diffraction peaks distinct from the starting materials (Na_2S, Sn_2S_3, and S) and Na_4SnS_4 shows up at 250 °C. Upon further heating to 350 °C, additional peaks that belong to a $Na_6Sn_2S_7$-like phase were detected and remained in the products through the following

cooling process. This suggests the new phase appearing at 250 °C is metastable and partially decomposes at higher temperatures. Similar phenomenon was also observed in multiple *in situ* XRD experiments with different types and amounts of halogen as shown in Table 5.2. Therefore, low-temperature calcination at 300°C was applied for anion-doped Na_4SnS_4 to suppress the decomposition of products and the formation of impurities. However, impurities are still formed in all anion-doped samples despite the adjusted heating conditions as seen from their XRD patterns in Figure 5.8.

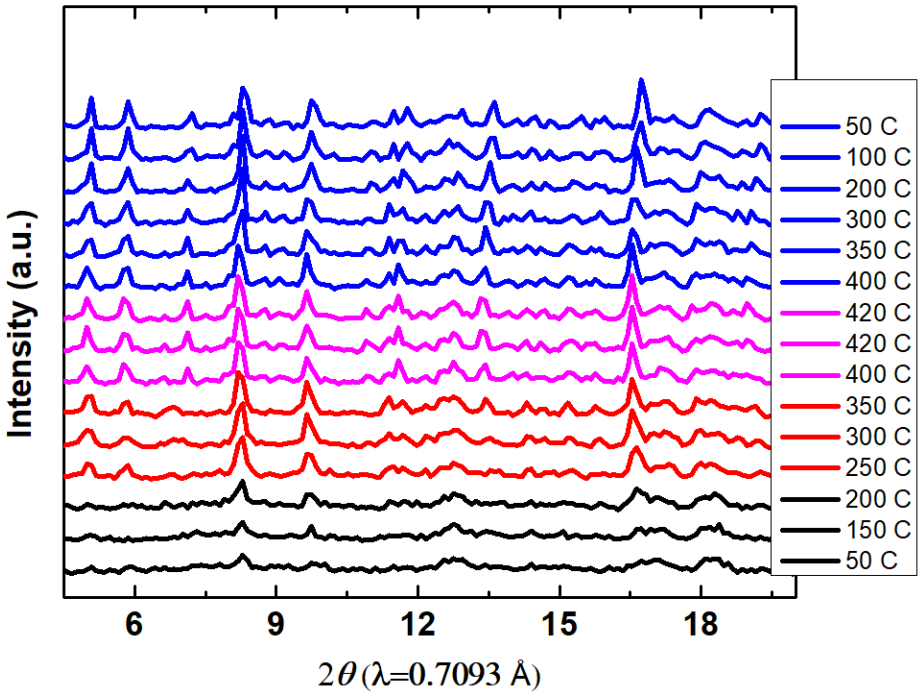

Figure 5.7 *In situ* XRD patterns during the heating and cooling process of $Na_{3.5}SnS_{3.5}Br_{0.5}$ ball-milled precursor (X=Br, x=0.5).

Table 5.2 Summary of *in situ* XRD experiments for $Na_{4-x}SnS_{4-x}X_x$ system ($X=Cl^-$, Br^-, I^-).

$Na_{4-x}SnS_{4-x}X_x$	Value of x	Highest heating temperature and duration	Temperature range for stable product
$Na_{4-x}SnS_{4-x}Cl_x$	0.1	550 °C 3h	400 °C ~ 450 °C
		420 °C 3h	Up to 420 °C
	0.5	450 °C 3h	250 °C ~350 °C
$Na_{4-x}SnS_{4-x}Br_x$	0.1	600 °C 3h	N/A
	0.5	600 °C 3h	250 °C ~400 °C
		420 °C 3h	250 °C ~350 °C
$Na_{4-x}SnS_{4-x}I_x$	0.1	550 °C 3h	N/A
	0.5	550 °C 3h	250 °C ~300 °C

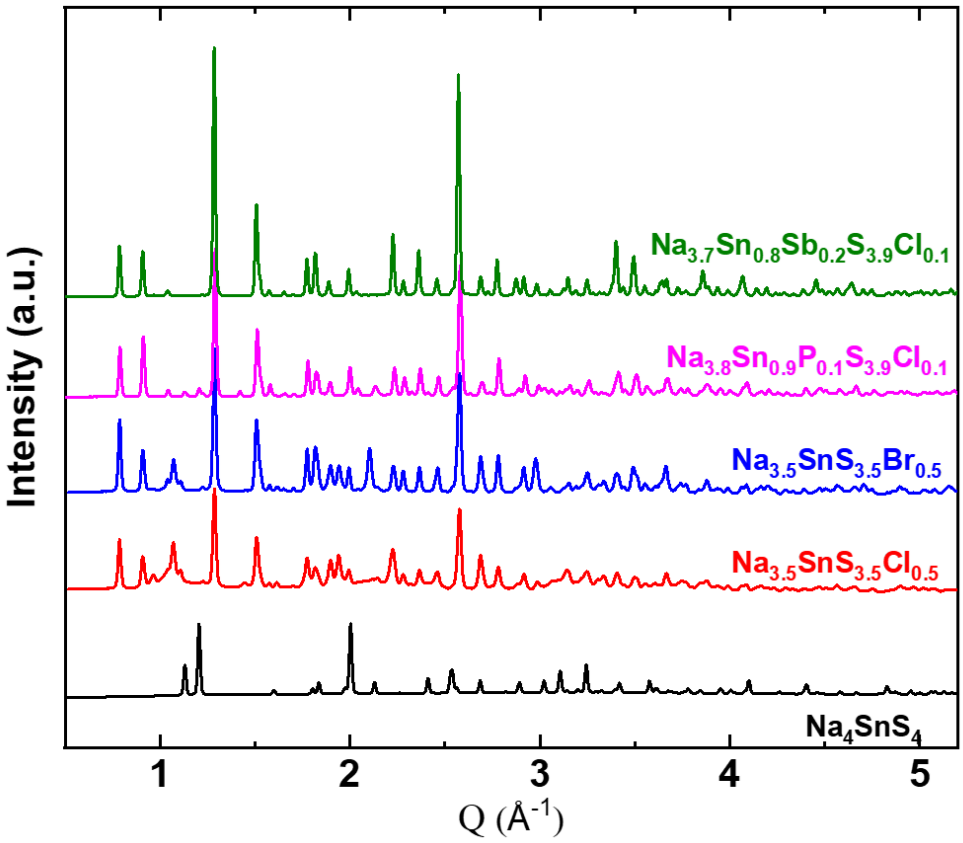

Figure 5.8 Synchrotron X-ray diffraction patterns of undoped- and aliovalent doped-Na_4SnS_4 samples.

5.2.1.3 Co-doping with cation (P^{5+}, Sb^{5+}) and anion (Cl^-, Br^-)

Cation-doping with A=P^{5+}/Sb^{5+} is then applied on top of anion-doping to create more Na vacancies and to stabilize the crystal structure. As an example, the following reaction is designed to dope *x* amount of X^- and *y* amount of Sb^{5+} into Na_4SnS_4:

$$(2\text{-}x\text{-}y/2)\ Na_2S + (1\text{-}x)\ SnS_2 + x/2\ Sb_2S_3 + x\ S + y\ NaX \rightarrow Na_{4\text{-}x\text{-}y}Sn_{1\text{-}x}Sb_xS_{4\text{-}y}X_y$$

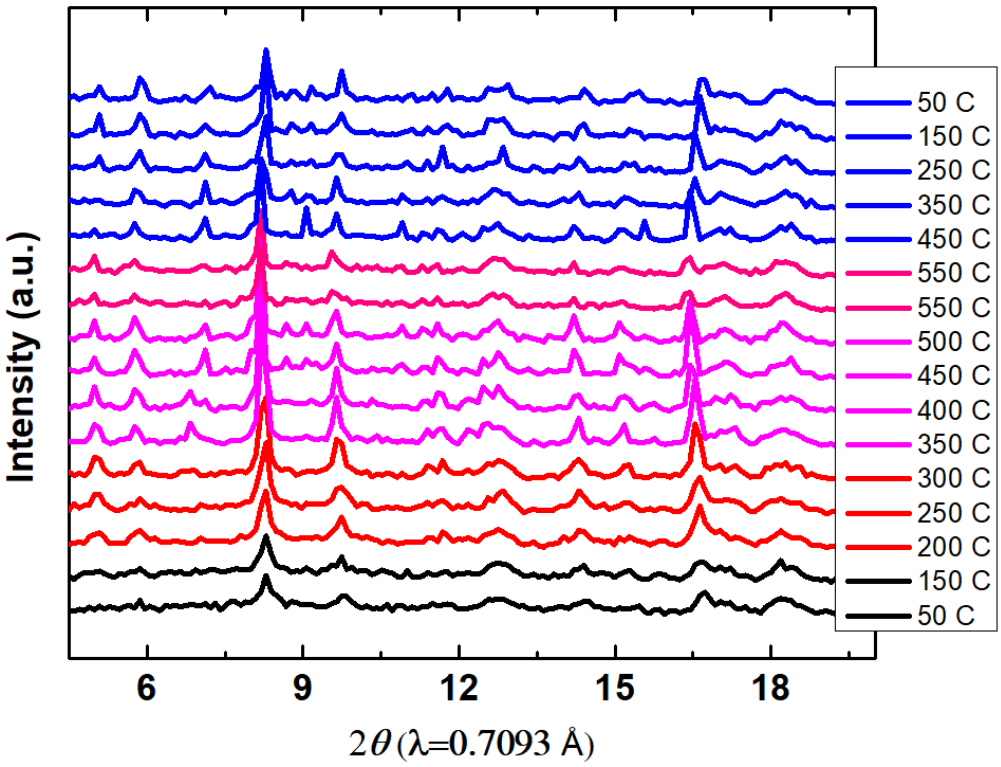

Figure 5.9 *In situ* XRD during the heating and cooling process of $Sb_{0.2}Cl_{0.3}$-doped Na_4SnS_4, or $Na_{3.5}Sn_{0.8}Sb_{0.2}S_{3.7}Cl_{0.3}$ (X=Cl=0.3, A=Sb=0.2).

The compositions of the co-doped samples are shown in Figure 5.2. For each point that represents the co-doped sample, its *y*-coordinate indicates the amount of cation (A = P^{5+} or Sb^{5+}) and *x*-coordinate indicates anion (X=Cl^- or Br^-) in each sample. The sum of *x*

and *y* then represents the total Na vacancies created by the design. *In situ* XRD of all samples have been conducted. As a typical result, the *in situ* XRD patterns during the heating and cooling process of $Na_{3.5}Sn_{0.8}Sb_{0.2}S_{3.7}Cl_{0.3}$ (A=0.2, X=0.3) precursor are shown in Figure 5.9 to demonstrate the formation processes of co-doped samples. Similar to the anion-doped samples, the same set of distinct diffraction peaks show up during the heating process up to 300°C and then signals from $Na_6Sn_2S_7$ impurity appear at higher temperatures. However, different from anion-doped samples, the impurity disappears at 500 °C, indicating better thermodynamic stability of the co-doped composition at high temperatures. On the other hand, during the cooling process, the signals of impurity appear again and remain until reaching room temperature. Guided by the *in situ* XRD results, in order to ensure full reaction, better crystallinity, and to eliminate the formation of impurities at the same time, a relatively high-temperature calcination at 550°C followed by quenching is adopted for all the co-doped samples.

The synchrotron XRD patterns of selected doped samples and the undoped Na_4SnS_4 are shown in Figure 5.8. Synthesized with optimized reaction conditions, the major phases of all doped samples are the same, a distinct phase from the original Na_4SnS_4 phase that is identified to belong to $I4_1/acd$ space group and identical to that of recently reported $Na_{11}Sn_2PS_{12}$ [194] and $Na_{11}Sn_2SbS_{12}$ [170] compounds. Compared with anion-doped samples, which contain impurity phases that can hardly be eliminated via optimization of synthesis conditions, co-doped samples exhibit higher purity within certain doping limits. More synchrotron XRD patterns of co-doped samples are summarized in Figure 5.10. As summarized in Figure 5.2 with different colors of sample points, for anion X = 0.1 ~ 0.3, when the total amount of anion and cation dopants (i.e. the total designed amount of Na

vacancies) exceeds 0.4 (i.e., A+X > 0.4), impurities always form and cannot be eliminated by adjusting synthesis conditions. $Na_{3.4}Sn_{0.7}P_{0.3}S_{3.7}Cl_{0.3}$ and $Na_{3.4}Sn_{0.7}Sb_{0.3}S_{3.7}Cl_{0.3}$ shown in Figure 5.10 are two samples with the most pronounced impurity signals. This suggests that the maximum total amount of dopants (or the total amount of Na vacancies) that can be introduced in the Na_4SnS_4 lattice with thermodynamic stability is limited, which is around 0.4 per formula unit. This limit seems to have little to do with the type and size of cation (P^{5+} or Sb^{5+}) and anion (Br^- or Cl^-) used. Rather it seems to be controlled by the energetics associated with the amount of Na vacancy. When A+X = 0.4, such as shown by XRD patterns of $Na_{3.6}Sn_{0.8}P_{0.2}S_{3.8}Cl_{0.2}$ and $Na_{3.6}Sn_{0.8}Sb_{0.2}S_{3.8}Cl_{0.2}$ (A= P^{5+}/Sb^{5+} = 0.2, X = Cl^- = 0.2), signals of minor $Na_6Sn_2S_7$ impurities are detected, consistent with the signals observed in *in situ* XRD patterns. When 0.2 < A+X < 0.4, products with high purity are obtained. However, when *x* is small and the composition is closer to the end member Na_4SnS_4, the competing formation kinetics with Na_4SnS_4 phase also increases the fraction of Na_4SnS_4 as the secondary phase. Specifically, for X = Cl^-/Br^- =0.1, when cation dopant is P^{5+}, only 0.1 P can be doped with minor Na_4SnS_4 impurities. On the other hand, when cation dopant is Sb^{5+}, 0.2 Sb can be doped with no detectable impurities. This comparison shows that the lower limit of the solid solution range is cation dependent, which may be due to their different sizes. Since the detected impurities Na_4SnS_4 and $Na_6Sn_2S_7$ are both low conductive compounds and therefore are detrimental to the overall ionic conduction, it is expected that the doped samples with higher purities, i.e., A+X < 0.4, will show higher conductivities. The crystal structures of the four samples with A+X < 0.4 are analyzed in detail in the following section.

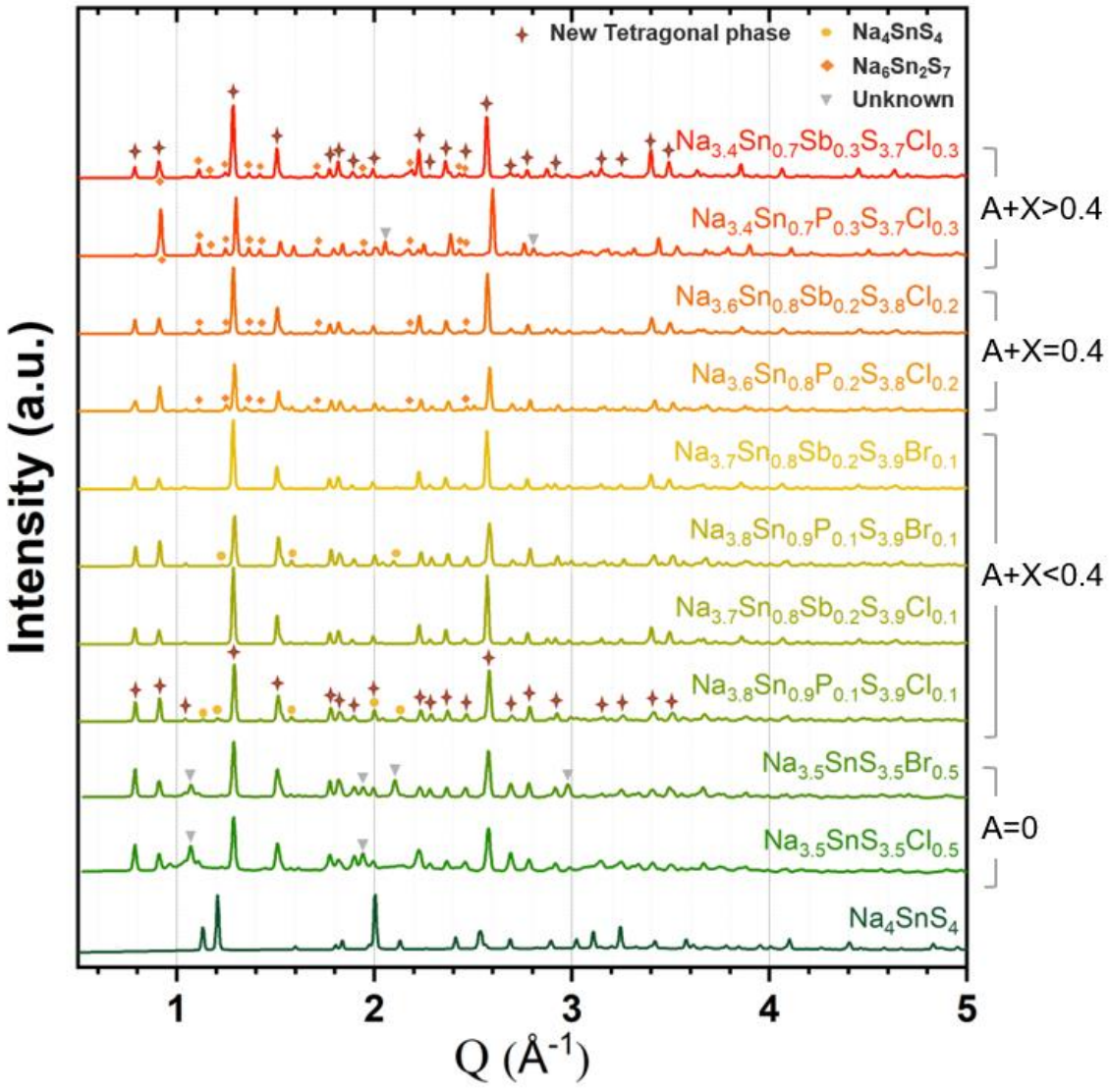

Figure 5.10 Synchrotron XRD patterns of the undoped, anion-doped, and co-doped Na_4SnS_4 samples.

5.2.2 Structural characterizations

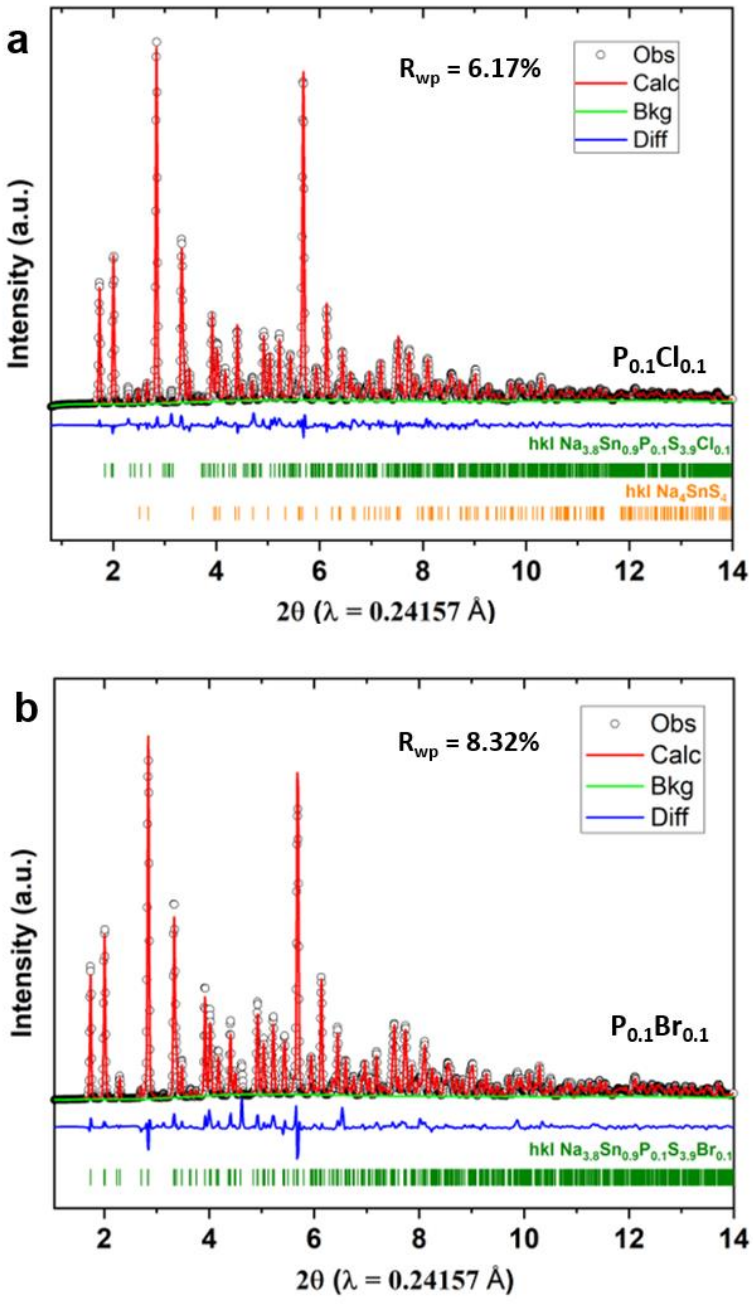

Figure 5.11 Synchrotron powder XRD patterns and the Rietveld refinement of $Na_{4-x-y}Sn_{1-x}A_xS_{4-y}X_y$ with the dopants A_xX_y being (a) $P_{0.1}Cl_{0.1}$ (b) $P_{0.1}Br_{0.1}$.

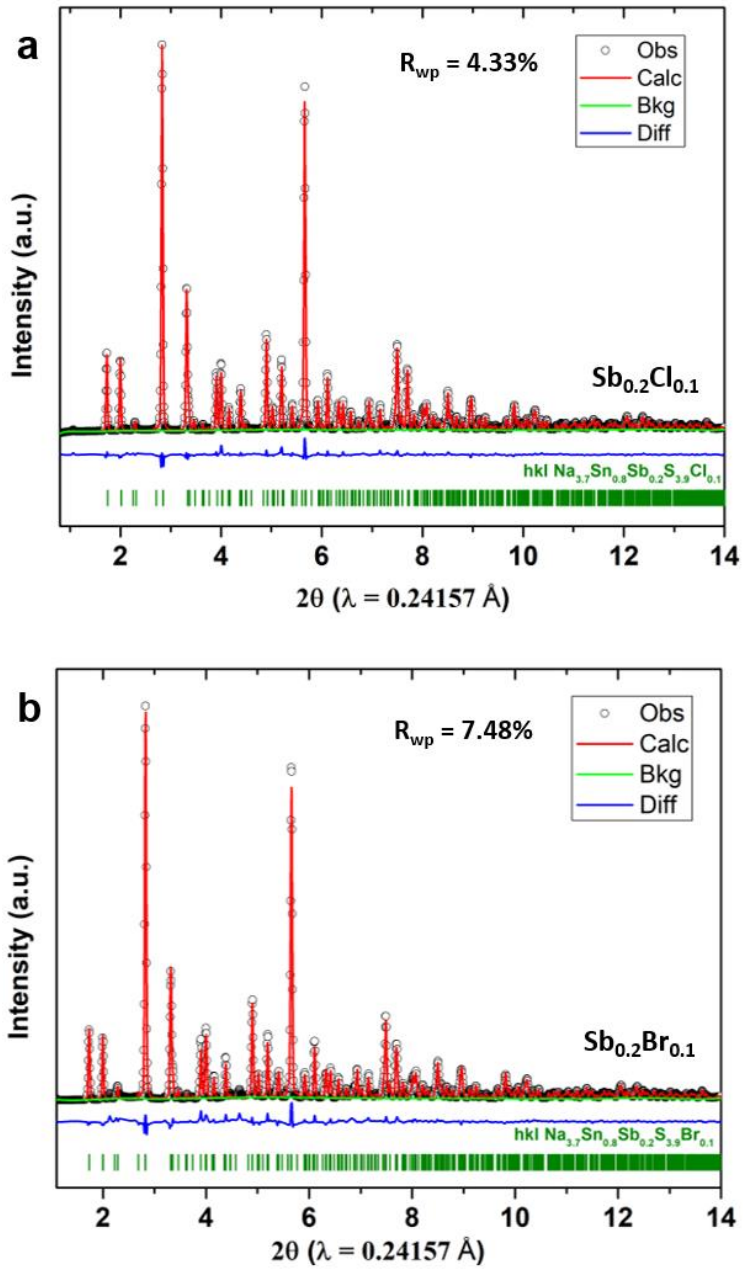

Figure 5.12 Synchrotron powder XRD patterns and the Rietveld refinement of $Na_{4-x-y}Sn_{1-x}A_xS_{4-y}X_y$ with the dopants A_xX_y being (a) $Sb_{0.2}Cl_{0.1}$ (b) $Sb_{0.2}Br_{0.1}$.

Samples with least impurities were selected for synchrotron XRD and in-depth structure characterizations, including $Na_{3.8}Sn_{0.9}P_{0.1}S_{3.9}Cl_{0.1}$, $Na_{3.8}Sn_{0.9}P_{0.1}S_{3.9}Br_{0.1}$, $Na_{3.7}Sn_{0.8}Sb_{0.2}S_{3.9}Cl_{0.1}$, and $Na_{3.7}Sn_{0.8}Sb_{0.2}S_{3.9}Br_{0.1}$. Rietveld refinement results against synchrotron XRD patterns are shown in Figure 5.11 and Figure 5.12. All four samples can be described with a tetragonal space group $I4_1/acd$ as the primary phase with satisfying goodness-of-fit (GOF). While $Na_{3.8}Sn_{0.9}P_{0.1}S_{3.9}Cl_{0.1}$ contains 4.9 wt% Na_4SnS_4 impurity, the other samples all present high purity with no identifiable secondary phase. The refined cell parameters of four co-doped samples are listed in Table 5.3. More details can be found in Table 5.4 - Table 5.7 in the end of this subsection. The unit cell of $Na_{3.8}Sn_{0.9}P_{0.1}S_{3.9}Cl_{0.1}$ possesses lattice parameters of $a = b = 13.8042$ Å, $c = 27.4401$ Å, and V = 5228.83 Å^3. Similar parameters are also obtained for $Na_{3.8}Sn_{0.9}P_{0.1}S_{3.9}Br_{0.1}$. The parameters of (P, Cl/Br) co-doped samples are slightly larger than those of $Na_{11}Sn_2PS_{12}$. On the other hand, (Sb, Cl/Br) co-doped samples show larger lattice parameters than (P, Cl/Br)-doped samples mainly due to the larger cation Sb^{5+} introduced compared to P^{5+}. Specifically, $Sb_{0.2}Cl_{0.1}$-doped sample possesses V = 5284.21 Å^3, and $Sb_{0.2}Br_{0.1}$-doped sample V = 5295.83 Å^3.

Table 5.3 Refinement results for synchrotron X-ray diffraction patterns of $Na_{4-x-y}Sn_{1-x}A_xS_{4-y}X_y$ samples.

Dopants (A_xX_y)	Lattice parameters			Doping level ($x+y$)	Averaged Na occ.	R_{wp}
	a, b (Å)	c(Å)	V(Å^3)			
$P_{0.1}Cl_{0.1}$	13.804(2)	27.440(1)	5228.83	0.2	95.0% (5 sites)	6.17%
$P_{0.1}Br_{0.1}$	13.792(7)	27.440(3)	5220.20	0.2	95.0% (5 sites)	8.32%
$Sb_{0.2}Cl_{0.1}$	13.839(2)	27.590(3)	5284.21	0.3	85.4% (6 sites)	4.33%
$Sb_{0.2}Br_{0.1}$	13.850(4)	27.606(4)	5295.83	0.3	85.4% (6 sites)	7.48%

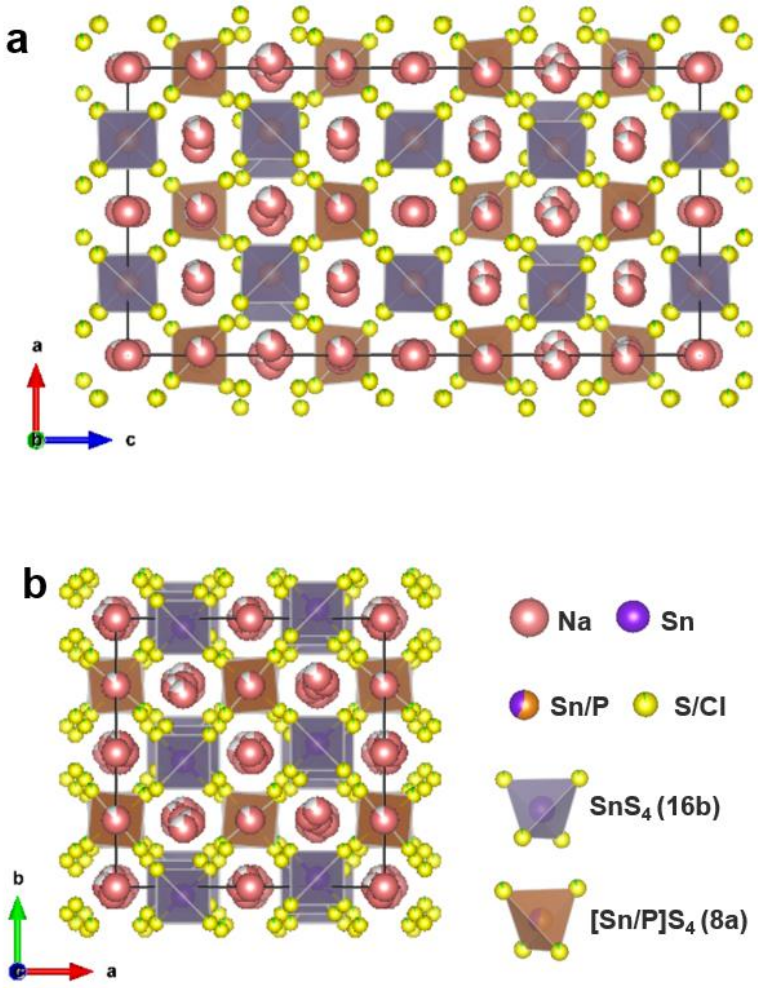

Figure 5.13 The crystal structure of ($P_{0.1}Cl_{0.1}$)-doped sample, or $Na_{3.8}Sn_{0.9}P_{0.1}S_{3.9}Cl_{0.1}$ in (a) [010] and (b) [001] views.

The crystal structure of $Na_{3.8}Sn_{0.9}P_{0.1}S_{3.9}Cl_{0.1}$ is shown as an example of the co-doped samples in Figure 5.13(a) and (b) in views along [010] and [001] directions, respectively. For (P, X)-doped samples, the unit cell contains one Sn site (16*e*) and one

P/Sn randomly shared site (8*a*), where the P/Sn ratio is refined to be 3:7. Therefore the overall P/Sn ratio is calculated to be 2.4 : (16+ 5.6) =1:9, consistent with the ratio in starting materials. With the fixed amount of anion ($Cl_{0.1}$ or $Br_{0.1}$), doping of more P^{5+} has been attempted but failed, suggesting that no more P^{5+} can be introduced into the structure without generating more impurities. As shown in Figure 5.13(a-b), $[PS_4]^{3-}$ and $[SnS_4]^{4-}$ tetrahedra are separated by Na^+ at five distinct crystallographic sites, which is similar to the un-doped Na_4SnS_4 phase except that most Na sites are not fully occupied. For $Na_{3.8}Sn_{0.9}P_{0.1}S_{3.9}Cl_{0.1}$, all Na sites present small deficiencies with an average occupancy of 95.0%. On the other hand, for $Na_{3.8}Sn_{0.9}P_{0.1}S_{3.9}Br_{0.1}$, Na1 and Na2 sites are fully occupied, whereas Na3-Na5 are partially occupied with an average occupancy of 92.5%. It is also worth noting that for $Na_{3.8}Sn_{0.9}P_{0.1}S_{3.9}Br_{0.1}$, instead of fully disordered Br/S sites, Br^- shows slightly different occupancy in three available sites, suggesting possible local-ordering of Br^- and S^{2-} at this site.

For the (Sb, X)-doped samples, the same crystal structure model of space group $I4_1/acd$ was adopted for Rietveld refinement. The unit cells of the two samples also contain one Sn site (16*e*) and one Sb/Sn disordered site (8*a*). Compared with P-doped samples, more Sb^{5+} can be doped at the 8*a* site, resulting in a Sb/Sn ratio of 6:4 and an overall Sb/Sn of 1:4. Therefore, the two samples are synthesized with the dopants of $Sb_{0.2}X_{0.1}$ ($X = Cl^-$, Br^-), which will create more Na vacancies than $Na_{3.8}Sn_{0.9}P_{0.1}S_{3.9}X_{0.1}$ compositions. It is also worth noting that an additional Na site (8*b*) is included for Sb-doped samples and it gives better refinement quality. Such a crystal structure was identical to the reported single crystal structure results of $Na_{11}Sn_2SbS_{12}$ by Nazar *et al.* [170]. For both $Sb_{0.2}X_{0.1}$-doped samples ($X=Cl^-$, Br^-), all Na sites present deficiencies except for the fully occupied Na4

site. Specifically, $Na_{3.7}Sn_{0.8}Sb_{0.2}S_{3.9}Cl_{0.1}$ and $Na_{3.7}Sn_{0.8}Sb_{0.2}S_{3.9}Br_{0.1}$ both present an average occupancy of 85.4%. Possible local ordering of Br^-/S^{2-} sites was also observed in $Na_{3.7}Sn_{0.8}Sb_{0.2}S_{3.9}Br_{0.1}$ sample, implying similar effect of anion-doping as seen in $P_{0.1}X_{0.1}$ doped-samples.

Scanning electron microscope (SEM) was used to investigate the morphology of the as-synthesized samples. Figure 5.14 and Figure 5.15 show the SEM images for the synthesized $Na_{3.8}Sn_{0.9}P_{0.1}S_{3.9}Br_{0.1}$ and $Na_{3.7}Sn_{0.8}Sb_{0.2}S_{3.9}Cl_{0.1}$ samples and their elemental mapping with energy dispersive X-ray (EDX) spectroscopy as examples, respectively. For these samples, the particles show irregular shapes and big variations in size. This inhomogeneity in particle size and morphology is partially due to the quenching process in synthesis. The particles in both samples are well-fused with reduced grain boundaries, which is commonly observed in sulfide-based SE compounds. This is also why cold pressing is usually sufficient for sulfides to deliver high ionic conductivity without significant grain boundaries resistance compared to oxides. The distribution of Na, Sn, S, P/Sb, and Cl/Br elements in the EDX mapping on the other hand confirms the good uniformity of the doped samples with no pronounce element or phase segregations.

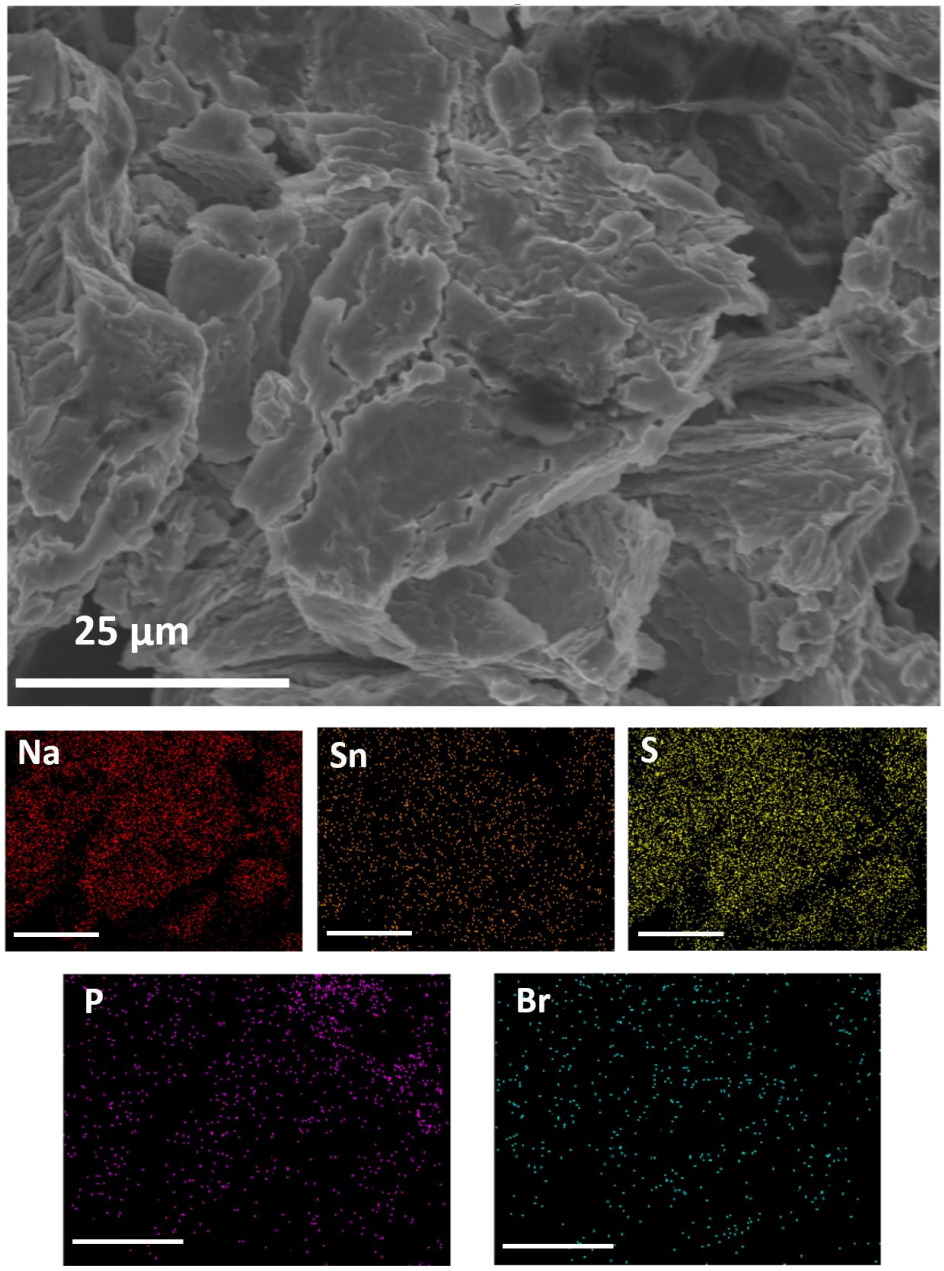

Figure 5.14 SEM images and EDX spectroscopy elemental mappings of $Na_{3.8}Sn_{0.9}P_{0.1}S_{3.9}Br_{0.1}$ in the $Na_{4-x-y}Sn_{1-x}A_xS_{4-y}X_y$ system (A=P=0.1, X=Br=0.1).

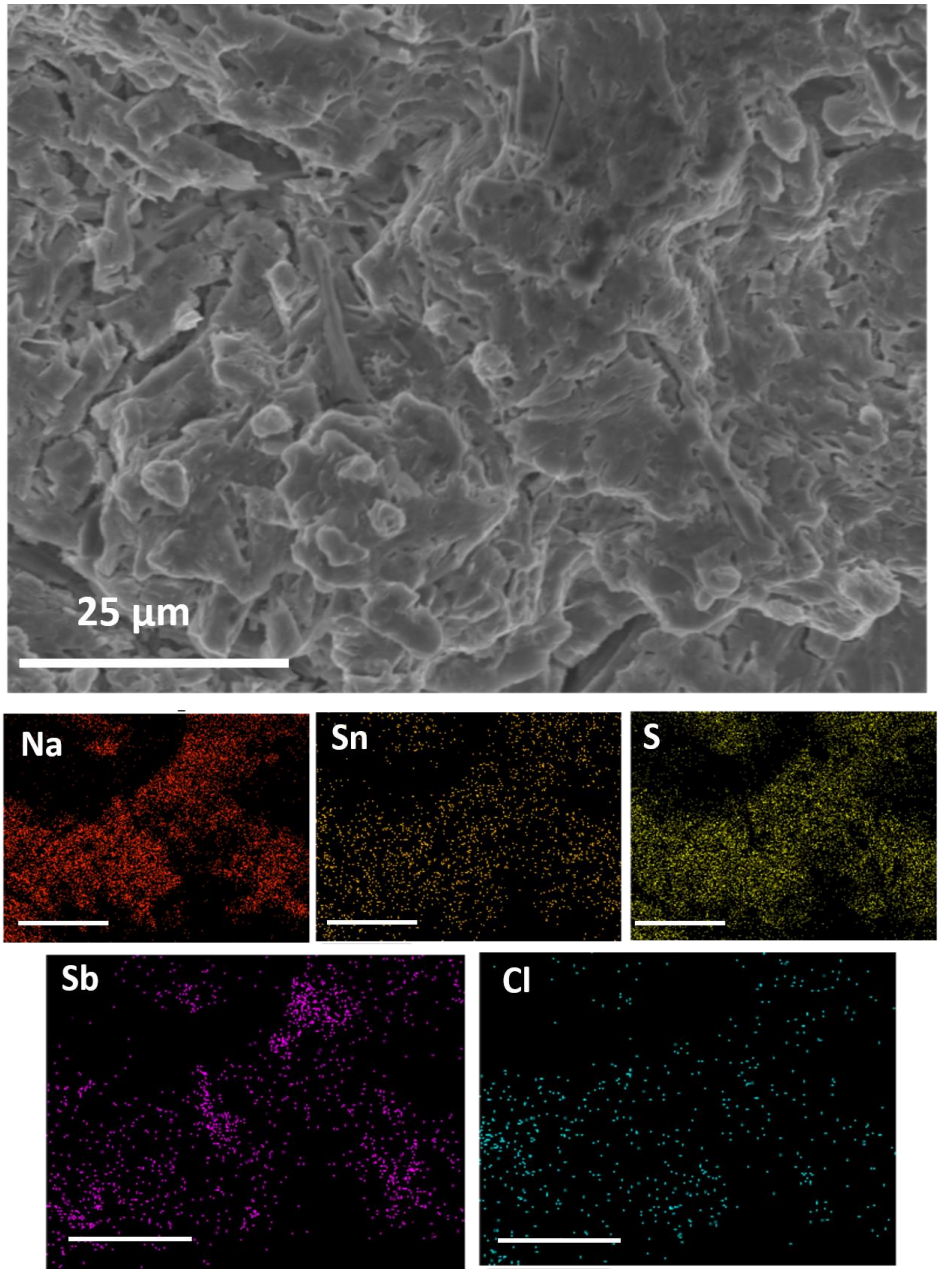

Figure 5.15 SEM images and EDX spectroscopy elemental mappings of $Na_{3.7}Sn_{0.8}Sb_{0.2}S_{3.9}Cl_{0.1}$ in the $Na_{4-x-y}Sn_{1-x}A_xS_{4-y}X_y$ system (A=Sb=0.2, X=Cl=0.1).

Table 5.4 Crystallographic data and Rietveld refinement results for $Na_{3.8}Sn_{0.9}P_{0.1}S_{3.9}Cl_{0.1}$.

Chemical Formula	$Na_{3.8}Sn_{0.9}P_{0.1}S_{3.9}Cl_{0.1}$ (dopants: $P_{0.1}Cl_{0.1}$)
Space Group	$I4_1/acd$ (No. 142)
Lattice Parameter	a=b= 13.8041(6) Å, c= 27.4400(6) Å
Unit Cell Volume	5228.83 $Å^3$

Atom	Site	x	y	z	Occ.	U_{iso}
P1	8a	0.5	0.25	0.125	0.300	0.022
Sn1	8a	0.5	0.25	0.125	0.700	0.022
Sn2	16e	0.2121(0)	0.5	0.25	1.000	0.025
Na1	16f	0.2286(0)	0.4785(1)	0.125	0.975(7)	0.067
Na2	16c	0.25	0.25	0.25	0.884(4)	0.044
Na3	16d	0.5	0.25	0.25610	0.969(4)	0.011
Na4	16e	0.4470(1)	0.5	0.25	0.960(7)	0.028
Na5	32g	0.2647(3)	0.7235(1)	0.1233(0)	0.954(9)	0.048
S1	32g	0.3952(5)	0.3390(2)	0.1721(4)	0.975	0.016
S2	32g	0.1105(0)	0.3959(5)	0.2020(9)	0.975	0.034
S3	32g	0.3074(9)	0.4031(4)	0.3033(1)	0.975	0.027
Cl1	32g	=x(S1)	=y(S1)	=z(S1)	=1-Occ(S1)	$=U_{iso}$(S1)
Cl2	32g	=x(S2)	=y(S2)	=z(S2)	=1-Occ(S2)	$=U_{iso}$(S2)
Cl3	32g	=x(S3)	=y(S3)	=z(S3)	=1-Occ(S3)	$=U_{iso}$(S3)

Table 5.5 Crystallographic data and Rietveld refinement results for $Na_{3.8}Sn_{0.9}P_{0.1}S_{3.9}Br_{0.1}$.

Chemical Formula	$Na_{3.8}Sn_{0.9}P_{0.1}S_{3.9}Br_{0.1}$ (dopants: $P_{0.1}Br_{0.1}$)
Space Group	$I4_1/acd$ (No. 142)
Lattice Parameter	a=b= 13.7927(4) Å, c= 27.4402(7) Å
Unit Cell Volume	5220.20 $Å^3$

Atom	Site	x	y	z	Occ.	U_{iso}
P1	8a	0.5	0.25	0.125	0.300	0.042
Sn1	8a	0.5	0.25	0.125	0.700	0.042
Sn2	16e	0.2104(0)	0.5	0.25	1.000	0.011
Na1	16f	0.2224(8)	0.4723(8)	0.125	1.000	0.105
Na2	16c	0.25	0.25	0.25	1.000	0.071
Na3	16d	0.5	0.25	0.25610	0.919(8)	0.024
Na4	16e	0.4523(4)	0.5	0.25	0.799(8)	0.001
Na5	32g	0.2691(7)	0.7222(7)	0.1202(7)	0.990(2)	0.046
S1	32g	0.3993(1)	0.3358(8)	0.1738(9)	0.990	0.026
S2	32g	0.1074(0)	0.3981(3)	0.2038(4)	0.960	0.024
S3	32g	0.3074(9)	0.4031(4)	0.3033(1)	0.975	0.005
Br1	32g	=x(S1)	=y(S1)	=z(S1)	=1-Occ(S1)	$=U_{iso}$(S1)
Br2	32g	=x(S2)	=y(S2)	=z(S2)	=1-Occ(S2)	$=U_{iso}$(S2)
Br3	32g	=x(S3)	=y(S3)	=z(S3)	=1-Occ(S3)	$=U_{iso}$(S3)

Table 5.6 Crystallographic data and Rietveld refinement results for $Na_{3.7}Sn_{0.8}Sb_{0.2}S_{3.9}Cl_{0.1}$.

Chemical Formula	$Na_{3.7}Sn_{0.8}Sb_{0.2}S_{3.9}Cl_{0.1}$ (dopants: $Sb_{0.2}Cl_{0.1}$)
Space Group	$I4_1/acd$ (No. 142)
Lattice Parameter	a=b= 13.8392(3) Å, c= 27.5902(6) Å
Unit Cell Volume	5284.21 $Å^3$

Atom	Site	x	y	z	Occ.	U_{iso}
Sb1	8a	0	0.25	0.375	0.600	0.021
Sn1	8a	0	0.25	0.375	0.400	0.018
Sn2	16e	0.2824(8)	0	0.25	1.000	0.016
Na1	8b	0	0.25	0.125	0.669	0.012
Na2	16d	0	0.25	0.0124(3)	0.869	0.046
Na3	16e	0.0327(1)	0	0.25	0.781	0.016
Na4	16c	0	0	0	1.000	0.041
Na5	16f	0.2293(9)	0.4793(9)	0.125	0.844	0.031
Na6	32g	0.0132(4)	0.0276(8)	0.1280(5)	0.861	0.018
S1	32g	0.1500(3)	0.3657(3)	0.0492(5)	0.975	0.033
S2	32g	0.1515(4)	0.0656(6)	0.0527(9)	0.975	0.010
S3	32g	0.1081(9)	0.1593(4)	0.3274(0)	0.975	0.046
Cl1	32g	=x(S1)	=y(S1)	=z(S1)	=1-Occ(S1)	$=U_{iso}$(S1)
Cl2	32g	=x(S2)	=y(S2)	=z(S2)	=1-Occ(S2)	$=U_{iso}$(S2)
Cl3	32g	=x(S3)	=y(S3)	=z(S3)	=1-Occ(S3)	$=U_{iso}$(S3)

Table 5.7 Crystallographic data and Rietveld refinement results for $Na_{3.7}Sn_{0.8}Sb_{0.2}S_{3.9}Br_{0.1}$.

Chemical Formula	$Na_{3.7}Sn_{0.8}Sb_{0.2}S_{3.9}Br_{0.1}$ (dopants: $Sb_{0.2}Br_{0.1}$)
Space Group	$I4_1/acd$ (No. 142)
Lattice Parameter	a=b= 13.8503(9) Å, c= 27.6064(0) Å
Unit Cell Volume	5295.83 $Å^3$

Atom	Site	x	y	z	Occ.	U_{iso}
Sb1	8a	0	0.25	0.375	0.600	0.020
Sn1	8a	0	0.25	0.375	0.400	0.001
Sn2	16e	0.2844(8)	0	0.25	1.000	0.018
Na1	8b	0	0.25	0.125	0.905	0.012
Na2	16d	0	0.25	0.0085(6)	0.864	0.035
Na3	16e	0.0311(4)	0	0.25	0.761	0.020
Na4	16c	0	0	0	1.000	0.055
Na5	16f	0.2308(0)	0.4808(0)	0.125	0.784	0.001
Na6	32g	0.0123(9)	0.0286(7)	0.1302(1)	0.844	0.029
S1	32g	0.1470(7)	0.3727(2)	0.0500(4)	0.970	0.102
S2	32g	0.1472(1)	0.0649(2)	0.0543(5)	0.969	0.017
S3	32g	0.1082(6)	0.1669(0)	0.3270(7)	0.986	0.038
Br1	32g	=x(S1)	=y(S1)	=z(S1)	=1-Occ(S1)	$=U_{iso}$(S1)
Br2	32g	=x(S2)	=y(S2)	=z(S2)	=1-Occ(S2)	$=U_{iso}$(S2)
Br3	32g	=x(S3)	=y(S3)	=z(S3)	=1-Occ(S3)	$=U_{iso}$(S3)

5.2.3 Ionic conductivity

In order to evaluate the ionic conductivities of the synthesized samples, the powders of these samples were pressed into pellets at room temperature and analyzed with electrochemical impedance spectroscopy (EIS). The Nyquist plots of the impedance for $Na_{3.8}Sn_{0.9}P_{0.1}S_{3.9}Cl_{0.1}$ and $Na_{3.7}Sn_{0.8}Sb_{0.2}S_{3.9}Cl_{0.1}$ at different temperatures are shown in

Figure 5.16. The impedance spectra in the high-frequency region show a small, incomplete semicircle, suggesting that the grain boundary resistance is low and the overall resistance is dominated by the bulk conductivity. This feature is similar to the previously reported sulfide conductors [81, 150], which typically have lower grain boundary resistance than oxides.

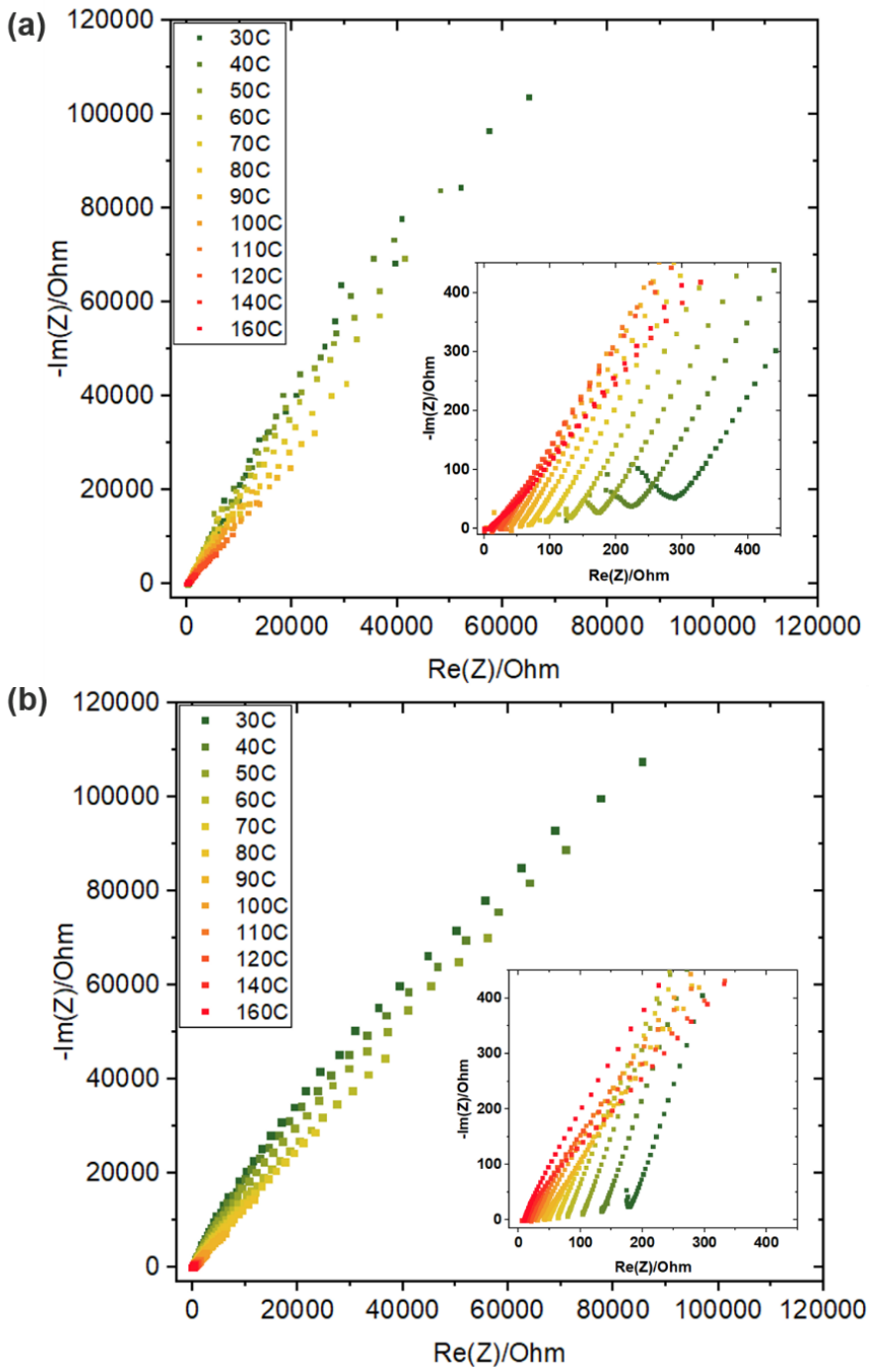

Figure 5.16 Nyquist impedance plots of (a) $Na_{3.8}Sn_{0.9}P_{0.1}S_{3.9}Cl_{0.1}$ ($P_{0.1}Cl_{0.1}$-doped Na_4SnS_4) and (b) $Na_{3.7}Sn_{0.8}Sb_{0.2}S_{3.9}Cl_{0.1}$ ($Sb_{0.2}Cl_{0.1}$-doped Na_4SnS_4) from 30°C to 160°C (the inset shows the zoomed-in region for details at higher temperatures).

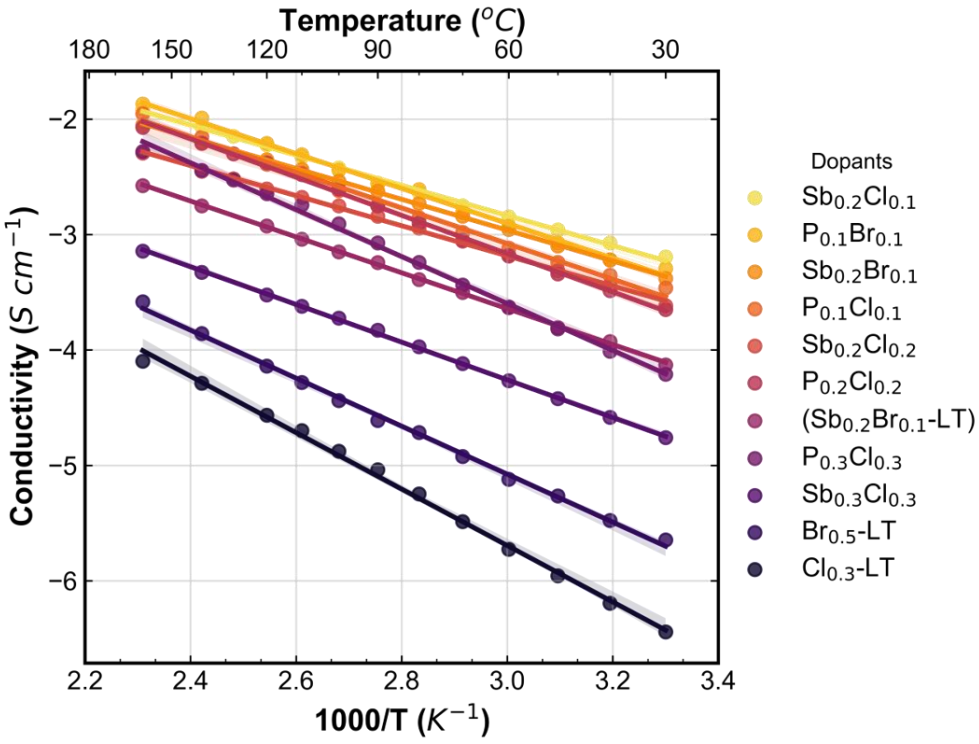

Figure 5.17 Arrhenius plots of conductivities of aliovalent doped Na_4SnS_4 samples. LT indicates samples synthesized at lower temperatures (300°C).

Table 5.8 Ionic conductivities (at 30°C) and activation energies of synthesized aliovalent doped Na_4SnS_4 samples.

Doping level	Dopants	$\sigma_{30°C}$ (mS cm^{-1})	E_a (eV)
Co-doping A+X < 0.4	$P_{0.1}Cl_{0.1}$	0.35	0.31
	$P_{0.1}Br_{0.1}$	0.51	0.30
	$Sb_{0.2}Cl_{0.1}$	**0.64**	**0.26**
	$Sb_{0.2}Br_{0.1}$	0.42	0.27
	$Sb_{0.2}Br_{0.1}$ (LT)	0.074	0.31
Co-doping A+X = 0.4	$P_{0.2}Cl_{0.2}$	0.22	0.33
	$Sb_{0.2}Cl_{0.2}$	0.24	0.27
Co-doping A+X > 0.4	$P_{0.3}Cl_{0.3}$	0.062	0.40
	$Sb_{0.3}Cl_{0.3}$	0.017	0.32
Anion-doping (X)	$Br_{0.5}$ (LT)	0.0023	0.41
	$Cl_{0.3}$ (LT)	3.6×10^{-4}	0.49

Compared with undoped Na_4SnS_4, which shows r.t. ionic conductivity of ~10^{-5} $mS \cdot cm^{-1}$, all the doped samples exhibit clear improvement in conductivity ranging from one to four orders of magnitude higher than that of Na_4SnS_4, demonstrating the effectiveness of the proposed aliovalent doping strategy for faster Na ion conduction via introducing Na vacancies. Very interestingly, through this systematical investigation and comparison, it indicates that the impacts of anion-, cation- and co-doping to the ionic conduction in this series of compounds are different.

1. Among the synthesized doped samples, the anion (Cl^- or Br^-) doped Na_4SnS_4 samples exhibit the lowest conductivities at 30 °C and the highest activation energies, as seen in two examples with dopants of $Br_{0.5}$ and $Cl_{0.3}$, although they in principle have relatively high Na vacancies. This may be partially ascribed to the presence of low conductive impurities, as illustrated in Figure 5.10. Yet majorly it seems to indicate that sole anion doping does not improve the conductivity as effectively as cation- and co-doping at the same level.
2. In contrast, the co-doped Na_4SnS_4 samples with higher purity exhibit one to three orders of magnitude improvement on r. t. conductivities than the anion-doped samples depending on specific doping levels. When the doping level $A+X \leq 0.4$, which produced the new phases with highest purity levels, the doped samples exhibit conductivities exceeding 0.1 $mS \cdot cm^{-1}$, which is a drastic improvement from undoped Na_4SnS_4 and is sufficiently high for solid-state battery applications.
3. In co-doped samples, Sb-doped samples with either Br- or Cl- co-doping show much lower activation energies and much higher conductivities than P-doped samples with either Br- or Cl- co-doping, as seen in Figure 5.18(a-c), indicating Sb

is a better choice of cation doping in this system. While with the same cation doping, the choice of Br or Cl anion dopant also has some impacts on the conductivity and activation energy. By adjusting the types and amounts of dopants in the framework, the highest r.t. conductivity of 0.64 $mS \cdot cm^{-1}$ was identified for the $Na_{3.7}Sn_{0.8}Sb_{0.2}S_{3.9}Cl_{0.1}$, which exhibits the lowest activation energy of 0.26 eV among all the doped samples. This is also lower than the reported activation energy of isostructural $Na_{11}Sn_2SbS_{12}$ [170], indicating the advantageous co-doping strategy in delivering lower energy barrier for ionic conduction. Such co-doping methods with various dopants applied in the Na_4SnS_4 system provides extensive compositional and structural flexibility to design high-performance ionic conductors efficiently and shows great potential in boosting ionic conductivity for suitable material systems.

The different impacts of the doping elements on conductivity and activation energy may be explained from multiple mechanisms. Here we first focus on the crystal structural factors, e.g. the size of the diffusion channels, which is essentially proportional to the unit cell size. The volume of unit cells for the four samples satisfying $A+X < 0.4$ and exhibiting the highest purity levels is shown in Figure 5.18(a). It can be seen that compared with (P, X)-doped samples, the (Sb, X)-doped samples possess larger unit cells mainly because of the larger cation Sb^{5+} than P^{5+} adopted. As a result, (Sb, X)-doped samples exhibit lower activation energies than (P, X)-doped ones due to the larger diffusion pathways provided by an expanded unit cell. This phenomenon is also observed in other co-doped samples as shown in Figure 5.18(c), where all the blue points (Sb, X-doped) show lower activation energies than the red points (P, X-doped). The impact of lattice volume or correspondingly

the diffusion channel size on ionic conductivity behavior has been observed in many ionic conductors and has been considered one of the key structural factors governing ionic transport as summarized in a recent review [195]. Other factors discussed in the review, including local disorder, defect type, and defect concentration are also critical factors in this system as discussed below.

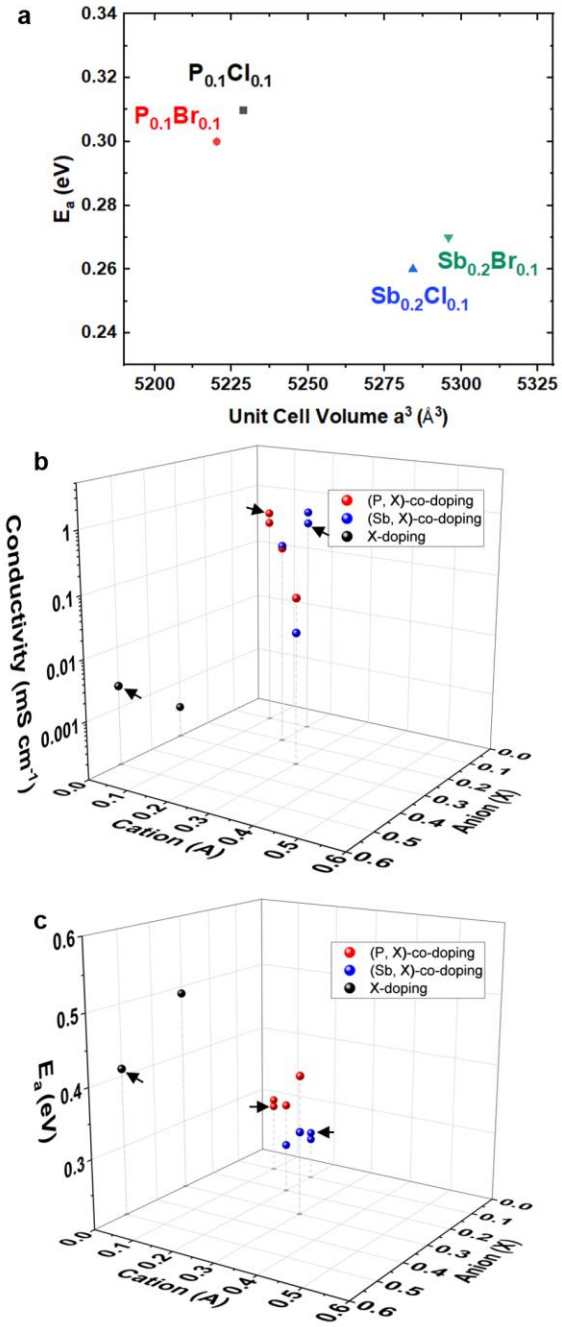

Figure 5.18 (a) The activation energies of four co-doped samples with highest purity and conductivity (i.e., $P_{0.1}Cl_{0.1}$-, $P_{0.1}Br_{0.1}$-, $Sb_{0.2}Cl_{0.1}$-, and $Sb_{0.2}Br_{0.1}$-doped Na_4SnS_4) with respect to the volumes of their unit cells. (b) Conductivities at 30°C and (c) activation energies of the aliovalent doped Na_4SnS_4 samples plotted as functions of the doping levels. Cation dopants of P^{5+} and Sb^{5+} are differentiated by different colors. Arrows in (b) and (c) indicate samples with Br-doping while all the other samples are Cl-doped.

The anion in co-doping methods also plays a critical role as seen from Figure 5.18 (b, c) and Table 5.8 where Cl- and Br-doped samples show distinctive activation energies and ionic conductivities at room temperature. Interestingly, Br-doping brings lower energy barrier and higher conductivities than Cl-doping for (P, X)-co-doped sample but not for (Sb, X)-co-doped sample, implying an interplay between the cations and anions in co-doping methods for the Na_4SnS_4 system. The $(P_{0.1}Br_{0.1})$-doped sample even shows higher conductivity than $(Sb_{0.2}Br_{0.1})$-doped sample at 30 °C despite the larger unit cell and more Na vacancies in the latter. This may be related to the specific Na site occupancies and site energies along the 3D diffusion channels in this tetragonal structure [170, 191], which are affected by various factors, such as the type and distribution of cation/anion dopants, local ordering, chemical bonding interactions, etc., and needs further investigations on the structural details.

It should also be noted that for the co-doped samples, although high-temperature (HT, > 500 °C) synthesis has been adopted and was able to form the target phase with high purity, it is also technically feasible to obtain the phase at lower temperatures (< 350 °C) based on the *in situ* XRD patterns in Figure 5.9. Therefore, co-doped samples were also synthesized by low-temperature (LT) solid-state reactions at 300 °C, and the XRD patterns of both HT- and LT-synthesized samples are shown in Figure 5.19. The same primary phase without XRD-visible impurities is formed for both synthetic routes while the HT sample exhibits slightly better crystallinity. The conductivity of $Na_{3.7}Sn_{0.8}Sb_{0.2}S_{3.9}Br_{0.1}$ by LT route was plotted in Figure 5.17 and included in Table 5.8. Compared with samples of the same composition but synthesized by HT calcination (550 °C) and quenching, the LT sample exhibits a lower conductivity of 0.074 $mS \cdot cm^{-1}$ and a higher activation energy of

0.31 eV. This indicates that the performance of sulfide-based ionic conductor is sensitive to synthesis procedures, which may affect the amorphous phase composition, particle size, grain boundary conditions, etc., and therefore have non-negligible impacts on the measured conductivity. This has also been observed and reported in many other sulfide-based material groups [5, 111, 150, 154, 196]. Considering the variables in the synthesis methods, there may still be room to further optimize the co-doped Na_4SnS_4 compounds for even higher conductivities.

Cyclic voltammogram (CV) test of $Sb_{0.2}Cl_{0.1}$-doped Na_4SnS_4 sample (or $Na_{3.7}Sn_{0.8}Sb_{0.2}S_{3.9}Cl_{0.1}$) was conducted to preliminarily evaluate its electrochemical stability. The results in Figure 5.20 show that in the scan from −0.5 V to 5 V, no significant current due to electrolyte decomposition is detected at high voltage, suggesting the co-doped sample is stable against most cathodes. Cathodic and anodic currents are observed near 0 V, corresponding to sodium plating and stripping. It is noted that the performance of solid electrolyte materials in batteries may not be fully represented or predicted by the CV test, as the compatibility with cathode/anode and the interfacial reactions also play important roles in solid state battery cells, as discussed in previous reports [29, 41]. More in-depth interfacial analysis against Na metal and cathode materials as well as the material behavior in full-cell batteries requires further investigation.

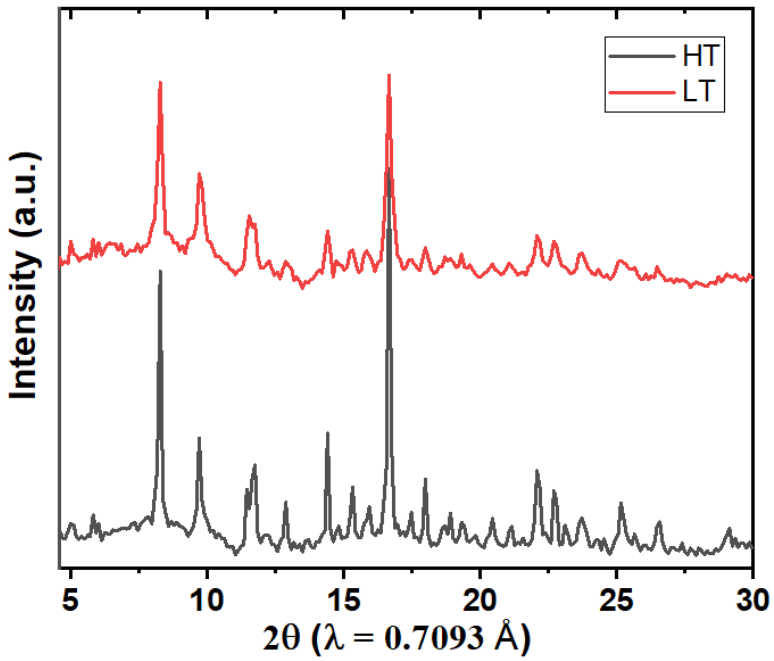

Figure 5.19 XRD patterns of $Na_{3.7}Sn_{0.8}Sb_{0.2}S_{3.9}Br_{0.1}$ ($Sb_{0.2}Br_{0.1}$-doped Na_4SnS_4) synthesized through high temperature (HT-550°C) and low temperature (LT-300°C) calcination.

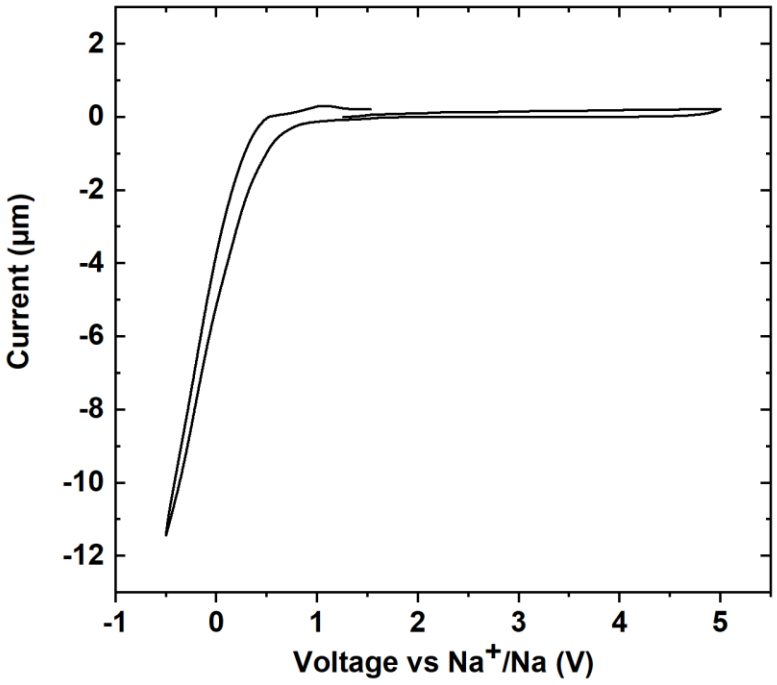

Figure 5.20 Cyclic voltammetry curves of $Sb_{0.2}Cl_{0.1}$-doped Na_4SnS_4 ($Na_{3.7}Sn_{0.8}Sb_{0.2}S_{3.9}Cl_{0.1}$) at 5 mV s^{-1}.

5.3 Summary

In this work, a series of novel Na ion conductors, $Na_{4-x-y}Sn_{1-x}A_xS_{4-y}X_y$, were designed and synthesized through aliovalent doping based on Na_4SnS_4 to create more Na vacancies and improve the ionic conductivity. A phase with the space group $I4_1/acd$ is formed in all the doped samples, including both anion-doped and (cation, anion)-co-doped samples. The highest possible doping level (i.e. the boundaries of these complicated phase diagrams) were revealed for different combinations of the dopants. Among these samples, co-doped samples within certain doping levels of cations (A = P^{5+}/Sb^{5+}) and anions (X = Cl^-/Br^-), i.e., A+X < 0.4, exhibit high purity of the new phase and show the highest level of conductivities, which are 4 orders of magnitude higher than the undoped Na_4SnS_4 and are among the highest conductivities reported in chalcogenide-based Na-ion conductors. It is confirmed that the creation of Na vacancies is the major reason for the boosted conductivity, while the selection of cation-, anion-, and co-doping also has a significant impact on both the conductivity and the activation energy. This work not only identifies a group of new Na superionic conductors with a wide range of chemical compositions, but also demonstrates an effective structural tuning method for new material explorations, which will trigger more studies on similar sulfide-based compounds and other material groups as solid electrolytes.

5.4 Methods

5.4.1 Synthesis of $Na_{4-x-y}Sn_{1-x}A_xS_{4-y}X_y$

The $Na_{4-x-y}Sn_{1-x}A_xS_{4-y}X_y$ samples are synthesized via solid state reactions. Starting materials including Na_2S (Sigma Aldrich, 98%), SnS_2 (American Elements, 99%), P_2S_5

(Sigma Aldrich, 99%), Sb_2S_3 (Sigma Aldrich, 96%), NaCl (Sigma Aldrich, 99.5%), and NaBr (Sigma Aldrich, 99%) are weighed and mixed with stoichiometric ratios of the designed formulas. Na_2S is used with 5% excess to compensate the loss during heating. The mixture is ball-milled at 300 rpm for 16 h and then pressed into pellets with a diameter of 0.5 inch. Each pellet weights about 0.3 g. The pellets are loaded into a quartz tube in an Ar-filled glove box, and then the tube is sealed. The tube is heated to 550 °C (HT-synthesis) or 300 °C (LT-synthesis) with a 3 °C/min ramping rate in a box furnace, dwelling for 24 h, and quenched on a copper plate to room temperature. The copper plate here serves as a good thermal conductor to facilitate the fast cooling process and the samples will typically be cooled to room temperature in 10~15 minutes. Then the tube is transferred into the glove box and the product powder is obtained through hand grinding with a mortar and a pestle after breaking the tube. The synthesized samples are stored in the Ar-filled glove box to avoid exposure to the air and moisture before being used for characterizations and electrochemical measurements.

5.4.2 Characterization

Crystal structures of the obtained samples are analyzed by X-Ray Diffraction (XRD) with using a D8 Advance X-ray Diffractometer (Bruker) equipped with a LynxEye detector and a Molybdenum tube ($\lambda\ K\alpha_1 = 0.7093$ Å). The samples are scanned in an air-tight sample container covered with a Kapton tape to avoid air and moisture. The samples are also investigated in sealed capillaries with synchrotron X-ray diffraction at beam lines 17-BM at the Advanced Photon Source (APS) at Argonne National Laboratory (ANL) and 28-ID-2 at the National Synchrotron Light Source II (NSLS-II) at Brookhaven National

Laboratory (BNL). Rietveld refinements against the synchrotron XRD data are performed using the EXPGUI suite of GSAS code [197].

To investigate the reaction mechanism in the synthesis process, *in situ* XRD is conducted on various $Na_{4-x-y}Sn_{1-x}A_xS_{4-y}X_y$ ball milled precursors using an Anton Paar HTK1200N furnace installed on the D8 Advance diffractometer. The powder precursors are sealed in quartz capillaries with a diameter of 1.0 mm in an Argon-filled glove box. Then the capillaries are mounted in the HTK1200N furnace and the *in situ* XRD process was conducted. The temperature profile includes a ramping process from r. t. to 550°C with multiple intermediate temperature holding steps as described in previous reports [97, 98]. XRD patterns are collected first at 50°C, then at each constant temperature from 150°C to 550°C with a step size of 50°C. After being held at 550°C for 3 hours, the chamber is cooled down to r. t. and additional XRD patterns are collected during the cooling process.

5.4.3 Electrochemical Tests

Electrochemical Impedance Spectroscopy (EIS) is used to determine the Na ionic conductivity of the samples. The AC impedance measurements are performed using a Bio-Logic VMP3 impedance analyzer in the frequency range from 1 MHz to 1 Hz with a voltage amplitude of 100 mV. The pellets for the measurements are cold-pressed from as-synthesized powders at 100 MPa pressure in an acrylic tube with an inner diameter of 0.5 inch. Two stainless-steel rods are used as the ion-blocking electrodes. Temperature-dependent conductivity measurements are performed from r. t. to 160 °C using a heatable pressing die with a temperature controller. Cyclic voltammetry using a Na |

$Na_{3.7}Sn_{0.8}Sb_{0.2}S_{3.9}Cl_{0.1}$ |Sn cell is measured at 5 mV s^{-1} with Sn as the work electrode and Na metal as the counter and reference electrode.

5.5 Notes to Chapter 5

This chapter is based on the paper entitled "Anion and cation co-doping of Na_4SnS_4 as sodium superionic conductors" published in Materials Today Physics [99].

5.6 References

[5] Kato, Y., S. Hori, T. Saito, K. Suzuki, M. Hirayama, A. Mitsui, M. Yonemura, H. Iba, and R. Kanno, *High-power all-solid-state batteries using sulfide superionic conductors.* Nature Energy, 2016. **1**(4): p. 16030.

[29] Tian, Y., T. Shi, W.D. Richards, J. Li, J.C. Kim, S.-H. Bo, and G. Ceder, *Compatibility issues between electrodes and electrolytes in solid-state batteries.* Energy Environ. Sci., 2017. **10**(5): p. 1150-1166.

[41] Tian, Y., Y. Sun, D.C. Hannah, Y. Xiao, H. Liu, K.W. Chapman, S.-H. Bo, and G. Ceder, *Reactivity-Guided Interface Design in Na Metal Solid-State Batteries.* Joule, 2019. **3**(4): p. 1037-1050.

[54] Kamaya, N., et al., *A lithium superionic conductor.* Nat Mater, 2011. **10**(9): p. 682-6.

[57] Deiseroth, H.J., S.T. Kong, H. Eckert, J. Vannahme, C. Reiner, T. Zaiss, and M. Schlosser, *Li_6PS_5X: a class of crystalline Li-rich solids with an unusually high Li^+ mobility.* Angew Chem Int Ed Engl, 2008. **47**(4): p. 755-8.

[80] Yu, Z., et al., *Exceptionally High Ionic Conductivity in $Na_3P_{0.62}As_{0.38}S_4$ with Improved Moisture Stability for Solid-State Sodium-Ion Batteries.* Adv Mater, 2017. **29**(16).

[81] Zhang, L., K. Yang, J. Mi, L. Lu, L. Zhao, L. Wang, Y. Li, and H. Zeng, *Na_3PSe_4: A Novel Chalcogenide Solid Electrolyte with High Ionic Conductivity.* Advanced Energy Materials, 2015. **5**(24): p. 1501294.

[89] Bo, S.-H., Y. Wang, and G. Ceder, *Structural and Na-ion conduction characteristics of $Na_3PS_xSe_{4-x}$.* J. Mater. Chem. A, 2016. **4**(23): p. 9044-9053.

[90] Xiong, S., Z. Liu, H. Rong, H. Wang, M. McDaniel, and H. Chen, *$Na_3SbSe_{4-x}S_x$ as Sodium Superionic Conductors.* Scientific Reports, 2018. **8**(1): p. 9146.

[96] Yang, L., et al., *Lithium-Doping Stabilized High-Performance P2–$Na_{0.66}Li_{0.18}Fe_{0.12}Mn_{0.7}O_2$ Cathode for Sodium Ion Batteries.* Journal of the American Chemical Society, 2019. **141**(16): p. 6680-6689.

[97] Liu, Z., et al., *$Li_{15}P_4S_{16}Cl_3$, a Lithium Chlorothiophosphate as a Solid-State Ionic Conductor.* Inorganic Chemistry, 2020. **59**(1): p. 226-234.

[98] Xiong, S., et al., *Computation-Guided Design of $LiTaSiO_5$, a New Lithium Ionic Conductor with Sphene Structure.* Advanced Energy Materials, 2019. **9**(22): p. 1803821.

[99] Xiong, S., Z. Liu, L. Yang, Y. Ma, W. Xu, J. Bai, and H. Chen, *Anion and cation co-doping of Na_4SnS_4 as sodium superionic conductors.* Materials Today Physics, 2020. **15**: p. 100281.

[111] Seino, Y., T. Ota, K. Takada, A. Hayashi, and M. Tatsumisago, *A sulphide lithium super ion conductor is superior to liquid ion conductors for use in rechargeable batteries.* Energy Environ. Sci., 2014. **7**(2): p. 627-631.

[139] Ellis, B.L. and L.F. Nazar, *Sodium and sodium-ion energy storage batteries.* Current Opinion in Solid State and Materials Science, 2012. **16**(4): p. 168-177.

[142] Yang, L., et al., *Design of high-performance cathode materials with single-phase pathway for sodium ion batteries: A study on P2-$Na_x(Li_yMn_{1-y})O_2$ compounds.* Journal of Power Sources, 2018. **381**: p. 171-180.

[145] Dunn, B., H. Kamath, and J.-M. Tarascon, *Electrical Energy Storage for the Grid: A Battery of Choices.* Science, 2011. **334**(6058): p. 928-935.

[150] Hayashi, A., K. Noi, A. Sakuda, and M. Tatsumisago, *Superionic glass-ceramic electrolytes for room-temperature rechargeable sodium batteries.* Nat Commun, 2012. **3**: p. 856.

[152] Chu, I.-H., C.S. Kompella, H. Nguyen, Z. Zhu, S. Hy, Z. Deng, Y.S. Meng, and S.P. Ong, *Room-Temperature All-solid-state Rechargeable Sodium-ion Batteries with a Cl-doped Na_3PS_4 Superionic Conductor.* Scientific Reports, 2016. **6**(1): p. 33733.

[154] Wang, H., Y. Chen, Z.D. Hood, G. Sahu, A.S. Pandian, J.K. Keum, K. An, and C. Liang, *An Air-Stable Na_3SbS_4 Superionic Conductor Prepared by a Rapid and Economic Synthetic Procedure.* Angew Chem Int Ed Engl, 2016. **55**(30): p. 8551-5.

[155] Banerjee, A., K.H. Park, J.W. Heo, Y.J. Nam, C.K. Moon, S.M. Oh, S.T. Hong, and Y.S. Jung, *Na_3SbS_4 : A Solution Processable Sodium Superionic Conductor for All-Solid-State Sodium-Ion Batteries.* Angew Chem Int Ed Engl, 2016. **55**(33): p. 9634-8.

[159] Kraft, M.A., et al., *Influence of Lattice Polarizability on the Ionic Conductivity in the Lithium Superionic Argyrodites Li_6PS_5X (X = Cl, Br, I).* J Am Chem Soc, 2017. **139**(31): p. 10909-10918.

[163] Zhang, L., D. Zhang, K. Yang, X. Yan, L. Wang, J. Mi, B. Xu, and Y. Li, *Vacancy-Contained Tetragonal Na_3SbS_4 Superionic Conductor.* Adv Sci (Weinh), 2016. **3**(10): p. 1600089.

[170] Ramos, E.P., Z. Zhang, A. Assoud, K. Kaup, F. Lalère, and L.F. Nazar, *Correlating Ion Mobility and Single Crystal Structure in Sodium-Ion Chalcogenide-Based Solid State Fast Ion Conductors: $Na_{11}Sn_2PnS_{12}$ (Pn = Sb, P).* Chemistry of Materials, 2018. **30**(21): p. 7413-7417.

[181] Tanibata, N., K. Noi, A. Hayashi, and M. Tatsumisago, *Preparation and characterization of highly sodium ion conducting Na_3PS_4–Na_4SiS_4 solid electrolytes.* RSC Adv., 2014. **4**(33): p. 17120-17123.

[189] Jumas, J.-C., E. Philippot, F. Vermot-Gaud-Daniel, M. Ribes, and M. Maurin, *Etude de la tétracoordination de l'etain dans deux orthothiostannates: Na_4SnS_4 et Ba_2SnS_4 (α).* Journal of Solid State Chemistry, 1975. **14**(4): p. 319-327.

[190] Moon, C.K., et al., *Vacancy-Driven Na^+ Superionic Conduction in New Ca-Doped Na_3PS_4 for All-Solid-State Na-Ion Batteries.* ACS Energy Letters, 2018. **3**(10): p. 2504-2512.

[191] Duchardt, M., U. Ruschewitz, S. Adams, S. Dehnen, and B. Roling, *Vacancy‐Controlled Na^+ Superion Conduction in $Na_{11}Sn_2PS_{12}$.* Angewandte Chemie International Edition, 2018. **57**(5): p. 1351-1355.

[192] Zhang, Z., et al., *Correlated Migration Invokes Higher Na^+‐Ion Conductivity in NaSICON‐Type Solid Electrolytes.* Advanced Energy Materials, 2019. **9**(42).

[193] Feng, X., P.-H. Chien, Z. Zhu, I.-H. Chu, P. Wang, M. Immediato-Scuotto, H. Arabzadeh, S.P. Ong, and Y.-Y. Hu, *Studies of Functional Defects for Fast Na-Ion Conduction in $Na_{3-y}PS_{4-x}Cl_x$ with a Combined Experimental and Computational Approach.* Advanced Functional Materials, 2019. **29**(9).

[194] Zhang, Z., E. Ramos, F. Lalère, A. Assoud, K. Kaup, P. Hartman, and L.F. Nazar, *$Na_{11}Sn_2PS_{12}$: a new solid state sodium superionic conductor.* Energy & Environmental Science, 2018. **11**(1): p. 87-93.

[195] Gao, Y., A.M. Nolan, P. Du, Y. Wu, C. Yang, Q. Chen, Y. Mo, and S.-H. Bo, *Classical and Emerging Characterization Techniques for Investigation of Ion Transport Mechanisms in Crystalline Fast Ionic Conductors.* Chemical Reviews, 2020. **120**(13): p. 5954-6008.

[196] Park, K.H., et al., *Solution-Processable Glass LiI-Li_4SnS_4 Superionic Conductors for All-Solid-State Li-Ion Batteries.* Adv Mater, 2016. **28**(9): p. 1874-83.

[197] Toby, B.H., *EXPGUI, a graphical user interface for GSAS.* JOURNAL OF APPLIED CRYSTALLOGRAPHY, 2001. **34**(2): p. 4.

CHAPTER 6. CONCLUSIONS AND PERSPECTIVES

6.1 Conclusions

In this dissertation, various Li and Na ionic conductor systems have been investigated to gain an in-depth understanding of their structural parameters and resulting conduction behavior for potential all-solid-state battery applications. Using advanced and emerging characterization techniques, such as *in situ* synchrotron X-ray diffraction, neutron diffraction, and *in situ* pair distribution function analysis, interesting and critical insights on the structural descriptors and their impact on ionic conduction have been revealed for various oxide- and sulfide-based material families. The key findings of our studies on these material systems are highlighted as follows: (1) Zr-doped $LiTaSiO_5$ has been demonstrated as a promising new lithium ionic conductor system by a joint experimental and computational study. First-principles computation method effectively aids the design of this new lithium ion conductor group by predicting the doping options to activate correlated Li^+ migration and the corresponding phase stability and conductivities. Advanced experimental methods are adopted to optimize the synthetic and processing conditions and achieve significantly improved conductivity, which are proved to be critical for oxide-based solid electrolyte materials. (2) Iso-valent doping for the solid solution series of $Na_3SbSe_{4-x}S_x$ has been confirmed to be effective in tuning the unit cell sizes and promoting fast ion transport. However, it also revealed a non-monotonic relationship between the unit cell size of the material and its Na^+ conductivity, suggesting that other structural parameters, such as structural distortion and chemical bonding, need to be carefully examined when adopting iso-valent substitution to enhance ion conduction.

(3) Intense milling process has been proved to be destructive for the long-range periodic structure of Na_3SbS_4 conductor based on a systematic investigation on structural evolution of milled Na_3SbS_4-NaCl mixtures using *in situ* XRD and PDF analysis. The structural units of $[SbS_4]^{3-}$ tetrahedra remain intact and will be rearranged to form conductive Na_3SbS_4 phase upon annealing. (4) Alio-valent doping has been demonstrated to be effective and flexible in tuning material structures and facilitating fast ion conduction based on the structural analysis on a series of aliovalent doped Na_4SnS_4 compounds (or $Na_{4-x-y}Sn_{1-x}A_xS_{4-y}X_y$, A = P^{5+}/Sb^{5+}, X = Cl^-/Br^-). The increased defect concentration and enlarged diffusion channels are identified the key drivers for the boosted conductivities in this material group.

6.2 Perspectives

Despite the tremendous research efforts and great progress in the development of fast Li/Na ion conductors during the past decade, the application of promising material candidates as solid electrolytes (SEs) in practical all-solid-state batteries (ASBs) still faces various technical challenges. There is still substantial room for further investigations on ion transport in solid materials and for improvements on SE material performance and compatibility in batteries. Based on this dissertation, a few research directions are proposed here for a better understanding on ion conduction in solids and accelerated material discovery and implementation in ASBs:

(1) Advanced and emerging characterization techniques at various length scales, such as local range, mesoscale, and long range, are critical to reveal accurate structural parameters and establish sound correlations to classical or revised ion transport mechanism. Due to the complexity of ion conduction in solids, single

technique is usually not sufficient to obtain the whole picture of the key structural descriptors. More complementary analyses can be effective and beneficial for an in-depth mechanistic understanding [195].

(2) Theoretical modeling and computational methods have been proved to be effective and powerful tools for both material structure analysis and new material discovery. Collaborations between computational and experimental researchers are expected to provide insightful material knowledge on structure-property-performance relationship to rationally guide and accelerate the development of promising ion conductors [116, 198, 199].

(3) Synthetic and processing methods are essential pieces of material development for successful end uses. More flexible, cost-effective, and sustainable synthetic and processing approaches need to be developed for the delivery of practical ASBs in the next stage. Particularly, processes that are scalable, less air-sensitive, and easy to implement in current LIB industry are highly desired.

(4) The electrochemical stability and interfacial compatibility of SE materials in the context of battery operating environment is still not well understood and requires stringent investigation with advanced experimental tools. *In situ* and *operando* methods have long been considered powerful tools in battery-related research but still face technical challenges for ASB studies [200]. Continued efforts in developing these methods for ASB characterizations are imperative and are expected to provide valuable information for cell- and device-level design and optimization.

With widely recognized technological benefits, all-solid-state batteries are attracting continuous R&D efforts in both academia and industry community. Collaborative works by researchers with various backgrounds in experimental material science, electrochemistry, solid-state physics, computation and theoretical modeling, etc., are playing significant roles in advancing our knowledge for this complicated and intriguing area. It is believed that further advancements in fast solid ion conductors and solid-state batteries by this diverse community will facilitate exciting innovations in energy storage technologies in the near future.

6.3 References

[116] Nolan, A.M., Y. Zhu, X. He, Q. Bai, and Y. Mo, *Computation-Accelerated Design of Materials and Interfaces for All-Solid-State Lithium-Ion Batteries.* Joule, 2018. **2**(10): p. 2016-2046.

[195] Gao, Y., A.M. Nolan, P. Du, Y. Wu, C. Yang, Q. Chen, Y. Mo, and S.-H. Bo, *Classical and Emerging Characterization Techniques for Investigation of Ion Transport Mechanisms in Crystalline Fast Ionic Conductors.* Chemical Reviews, 2020. **120**(13): p. 5954-6008.

[198] Sendek, A.D., Q. Yang, E.D. Cubuk, K.-A.N. Duerloo, Y. Cui, and E.J. Reed, *Holistic computational structure screening of more than 12 000 candidates for solid lithium-ion conductor materials.* Energy & Environmental Science, 2017. **10**(1): p. 306-320.

[199] Schmidt, J., M.R.G. Marques, S. Botti, and M.A.L. Marques, *Recent advances and applications of machine learning in solid-state materials science.* npj Computational Materials, 2019. **5**(1): p. 83.

[200] Boebinger, M.G., J.A. Lewis, S.E. Sandoval, and M.T. McDowell, *Understanding Transformations in Battery Materials Using in Situ and Operando Experiments: Progress and Outlook.* ACS Energy Letters, 2020. **5**(1): p. 335-345.

REFERENCES

[1] Cheng, X.-B., R. Zhang, C.-Z. Zhao, and Q. Zhang, *Toward Safe Lithium Metal Anode in Rechargeable Batteries: A Review.* Chemical Reviews, 2017. **117**(15): p. 10403-10473.

[2] Cheng, X.-B., C.-Z. Zhao, Y.-X. Yao, H. Liu, and Q. Zhang, *Recent Advances in Energy Chemistry between Solid-State Electrolyte and Safe Lithium-Metal Anodes.* Chem, 2019. **5**(1): p. 74-96.

[3] Chen, Y., Y. Luo, H. Zhang, C. Qu, H. Zhang, and X. Li, *The Challenge of Lithium Metal Anodes for Practical Applications.* Small Methods, 2019. **3**(7): p. 1800551.

[4] Kato, Y., K. Kawamoto, R. Kanno, and M. Hirayama, *Discharge Performance of All-Solid-State Battery Using a Lithium Superionic Conductor* $Li_{10}GeP_2S_{12}$. Electrochemistry, 2012. **80**(10): p. 749-751.

[5] Kato, Y., S. Hori, T. Saito, K. Suzuki, M. Hirayama, A. Mitsui, M. Yonemura, H. Iba, and R. Kanno, *High-power all-solid-state batteries using sulfide superionic conductors.* Nature Energy, 2016. **1**(4): p. 16030.

[6] Yabuuchi, N., K. Kubota, M. Dahbi, and S. Komaba, *Research Development on Sodium-Ion Batteries.* Chemical Reviews, 2014. **114**(23): p. 11636-11682.

[7] Nithya, C. and S. Gopukumar, *Sodium ion batteries: a newer electrochemical storage.* WIREs Energy and Environment, 2015. **4**(3): p. 253-278.

[8] Pan, H., Y.-S. Hu, and L. Chen, *Room-temperature stationary sodium-ion batteries for large-scale electric energy storage.* Energy & Environmental Science, 2013. **6**(8): p. 2338-2360.

[9] Liu, T., et al., *Exploring competitive features of stationary sodium ion batteries for electrochemical energy storage.* Energy & Environmental Science, 2019. **12**(5): p. 1512-1533.

[10] Ponrouch, A., E. Marchante, M. Courty, J.-M. Tarascon, and M.R. Palacín, *In search of an optimized electrolyte for Na-ion batteries.* Energy & Environmental Science, 2012. **5**(9): p. 8572-8583.

[11] Chen, R., Q. Li, X. Yu, L. Chen, and H. Li, *Approaching Practically Accessible Solid-State Batteries: Stability Issues Related to Solid Electrolytes and Interfaces.* Chemical Reviews, 2020. **120**(14): p. 6820-6877.

[12] Lopez, J., D.G. Mackanic, Y. Cui, and Z. Bao, *Designing polymers for advanced battery chemistries.* Nature Reviews Materials, 2019. **4**(5): p. 312-330.

[13] Shoji, M., E.J. Cheng, T. Kimura, and K. Kanamura, *Recent progress for all solid state battery using sulfide and oxide solid electrolytes.* Journal of Physics D: Applied Physics, 2019. **52**(10): p. 103001.

[14] Wang, Y., S. Song, C. Xu, N. Hu, J. Molenda, and L. Lu, *Development of solid-state electrolytes for sodium-ion battery–A short review.* Nano Materials Science, 2019. **1**(2): p. 91-100.

[15] Kim, J.-J., K. Yoon, I. Park, and K. Kang, *Progress in the Development of Sodium-Ion Solid Electrolytes.* Small Methods, 2017. **1**(10): p. 1700219.

[16] Lee, Y.-G., et al., *High-energy long-cycling all-solid-state lithium metal batteries enabled by silver–carbon composite anodes.* Nature Energy, 2020. **5**(4): p. 299-308.

[17] Owens, B.B., *Solid state electrolytes: overview of materials and applications during the last third of the Twentieth Century.* Journal of Power Sources, 2000. **90**(1): p. 2-8.

[18] Knauth, P. and H.L. Tuller, *Solid-State Ionics: Roots, Status, and Future Prospects.* Journal of the American Ceramic Society, 2002. **85**(7): p. 1654-1680.

[19] Goodenough, J.B., *Fast Ionic Conduction in Solids*, in *Concise Encyclopedia of Advanced Ceramic Materials*, R.J. Brook, Editor. 1991, Pergamon: Oxford. p. 143-147.

[20] Okumura, T., S. Taminato, T. Takeuchi, and H. Kobayashi, *Minimizing the Grain Boundary Resistance of Li-Ion-Conducting Oxide Electrolyte by Controlling Liquid-Phase Formation During Sintering.* ACS Applied Energy Materials, 2018. **1**(11): p. 6303-6311.

[21] Dawson, J.A., P. Canepa, T. Famprikis, C. Masquelier, and M.S. Islam, *Atomic-Scale Influence of Grain Boundaries on Li-Ion Conduction in Solid Electrolytes for All-Solid-State Batteries.* Journal of the American Chemical Society, 2018. **140**(1): p. 362-368.

[22] Chen, B., C. Xu, and J. Zhou, *Insights into Grain Boundary in Lithium-Rich Anti-Perovskite as Solid Electrolytes.* Journal of The Electrochemical Society, 2018. **165**(16): p. A3946-A3951.

[23] Kim, J., J. Kim, M. Avdeev, H. Yun, and S.-J. Kim, *$LiTa_2PO_8$: a fast lithium-ion conductor with new framework structure.* Journal of Materials Chemistry A, 2018. **6**(45): p. 22478-22482.

[24] Banerjee, A., X. Wang, C. Fang, E.A. Wu, and Y.S. Meng, *Interfaces and Interphases in All-Solid-State Batteries with Inorganic Solid Electrolytes.* Chemical Reviews, 2020. **120**(14): p. 6878-6933.

[25] Xiao, Y., Y. Wang, S.-H. Bo, J.C. Kim, L.J. Miara, and G. Ceder, *Understanding interface stability in solid-state batteries.* Nature Reviews Materials, 2020. **5**(2): p. 105-126.

[26] Pervez, S.A., M.A. Cambaz, V. Thangadurai, and M. Fichtner, *Interface in Solid-State Lithium Battery: Challenges, Progress, and Outlook.* ACS Applied Materials & Interfaces, 2019. **11**(25): p. 22029-22050.

[27] Froboese, L., J.F.v.d. Sichel, T. Loellhoeffel, L. Helmers, and A. Kwade, *Effect of Microstructure on the Ionic Conductivity of an All Solid-State Battery Electrode.* Journal of The Electrochemical Society, 2019. **166**(2): p. A318-A328.

[28] Nakamura, T., K. Amezawa, J. Kulisch, W.G. Zeier, and J. Janek, *Guidelines for All-Solid-State Battery Design and Electrode Buffer Layers Based on Chemical Potential Profile Calculation.* ACS Applied Materials & Interfaces, 2019. **11**(22): p. 19968-19976.

[29] Tian, Y., T. Shi, W.D. Richards, J. Li, J.C. Kim, S.-H. Bo, and G. Ceder, *Compatibility issues between electrodes and electrolytes in solid-state batteries.* Energy Environ. Sci., 2017. **10**(5): p. 1150-1166.

[30] Miara, L.J., W.D. Richards, Y.E. Wang, and G. Ceder, *First-Principles Studies on Cation Dopants and Electrolyte|Cathode Interphases for Lithium Garnets.* Chemistry of Materials, 2015. **27**(11): p. 4040-4047.

[31] Auvergniot, J., A. Cassel, J.-B. Ledeuil, V. Viallet, V. Seznec, and R. Dedryvère, *Interface Stability of Argyrodite Li_6PS_5Cl toward $LiCoO_2$, $LiNi_{1/3}Co_{1/3}Mn_{1/3}O_2$, and $LiMn_2O_4$ in Bulk All-Solid-State Batteries.* Chemistry of Materials, 2017. **29**(9): p. 3883-3890.

[32] Richards, W.D., L.J. Miara, Y. Wang, J.C. Kim, and G. Ceder, *Interface Stability in Solid-State Batteries.* Chemistry of Materials, 2016. **28**(1): p. 266-273.

[33] Wenzel, S., S. Randau, T. Leichtweiß, D.A. Weber, J. Sann, W.G. Zeier, and J. Janek, *Direct Observation of the Interfacial Instability of the Fast Ionic Conductor $Li_{10}GeP_2S_{12}$ at the Lithium Metal Anode.* Chemistry of Materials, 2016. **28**(7): p. 2400-2407.

[34] Sakuda, A., H. Kitaura, A. Hayashi, K. Tadanaga, and M. Tatsumisago, *Modification of Interface Between $LiCoO_2$ Electrode and $Li_2S–P_2S_5$ Solid Electrolyte Using $Li_2O–SiO_2$ Glassy Layers.* Journal of The Electrochemical Society, 2009. **156**(1): p. A27.

[35] Wenzel, S., T. Leichtweiss, D. Krüger, J. Sann, and J. Janek, *Interphase formation on lithium solid electrolytes—An in situ approach to study interfacial reactions by photoelectron spectroscopy.* Solid State Ionics, 2015. **278**: p. 98-105.

[36] Fan, X., X. Ji, F. Han, J. Yue, J. Chen, L. Chen, T. Deng, J. Jiang, and C. Wang, *Fluorinated solid electrolyte interphase enables highly reversible solid-state Li metal battery.* Science Advances, 2018. **4**(12): p. eaau9245.

[37] Sun, B., Y. Jin, J. Lang, K. Liu, M. Fang, and H. Wu, *A painted layer for high-rate and high-capacity solid-state lithium–metal batteries.* Chemical Communications, 2019. **55**(47): p. 6704-6707.

[38] Han, X., et al., *Negating interfacial impedance in garnet-based solid-state Li metal batteries.* Nature Materials, 2017. **16**(5): p. 572-579.

[39] Luo, W., et al., *Reducing Interfacial Resistance between Garnet-Structured Solid-State Electrolyte and Li-Metal Anode by a Germanium Layer.* Advanced Materials, 2017. **29**(22): p. 1606042.

[40] Fu, K., et al., *Toward garnet electrolyte–based Li metal batteries: An ultrathin, highly effective, artificial solid-state electrolyte/metallic Li interface.* Science Advances, 2017. **3**(4): p. e1601659.

[41] Tian, Y., Y. Sun, D.C. Hannah, Y. Xiao, H. Liu, K.W. Chapman, S.-H. Bo, and G. Ceder, *Reactivity-Guided Interface Design in Na Metal Solid-State Batteries.* Joule, 2019. **3**(4): p. 1037-1050.

[42] Kato, T., T. Hamanaka, K. Yamamoto, T. Hirayama, F. Sagane, M. Motoyama, and Y. Iriyama, *In-situ $Li_7La_3Zr_2O_{12}/LiCoO_2$ interface modification for advanced all-solid-state battery.* Journal of Power Sources, 2014. **260**: p. 292-298.

[43] Liu, Y., C. Li, B. Li, H. Song, Z. Cheng, M. Chen, P. He, and H. Zhou, *Germanium Thin Film Protected Lithium Aluminum Germanium Phosphate for Solid-State Li Batteries.* Advanced Energy Materials, 2018. **8**(16): p. 1702374.

[44] Bates, J.B., N.J. Dudney, B. Neudecker, A. Ueda, and C.D. Evans, *Thin-film lithium and lithium-ion batteries.* Solid State Ionics, 2000. **135**(1): p. 33-45.

[45] Xia, Y., T. Fujieda, K. Tatsumi, P.P. Prosini, and T. Sakai, *Thermal and electrochemical stability of cathode materials in solid polymer electrolyte.* Journal of Power Sources, 2001. **92**(1): p. 234-243.

[46] Sun, B., C. Xu, J. Mindemark, T. Gustafsson, K. Edström, and D. Brandell, *At the polymer electrolyte interfaces: the role of the polymer host in interphase layer formation in Li-batteries.* Journal of Materials Chemistry A, 2015. **3**(26): p. 13994-14000.

[47] Xu, C., B. Sun, T. Gustafsson, K. Edström, D. Brandell, and M. Hahlin, *Interface layer formation in solid polymer electrolyte lithium batteries: an XPS study.* Journal of Materials Chemistry A, 2014. **2**(20): p. 7256-7264.

[48] Thomas, J., *Solid state electrochemistry. Edited by Peter G. Bruce, Cambridge University Press.* Advanced Materials, 1996. **8**(4): p. 360-360.

[49] Owens, B.B. and G.R. Argue, *High-Conductivity Solid Electrolytes: MAg_4I_5.* Science, 1967. **157**(3786): p. 308-310.

[50] Wiedersich, H. and W.V. Johnston, *On the thermodynamic properties of the solid electrolyte $RbAg_4I_5$.* Journal of Physics and Chemistry of Solids, 1969. **30**(3): p. 475-482.

[51] Briant, J.L. and G.C. Farrington, *Ionic conductivity in Li^+-Na^+ beta and beta ″ alumina.* Solid State Ionics, 1981. **5**: p. 207-210.

[52] Yung-Fang Yu, Y. and J.T. Kummer, *Ion exchange properties of and rates of ionic diffusion in beta-alumina.* Journal of Inorganic and Nuclear Chemistry, 1967. **29**(9): p. 2453-2475.

[53] Kanno, R. and M. Murayama, *Lithium Ionic Conductor Thio-LISICON: The Li_2S-GeS_2-P_2S_5 System.* Journal of The Electrochemical Society, 2001. **148**(7): p. A742.

[54] Kamaya, N., et al., *A lithium superionic conductor.* Nat Mater, 2011. **10**(9): p. 682-6.

[55] Minami, K., F. Mizuno, A. Hayashi, and M. Tatsumisago, *Lithium ion conductivity of the Li_2S–P_2S_5 glass-based electrolytes prepared by the melt quenching method.* Solid State Ionics, 2007. **178**(11-12): p. 837-841.

[56] Hayashi, A., *Characterization of Li_2S-P_2S_5 glass-ceramics as a solid electrolyte for lithium secondary batteries.* Solid State Ionics, 2004. **175**(1-4): p. 683-686.

[57] Deiseroth, H.J., S.T. Kong, H. Eckert, J. Vannahme, C. Reiner, T. Zaiss, and M. Schlosser, *Li_6PS_5X: a class of crystalline Li-rich solids with an unusually high Li^+ mobility.* Angew Chem Int Ed Engl, 2008. **47**(4): p. 755-8.

[58] Boulineau, S., M. Courty, J.-M. Tarascon, and V. Viallet, *Mechanochemical synthesis of Li-argyrodite Li_6PS_5X (X=Cl, Br, I) as sulfur-based solid electrolytes for all solid state batteries application.* Solid State Ionics, 2012. **221**: p. 1-5.

[59] Rao, R.P. and S. Adams, *Studies of lithium argyrodite solid electrolytes for all-solid-state batteries.* physica status solidi (a), 2011. **208**(8): p. 1804-1807.

[60] Cussen, E.J., *The structure of lithium garnets: cation disorder and clustering in a new family of fast Li^+ conductors.* Chemical Communications, 2006(4): p. 412-413.

[61] Kasper, H.M., *Series of rare earth garnets $Ln_3M_2Li_3O_{12}$ (M=Te, W).* Inorganic Chemistry, 1969. **8**(4): p. 1000-1002.

[62] Buschmann, H., et al., *Structure and dynamics of the fast lithium ion conductor "$Li_7La_3Zr_2O_{12}$".* Physical Chemistry Chemical Physics, 2011. **13**(43): p. 19378-19392.

[63] Goodenough, J.B., H.Y.P. Hong, and J.A. Kafalas, *Fast Na^+-ion transport in skeleton structures.* Materials Research Bulletin, 1976. **11**(2): p. 203-220.

[64] Anantharamulu, N., K. Koteswara Rao, G. Rambabu, B. Vijaya Kumar, V. Radha, and M. Vithal, *A wide-ranging review on Nasicon type materials.* Journal of Materials Science, 2011. **46**(9): p. 2821-2837.

[65] Aono, H., E. Sugimoto, Y. Sadaoka, N. Imanaka, and G.y. Adachi, *Ionic Conductivity of Solid Electrolytes Based on Lithium Titanium Phosphate.* Journal of The Electrochemical Society, 1990. **137**(4): p. 1023-1027.

[66] Inaguma, Y., C. Liquan, M. Itoh, T. Nakamura, T. Uchida, H. Ikuta, and M. Wakihara, *High ionic conductivity in lithium lanthanum titanate.* Solid State Communications, 1993. **86**(10): p. 689-693.

[67] Itoh, M., Y. Inaguma, W.-H. Jung, L. Chen, and T. Nakamura, *High lithium ion conductivity in the perovskite-type compounds $Ln_{12}Li_{12}TiO_3$(Ln=La,Pr,Nd,Sm).* Solid State Ionics, 1994. **70-71**: p. 203-207.

[68] Santibáñez-Mendieta, A.B., et al., *$La_3Li_3W_2O_{12}$: Ionic Diffusion in a Perovskite with Lithium on both A- and B-Sites.* Chemistry of Materials, 2016. **28**(21): p. 7833-7851.

[69] Bachman, J.C., et al., *Inorganic Solid-State Electrolytes for Lithium Batteries: Mechanisms and Properties Governing Ion Conduction.* Chem Rev, 2016. **116**(1): p. 140-62.

[70] Manthiram, A., X. Yu, and S. Wang, *Lithium battery chemistries enabled by solid-state electrolytes.* Nature Reviews Materials, 2017. **2**(4): p. 16103.

[71] Guo, X. and J. Maier, *Grain Boundary Blocking Effect in Zirconia: A Schottky Barrier Analysis.* Journal of The Electrochemical Society, 2001. **148**(3): p. E121.

[72] Moriwake, H., X. Gao, A. Kuwabara, C.A.J. Fisher, T. Kimura, Y.H. Ikuhara, K. Kohama, T. Tojigamori, and Y. Ikuhara, *Domain boundaries and their influence on Li migration in solid-state electrolyte (La,Li)TiO_3.* Journal of Power Sources, 2015. **276**: p. 203-207.

[73] Chung, H. and B. Kang, *Increase in grain boundary ionic conductivity of $Li_{1.5}Al_{0.5}Ge_{1.5}(PO_4)_3$ by adding excess lithium.* Solid State Ionics, 2014. **263**: p. 125-130.

[74] Lian, P.-J., B.-S. Zhao, L.-Q. Zhang, N. Xu, M.-T. Wu, and X.-P. Gao, *Inorganic sulfide solid electrolytes for all-solid-state lithium secondary batteries.* Journal of Materials Chemistry A, 2019. **7**(36): p. 20540-20557.

[75] Hayashi, A., A. Sakuda, and M. Tatsumisago, *Development of Sulfide Solid Electrolytes and Interface Formation Processes for Bulk-Type All-Solid-State Li and Na Batteries.* Frontiers in Energy Research, 2016. **4**(25).

[76] Richards, W.D., Y. Wang, L.J. Miara, J.C. Kim, and G. Ceder, *Design of $Li_{1+2x}Zn_{1-x}PS_4$, a new lithium ion conductor.* Energy & Environmental Science, 2016. **9**(10): p. 3272-3278.

[77] Krauskopf, T., S.P. Culver, and W.G. Zeier, *Bottleneck of Diffusion and Inductive Effects in $Li_{10}Ge_{1-x}Sn_xP_2S_{12}$.* Chemistry of Materials, 2018. **30**(5): p. 1791-1798.

[78] Luo, Y., X. Li, Y. Zhang, L. Ge, H. Chen, and L. Guo, *Electrochemical properties and structural stability of Ga- and Y- co-doping in $Li_7La_3Zr_2O_{12}$ ceramic electrolytes for lithium-ion batteries.* Electrochimica Acta, 2019. **294**: p. 217-225.

[79] Mehrer, H., *Diffusion in solids: fundamentals, methods, materials, diffusion-controlled processes*. Vol. 155. 2007: Springer Science & Business Media.

[80] Yu, Z., et al., *Exceptionally High Ionic Conductivity in $Na_3P_{0.62}As_{0.38}S_4$ with Improved Moisture Stability for Solid-State Sodium-Ion Batteries.* Adv Mater, 2017. **29**(16).

[81] Zhang, L., K. Yang, J. Mi, L. Lu, L. Zhao, L. Wang, Y. Li, and H. Zeng, *Na_3PSe_4: A Novel Chalcogenide Solid Electrolyte with High Ionic Conductivity.* Advanced Energy Materials, 2015. **5**(24): p. 1501294.

[82] Deng, Z., et al., *Ca-doped $Na_2Zn_2TeO_6$ layered sodium conductor for all-solid-state sodium-ion batteries.* Electrochimica Acta, 2019. **298**: p. 121-126.

[83] Arbi, K., J.M. Rojo, and J. Sanz, *Lithium mobility in titanium based Nasicon $Li_{1+x}Ti_{2-x}Al_x(PO_4)_3$ and $LiTi_{2-x}Zr_x(PO_4)_3$ materials followed by NMR and impedance spectroscopy.* Journal of the European Ceramic Society, 2007. **27**(13): p. 4215-4218.

[84] Bernges, T., S.P. Culver, N. Minafra, R. Koerver, and W.G. Zeier, *Competing Structural Influences in the Li Superionic Conducting Argyrodites $Li_6PS_{5-x}Se_xBr$ ($0 \leqslant x \leqslant 1$) upon Se Substitution.* Inorganic Chemistry, 2018. **57**(21): p. 13920-13928.

[85] Kraft, M.A., et al., *Influence of Lattice Polarizability on the Ionic Conductivity in the Lithium Superionic Argyrodites Li_6PS_5X (X = Cl, Br, I).* Journal of the American Chemical Society, 2017. **139**(31): p. 10909-10918.

[86] Rodger, A.R., J. Kuwano, and A.R. West, *Li^+ ion conducting γ solid solutions in the systems Li_4XO_4-Li_3YO_4: X=Si, Ge, Ti; Y=P, As, V; Li_4XO_4-$LiZO_2$: Z=Al, Ga, Cr and Li_4GeO_4-Li_2CaGeO_4.* Solid State Ionics, 1985. **15**(3): p. 185-198.

[87] Martínez-Juárez, A., C. Pecharromán, J.E. Iglesias, and J.M. Rojo, *Relationship between Activation Energy and Bottleneck Size for Li^+ Ion Conduction in NASICON Materials of Composition $LiMM'(PO_4)_3$; M, M' = Ge, Ti, Sn, Hf.* The Journal of Physical Chemistry B, 1998. **102**(2): p. 372-375.

[88] Ong, S.P., Y. Mo, W.D. Richards, L. Miara, H.S. Lee, and G. Ceder, *Phase stability, electrochemical stability and ionic conductivity of the $Li_{10\pm1}MP_2X_{12}$ (M = Ge, Si, Sn, Al or P, and X = O, S or Se) family of superionic conductors.* Energy & Environmental Science, 2013. **6**(1): p. 148-156.

[89] Bo, S.-H., Y. Wang, and G. Ceder, *Structural and Na-ion conduction characteristics of $Na_3PS_xSe_{4-x}$.* J. Mater. Chem. A, 2016. **4**(23): p. 9044-9053.

[90] Xiong, S., Z. Liu, H. Rong, H. Wang, M. McDaniel, and H. Chen, *$Na_3SbSe_{4-x}S_x$ as Sodium Superionic Conductors.* Scientific Reports, 2018. **8**(1): p. 9146.

[91] Minafra, N., S.P. Culver, C. Li, A. Senyshyn, and W.G. Zeier, *Influence of the Lithium Substructure on the Diffusion Pathways and Transport Properties of the Thio-LISICON $Li_4Ge_{1-x}Sn_xS_4$.* Chemistry of Materials, 2019. **31**(10): p. 3794-3802.

[92] Kawai, H. and J. Kuwano, *Lithium Ion Conductivity of A - Site Deficient Perovskite Solid Solution $La_{0.67-x}Li_{3x}TiO_3$.* Journal of The Electrochemical Society, 1994. **141**(7): p. L78-L79.

[93] Kraft, M.A., et al., *Inducing High Ionic Conductivity in the Lithium Superionic Argyrodites $Li_{6+x}P_{1-x}Ge_xS_5I$ for All-Solid-State Batteries.* Journal of the American Chemical Society, 2018. **140**(47): p. 16330-16339.

[94] Yu, C., L. van Eijck, S. Ganapathy, and M. Wagemaker, *Synthesis, structure and electrochemical performance of the argyrodite Li_6PS_5Cl solid electrolyte for Li-ion solid state batteries.* Electrochimica Acta, 2016. **215**: p. 93-99.

[95] Yoon, W.-S., et al., *In situ soft XAS study on nickel-based layered cathode material at elevated temperatures: A novel approach to study thermal stability.* Scientific Reports, 2014. **4**(1): p. 6827.

[96] Yang, L., et al., *Lithium-Doping Stabilized High-Performance P2–$Na_{0.66}Li_{0.18}Fe_{0.12}Mn_{0.7}O_2$ Cathode for Sodium Ion Batteries.* Journal of the American Chemical Society, 2019. **141**(16): p. 6680-6689.

[97] Liu, Z., et al., *$Li_{15}P_4S_{16}Cl_3$, a Lithium Chlorothiophosphate as a Solid-State Ionic Conductor.* Inorganic Chemistry, 2020. **59**(1): p. 226-234.

[98] Xiong, S., et al., *Computation-Guided Design of $LiTaSiO_5$, a New Lithium Ionic Conductor with Sphene Structure.* Advanced Energy Materials, 2019. **9**(22): p. 1803821.

[99] Xiong, S., Z. Liu, L. Yang, Y. Ma, W. Xu, J. Bai, and H. Chen, *Anion and cation co-doping of Na_4SnS_4 as sodium superionic conductors.* Materials Today Physics, 2020. **15**: p. 100281.

[100] Krauskopf, T., S.P. Culver, and W.G. Zeier, *Local Tetragonal Structure of the Cubic Superionic Conductor Na_3PS_4.* Inorganic Chemistry, 2018. **57**(8): p. 4739-4744.

[101] He, X., Q. Bai, Y. Liu, A.M. Nolan, C. Ling, and Y. Mo, *Crystal Structural Framework of Lithium Super-Ionic Conductors.* Advanced Energy Materials, 2019. **9**(43): p. 1902078.

[102] He, X., Y. Zhu, and Y. Mo, *Origin of fast ion diffusion in super-ionic conductors.* Nature Communications, 2017. **8**(1): p. 15893.

[103] Mo, Y., S.P. Ong, and G. Ceder, *First Principles Study of the $Li_{10}GeP_2S_{12}$ Lithium Super Ionic Conductor Material.* Chemistry of Materials, 2012. **24**(1): p. 15-17.

[104] Wang, Y., W.D. Richards, S.P. Ong, L.J. Miara, J.C. Kim, Y. Mo, and G. Ceder, *Design principles for solid-state lithium superionic conductors.* Nat Mater, 2015. **14**(10): p. 1026-31.

[105] Jain, A., et al., *Commentary: The Materials Project: A materials genome approach to accelerating materials innovation.* APL Materials, 2013. **1**(1): p. 011002.

[106] Wang, Y., W.D. Richards, S.P. Ong, L.J. Miara, J.C. Kim, Y. Mo, and G. Ceder, *Design principles for solid-state lithium superionic conductors.* Nature Materials, 2015. **14**(10): p. 1026-1031.

[107] Bachman, J.C., et al., *Inorganic Solid-State Electrolytes for Lithium Batteries: Mechanisms and Properties Governing Ion Conduction.* Chemical Reviews, 2016. **116**(1): p. 140-162.

[108] Wang, Y., W.D. Richards, S.P. Ong, L.J. Miara, J.C. Kim, Y. Mo, and G. Ceder, *Design principles for solid-state lithium superionic conductors.* Nature Materials, 2015. **14**: p. 1026.

[109] Janek, J. and W.G. Zeier, *A solid future for battery development.* Nature Energy, 2016. **1**: p. 16141.

[110] Park, K.H., Q. Bai, D.H. Kim, D.Y. Oh, Y. Zhu, Y. Mo, and Y.S. Jung, *Design Strategies, Practical Considerations, and New Solution Processes of Sulfide Solid Electrolytes for All-Solid-State Batteries.* Advanced Energy Materials, 2018. **8**(18).

[111] Seino, Y., T. Ota, K. Takada, A. Hayashi, and M. Tatsumisago, *A sulphide lithium super ion conductor is superior to liquid ion conductors for use in rechargeable batteries.* Energy Environ. Sci., 2014. **7**(2): p. 627-631.

[112] Thangadurai, V., S. Narayanan, and D. Pinzaru, *Garnet-type solid-state fast Li ion conductors for Li batteries: critical review.* Chem Soc Rev, 2014. **43**(13): p. 4714-27.

[113] Murugan, R., V. Thangadurai, and W. Weppner, *Fast Lithium Ion Conduction in Garnet-Type $Li_7La_3Zr_2O_{12}$.* Angewandte Chemie International Edition, 2007. **46**(41): p. 7778-7781.

[114] Aono, H., E. Sugimoto, Y. Sadaoka, N. Imanaka, and G.-y. Adachi, *Ionic conductivity and sinterability of lithium titanium phosphate system.* Solid State Ionics, 1990. **40-41**: p. 38-42.

[115] Zhu, Y., X. He, and Y. Mo, *Origin of Outstanding Stability in the Lithium Solid Electrolyte Materials: Insights from Thermodynamic Analyses Based on First-Principles Calculations.* ACS Applied Materials & Interfaces, 2015. **7**(42): p. 23685-23693.

[116] Nolan, A.M., Y. Zhu, X. He, Q. Bai, and Y. Mo, *Computation-Accelerated Design of Materials and Interfaces for All-Solid-State Lithium-Ion Batteries.* Joule, 2018. **2**(10): p. 2016-2046.

[117] Zhu, Y., X. He, and Y. Mo, *Strategies Based on Nitride Materials Chemistry to Stabilize Li Metal Anode.* Adv Sci (Weinh), 2017. **4**(8): p. 1600517.

[118] He, X., Y. Zhu, and Y. Mo, *Origin of fast ion diffusion in super-ionic conductors.* Nature Communications, 2017. **8**: p. 15893.

[119] Zachariasen, W.H., *II. The Crystal Structure of Titanite.* Zeitschrift für Kristallographie - Crystalline Materials, 1930. **73**(1): p. 7-16.

[120] Sebastian, L., J. Gopalakrishnan, and Y. Piffard, *Synthesis, crystal structure and lithium ion conductivity of $LiMgFSO_4$.* Journal of Materials Chemistry, 2002. **12**(2): p. 374-377.

[121] Genkina, E.A., B. Mill, and S. Kirsch, *Crystal structures of the sphenes $NaSbGeO_5$, $NaTaGeO_5$, and $LiTaSiO_5$.* Soviet physics. Crystallography, 1992. **37**: p. 769-772.

[122] Jain, A., et al., *Commentary: The Materials Project: A materials genome approach to accelerating materials innovation.* APL Materials, 2013. **1**(1).

[123] He, X., Y. Zhu, A. Epstein, and Y. Mo, *Statistical variances of diffusional properties from ab initio molecular dynamics simulations.* npj Computational Materials, 2018. **4**(1).

[124] Weber, D.A., A. Senyshyn, K.S. Weldert, S. Wenzel, W. Zhang, R. Kaiser, S. Berendts, J. Janek, and W.G. Zeier, *Structural Insights and 3D Diffusion Pathways within the Lithium Superionic Conductor Li10GeP2S12.* Chemistry of Materials, 2016. **28**(16): p. 5905-5915.

[125] Breuer, S., D. Prutsch, Q. Ma, V. Epp, F. Preishuber-Pflügl, F. Tietz, and M. Wilkening, *Separating bulk from grain boundary Li ion conductivity in the sol–gel prepared solid electrolyte $Li_{1.5}Al_{0.5}Ti_{1.5}(PO_4)_3$.* Journal of Materials Chemistry A, 2015. **3**(42): p. 21343-21350.

[126] Han, F., et al., *Interphase Engineering Enabled All-Ceramic Lithium Battery.* Joule, 2018. **2**(3): p. 497-508.

[127] Thangadurai, V., H. Kaack, and W.J.F. Weppner, *Novel Fast Lithium Ion Conduction in Garnet-Type $Li_5La_3M_2O_{12}$ (M = Nb, Ta).* Journal of the American Ceramic Society, 2003. **86**(3): p. 437-440.

[128] Kresse, G. and J. Furthmuller, *Efficient iterative schemes for ab initio total-energy calculations using a plane-wave basis set.* Physical Review B, 1996. **54**(16): p. 11169–11186.

[129] Perdew, J.P., M. Ernzerhof, and K. Burke, *Rationale for mixing exact exchange with density functional approximations.* The Journal of Chemical Physics, 1996. **105**(22): p. 9982–9985.

[130] Jain, A., G. Hautier, C.J. Moore, S. Ping Ong, C.C. Fischer, T. Mueller, K.A. Persson, and G. Ceder, *A high-throughput infrastructure for density functional theory calculations.* Computational Materials Science, 2011. **50**(8): p. 2295–2310.

[131] Jain, A., G. Hautier, S.P. Ong, C.J. Moore, C.C. Fischer, K.A. Persson, and G. Ceder, *Formation enthalpies by mixing GGA and GGA+U calculations.* Physical Review B, 2011. **84**(4): p. 045115.

[132] He, X. and Y. Mo, *Accelerated materials design of $Na_{0.5}Bi_{0.5}TiO_3$ oxygen ionic conductors based on first principles calculations.* Physical Chemistry Chemical Physics, 2015. **17**(27): p. 18035-18044.

[133] Willems, T.F., C.H. Rycroft, M. Kazi, J.C. Meza, and M. Haranczyk, *Algorithms and tools for high-throughput geometry-based analysis of crystalline porous materials.* Microporous and Mesoporous Materials, 2012. **149**(1): p. 134-141.

[134] Martin, R.L., B. Smit, and M. Haranczyk, *Addressing challenges of identifying geometrically diverse sets of crystalline porous materials.* J Chem Inf Model, 2012. **52**(2): p. 308-18.

[135] Shannon, R.D., *Revised effective ionic radii and systematic studies of interatomic distances in halides and chalcogenides.* Acta crystallographica section A: crystal

physics, diffraction, theoretical and general crystallography, 1976. **32**(5): p. 751-767.

[136] Nose, S., *Constant temperature molecular dynamics methods.* Progress of Theoretical Physics Supplement, 1991. **103**: p. 1–46.

[137] He, X., Y. Zhu, A. Epstein, and Y. Mo, *Statistical variances of diffusional properties from ab initio molecular dynamics simulations.* npj Computational Materials, 2018. **4**(1): p. 18.

[138] Toby, B.H., *EXPGUI, a graphical user interface for GSAS.* Journal of Applied Crystallography, 2001. **34**.

[139] Ellis, B.L. and L.F. Nazar, *Sodium and sodium-ion energy storage batteries.* Current Opinion in Solid State and Materials Science, 2012. **16**(4): p. 168-177.

[140] Larcher, D. and J.M. Tarascon, *Towards greener and more sustainable batteries for electrical energy storage.* Nature Chemistry, 2015. **7**(1): p. 19-29.

[141] Bai, Q., L. Yang, H. Chen, and Y. Mo, *Computational Studies of Electrode Materials in Sodium-Ion Batteries.* Advanced Energy Materials, 2018. **8**(17): p. 1702998.

[142] Yang, L., et al., *Design of high-performance cathode materials with single-phase pathway for sodium ion batteries: A study on P2-$Na_x(Li_yMn_{1-y})O_2$ compounds.* Journal of Power Sources, 2018. **381**: p. 171-180.

[143] Hong, S.Y., Y. Kim, Y. Park, A. Choi, N.-S. Choi, and K.T. Lee, *Charge carriers in rechargeable batteries: Na ions vs. Li ions.* Energy & Environmental Science, 2013. **6**(7): p. 2067-2081.

[144] Ma, X., K. An, J. Bai, and H. Chen, *$NaAlTi_3O_8$, A Novel Anode Material for Sodium Ion Battery.* Scientific Reports, 2017. **7**(1): p. 162.

[145] Dunn, B., H. Kamath, and J.-M. Tarascon, *Electrical Energy Storage for the Grid: A Battery of Choices.* Science, 2011. **334**(6058): p. 928-935.

[146] Lu, X., G. Xia, J.P. Lemmon, and Z. Yang, *Advanced materials for sodium-beta alumina batteries: Status, challenges and perspectives.* Journal of Power Sources, 2010. **195**(9): p. 2431-2442.

[147] Jung, Y.S., D.Y. Oh, Y.J. Nam, and K.H. Park, *Issues and Challenges for Bulk-Type All-Solid-State Rechargeable Lithium Batteries using Sulfide Solid Electrolytes.* Israel Journal of Chemistry, 2015. **55**(5): p. 472-485.

[148] Richards, W.D., T. Tsujimura, L.J. Miara, Y. Wang, J.C. Kim, S.P. Ong, I. Uechi, N. Suzuki, and G. Ceder, *Design and synthesis of the superionic conductor $Na_{10}SnP_2S_{12}$.* Nature Communications, 2016. **7**(1): p. 11009.

[149] Kandagal, V.S., M.D. Bharadwaj, and U.V. Waghmare, *Theoretical prediction of a highly conducting solid electrolyte for sodium batteries: $Na_{10}GeP_2S_{12}$.* Journal of Materials Chemistry A, 2015. **3**(24): p. 12992-12999.

[150] Hayashi, A., K. Noi, A. Sakuda, and M. Tatsumisago, *Superionic glass-ceramic electrolytes for room-temperature rechargeable sodium batteries.* Nat Commun, 2012. **3**: p. 856.

[151] Tanibata, N., K. Noi, A. Hayashi, and M. Tatsumisago, *Preparation and characterization of highly sodium ion conducting Na_3PS_4–Na_4SiS_4 solid electrolytes.* RSC Advances, 2014. **4**(33): p. 17120-17123.

[152] Chu, I.-H., C.S. Kompella, H. Nguyen, Z. Zhu, S. Hy, Z. Deng, Y.S. Meng, and S.P. Ong, *Room-Temperature All-solid-state Rechargeable Sodium-ion Batteries with a Cl-doped Na_3PS_4 Superionic Conductor.* Scientific Reports, 2016. **6**(1): p. 33733.

[153] Bo, S.-H., Y. Wang, J.C. Kim, W.D. Richards, and G. Ceder, *Computational and Experimental Investigations of Na-Ion Conduction in Cubic Na_3PSe_4.* Chemistry of Materials, 2016. **28**(1): p. 252-258.

[154] Wang, H., Y. Chen, Z.D. Hood, G. Sahu, A.S. Pandian, J.K. Keum, K. An, and C. Liang, *An Air-Stable Na_3SbS_4 Superionic Conductor Prepared by a Rapid and Economic Synthetic Procedure.* Angew Chem Int Ed Engl, 2016. **55**(30): p. 8551-5.

[155] Banerjee, A., K.H. Park, J.W. Heo, Y.J. Nam, C.K. Moon, S.M. Oh, S.T. Hong, and Y.S. Jung, *Na_3SbS_4 : A Solution Processable Sodium Superionic Conductor for All-Solid-State Sodium-Ion Batteries.* Angew Chem Int Ed Engl, 2016. **55**(33): p. 9634-8.

[156] Eisenmann, B.a.R.Z., *Selenoantimonate: Darstellung und Struktur von Na_3SbSe_4, K_3SbSe_4 und $[Ba(en)_4]_2[Ba(en)_3](SbSe_4)_2$/ Selenoantimonates(V): Preparation and Crystal Structure of Na_3SbSe_4, K_3SbSe_4 and $[Ba(en)_4]_2[Ba(en)_3](SbSe_4)_2$.* Zeitschrift für Naturforschung B, 1989. **44**(3): p. 8.

[157] Rao, R.P., H. Chen, L.L. Wong, and S. Adams, *$Na_{3+x}M_xP_{1-x}S_4$ (M = Ge^{4+}, Ti^{4+}, Sn^{4+}) enables high rate all-solid-state Na-ion batteries $Na_{2+2\delta}Fe_{2-\delta}(SO_4)_3|Na_{3+x}M_xP_{1-x}S_4|Na_2Ti_3O_7$.* Journal of Materials Chemistry A, 2017. **5**(7): p. 3377-3388.

[158] Ohno, S., et al., *How Certain Are the Reported Ionic Conductivities of Thiophosphate-Based Solid Electrolytes? An Interlaboratory Study.* ACS Energy Letters, 2020. **5**(3): p. 910-915.

[159] Kraft, M.A., et al., *Influence of Lattice Polarizability on the Ionic Conductivity in the Lithium Superionic Argyrodites Li_6PS_5X (X = Cl, Br, I).* J Am Chem Soc, 2017. **139**(31): p. 10909-10918.

[160] Krauskopf, T., C. Pompe, M.A. Kraft, and W.G. Zeier, *Influence of Lattice Dynamics on Na^+ Transport in the Solid Electrolyte $Na_3PS_{4-x}Se_x$.* Chemistry of Materials, 2017. **29**(20): p. 8859-8869.

[161] Bo, S.-H., Y. Wang, and G. Ceder, *Structural and Na-ion conduction characteristics of $Na_3PS_xSe_{4-x}$.* Journal of Materials Chemistry A, 2016. **4**(23): p. 9044-9053.

[162] Zhu, Z., I.-H. Chu, Z. Deng, and S.P. Ong, *Role of Na^+ Interstitials and Dopants in Enhancing the Na^+ Conductivity of the Cubic Na_3PS_4 Superionic Conductor.* Chemistry of Materials, 2015. **27**(24): p. 8318-8325.

[163] Zhang, L., D. Zhang, K. Yang, X. Yan, L. Wang, J. Mi, B. Xu, and Y. Li, *Vacancy-Contained Tetragonal Na_3SbS_4 Superionic Conductor.* Adv Sci (Weinh), 2016. **3**(10): p. 1600089.

[164] Toby, B.H., *EXPGUI, a graphical user interface for GSAS.* Journal of Applied Crystallography, 2001. **34**(2): p. 210-213.

[165] Kim, S.K., A. Mao, S. Sen, and S. Kim, *Fast Na-Ion Conduction in a Chalcogenide Glass–Ceramic in the Ternary System $Na_2Se–Ga_2Se_3–GeSe_2$.* Chemistry of Materials, 2014. **26**(19): p. 5695-5699.

[166] Yamanaka, T., A. Hayashi, A. Yamauchi, and M. Tatsumisago, *Preparation of magnesium ion conducting $MgS–P_2S_5–MgI_2$ glasses by a mechanochemical technique.* Solid State Ionics, 2014. **262**: p. 601-603.

[167] Canepa, P., et al., *High magnesium mobility in ternary spinel chalcogenides.* Nature Communications, 2017. **8**(1): p. 1759.

[168] Minami, K., A. Hayashi, and M. Tatsumisago, *Crystallization Process for Superionic $Li_7P_3S_{11}$ Glass-Ceramic Electrolytes.* Journal of the American Ceramic Society, 2011. **94**(6): p. 1779-1783.

[169] Hayashi, A., K. Minami, F. Mizuno, and M. Tatsumisago, *Formation of Li^+ superionic crystals from the $Li_2S–P_2S_5$ melt-quenched glasses.* Journal of Materials Science, 2008. **43**(6): p. 1885-1889.

[170] Ramos, E.P., Z. Zhang, A. Assoud, K. Kaup, F. Lalère, and L.F. Nazar, *Correlating Ion Mobility and Single Crystal Structure in Sodium-Ion Chalcogenide-Based Solid State Fast Ion Conductors: $Na_{11}Sn_2PnS_{12}$ (Pn = Sb, P).* Chemistry of Materials, 2018. **30**(21): p. 7413-7417.

[171] Fukushima, A., A. Hayashi, H. Yamamura, and M. Tatsumisago, *Mechanochemical synthesis of high lithium ion conducting solid electrolytes in a Li_2S-P_2S_5-Li_3N system.* Solid State Ionics, 2017. **304**: p. 85-89.

[172] Tarascon, J.-M., M. Morcrette, J. Saint, L. Aymard, and R. Janot, *On the benefits of ball milling within the field of rechargeable Li-based batteries.* Comptes Rendus Chimie, 2005. **8**(1): p. 17-26.

[173] Rao, R.P., X. Zhang, K.C. Phuah, and S. Adams, *Mechanochemical synthesis of fast sodium ion conductor $Na_{11}Sn_2PSe_{12}$ enables first sodium–selenium all-solid-state battery.* Journal of Materials Chemistry A, 2019. **7**(36): p. 20790-20798.

[174] Rangasamy, E., Z. Liu, M. Gobet, K. Pilar, G. Sahu, W. Zhou, H. Wu, S. Greenbaum, and C. Liang, *An Iodide-Based $Li_7P_2S_8I$ Superionic Conductor.* Journal of the American Chemical Society, 2015. **137**(4): p. 1384-1387.

[175] Sedlmaier, S.J., S. Indris, C. Dietrich, M. Yavuz, C. Dräger, F. von Seggern, H. Sommer, and J. Janek, *Li_4PS_4I: A Li^+ Superionic Conductor Synthesized by a Solvent-Based Soft Chemistry Approach.* Chemistry of Materials, 2017. **29**(4): p. 1830-1835.

[176] Ujiie, S., A. Hayashi, and M. Tatsumisago, *Structure, ionic conductivity and electrochemical stability of Li_2S–P_2S_5–LiI glass and glass–ceramic electrolytes.* Solid State Ionics, 2012. **211**: p. 42-45.

[177] Wang, X., S. Tan, X.-Q. Yang, and E. Hu, *Pair distribution function analysis: Fundamentals and application to battery materials.* Chinese Physics B, 2020. **29**(2): p. 028802.

[178] Billinge, S.J.L., *The rise of the X-ray atomic pair distribution function method: a series of fortunate events.* Philosophical Transactions of the Royal Society A: Mathematical, Physical and Engineering Sciences, 2019. **377**(2147): p. 20180413.

[179] Shiotani, S., K. Ohara, H. Tsukasaki, S. Mori, and R. Kanno, *Pair distribution function analysis of sulfide glassy electrolytes for all-solid-state batteries: Understanding the improvement of ionic conductivity under annealing condition.* Scientific Reports, 2017. **7**(1): p. 6972.

[180] Dong, B., M.P. Stockham, P.A. Chater, and P.R. Slater, *X-ray pair distribution function analysis and electrical and electrochemical properties of cerium doped $Li_5La_3Nb_2O_{12}$ garnet solid-state electrolyte.* Dalton Transactions, 2020. **49**(33): p. 11727-11735.

[181] Tanibata, N., K. Noi, A. Hayashi, and M. Tatsumisago, *Preparation and characterization of highly sodium ion conducting Na_3PS_4–Na_4SiS_4 solid electrolytes.* RSC Adv., 2014. **4**(33): p. 17120-17123.

[182] Hibi, Y., N. Tanibata, A. Hayashi, and M. Tatsumisago, *Preparation of sodium ion conducting Na_3PS_4–NaI glasses by a mechanochemical technique.* Solid State Ionics, 2015. **270**: p. 6-9.

[183] Dietrich, C., et al., *Local Structural Investigations, Defect Formation, and Ionic Conductivity of the Lithium Ionic Conductor $Li_4P_2S_6$.* Chemistry of Materials, 2016. **28**(23): p. 8764-8773.

[184] Dietrich, C., D.A. Weber, S.J. Sedlmaier, S. Indris, S.P. Culver, D. Walter, J. Janek, and W.G. Zeier, *Lithium ion conductivity in $Li_2S–P_2S_5$ glasses – building units and local structure evolution during the crystallization of superionic conductors Li_3PS_4, $Li_7P_3S_{11}$ and $Li_4P_2S_7$.* Journal of Materials Chemistry A, 2017. **5**(34): p. 18111-18119.

[185] Juhás, P., C.L. Farrow, X. Yang, K.R. Knox, and S.J. Billinge, *Complex modeling: a strategy and software program for combining multiple information sources to solve ill posed structure and nanostructure inverse problems.* Acta Crystallographica Section A, 2015. **71**(6): p. 562-568.

[186] Ravel, B. and M. Newville, *ATHENA, ARTEMIS, HEPHAESTUS: data analysis for X-ray absorption spectroscopy using IFEFFIT.* Journal of Synchrotron Radiation, 2005. **12**(4): p. 537-541.

[187] Qiu, X., J.W. Thompson, and S.J. Billinge, *PDFgetX2: a GUI-driven program to obtain the pair distribution function from X-ray powder diffraction data.* Journal of Applied Crystallography, 2004. **37**(4): p. 678-678.

[188] Farrow, C.L., P. Juhas, J.W. Liu, D. Bryndin, E.S. Božin, J. Bloch, T. Proffen, and S.J.L. Billinge, *PDFfit2 and PDFgui: computer programs for studying nanostructure in crystals.* Journal of Physics: Condensed Matter, 2007. **19**(33): p. 335219.

[189] Jumas, J.-C., E. Philippot, F. Vermot-Gaud-Daniel, M. Ribes, and M. Maurin, *Etude de la tétracoordination de l'etain dans deux orthothiostannates: Na_4SnS_4 et Ba_2SnS_4 (α).* Journal of Solid State Chemistry, 1975. **14**(4): p. 319-327.

[190] Moon, C.K., et al., *Vacancy-Driven Na^+ Superionic Conduction in New Ca-Doped Na_3PS_4 for All-Solid-State Na-Ion Batteries.* ACS Energy Letters, 2018. **3**(10): p. 2504-2512.

[191] Duchardt, M., U. Ruschewitz, S. Adams, S. Dehnen, and B. Roling, *Vacancy‐Controlled Na^+ Superion Conduction in $Na_{11}Sn_2PS_{12}$.* Angewandte Chemie International Edition, 2018. **57**(5): p. 1351-1355.

[192] Zhang, Z., et al., *Correlated Migration Invokes Higher Na^+‐Ion Conductivity in NaSICON‐Type Solid Electrolytes.* Advanced Energy Materials, 2019. **9**(42).

[193] Feng, X., P.-H. Chien, Z. Zhu, I.-H. Chu, P. Wang, M. Immediato-Scuotto, H. Arabzadeh, S.P. Ong, and Y.-Y. Hu, *Studies of Functional Defects for Fast Na-Ion Conduction in $Na_{3-y}PS_{4-x}Cl_x$ with a Combined Experimental and Computational Approach.* Advanced Functional Materials, 2019. **29**(9).

[194] Zhang, Z., E. Ramos, F. Lalère, A. Assoud, K. Kaup, P. Hartman, and L.F. Nazar, *$Na_{11}Sn_2PS_{12}$: a new solid state sodium superionic conductor.* Energy & Environmental Science, 2018. **11**(1): p. 87-93.

[195] Gao, Y., A.M. Nolan, P. Du, Y. Wu, C. Yang, Q. Chen, Y. Mo, and S.-H. Bo, *Classical and Emerging Characterization Techniques for Investigation of Ion Transport Mechanisms in Crystalline Fast Ionic Conductors.* Chemical Reviews, 2020. **120**(13): p. 5954-6008.

[196] Park, K.H., et al., *Solution-Processable Glass LiI-Li_4SnS_4 Superionic Conductors for All-Solid-State Li-Ion Batteries.* Adv Mater, 2016. **28**(9): p. 1874-83.

[197] Toby, B.H., *EXPGUI, a graphical user interface for GSAS.* JOURNAL OF APPLIED CRYSTALLOGRAPHY, 2001. **34**(2): p. 4.

[198] Sendek, A.D., Q. Yang, E.D. Cubuk, K.-A.N. Duerloo, Y. Cui, and E.J. Reed, *Holistic computational structure screening of more than 12 000 candidates for solid lithium-ion conductor materials.* Energy & Environmental Science, 2017. **10**(1): p. 306-320.

[199] Schmidt, J., M.R.G. Marques, S. Botti, and M.A.L. Marques, *Recent advances and applications of machine learning in solid-state materials science.* npj Computational Materials, 2019. **5**(1): p. 83.

[200] Boebinger, M.G., J.A. Lewis, S.E. Sandoval, and M.T. McDowell, *Understanding Transformations in Battery Materials Using in Situ and Operando Experiments: Progress and Outlook.* ACS Energy Letters, 2020. **5**(1): p. 335-345.